

PREDICTING THE INFLUENCE OF WEAVE ARCHITECTURE ON THE STRESS
RELAXATION BEHAVIOR OF WOVEN COMPOSITE USING FINITE ELEMENT
BASED MICROMECHANICS

A Thesis by

Anand Vijay Karuppiah

Bachelor of Engineering, Anna University, 2012

Submitted to the Department of Aerospace Engineering
and the faculty of the Graduate School of
Wichita State University
in partial fulfillment of
the requirements for the degree of
Master of Science

December 2016

© Copyright 2016 by Anand Vijay Karuppiyah

All Rights Reserved

**PREDICTING THE INFLUENCE OF WEAVE ARCHITECTURE ON THE STRESS
RELAXATION BEHAVIOR OF WOVEN COMPOSITE USING FINITE ELEMENT BASED
MICROMECHANICS**

The following faculty members have examined the final copy of this thesis for form and content, and recommend that it be accepted in partial fulfillment of the requirement for the degree of Master of Science with a major in Aerospace Engineering.

Suresh Raju Keshavanarayana, Committee Chair

Charles Yang, Committee Member

Ramazan Asmatulu, Committee Member

DEDICATION

I dedicate my thesis to

my beloved grandfather Arunachalam and my grandmother Savithri

And

To my father MS Karuppiah, my mother K Pappa and my brother KR Arun, for their

love, patience, immense support and sacrifices

ACKNOWLEDGEMENT

First of all, I am thankful to GOD and my family for their blessing and support over my studies and research. Especially to my brother for being patient, and more supportive throughout my masters.

I wish to express my deep sense of gratitude to my advisor Dr.Suresh Keshavanarayana for supporting me both financially and morally. Without his constant guidance and patience, this work would have never been completed. His emphasis on quality adds a great deal to the learning process and advancement of my research.

I would also like to thank my colleagues and friends Akhil, Bhupen, Manoj, Aswini and Aakash for their support on experiments. My special thanks to Kevontrez and Abhiruchika for their full support on thermal analysis.

I owe special thanks to the people of National Institute for Aviation research (NIAR) Ping, Ruchira, Chi, and Chandika for the guidance of experiments and solving problems. I would also like to express my gratitude to Dr. Charles Yang and Dr. Ramazan Asmatulu for serving on my thesis committee and providing the valuable time from their busy schedules.

ABSTRACT

Advanced textile composites employed in automobile and aerospace industries are heterogeneous and viscoelastic in nature. In an attempt to predict its true macro-level viscoelastic response, a finite element based micromechanics model of 5320-8HS (8-harness satin weave) woven composite was assembled to capture the effects of the individual constituents and their microstructure. The study was focused on the influence of weave architecture over its effective response. The model was developed from the microscopy of woven composite cross section using sub-cell modeling approach. It is idealized to contain a linearly viscoelastic matrix and orthogonally interlaced unidirectional composite tows with undulation and floating regions. All the free surfaces are subjected to kinematic conditions of periodic symmetry to recreate Representative Unit cell (RUC) of 8-harness satin weave architecture. Constitutive model of viscoelastic material assumed to follow Prony series. Time-dependent Poisson's ratio is also incorporated in the unit cell model with an assumption of constant bulk modulus.

Experiments are performed on the 5320-1 EO (Extended Out time) epoxy resin and 5320-8HS woven composite under uniaxial tension and 3-point bending. Problems related with axial testing are summarized and results are compared with model predictions. Utilizing the finite element analysis of microstructure, axial and shear stress distribution for both fiber bundle and neat resin was analyzed in the region of contact and maximum stress concentration. Interestingly, the results of current study indicate that shear relaxation of tow undulation and gap region of neat resin along thickness dominate the effective response under tension and shear. Furthermore, stress relaxation predicted by laminate model under 3-point bending for different stacking sequence compare very well with the test data.

TABLE OF CONTENTS

Chapter	Page
1. INTRODUCTION	1
2. BACKGROUND AND LITERATURE REVIEW	4
2.1 Polymer	4
2.2 Time-Dependent Behavior of Polymers	5
2.3 Mathematical Models of Viscoelastic material.....	6
2.3.1 The Maxwell model.....	6
2.3.2 The Generalized Maxwell Model	8
2.3.3 Constitutive model for linear viscoelastic material	9
2.4 Polymer Matrix Composites (PMCs)	10
2.4.1 Macro-Mechanical Approach	10
2.4.2 Micro-Mechanical Approach.....	10
2.5 Earlier history of works	11
2.5.1 Influence of Continuous fiber system on polymer viscoelasticity	11
2.5.2 Influence of weave architecture on polymer viscoelasticity.....	18
2.5.3 Limitations.....	23
2.6 Motivation and Objective of Research	23
3. EXPERIMENTAL APPROACH.....	25
3.1 Materials	25
3.2 Fabrication of Resin Specimens.....	26
3.2.1 Mold Preparation	26
3.2.2 5320-1 Resin Specimen	27
3.3 Glass Transition Temperature (T_g) of 5320-1 Resin.....	29
3.4 Determination of Linear Viscoelastic Region (LVR)	30
3.5 Stress Relaxation of 5320-1 Epoxy Resin	33
3.6 Time-Temperature Superposition (TTS) and Shift function	34
3.7 Fabrication of 5320-8HS Specimen.....	35
3.8 Uniaxial Tension Testing.....	36
3.9 Problems and limitations of uniaxial testing.....	38
3.10 3-Point Bending Test	38
4. COMPUTATIONAL MICROMECHANICS MODEL AND MESH GENERATION ...	40
4.1 Geometry of 8-harness Satin Unit Cell	40
4.2 Mesh Generation	48
4.2.1 Development of primary subcells	49
4.2.2 Assembly of developed binary subcells	52
4.2.3 Development of complete unit cell of 8-harness weave architecture	53
5. FINITE ELEMENT BASED MICROMECHANICS APPROACH	56
5.1 Finite Element Approach	56
5.2 Thermomechanical properties of fiber bundles/tows.....	57

TABLE OF CONTENTS (continued)

Chapter	Page
5.2.1 Unit Cell Model of Unidirectional Composite	57
5.3 Thermomechanical Properties of 8-HS Unit cell.....	60
5.4 Geometry and contact body definition.....	61
5.5 Load cases and Boundary Conditions.....	63
5.5.1 Periodic Constraints and Boundary Conditions.....	63
5.5.2 Load cases.....	64
5.6 Determination of Thermomechanical properties	67
5.6.1 Elastic Properties	67
5.6.2 Coefficient of Thermal Expansion (CTE) and Viscoelastic Properties	68
5.7 Macro mechanical Model of 5320-8HS woven composite.....	69
6. VALIDATION OF MICROMECHANICS MODEL.....	71
6.1 Validation of Elastic Properties	71
6.2 Uniaxial Tension.....	72
6.2.1 Case 1 and Case 2: 0 and 90 degree (Fill and Warp direction)	72
6.2.2 Case 3: 45 degree (In-Plane Shear)	78
6.3 3-Point Bending	81
6.3.1 Case 1: [0/90] _s	81
6.3.2 Case 2: [±45] _s	84
7. RESULTS AND DISCUSSIONS	87
7.1 Micromechanical Analysis of Satin Weave Architecture	87
7.1.1 Stress distribution	87
7.1.2 Case 1: Axial loading along fill direction (along x-axis)	89
7.1.3 Case 2: Tangential loading along warp direction (in-plane shear)	106
7.2 Macromechanical Analysis under flexural loading	117
7.2.1 Case 1: [0/90] _s	117
7.2.2 Case 2: [±45] _s	121
8. CONCLUSIONS AND FUTURE WORK	126
8.1 Conclusion	126
8.2 Future Study.....	128
REFERENCES	130
APPENDICES	136
Appendix A	137
Appendix B	140
Appendix C	143
Appendix D	148
Appendix E	150
Appendix F.....	156

LIST OF TABLES

Table		Page
1.	Measured dimensions of an 8-harness satin unit cell	43
2.	Assembly Matrix for Binary subcells of 8-harness weave architecture	49
3.	Five primary subcells to model full 8-harness unit cell	51
4.	Elastic and thermal properties of the fiber and neat resin	59
5.	Relaxation times and coefficients of the Prony series for 5320-1 Epoxy Resin	60
6.	Elastic Properties of 5320-8HS woven composite	72

LIST OF FIGURES

Figure	Page
1. Different Types of Weave Architecture	2
2. Molecular Structure of Thermoplastic and Thermoset Polymers.....	4
3. Stress Relaxation Behavior of Different materials under constant deformation	6
4. Schematics of a Maxwell Model	7
5. The Generalized Maxwell model	9
6. Repeating Unit cell model of Aboudi.....	13
7. Geometry of the unit cell	14
8. Repeating cell in GMC consisting of N subcells in all three directions.....	15
9. Mori-Tanaka model with distinct inclusion [left]and Benveniste model with annular interface region [right].....	16
10. Unit cell model from different types of fiber packing's: a) Hexagonal Array b) Square Array c) Bidirectional crossed array.....	17
11. Unit cell of Plain Weave fabric	19
12. Comparison of theoretical and experimental data at different loads and 66°C	19
13. 3D Unit cell of Plain Weave a) without matrix b) with matrix	21
14. creep compliance of the plain weave fabric by Shrotriya a) Fill direction b) Warp direction.....	21
15. Normalized Creep Compliance Curves of 2D Finite element based micromechanics model of plain weave : 5) Viscoelastic fiber bundle 5A) Elastic fiber bundle 5B) Matrix with constant bulk modulus 5C) Shifted Relaxation spectrum of case 5B	22
16. Prepreg material of 5320-8HS woven composite.....	25
17. Roll of 5320-1 EO epoxy resin material.....	26
18. Silicon Mold preparation	27

LIST OF FIGURES (continued)

Figure		Page
19.	Specimen preparation of 5320-1 Epoxy resin	28
20.	Differential Scanning Calorimeter (DSC) Q2000 series of TA Instruments	29
21.	Glass Transition Temperature (Tg) of 5320-1 Epoxy Resin	30
22.	Linear viscoelastic Region of 5320-1 Epoxy Resin Using Dynamic Mechanical Analyzer (DMA)	31
23.	Linear viscoelastic Region (LVR) of 5320-8HS	32
24.	Verification of Linear viscoelastic Region for 5320-8HS after loading	32
25.	Test Setup for Stress Relaxation of 5320-1 Epoxy Resin Using Dynamic Mechanical Analyzer (DMA)	33
26.	Construction of master curve from distinct curves of individual temperatures	35
27.	Vacuum Bagging	36
28.	Stress Relaxation Test setup of 5320-8HS woven composite using 810 Material Test System (MTS) (5500lbf load cell).....	37
29.	Stress Relaxation of 5320-8HS and 5320-1 epoxy resin under 3-Point Bending using Dynamic Mechanical Analyzer (DMA)	39
30.	Schematics of a) Axio Vision Microscope b) Potted 5320-8HS Specimens.....	41
31.	Photomicrograph of 5320-8HS Laminate	41
32.	Repetitive Unit Cell (RUC) Of 5320-8HS Woven Composite (Top View of 5320-8HS Prepreg material)	42
33.	Dimensions of 5320-8HS Unit cell	42
34.	Greyscale image of tow cross section (ROI-Region of Interest).....	42
35.	Geometry of 5320-8HS unit cell with no resin	44
36.	Geometry of 5320-8HS unit cell with resin	45

LIST OF FIGURES (continued)

Figure	Page
37. Solid geometry of fill and warp tows	50
38. Reflectional symmetries of subcell 1	50
39. Assembly of binary subcells for 8-harness weave architecture.....	52
40. Generated mesh of a) Fill Tows and b) Warp Tows	53
41. Generated mesh of Interlaced tows and neat resin	54
42. Fully assembled discretized unit cell model of 8-harness woven composite	55
43. Micromechanics Approach for stress relaxation analysis of 5320-8HS woven composite	57
44. Unit cells of Unidirectional Composite.....	58
45. Hexagonal array Of unidirectional composite.....	59
46. Contact table for 5320-8HS Unit cell model	61
47. Contact Bodies of 5320-8HS Unit cell model a)With Resin b)Without Resin	62
48. Defining constant dilatation and assumed strain in the MSC MARC FEA	63
49. Schematics of a) unit cell, and their periodic boundary conditions for.....	65
50. Schematics of periodic boundary conditions of unit cell for.....	66
51. Homogenized solid model of 5320-8HS laminate	69
52. Boundary conditions of 3-Point Bending Model a) Front View b) Side view	70
53. Comparison of reduction in modulus among numerical and experimental results of 5320-8HS [0/90]loaded along fill direction and 5320-1 Resin at 80 °C (Tension).....	73
54. Normalized relaxation curves of 5320-8HS [0/90] loaded along fill direction and 5320-1 Epoxy resin under isothermal condition of 80 °C (Tension).....	74
55. Normalized relaxation curves of 5320-8HS [0/90] loaded along fill direction and 5320-1 Epoxy resin under isothermal condition of 100 °C (Tension).....	74

LIST OF FIGURES (continued)

Figure		Page
56.	Normalized relaxation curves of 5320-8HS [0/90] loaded along fill direction and 5320-1 Epoxy resin under isothermal condition of 120 °C (Tension).....	75
57.	Normalized relaxation curves of 5320-8HS [0/90] loaded along fill direction and 5320-1 Epoxy resin under isothermal condition of 160 °C (Tension).....	75
58.	Normalized relaxation curves of 5320-8HS [0/90] loaded along warp direction and 5320-1 Epoxy resin under isothermal condition of 80 °C (Tension)	76
59.	Normalized relaxation curves of 5320-8HS [0/90] loaded along warp direction and 5320-1 Epoxy resin under isothermal condition of 100 °C (Tension)	76
60.	Normalized relaxation curves of 5320-8HS [0/90] loaded along warp direction and 5320-1 Epoxy resin under isothermal condition of 120°C (Tension)	77
61.	Normalized relaxation curves of 5320-8HS [0/90] loaded along warp direction and 5320-1 Epoxy resin under isothermal condition of 160 °C (Tension)	77
62.	Comparison of reduction in modulus among 5320-8HS oriented at [± 45]and 5320-1 Resin at 80 °C (Tension)	78
63.	Normalized relaxation curves of 5320-8HS [± 45]and 5320-1 Epoxy resin under isothermal condition of 80 °C (Tension)	79
64.	Normalized relaxation curves of 5320-8HS [± 45]and 5320-1 Epoxy resin under isothermal condition of 100 °C (Tension)	79
65.	Normalized relaxation curves of 5320-8HS [± 45]and 5320-1 Epoxy resin under isothermal condition of 120 °C (Tension)	80
66.	Normalized relaxation curves of 5320-8HS [± 45]and 5320-1 Epoxy resin under isothermal condition of 160 °C (Tension)	80
67.	Normalized relaxation curves of 5320-8HS [0/90]s and 5320-1 Epoxy resin under isothermal condition of 80 °C (3-point bending)	82
68.	Normalized relaxation curves of 5320-8HS [0/90]s and 5320-1 Epoxy resin under isothermal condition of 100 °C (3-point bending)	82
69.	Normalized relaxation curves of 5320-8HS [0/90]s and 5320-1 Epoxy resin under isothermal condition of 120 °C (3-point bending)	83

LIST OF FIGURES (continued)

Figure	Page
70. Normalized relaxation curves of 5320-8HS [0/90]s and 5320-1 Epoxy resin under isothermal condition of 160 °C (3-point bending)	83
71. Comparison of reduction in modulus among 5320-8HS oriented at [±45]s and 5320-1 Resin at 160 °C (3-point bending).....	84
72. Normalized relaxation curves of 5320-8HS [±45]s and 5320-1 Epoxy resin under isothermal condition of 80 °C (3-point bending)	85
73. Normalized relaxation curves of 5320-8HS [±45]s and 5320-1 Epoxy resin under isothermal condition of 100 °C (3-point bending)	85
74. Normalized relaxation curves of 5320-8HS [±45]s and 5320-1 Epoxy resin under isothermal condition of 120 °C (3-point bending)	86
75. Normalized relaxation curves of 5320-8HS [±45]s and 5320-1 Epoxy resin under isothermal condition of 160 °C (3-point bending)	86
76. Region of Interest (ROI) in the tows of 5320-8HS unit cell model	88
77. Region of Interest (ROI) in the neat resin of 5320-8HS unit cell model	89
78. Stress contours for component 11 of stress (σ_{11}) of fill tow#5 at different loading times under isothermal condition of 80 °C.....	90
79. Distribution of normalized component 11 of stress (σ_{11}) for fill tow#5 at different loading times under isothermal condition of 80 °C.....	91
80. Stress contours for component 11 of stress (σ_{11}) of warp tow#5 at different loading times under isothermal condition of 80 °C.....	91
81. Distribution of component 11 of stress (σ_{11}) for warp tow#5 at different loading times under isothermal condition of 80 °C	92
82. Distribution of normalized component 11 of stress (σ_{11}) for warp tow#5 at different loading times under isothermal condition of 80 °C.....	92
83. Stress contours for component 11 of stress (σ_{11}) of neat resin located between interlaced tows at different loading times under isothermal condition of 80 °C (ROI-Region of Interest).....	93

LIST OF FIGURES (continued)

Figure	Page
84. Distribution of component 11 of stress (σ_{11}) for neat resin located between interlaced tows at different loading times under isothermal condition of 80 °C.....	93
85. Distribution of normalized component 11 of stress (σ_{11}) for fill tow#5 at different relaxation times under isothermal condition of 80 °C (Base : Peak stress of every increment).....	94
86. Distribution of normalized Component 11 of stress (σ_{11}) for fill tow#5 at different relaxation times under isothermal condition of 80 °C (Base : stress at t=60s)	95
87. Distribution of component 11 of stress (σ_{11}) for warp tow#5 at different relaxation times under isothermal condition of 80 °C.....	95
88. Distribution of normalized Component 11 for stress (σ_{11}) for warp tow#5 at different relaxation times under isothermal condition of 80 °C (Base : stress at t=60s)	96
89. Distribution of Component 11 of stress (σ_{11}) for neat resin located between interlaced tows at different relaxation times under isothermal condition of 80 °C.....	96
90. Region of Interest (ROI) from the cut section of fill tow#5	97
91. Comparison of all the stress components for fill tow#5 in the contact region of Resin during relaxation at 80 °C.....	98
92. Comparison of all the stress components for fill tow#5 in the vicinity of Warp tow#5 during relaxation at 80 °C.....	98
93. Relaxation curves of components 11, 22 and 23 of stress for fill tow#5 in the contact region of Resin at 100 °C	99
94. Relaxation curves of components 12 and 33 of stress for fill tow#5 in the contact region of Resin 120 °C	99
95. Relaxation curve of component 11 of stress for fill tow#5 in the contact region of Resin at 160 °C.....	100
96. Region of Interest (ROI) from warp tow#5	100

LIST OF FIGURES (continued)

Figure	Page
97. Comparison of all the stress components for warp tow#5 in the contact region of Resin during relaxation at 80 °C.....	101
98. Relaxation curves of components 11 and 12 of stress for warp tow#5 in the contact region of Resin at 100 °C	101
99. Relaxation curves of components 23 and 12 of stress for warp tow#5 in the contact region of Resin at 120 °C	102
100. Relaxation curves of components 22 and 31 of stress for warp tow#5 in the contact region of Resin at 160 °C	102
101. Region of Interest (ROI) from neat resin	103
102. Comparison of all the stress components for neat resin in the vicinity of interlaced tows (ROI-01) during relaxation at 80 °C.....	104
103. Comparison of all the stress components for neat resin in the vicinity of interlaced tows (ROI-02) during relaxation at 80 °C.....	104
104. Relaxation curves of components 12 and 23 of stress for neat resin in the vicinity of interlaced tows (ROI-01) at 100 °C.....	105
105. Relaxation curve of component 12 of stress for neat resin in the vicinity of interlaced tows (ROI-01) at 120 °C.....	105
106. Relaxation curve of component 22 of stress for neat resin in the vicinity of interlaced tows (ROI-01) at 160 °C.....	106
107. Distribution of component 12 of stress (σ_{12}) for fill tow#5 at different loading times under isothermal condition of 80 °C	107
108. Distribution of component 12 of stress (σ_{12}) for warp tow#5 at different loading times under isothermal condition of 80 °C	108
109. Distribution of component 12 of stress (σ_{12}) for neat resin located between interlaced tows at different loading times under isothermal condition of 80 °C.....	108

LIST OF FIGURES (continued)

Figure	Page
110. Distribution of normalized component 12 of stress (σ_{12}) for fill tow#5 at different relaxation times under isothermal condition of 80 °C (Base : Peak stress of every increment).....	109
111. Distribution of component 12 of stress (σ_{12}) for fill tow#5 at different relaxation times under isothermal condition of 80 °C (Base : Peak stress of every increment) ...	110
112. Distribution of component 12 of stress (σ_{12}) for neat resin located between interlaced tows at different relaxation times under isothermal condition of 80 °C.....	110
113. Region of Interest (ROI) from fill and warp tow#5	111
114. Comparison of all the stress components for Fill tow#5 in the region of interest (ROI) during relaxation at 80 °C.....	112
115. Relaxation curves of component 12 of stress for fill tow#5 at elevated temperatures.	112
116. Comparison of all the stress components for warp tow#5 in the region of interest (ROI) during relaxation at 80 °C.....	113
117. Relaxation curves of component 33 and 12 of stresses for warp tow#5 in the region of interest (ROI) at 160 °C.....	113
118. Relaxation curves of component 12 of stress for warp tow#5 at elevated temperatures	114
119. Region of Interest (ROI) from fill and warp tow#5	115
120. Comparison of all the stress components for neat region in the region of interest (ROI) during relaxation at 80 °C.....	115
121. Relaxation curves of component 12 of stress for warp tow#5 at elevated temperatures	116
122. Relaxation curves of component 33 of stress for warp tow#5 at elevated temperatures	116
123. Region of interest (ROI) in the laminate model [0/90]s a) Below loading nose b) 4.5mm away from loading nose.....	118

LIST OF FIGURES (continued)

Figure	Page
124. Relaxation curves of component 11 of stress for laminate model [0/90]s at different relaxation times under isothermal condition of 160 °C (ROI-01).....	119
125. Relaxation curves of component 11 of stress for laminate model [0/90]s at different relaxation times under isothermal condition of 160 °C (ROI-02).....	119
126. Relaxation curves of component 12 of stress for laminate model [0/90]s at different relaxation times under isothermal condition of 160 °C (ROI-01).....	120
127. Relaxation curves of component 12 of stress for laminate model [0/90]s at different relaxation times under isothermal condition of 160 °C (ROI-02).....	120
128. Region of interest (ROI) in the laminate model [±45]s below loading nose.....	121
129. Region of interest (ROI) in the laminate model [±45]s 4.5mm away from loading nose	122
130. Relaxation curves of component 11 of stress for laminate model [±45]s at different relaxation times under isothermal condition of 160 °C (ROI-01).....	122
131. Relaxation curves of component 12 of stress for laminate model [±45]s at different relaxation times under isothermal condition of 160 °C (ROI-01).....	123
132. Relaxation curves of component 31 of stress for laminate model [±45]s at different relaxation times under isothermal condition of 160 °C (ROI-01).....	123
133. Relaxation curves of component 11 of stress for laminate model [±45]s at different relaxation times under isothermal condition of 160 °C (ROI-02).....	124
134. Relaxation curves of component 12 of stress for laminate model [±45]s at different relaxation times under isothermal condition of 160 °C (ROI-02).....	124
135. Relaxation curves of component 31 of stress for laminate model [±45]s at different relaxation times under isothermal condition of 160 °C (ROI-02).....	125

NOMENCLATURE

- UD Unidirectional
- 8HS 8-harness satin weave
- RUC Repetitive Unit Cell
- RVE Represent Volume Element
- EO Extended Out-time
- LVR Linear Viscoelastic Region
- TTS Time-Temperature Superposition
- PBC Periodic Boundary Conditions
- SBC Symmetric Boundary Condition
- FS Flat Surface
- ROI Region of Interest
- FEA Finite Element Analysis
- CTE Coefficient of Thermal Expansion

LIST OF SYMBOLS

n_s	number of subcells between consecutive interlaced regions
n_g	number of subcells along one direction of unit cell
W_f	subcell length along fill direction
W_w	subcell length along warp direction
g_f	gap between fill tows
g_w	gap between warp tows
j	tow number
h_f	thickness of fill tow
h_f	thickness of warp tow
h_m	thickness of neat resin
h	thickness of unit cell
λ	wavelength of undulation region
a_w	width of warp tow
a_f	width of fill tow
a_s	width of flatness in tow cross section
a_i	width of wavy region of undulation
k	scale factor
a_s	length of flatness region
α	crimp angle
E_i	relaxation coefficient of i^{th} term
λ_i	relaxation time of i^{th} term
MPa	megapascal
°	degree
mm	millimeter
s	seconds
σ	stress
ε	strain
E	young's modulus of elasticity
G	shear modulus of elasticity

LIST OF SYMBOLS (continued)

- u displacement along x-axis
- v displacement along y-axis
- w displacement along z-axis
- ΔT Change in temperature

CHAPTER 1

INTRODUCTION

A composite material can be defined as a selective combination of two or more distinct materials to form a new material with enhanced properties [1]. In general, a traditional polymeric composite system i.e., the polymer reinforced with continuous fibers, is the predominant one used in the aerospace and automobile structural applications. Because of less weight, maximum achievable stiffness and strength, continuous fibers are used for a prolonged period of time. In traditional polymeric composite, the load is predominantly carried by the fibers oriented along the loading directions. The process of manufacturing these composite materials is expensive and slow. This is due to the specific methods of manufacturing involved in the continuous fibers system such as hand lay-up, prepreg lay-up, vacuum bagging processing, resin transfer molding, and so on [1].

In recent years, advanced textile composites have become widespread in many aerospace structural applications due to the efficiency of reinforcing more directions and their unique ability of forming complex curvatures while maintaining their desirable properties [2]. In addition, they have better out of plane stiffness and toughness properties than traditional tape laminates [3]. Furthermore, they provide enhanced impact resistance, better resistance over fatigue and corrosion. Moreover, woven composites are easier and cheaper to handle and fabricate as compare with traditional polymeric composites [1]. Textile composites are a network of fiber bundles (tows) interlaced to each other with different weave pattern impregnated in the polymeric resin to create plies as shown in Figure 1. Tows along the axis are commonly called as “Fill”, and the one perpendicular to the axis are called as “Warp” [4]. Different types of weaves are illustrated in the Figure 1.

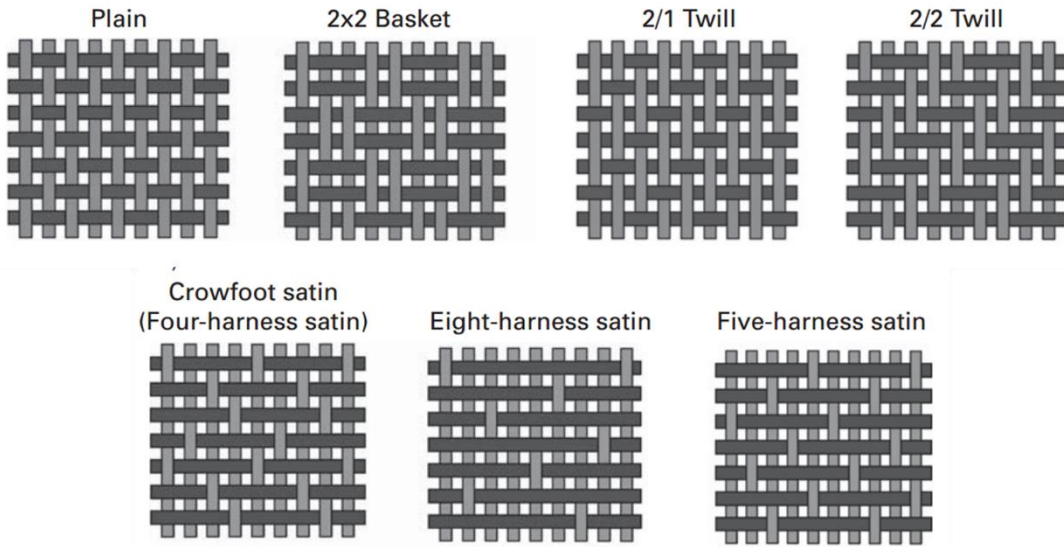


Figure 1. Different Types of Weave Architecture [4]

However, these polymeric composites are heterogeneous and viscoelastic in nature. When these materials are loaded under constant deformation, stress induced in the material decreases as a function of time as well as temperature. This response is generally referred as “stress relaxation” behavior. Stress relaxation is one of the widely used concepts to evaluate the time period over which the viscoelastic material can withstand loads without losing structural integrity. Therefore, in-depth knowledge of stress relaxation response of woven composites is vital for the accurate design of large scale composite structures [5].

Due to the complex weave architecture, this fabric system displays various response mechanisms that differ from the traditional polymeric composite. These include: friction as the interwoven tows slide each other, crimp interchange which is the transfer of undulation between the interlaced tows, slip which is due to the relative rotation of adjacent tows in shear as a result of normal loading [2]. Thus, experimentally predicting their stress relaxation response under uniaxial loading is a tedious and expensive process. In addition, its value drastically alters with varying fiber volume fraction of the material as compared to the pure polymer.

In this study, our area of interest is 8-harness satin weave architecture. These satin weave is made up of seven number of floating warp tows across a fill tows to bring the former to one face and the later to the opposite face of the fabric. The interlacing floats of 7 tows between consecutive interlacing are illustrated in Figure 1. These satin weaves are drape and slide extremely well and can adopt complicated contours in the mold [1]. Therefore, it is widely used in the high temperature applications like space shuttle, nose of rocket ...etc.

In order to have thorough understanding of the macro-level response, it is essential to study the mechanics of microstructure (i.e., fiber bundles and neat resin) of the woven composites. Two analysis methods available to study the effect of constituents are: Analytical (closed form) and Numerical methods. Analytical methods involve more approximation, are less accurate, and the geometry effect is often ignored. While numerical methods involving finite element analysis provides high accuracy with less approximations and they require a discretization of geometry for specific case [6]. Thus, in this research, numerical method involving finite element based micromechanics approach was adopted to investigate the effect of the weave architecture on the stress relaxation behavior of the fabric composite and results were compared with the experiments for verifications.

CHAPTER 2

BACKGROUND AND LITERATURE REVIEW

This chapter describes the theory of stress relaxation behavior of polymers and their mathematical models, various methods of predicting stress relaxation behavior of advanced composites, and their history and limitations.

2.1 Polymer

Composite is a reinforcement of fibers and matrix. A matrix is a continuous phase and gives a shape to the structure of composite system. Primary roles of these matrices are

1. to surround and holds the fibers together.
2. to protect the reinforcement from the environment.

Polymer matrices are the most commonly used matrices due to their ease of fabrication of complex geometry with low tooling and manufacturing cost. Therefore, 90% of advanced composite materials used in the aerospace industries have polymeric materials as their matrix system [7]. According to Robert Jones [7], “*Polymers are macromolecules that are composed of repeated subunits connected together*” as illustrated in Figure 2.

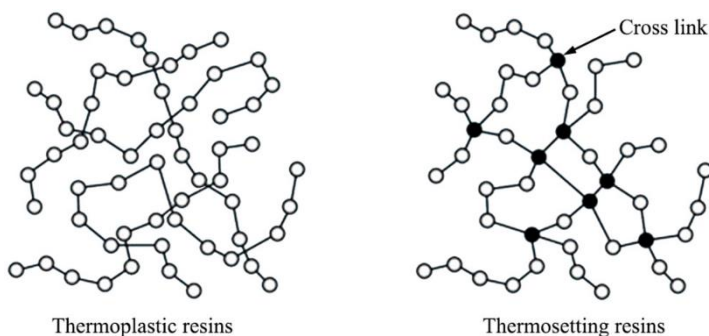


Figure 2. Molecular Structure of Thermoplastic and Thermoset Polymers [8]

These polymers are categorized into *thermoplastics* and *thermosets*. Thermoplastics (e.g., Polypropylene, Polyethylene, Polyvinyl chloride, etc.) are polymers that are not cross-

linked permanently and can be softened and reshaped by heating. Thermoplastics polymers can be reheated and cooled without much degradation and makes them suitable for recycling. In contrast, thermoset polymers (e.g., Polyester, Epoxy, Phenolic resins, etc.) are cross-linked through addition of energy like heat or irradiation [8]. During the curing process, the monomers are permanently cross-linked to form a complex three-dimensional molecular network structure. Therefore, thermosets are generally more stiff and strong when compared with thermoplastics [8].

2.2 Time-Dependent Behavior of Polymers

In general, traditional structural materials like metals and their alloys exhibit elastic behavior in nature. In other words, when the material is loaded and unloaded within elastic limit, instantaneous strain developed by the material will disappear upon removal of load [9]. And further, upon constant deformation, stress induced in the material remains constant with time. In case of viscous materials, induced state of stress will dissipate with time. Unlike these conventional structural materials, polymers have a unique characteristic of viscoelasticity [9].

Viscoelasticity is a property of material which exhibits both elastic and viscous behavior in nature. This behavior is sensitive to the material's chemistry and microstructure [9]. In a polymer the instantaneous strain is due to the stretching and bending of atomic bond and delayed elastic response is attributed to the chain uncoiling of molecules. The viscous flow is mainly due to the chains slipping past each other [9].

When the material is loaded under constant deformation, stress induced on the material decreases as a function of time as well as temperature. This is called "stress relaxation" [10]. During stress relaxation, polymer molecules move relative to one another and gradually accommodate the strain by conformational extension rather than bond distortion. This

rearrangement of molecules continues and stress required holding the strain dies away to the equilibrium position after a prolonged period of time. Since time is a very important parameter in their behavior, they are also called as “Time-Dependent Materials” [10]. Figure 3 shows the typical response of three different materials: elastic solid, viscous fluid and viscoelastic materials.

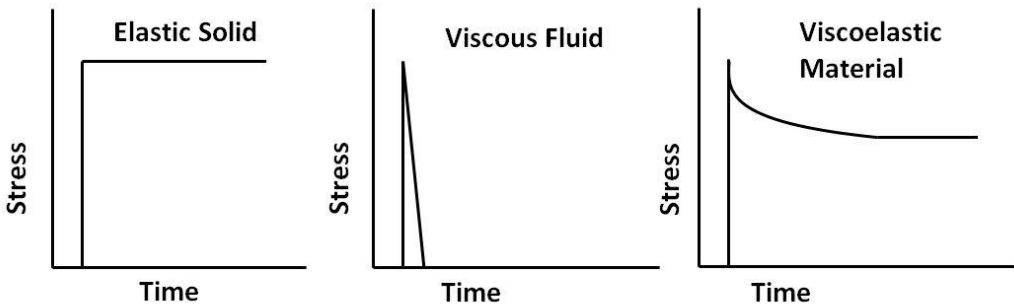


Figure 3. Stress Relaxation Behavior of Different materials under constant deformation [5]

These time-dependent phenomena may have a considerable effect on the stress distribution developed in a structural member. The stress at a specific point in the material may vary significantly with even though the applied displacement is constant [10]. A linear viscoelastic model is the simplest way of explicitly describing stress relaxation and time-dependent behavior of the polymers. There are some basic mathematical models available to describe the mechanical behavior of viscoelastic material.

2.3 Mathematical Models of Viscoelastic material

2.3.1 The Maxwell model [11]

Maxwell [11] was the first one to develop a mathematical model to describe the characteristic nature of viscoelastic materials. He proposed a mechanical analogy between viscoelastic materials and a series combination of spring and dashpot. Figure 4 displays the

schematics of the Maxwell element. Here, spring element represents the elastic behavior, whereas viscous element represents the viscous response of the material.



Figure 4. Schematics of a Maxwell Model

Where E is the instantaneous Elastic modulus of the spring while μ is the viscosity of liquid in the dashpot. Relaxation time τ is defined [11] as.

$$\tau = \frac{\mu}{E} \quad (2.1)$$

The equation of motion of the Maxwell Model [11] can be defined as

$$\frac{d\varepsilon}{dt} = \frac{1}{E} \frac{d\sigma}{dt} + \frac{\sigma}{\mu} \quad (2.2)$$

In the stress relaxation experiment, the rate of change of strain becomes zero after a constant strain is applied to the system. Therefore, equation (2.2) [11] can be written as,

$$\frac{d\sigma}{\sigma} = -dt \frac{E}{\mu} = -\frac{dt}{\tau} \quad (2.3)$$

integration equation (2.3) from σ_o at time 0 to $\sigma(t)$ at time t gives [11]

$$\ln \sigma(t) = \ln \sigma_o - \frac{t}{\tau} \quad (2.4)$$

taking exponential on both side of equation (2.4) and then dividing by ε_o gives [11]

$$\frac{\sigma(t)}{\varepsilon_o} = \frac{\sigma_o}{\varepsilon_o} e^{-\frac{t}{\tau}} \quad (2.5)$$

which simplifies [11] to

$$E(t) = E e^{-\frac{t}{\tau}} \quad (2.6)$$

where, E is the modulus of the spring, $E(t)$ is the instantaneous Elastic modulus, t is the time and τ is the relaxation time.

2.3.2 The Generalized Maxwell Model [12]

Generalized Maxwell model consist of an arbitrary number of Maxwell model, which are connected in parallel as shown in the Figure 5. It allows more accuracy upon fitting experimentally generated mechanical behavior of the material [12].

The stress in the i^{th} Maxwell element of the Maxwell-Wiechert model [12] is written as

$$\sigma_1 = \sigma_2 = \sigma_i \quad (2.7)$$

Model with n elements is considered to be a summation of all individual elements and expressed as [12]

$$\sigma = \sum_{i=1}^n \sigma_i \quad (2.8)$$

Deformation for the i^{th} element and full model is written as [12]

$$\varepsilon_1 = \varepsilon_{i1} + \varepsilon_{2i} \quad (2.9)$$

and for the full model [12]

$$\varepsilon = \varepsilon_1 = \varepsilon_2 = \varepsilon_i \quad (2.10)$$

The governing equation for the Maxwell-Wiechert model is written as [12]

$$\dot{\varepsilon} = \frac{\dot{\sigma}_i}{E_i} + \frac{\sigma_i}{\eta_i} \quad (2.11)$$

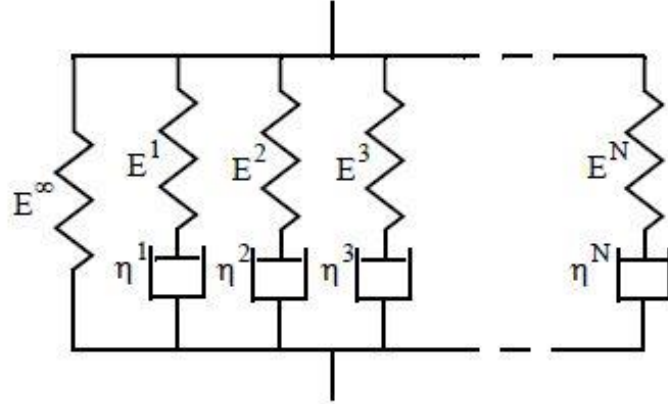


Figure 5 The Generalized Maxwell model [13]

Stress relaxation of the Maxwell-wiechart model can be derived by integrating equation (2.11) and substituting their results into equation (2.8) to give the following Prony series relation [12]

$$E(t) = E^\infty + \sum_{i=1}^N E_i e^{-t/\lambda_i} \quad (2.12)$$

Which represents N models with relaxation times λ_i . Where $\lambda_i = \frac{\eta_i}{E_i}$ - Long term Elastic moduli and E_i - coefficients of relaxation.

2.3.3 Constitutive model for linear viscoelastic material [13]

The integral representation of the linear theory of viscoelasticity is represented using Boltzmann's superposition integral [13] which is called a “Volterra's integral equation or Hereditary Integral”. Viscoelastic constitute law can be expressed using relaxation based formulation. The constitute equation for the stress relaxation [13] is given by

$$\sigma(t) = \int_{-\infty}^t E(t-\tau) \dot{\epsilon}(\tau) d\tau \quad (2.13)$$

Whereas the relaxation modulus is a smooth, positive and decreases as a function of time. Generally, the kernel functions are represented via Prony series/ Maxwell-wiechart model.

2.4 Polymer Matrix Composites (PMCs)

Stress Relaxation behavior of polymer has considerable effect on the fiber reinforcement, especially on transverse direction which is dominated by the matrix. Generally, two methods adopted to evaluate the global properties of composites are a *macro-mechanical modeling approach* and a *micro-mechanical approach*.

2.4.1 Macro-Mechanical Approach

Macro-mechanical approach is a method of evaluating composite behavior under lamina and laminate level by considering the effect of individual plies, their interaction and stacking sequence [6]. In this approach, experimental data from the standard test coupons are utilized to build a constitutive equation of polymeric composites. Macro-mechanical approach treat composite as a homogeneous orthotropic continuum. The main setback of this method is the required experimentation to evaluate various material constants and functions in the constitutive equation are more expensive and time-consuming. Moreover, local variation due to the constituents of the composite cannot be predicted by these models [6].

2.4.2 Micro-Mechanical Approach

Micromechanical approach has been used for a long time to analyze fiber reinforced composite. With an improvement in numerical computation techniques, detailed analyses of micromechanics are being studied nowadays. This approach based with an assumption of replacing complex microstructure of advanced composites with Representative Volume Element (RVE) or Representative Unit Cell (RUC) [1]. Representative Volume Element or Representative Unit cell is defined as a small part and repeating pattern of the whole composite, which represents all the features of the composite with the tessellations of RUC [1]. It is an assemblage of fiber/tows and neat resin with an idealized geometry of microstructure. The RUC

is modelled to have same fiber volume fraction as the composite laminate and the corresponding material properties of fiber and neat resin can be defined individually. Then the overall response of the composite laminate can be predicted with the aid of assemblage of individual constituents. Assumptions of the micromechanics model in the viscoelastic analysis are as follows [1]

- Perfect bonding between fiber and neat resin.
- The fibers are continuous and parallel.
- The fibers are assumed to be transversely isotropic and follow the Hooke's law on elastic behavior.
- The fibers are assumed to have a uniform strength.
- The composite is voids free.

2.5 Earlier history of works

Micromechanics have been used more than 20 years to study the effect of constituents on the composite structure. Two categories of method available to model the micromechanics of these continuous fiber reinforced composites are *the analytical method and finite element method*. Many researchers have developed both analytical and numerical models to study the stress relaxation behavior of polymer reinforced composites using micromechanics approach. But still there is a lack of research works on investigation of advanced textile composites due to complex geometry and computational cost. Before proceeding to the woven fabric, histories of stress relaxation and other viscoelastic analysis of polymeric composites were described in the following.

2.5.1 Influence of Continuous fiber system on polymer viscoelasticity

When we trace back to the history of stress relaxation analysis, Hashin [14] was the first one to develop analytical model to define the viscoelastic phenomena of heterogeneous media in

terms of stress relaxation and creep functions. He related effective elastic modulus with the developed functions using the correspondence principle of linear viscoelasticity to capture the macroscopic behavior of viscoelastic material in dilatation and shear.

Later, Hashin [15] also developed a correspondence principle to characterize the effective complex moduli of viscoelastic composites in terms of effective elastic moduli. The method is imposed on the composite sphere assemblage model to determine complex moduli of isotropic particulate composite. He found good relations with the experimental results.

Aboudi [16] developed a micromechanics model consisting of square fiber embedded in the matrix phase to capture the effective elastic response of unidirectional composite utilizing the constituent's properties. Further, Yancey and Pindera [17] applied the inverse Laplace domain to the aboudi's micromechanics model as shown in the Figure 6 to predict the creep response of unidirectional composite. The developed model was assumed to contain linearly viscoelastic matrices and elastic fibers. The inverse of effective moduli in the Laplace domain to the time domain accomplished using the Bellman method. The effective moduli are expressed in terms of the phase moduli and volume fractions of the micromechanics model provide a straightforward application of the viscoelastic correspondence principle. Model predictions were validated with the creep behavior of T300/934 graphite/epoxy unidirectional coupons at two different temperatures. Very good correlation between theory and experiment was found for a given small creep strains.

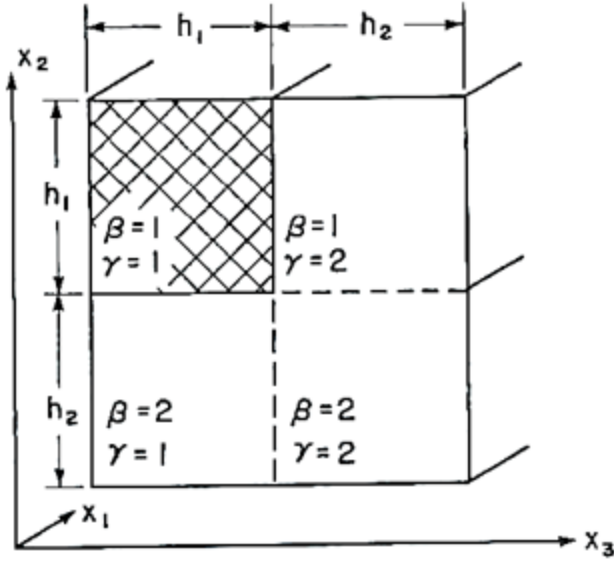


Figure 6. Repeating Unit cell model of Aboudi[16]

Brinson and Knauss [18] applied dynamic correspondence principle of linear viscoelasticity in a 2D finite element model to solve boundary value problems under plane strain condition. They studied multiphase viscoelastic analysis of composite to obtain global complex moduli. The model assumed to have square array packing and accounted the effect of coupled interactive deformation of the phases. Their study concluded that the composite moduli were dominated by the matrix except for the loss moduli at high frequency domains, for which soft material controls dissipation independent to fiber volume fraction and phase orientation. Also, their study confirms that composite properties are affected more by stiff inclusions in a softer material.

Barbero [19] developed an explicit analytical expression for both relaxation and creep phenomena of composites by applying the correspondence principle of linear viscoelasticity theory in the Laplace domain. He utilized the elastic model with periodic microstructure to analyze the viscoelastic behavior of composites as shown in the Figure 7. Furthermore,

relaxation and the creep functions of composites are numerically inverted in the time domain to display the viscoelastic behavior of the matrix. His model gives closer predictions with the experimental creep response under axial, transverse and shear loading.

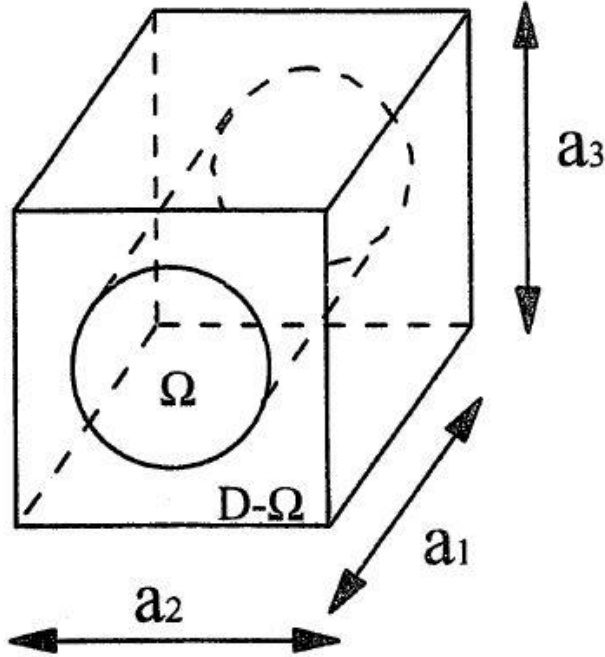


Figure 7. Geometry of the unit cell [19]

Aboudi [20] applied the Simo's 3D finite strain viscoelastic model [21] to predict the overall finite viscoelastic response of multiphase composite with short fibers using the micromechanics approach in the framework of the generalized method of cells (GMC). The micromechanical analysis was performed based on the tangent approach in conjunction with incremental procedure, where satisfaction of equilibrium equations in the sub-cell is primary concern. Every constituent in the model assumed to behave as a nonlinearly viscoelastic material with large deformation. Continuity of displacement and traction increment between the subcells were fulfilled throughout the analysis.

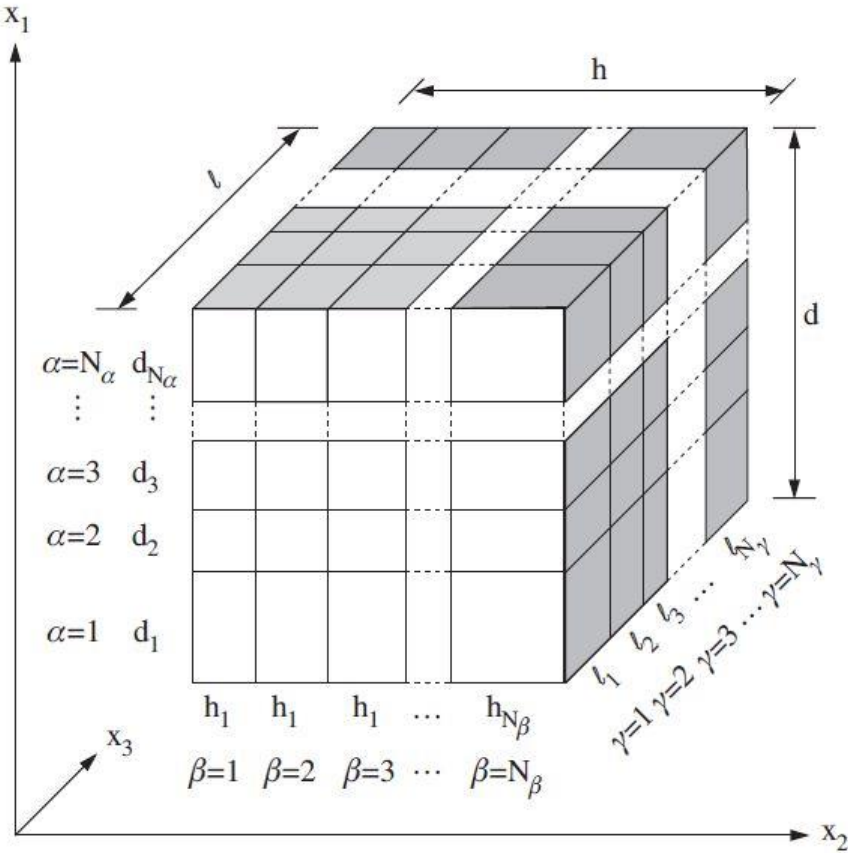


Figure 8. Repeating cell in GMC consisting of N subcells in all three directions[20]

Fisher and Brinson [22] investigated the mechanical behavior of three phase viscoelastic composite using the micromechanics model of Mori-Tanaka (MT) [23] and Benveniste (modified Mori-Tanaka model) [24]. Micromechanics model included the effect of interface regions due to voids, mechanical imperfections and other inconsistencies. The model predictions were compared with 2D finite element analysis of hexagonally packed unit cell model with inclusions and assumed plane strain conditions. From the results, it was concluded that model predictions give good correlation with FEA results when the matrix is the softer material. Also, they found that interface region does not have any influence over the composite aging shift rates observed in experimentation.

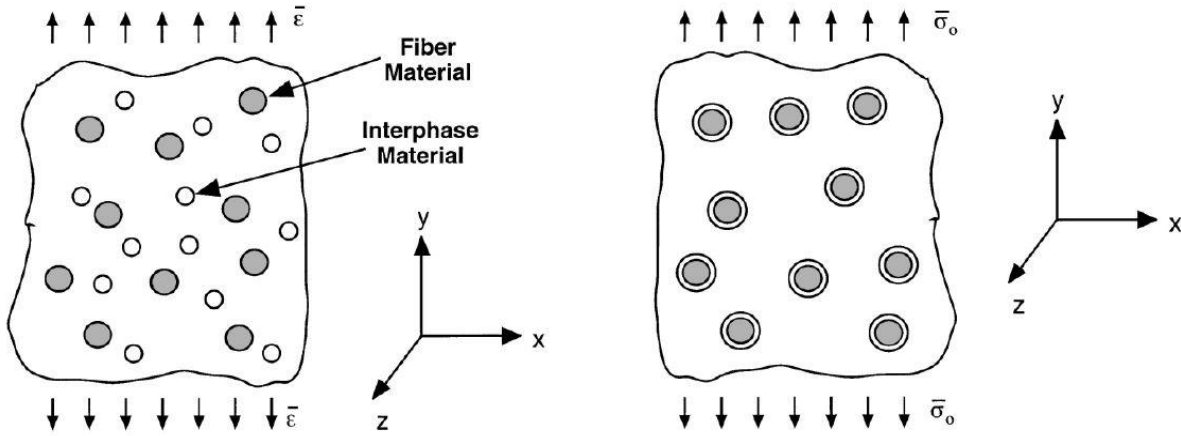


Figure 9. Mori-Tanaka model[23] with distinct inclusion [left]and Benveniste model[24] with annular interface region [right]

Karami [25] proposed an efficient computational algorithm to ascertain the viscoelastic property of fibrous composite. Finite element based micromechanical model of unidirectional composite was developed and subjected to six specified loading conditions under periodic constraints. Developed model assumed to contain elastic fiber and viscoelastic resin. Volume averaging scheme was enforced on his model to capture the averaged response of fiber and resin. Viscoelastic properties of constituents as well as composite assumed to follow the Prony series. Verification of proposed algorithm was carried out using different types of fiber packing's in the commercial software ABAQUS. Fiber packing of different unit cell models was illustrated in the Figure 10. From the finite element analysis, it was concluded that the pure viscoelastic matrix has higher shear strength than the longitudinal or transverse strength. However, they decay with respect to time. Also, compliance of unidirectional composite decreases with increase in fiber volume fraction. Furthermore, the square packing geometry was found to be stiffer than the hexagonal packing geometry.

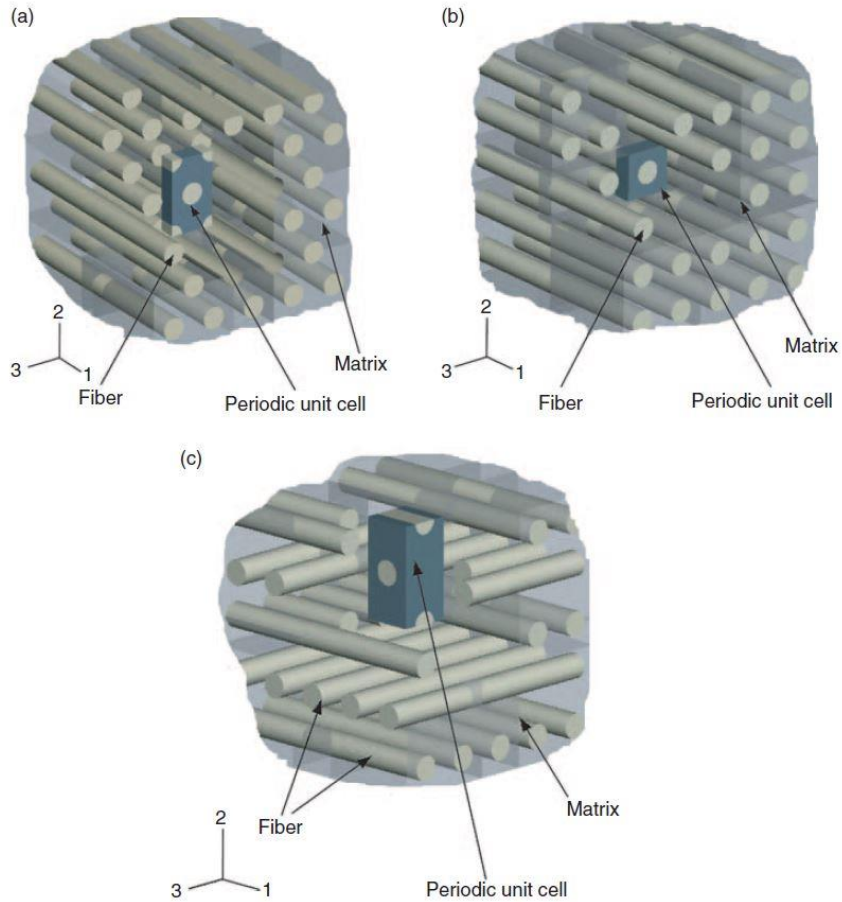


Figure 10. Unit cell model from different types of fiber packing's: a) Hexagonal Array b) Square Array c) Bidirectional crossed array [25]

Abadi [26] derived closed-form analytical expressions to determine the stress relaxation response of graphite/epoxy composite as a function of matrix and fiber properties. Stress partitioning factors (SPF) were included in the model to characterize the transverse axial stress and shear stress in each of the constituents of viscoelastic composite based on the time domain and fiber volume fraction. Predictions were compared with the finite element analysis of micromechanics model with square packing under axial and shear loadings. From the experimental studies of polymers, he also revealed Poisson's ratio has time dependent behavior and their effect was added in the proposed model. His analytical results were found to be in good correlation with numerical results for anisotropic response of composite materials. From the

micromechanical analysis, he concluded that the time required by the stress state to reach a stable condition reduces in the composite materials having higher fiber volume fraction. Besides, variation of Poisson's ratio during loading for different fiber volume fraction was found to be similar. He also observed that shear stress is highly depending on the fiber volume fraction in the start, but the long term shear stress has lower dependency to the fiber volume fraction.

From the above studies, it is clear that the finite element based micromechanical analysis of stress relaxation accounting the effect of elastic fiber and viscoelastic resin is able to capture the experimental behavior of unidirectional composites more accurately.

2.5.2 Influence of weave architecture on polymer viscoelasticity

Unlike traditional continuous fiber system, woven composites do not display uniform strain distribution under uniaxial load. The crimped fiber bundles under tension tend to straighten out, and thereby creates warpage along thickness in the lamina [27]. In order to characterize the residual stresses and to design dimensionally stable composite structures, it is important to have thorough understanding of micromechanics of woven composite. The following studies investigated the effect of weave architecture on the polymer viscoelasticity.

Govindarajan et al [28] were the first one to investigate the creep response of graphite/epoxy woven composites analytically through integration of various models (i.e., Plain Weave). Like previous researchers, he applied the elastic-viscoelastic correspondence on the fiber undulation model developed by Ishikawa and Chou [29]. The model was assumed to follow constant strain condition and considers the longitudinal and transverse fibers individually. Plain weave model was considered to be an assembled setup of viscoelastic matrix and undulated elastic fiber as shown in the Figure 11. The matrix is modelled by a four parameter model as a Maxwell-Voigt combination. The experimental results of the woven fabric were analyzed

through the model under reverse simulation to extract the constituent's properties. Then, the model was imposed under different load levels to predict the creep response of woven composite. The analytical models in conjunction with Arrhenius equation were used to predict the creep response of fabric at elevated temperatures. His analytical predictions were well correlated with the experimental results as illustrated in the Figure 12.

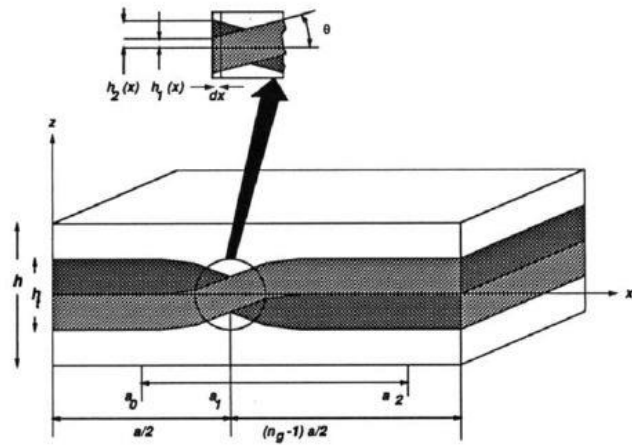


Figure 11. Unit cell of Plain Weave fabric [28]

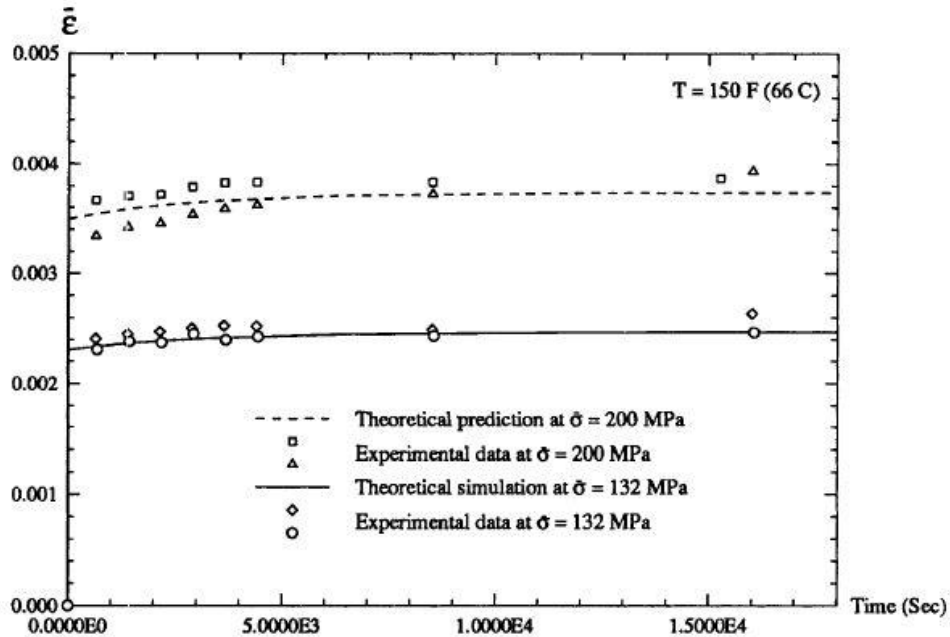


Figure 12. Comparison of theoretical and experimental data at different loads and 66°C [28]

Shrotriya and Sottos [30] developed micromechanics models to predict creep and relaxation response of woven composite by applying elastic –viscoelastic correspondence on the elastic models developed by Sottos et al [31] and Lee & Harris [32].The model utilizes the geometry and material properties of fiber and resin. The material properties of the matrix were determined from the samples of epoxy resin extracted from B-staged prepreg. Micromechanics model assumed to contain elastic fiber bundle and viscoelastic matrix. Predicted unrelaxed modulus was closer to the experimental data, but relaxation modulus was significantly under predicted. Study concluded that relaxation of fabric not only depends on viscoelastic polymers but also on the weave geometry.

Later, Shrotriya [33] also developed a 2D finite element model of woven fabric and analyzed under plane strain condition to predict the creep compliance of woven fabric considering a weave geometry and different boundary conditions. The model predictions displayed the general trend of experimental results, but did not match the spectrum of the creep compliance curves.

Further, Sottos et al [34] investigated a 3D micromechanical model of plain weave composite with accurate characterization of woven geometry to capture the creep compliance as displayed in Figure 13. The viscoelastic properties of the straight, transversely isotropic fiber bundle are calculated using the correspondence principle and the micro-mechanical relations based on the self-consistent field model. Symmetric boundary conditions and traction free surface were analyzed in the domain of their unit cell. Furthermore, the deviation increases when the material approaches the fully relaxed regime. In addition, research investigated the effect of elastic fiber bundles and relaxed bundles on the creep behavior. Even though the 3D finite element model capture the general trend of the experiment, results were under predicted as

compare with the 2D model over the entire relaxation regime of the composite in both the fill and warp directions as shown in Figure 14. Their study concluded that spectrum of the bundle relaxation needs to be corrected and 3D finite element based micromechanics model improves creep compliance predictions.

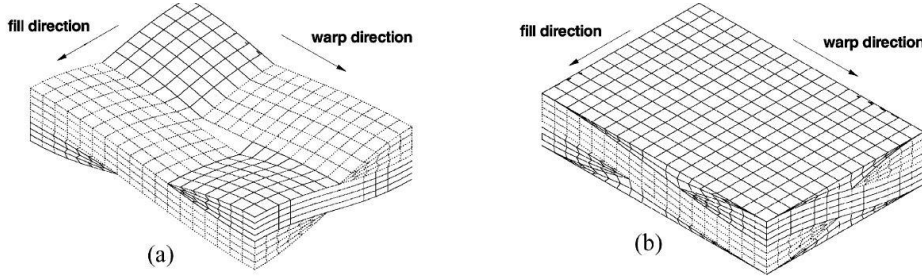


Figure 13. 3D Unit cell of Plain Weave a) without matrix b) with matrix [34]

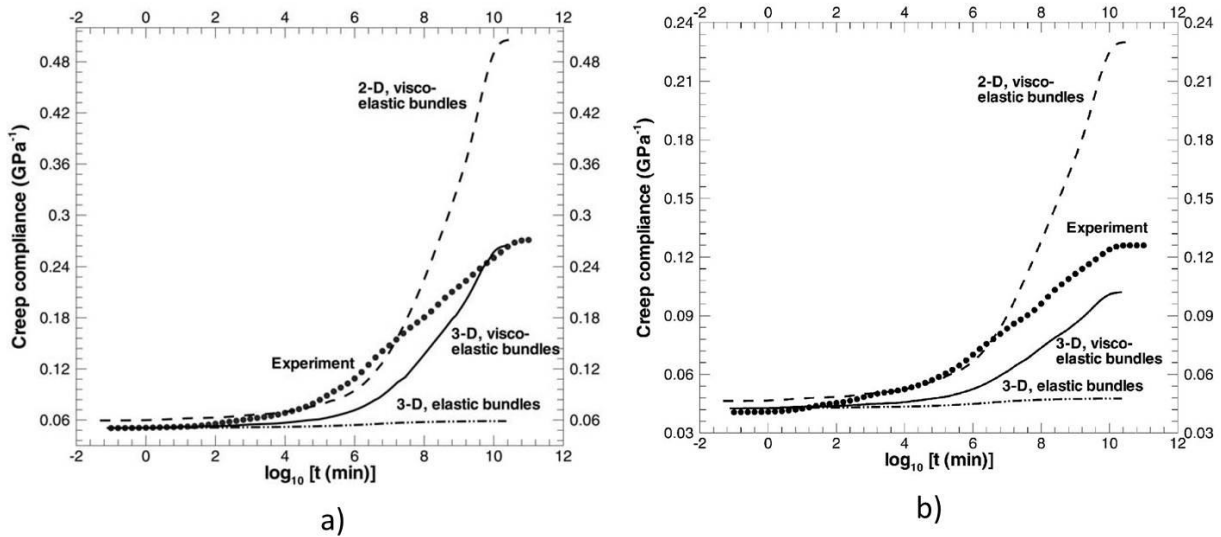


Figure 14. creep compliance of the plain weave fabric by Shrotriya a) Fill direction b) Warp direction [34]

Shrotriya and Sottos [35] extended their study on viscoelastic response of woven composite utilizing their previous analytical and finite element method approach. An elastic-

viscoelastic principle was applied in their elastic micromechanical models [31] to predict the time dependent behavior of woven composite. Analytical results were then compared with experimental data, and defects of the model were identified and desired correction was made to predict the fabric behavior. On other hand, a 2D finite element based micromechanical model of woven fabric was developed to study the influence of the boundary conditions and Poisson's relaxation. Parametric study was done using the FEA model to investigate the influence of constant and relaxed Poisson's ratio of matrix on the fabric creep response as shown in Figure 15.

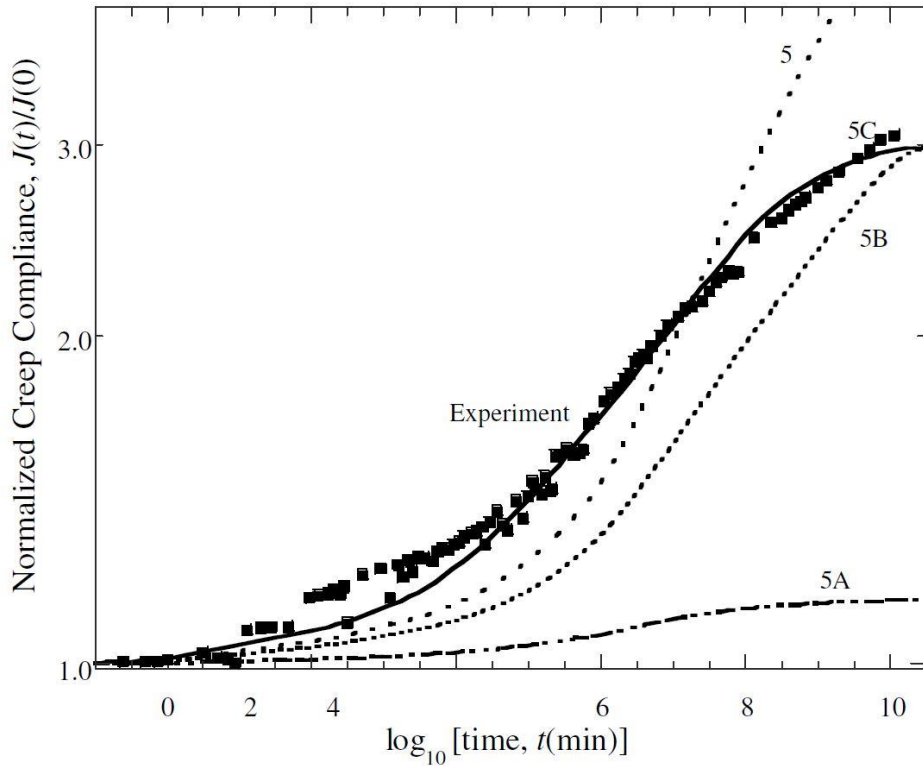


Figure 15. Normalized Creep Compliance Curves of 2D Finite element based micromechanics model of plain weave : 5) Viscoelastic fiber bundle (3D) 5A) Elastic fiber bundle (3D) 5B) Matrix with constant bulk modulus 5C) Shifted Relaxation spectrum of case 5B [35]

Results show that the model with influence of relaxed fiber bundle and matrix Poisson's ratio improves the predictions of 2D model. In addition, shifted time frame of 2 decades gives closer predictions when compared to experimental data. Their study concluded that the time

dependent response of woven fabric creep compliance is highly influenced by the bundle relaxation spectrum and relaxation of Poisson's ratio [35].

2.5.3 Limitations

Most of the research studies reported in open literature have addressed the viscoelastic behavior of unidirectional composites with different stacking sequence [14-26]. Only few studies investigated the woven composites that address undulations (i.e., Plain weave) [27-35]. But there are other weave types which incorporate combination of both floats and undulation e.g., twill and satin weaves, which are not studied yet due to complex geometry and computational cost. Also, presented studies utilized analytical models to predict fiber bundle properties where fiber and resin geometric interactions were not captured. Since most of their parametric study was performed on 2D FEA, the effect of interlaced tows and varying cross section of the tows was not included. Thereby, stiffness of fabric was under predicted.

2.6 Motivation and Objective of Research

The scope of this research is to predict the influence of weave architecture on the stress relaxation behavior of woven fabric composite that incorporates both undulation and waviness using finite element based micromechanics model. The fabric type used for this current study is 8-harness satin weave. Full unit cell geometry is considered for this study to evaluate the antisymmetric characteristic of the woven composite structure in the viscoelastic behavior. The assumptions in the computational micromechanical model are as follows

1. Developed model is an idealized geometry consisting of linearly viscoelastic matrix and orthogonally interlaced unidirectional composite with waviness and floating regions.
2. Both fill and warp tows are assumed to contain equal fiber volume fraction.

3. Cross-sections of tows are assumed to be a flattened lenticular shape.
4. Constitutive model of viscoelastic matrix is assumed to follow the Prony series.
5. Time dependent Poisson's ratio is incorporated for viscoelastic material with an assumption of constant bulk modulus.

Unit cell model is developed and analyzed using Hypermesh v11.0 [36] and MSC MARC FEA [13] commercial software. Kinematics of periodic constraints is imposed on the developed model to recreate the Repetitive Unit cell (RUC) of 8-harness laminate. In order to account the fiber/resin interaction in the fiber bundles/tows, hexagonally packed unit model of unidirectional composite was utilized to predict the thermomechanical properties of tows. Stress relaxation response of 8-harness woven fabric is basically a function of carbon fiber bundles, epoxy matrix as well as the geometry of the weave architecture. Numerical predictions were then correlated with experimental results for validation. This fruitful combination of mechanics of material and micromechanics not only predict the effective response of the woven composite, but also to analyze the heterogeneous state of stress and their variation in the adjacent fiber bundles and neat resin as a function of time and elevated temperatures.

CHAPTER 3

EXPERIMENTAL APPROACH

This chapter contains information regarding the material systems, specimen fabrication and experimental approaches followed in the study of stress relaxation behavior of neat resin and woven fabric composites. In addition, limitations and problems associated with experiments are also discussed in this chapter.

3.1 Materials

Cycom® 5320-1 EO epoxy resin [35] and commercial prepreg of 5320-8HS [37] woven fabric were the two material system used for this study and illustrated in the Figure 16 and Figure 17. The material is designed for vacuum bag or out of autoclave manufacturing of aerospace primary and other structures due to their superior performance [37]. This prepreg uses Cytec Thorne® T-650/35 3K eight harness satin (8HS) carbon fibers [38] with 370gsm fiber areal weight and 36% resin content. These carbon fibers are continuous, possess high strength and modulus, along with excellent oxidation resistance, and composite performance [38].



Figure 16. Prepreg material of 5320-8HS woven composite



Figure 17. Roll of 5320-1 EO epoxy resin material

3.2 Fabrication of Resin Specimens

3.2.1 Mold Preparation

In order to cure the 5320-1 resin samples in the proper shapes necessary for testing, silicon molds were first created. The molds were made by first lightly gluing four or five aluminum samples to the base of plastic hexagonal cups. In a separate cup of the same shape and size, the base and catalyst for the silicon were weighed and mixed together using the manufacturer's recommended ratio. After thorough mixing, the silicon was slowly poured onto the aluminum samples until the desired thickness of the mold was obtained. Then the mold was vacuumed for approximately 30 minutes under a cyclic pressure with a lower and upper limits of 5kPa and 20kPa. This helped minimize the air bubbles in the mold during mixing, because they could act as voids and weaken the structural integrity of the molds. Once air bubbles were reduced, the mold was taken out of the vacuum and left to cure at room temperature for 24 hours, according to the manufacturer's recommended cure time. After the mold was properly cured, the silicon was removed from the cup and the aluminum samples were also removed by manually

applying pressure to the back of the mold [39]. Molds were made for dogbone shape in accordance to ASTM D1708 [40]. Figure 18 displays the systematic procedure of silicone mold preparation.

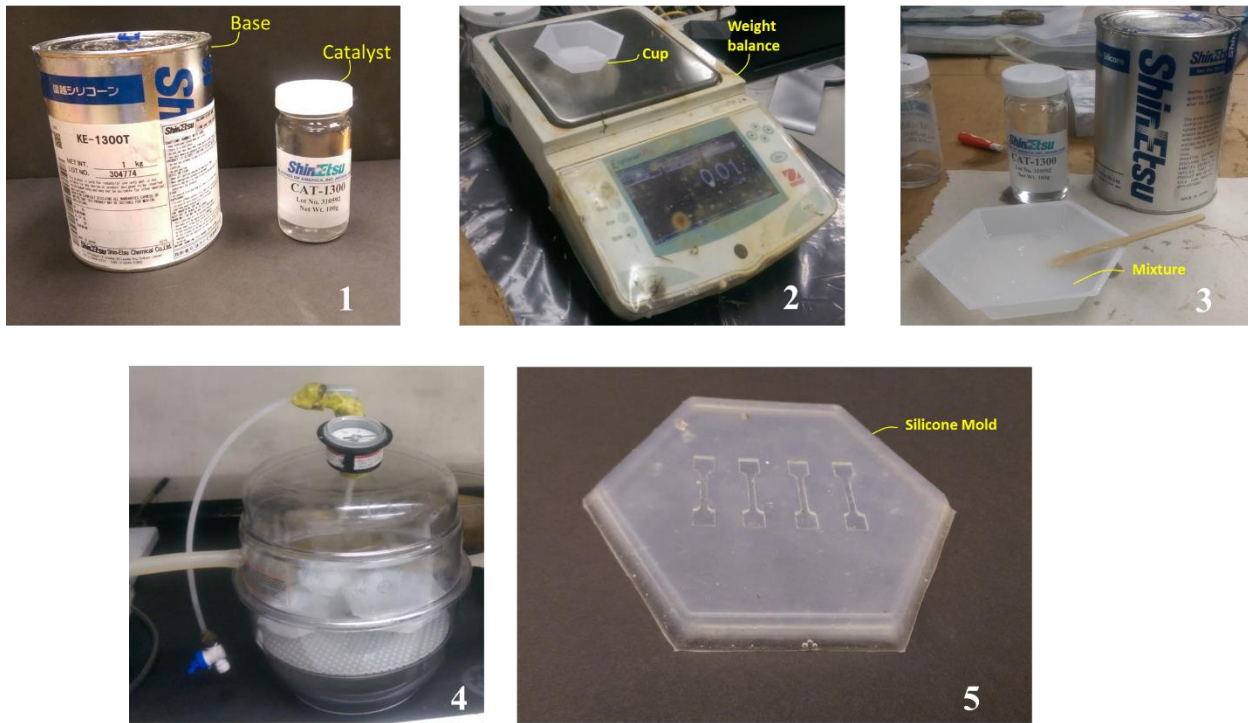


Figure 18. Silicon Mold preparation

3.2.2 5320-1 Resin Specimen

Uncured 5230-1 epoxy resin (B-staged film), which was normally kept in a freezer during inactivity to avoid accidental curing, was placed into the silicon molds to completely fill the recesses created by the aluminum samples. In addition, a thermocouple was attached to one of the recesses to monitor the curing temperature of resin. The mold was turned upside-down and laid-up against a thin aluminum tool. It was then covered with thermal release film, an aluminum caul sheet, a breather and vacuum bag fixed with sealant tape for debulking. Before placing the laid-up samples into the oven for curing, they were debulked at a constant vacuum pressure of 27kPa for at least 30 minutes. While curing in the oven, the samples were held under a constant

pressure of 24kPa. Appendix A displays the manufacturer recommended cure cycle and temperature log of 5320-1 epoxy resin.

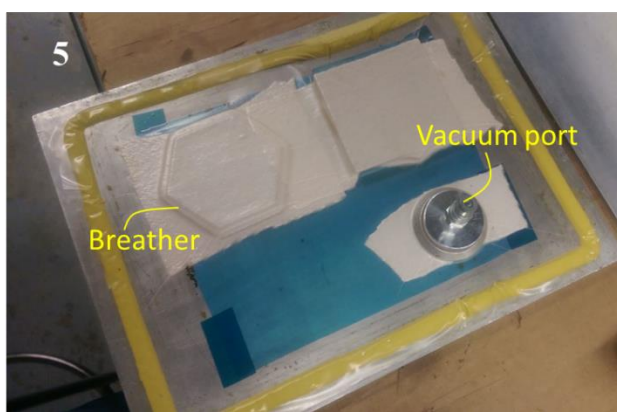
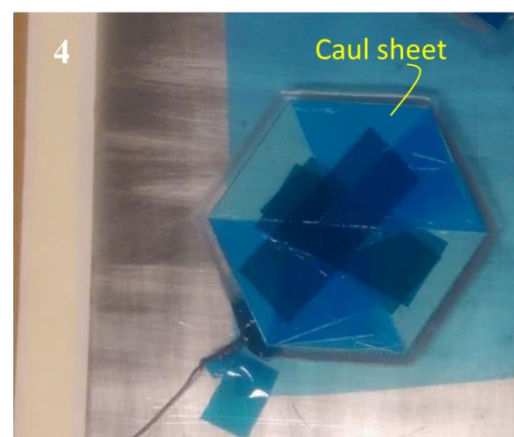
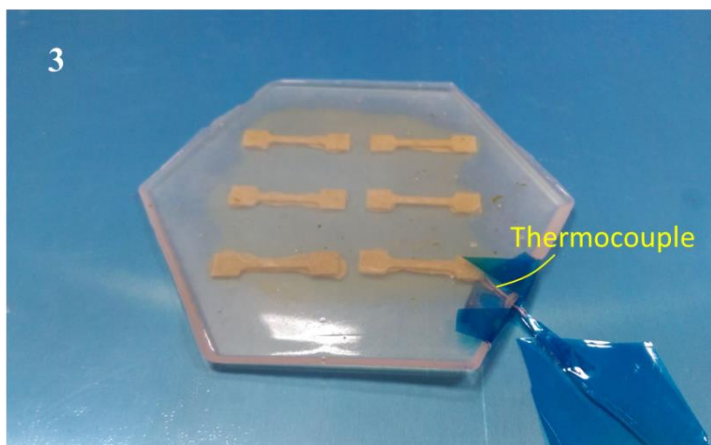
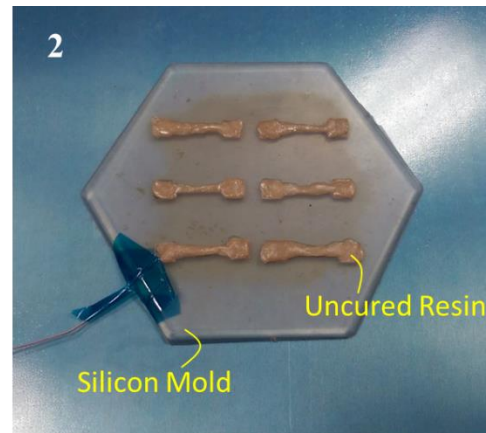
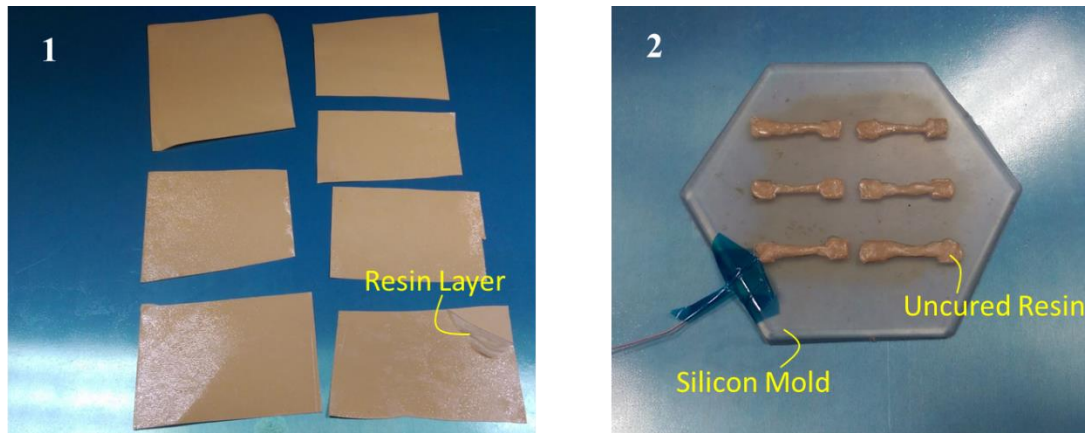


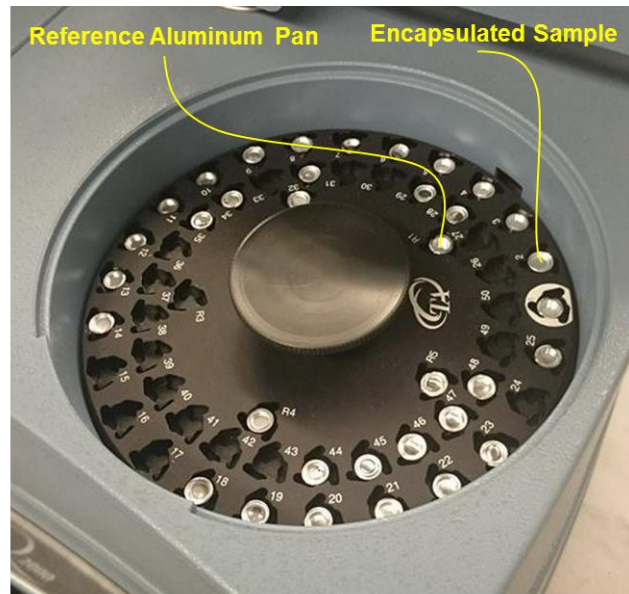
Figure 19. Specimen preparation of 5320-1 Epoxy resin

3.3 Glass Transition Temperature (T_g) of 5320-1 Resin

Since 5320-1 epoxy resin is a viscous fluid, it could flow and possibly damage a testing apparatus during stress relaxation experiments. To prevent this from occurring, the cured samples were tested for the glass transition temperature in the Q2000 Differential Scanning Calorimetry (DSC) [41]. This was done by taking small circular 5320-1 epoxy resin samples with a mass of 10-15 mg and subjecting them to a thermal ramp with a heating rate of 10°C per minute. To measure the glass transition temperature, the specimens had to be ramped to temperatures well beyond their curing temperature. The measured heat flow was then plotted versus the temperature, and the glass transition temperature was identified according to ASTM E 1356-08 as shown in the Figure 21 [42].



Differential Scanning Calorimeter



DSC Sample Tray

Figure 20. Differential Scanning Calorimeter (DSC) Q2000 series of TA Instruments [41]

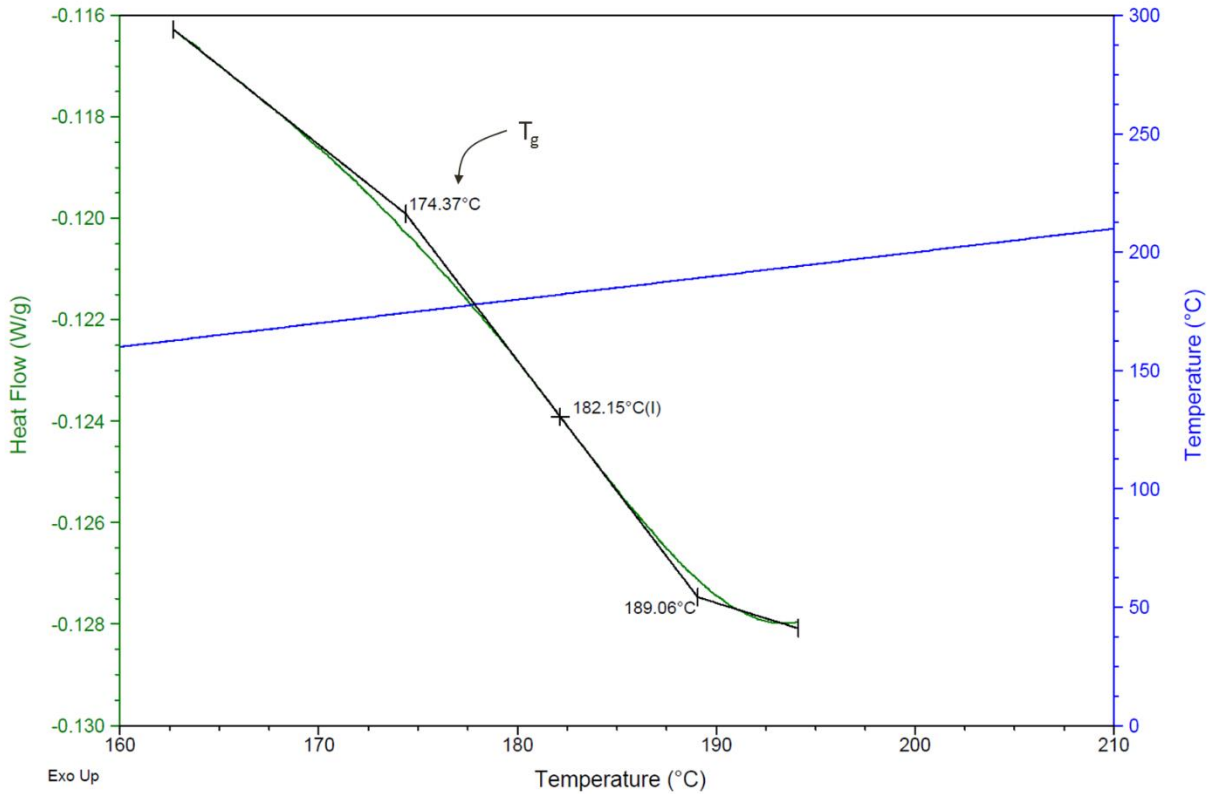


Figure 21. Glass Transition Temperature (T_g) of 5320-1 Epoxy Resin

3.4 Determination of Linear Viscoelastic Region (LVR)

Usually, rheological properties of a viscoelastic material are independent of strain level when the strain is within a critical strain limit. This region of strain level is called the Linear Viscoelastic Region (LVR) [43]. Within the LVR, material response was recorded without any damage in their structure. Therefore, a strain sweep experiment was performed on the 5320-1 epoxy resin using Q800 Dynamic Mechanical Analyzer (DMA) [44] to decide appropriate strain limit. Also, LVR can be verified by the following relation after loading [43],

$$\frac{\sigma(t_1)}{\varepsilon(t_1)} = \frac{\sigma(t_2)}{\varepsilon(t_2)} \quad (3.1)$$

From the linear viscoelastic region, a common strain rate of 0.1% was chosen for 5320-1 epoxy resin. Selected strain rate stays in the region of 96% or more of its magnitude of

normalized storage modulus as shown in Figure 22. Since the resin content in the 5320-8HS is identical, similar strain rate was selected for small specimens tested in DMA.

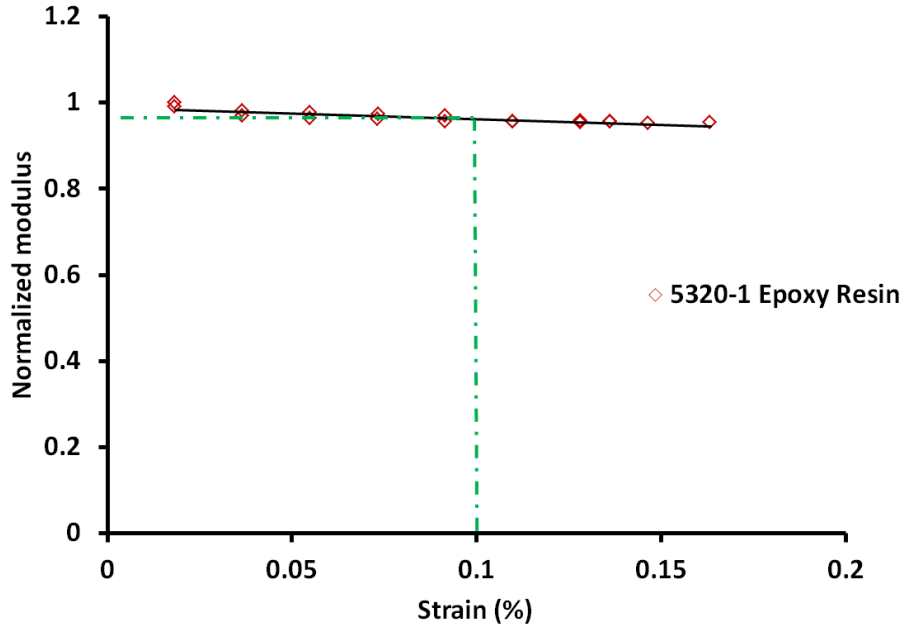


Figure 22. Linear viscoelastic Region of 5320-1 Epoxy Resin Using Dynamic Mechanical Analyzer (DMA)

For 5320-8HS longer specimens, strain limit was selected based on the load cell and critical strain level which was predicted from the creep curves [45]. Figure 23 and Figure 24 illustrate the LVR of 5320-8HS and verification of LVR at elevated temperatures.

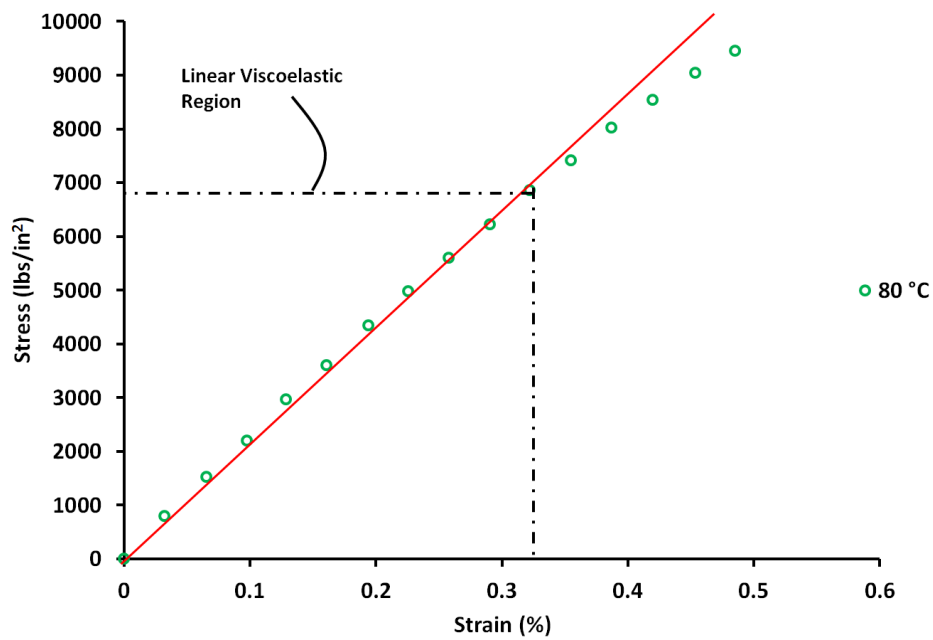


Figure 23. Linear viscoelastic Region (LVR) of 5320-8HS

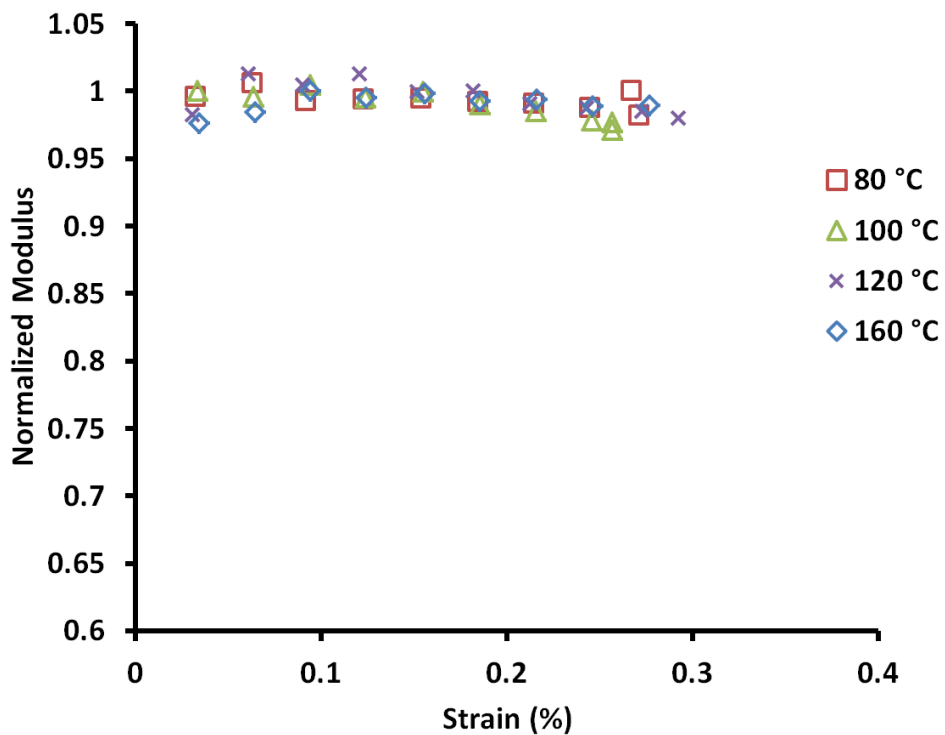


Figure 24. Verification of Linear viscoelastic Region for 5320-8HS after loading

3.5 Stress Relaxation of 5320-1 Epoxy Resin

The Q800 Dynamic Mechanical Analyzer (DMA) [44] was used to test for stress relaxation. The dogbone-shaped samples with a length of 25 ± 0.015 mm were tested using tension clamps. In all cases, the samples were loaded at a constant strain of 0.1% and isothermally held for 15 minutes. In order to get the stress relaxation behavior across a proper temperature range, the samples were isothermally held at room temperature, incremented by 10°C , and then isothermally held again. This process was repeated until the temperature surpassed the glass transition temperature of the samples. The relaxation modulus was only measured during the isothermal hold once the constant strain was instantaneously applied. It should be noted that in all cases the samples and clamps were covered by a wire mesh during testing to ensure the temperature distribution remained constant as displayed in Figure 25.

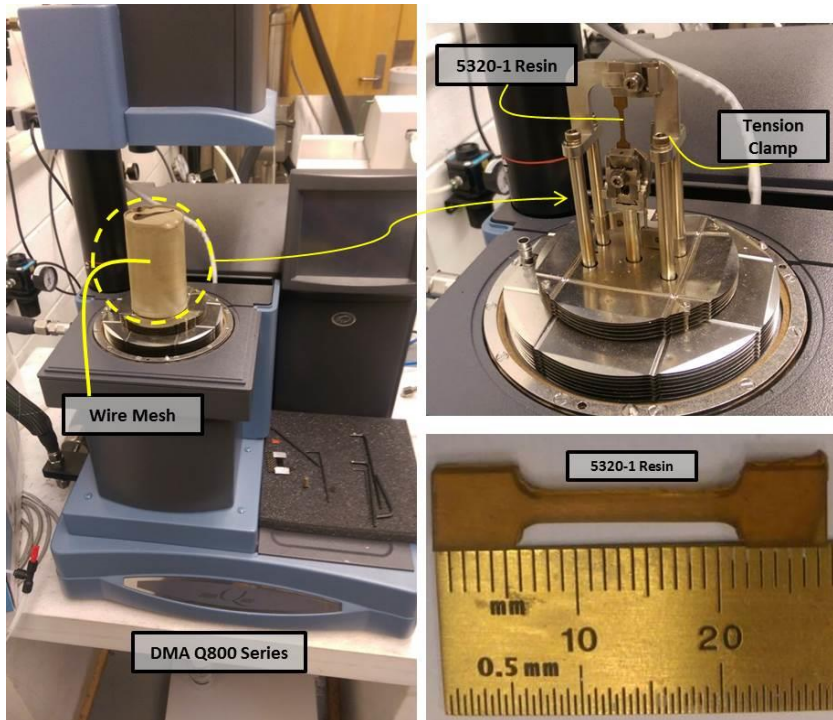


Figure 25. Test Setup for Stress Relaxation of 5320-1 Epoxy Resin Using Dynamic Mechanical Analyzer (DMA) [44]

3.6 Time-Temperature Superposition (TTS) and Shift function

Under constant deformation, polymers undergo a molecular rearrangement as a function of time resulting in decay of stress with deformation history. Tobolsky and Andrew [46] found the existence of similarity in the time- and temperature- dependent mechanical behavior of polymers and came up with a relationship, which is now widely known as “*Time-Temperature Superposition(TTS) principle*”. According to TTS principle, mechanical behavior of polymers at elevated temperatures is proportional to the behavior of material in longer time intervals (i.e., at low frequencies). Therefore, it allows to predict the long term behavior of material at certain temperature utilizing the short term behavior of material at various temperatures.

After stress relaxation testing, the data was analyzed using the TTS principle and manually calculating the shift factors. First, the relaxation modulus for each temperature was superimposed onto a single plot under the same logarithmic time scale. Then, one curve which shows the greatest relaxation modulus was chosen as a reference. A linear horizontal shift performed for each subsequent temperature's relaxation modulus with respect to the reference curve to generate a master curve as shown in Figure 26. The amount of horizontal shift required before superimposing is called as a horizontal shift factor (a_T). The discrete values of a shift factors were fitted with the well-known William-Landel-Ferry (WLF) equation [47] associated with TTS. The WLF equation is expressed as follows

$$a_T = \frac{-C_1(T - T_o)}{C_2 + (T - T_o)} \quad (3.2)$$

where T_o is the reference temperature (in K), T is the temperature of interest (in K), C_1 and C_2 are constants obtained from curve-fitting. For the purposes of numerical analysis, the generated master curve was fitted with a Prony series using equation (2.12).

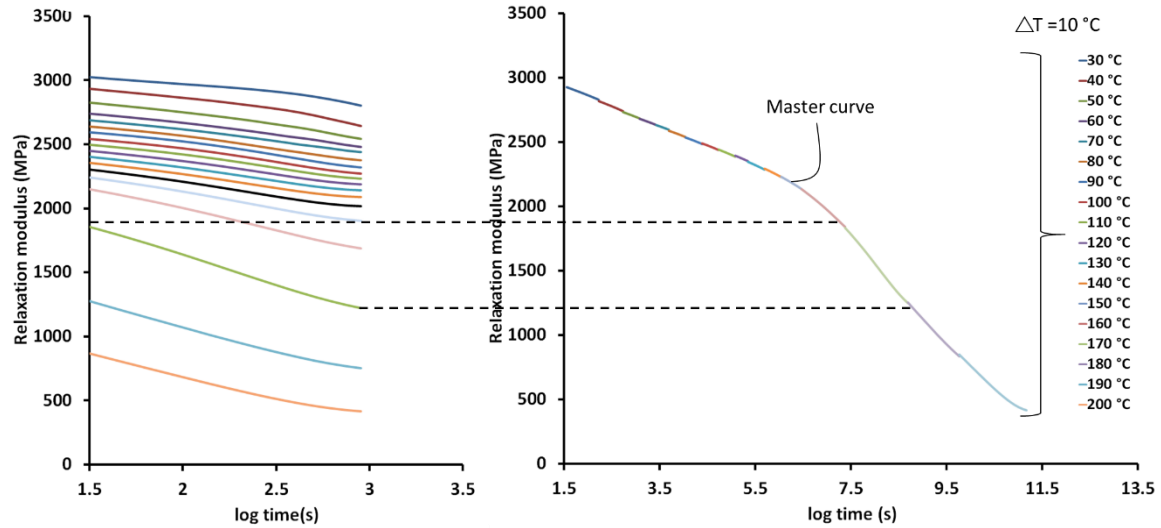


Figure 26. Construction of master curve from distinct curves of individual temperatures

3.7 Fabrication of 5320-8HS Specimen

Unlike the resin, silicon molds were not necessary for the fiber-reinforced composites, so the uncured prepreg plies could immediately be laid-up. Due to the presence of the reinforced fibers, the plies had to be stacked in squares following a sequence in which the fiber directions were considered. For the case of 5320-8HS the fill direction was taken as the [0°] direction.

First, aluminum flat support tool was wiped with acetone and released with a release agent. Then, plies of uncured 5320-8HS prepreg material were stacked up as per the test matrix summarized in Appendix A. Once laid-up, the plies were debulked for at least 30 minutes as shown in Figure 27 and then cured in oven following the similar cure cycle of 5320-1 epoxy resin. A minimum of 26 in Hg vacuum was applied throughout the debulking and curing process. Then, the 5320-8HS samples were cut using water jet cutter after passing through CT-scan. Schematics and test matrix of prepared specimens are presented in Appendix A.

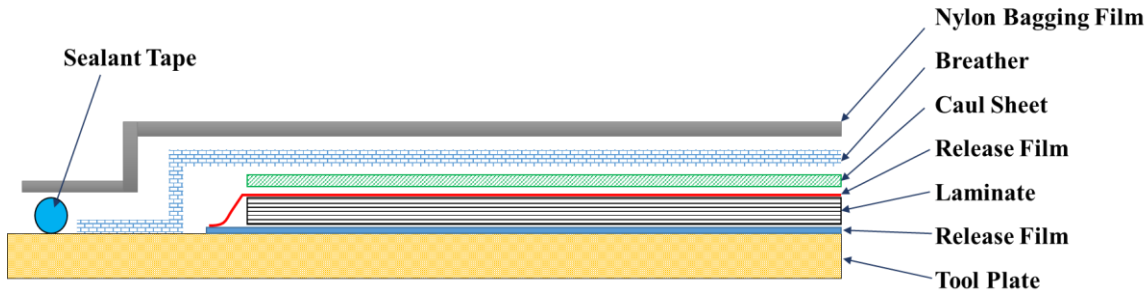


Figure 27. Vacuum Bagging

3.8 Uniaxial Tension Testing

Stress relaxation tests under uniaxial tension was performed on 5320-8HS specimen with a dimension of $279.00\text{ mm} \times 25.40\text{ mm} \times 0.76\text{ mm}$ using 810 Material Test System (MTS) Machine [48] at National Institute for Aviation Research (NIAR). Specimen were clamped by *flat surface* (FS) wedges with a gripping pressure of 5.52 MPa to avoid slippage of specimen. In addition, an extensometer of gauge length 25.4 mm, was mounted to the gage region of specimen to measure the strains. Emery cloth was bonded on the specimen surface using high temperature glue to avoid slippage of extensometer. The extensometer was used to control the pre-strain imposed on the specimens prior to monitoring relaxation. To monitor the temperature, type-K thermocouples were attached on both specimen and actuator. Temperature was monitored and recorded using digital thermometer. Mechanical loading was controlled by MultiPurpose Testware® (MPT) software [49] throughout the experiment and thermal load was manually controlled with respect to time. Specimens were tested under isothermal conditions at four different temperatures (i.e., 80 °C, 100 °C, 120 °C, 160 °C). Soon after testing at each temperature, specimen was removed and the oven was cooled down to room temperature. Appendix A illustrates the test procedure, temperature log and schematics of test specimen. Figure 28 shows the test set up involved in the stress relaxation of 5320-8HS woven composite.

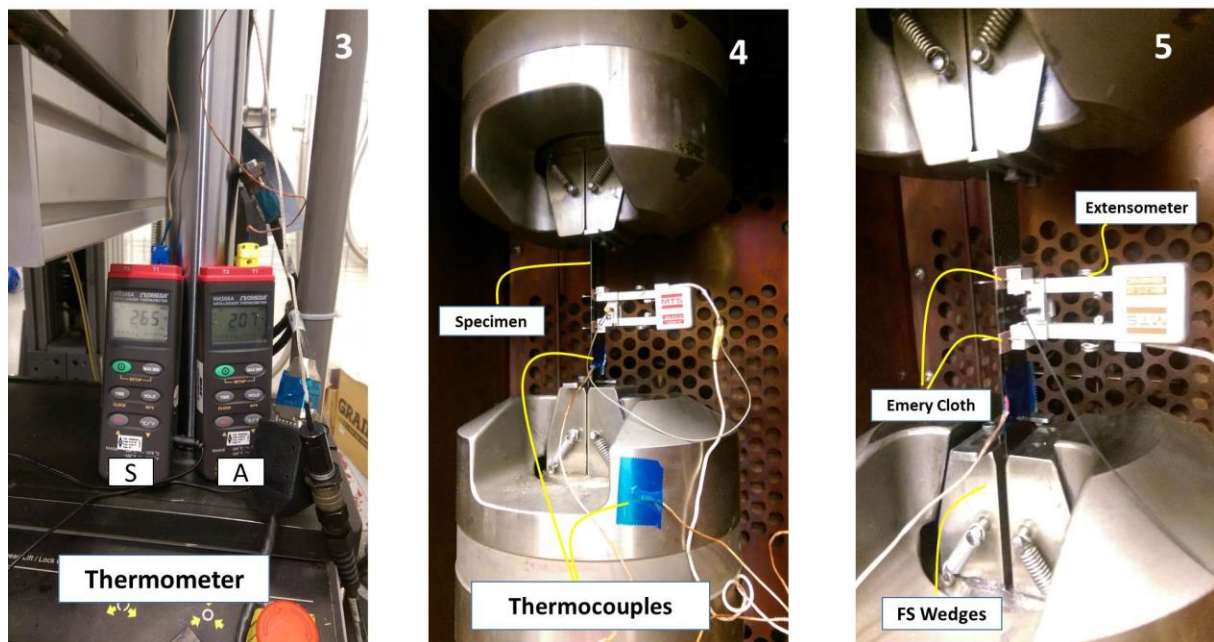


Figure 28. Stress Relaxation Test setup of 5320-8HS woven composite using 810 Material Test System (MTS) (5500lbf load cell)

3.9 Problems and limitations of uniaxial testing

From the temperature measurement log of actuator and specimen, a temperature difference was observed as shown in the Appendix A. This may be attributed to be due to different thermal conductivities and specific heat of two different materials. This in turn induces additional strain due to CTE mismatches between specimen and wedges, and affects the overall response of specimen. Even though applied strain was kept constant, as the time progresses, creep strain will start to develop in the microstructure and elastic strain in the gauge region will then reduce with respect to time as illustrated in the Appendix A. Therefore, testing at elevated temperatures will further cause lack of information regarding change in gauge length at every increment of temperature. In addition, specimen may also have higher chance of micro slippage and localized stress relaxation in the clamping region of specimen. In order to overcome all these difficulties, 3-point bending analysis was performed on smaller specimens using DMA, where sample is simply supported. It helps to capture the influence of fiber weave architecture on stress relaxation behavior of 5320-8HS.

3.10 3-Point Bending Test

Similar to tension test of 5320-1 epoxy resin, stress relaxation behavior of 5320-8HS and 5320-1 epoxy resin was measured under a three-point bending test mode using a Dynamic Mechanical Analyzer (DMA) [44] as shown in Figure 29. All the samples were rectangular in shape with dimensions of 36 mm × 5 mm × 0.51 mm. To gather data, the specimens were subjected to a constant strain through a range of isothermal temperature holds that surpassed the material's glass transition temperature. Appendix A displays the schematics of test specimen.

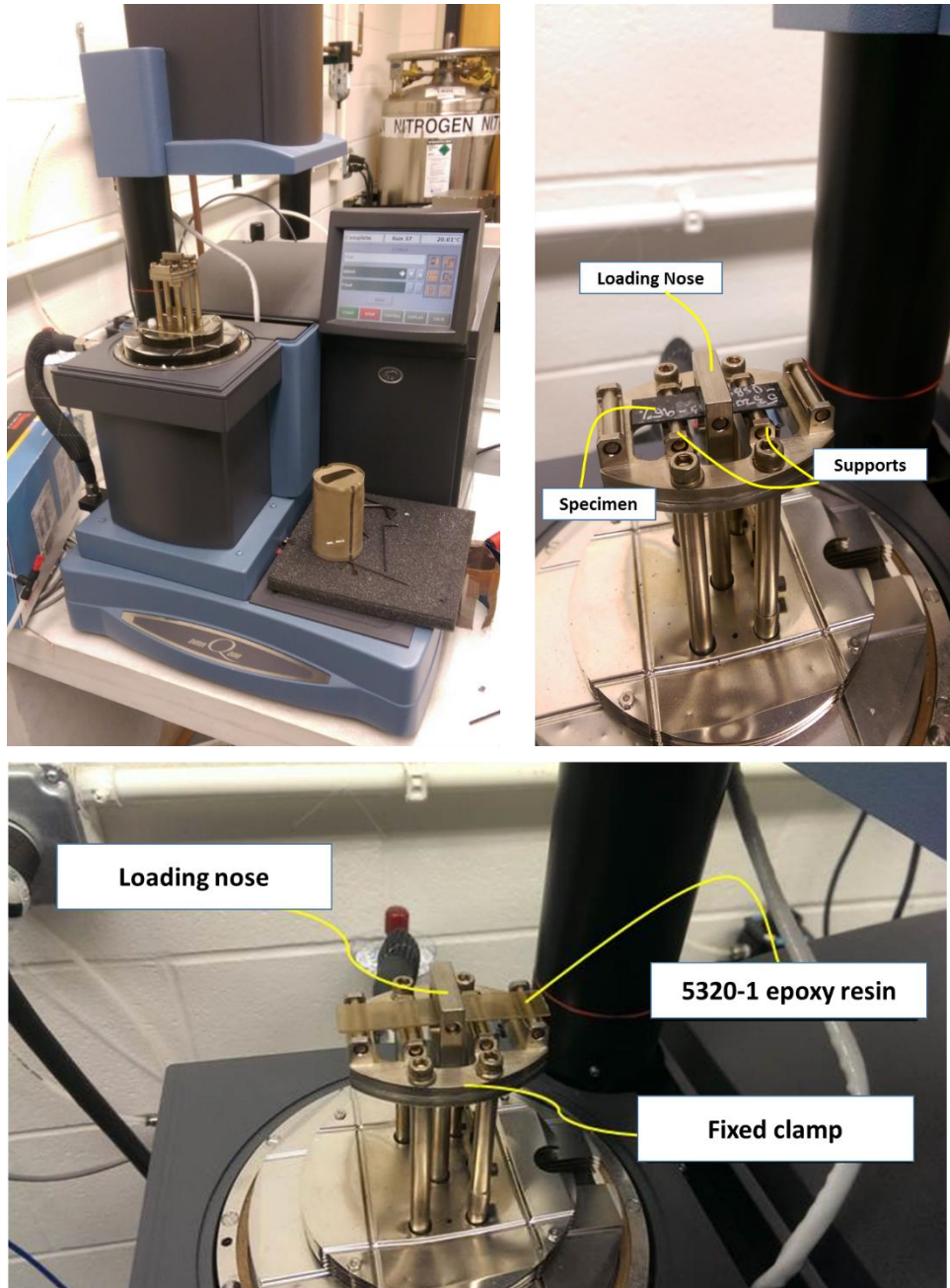


Figure 29. Stress Relaxation of 5320-8HS and 5320-1 epoxy resin under 3-Point Bending using Dynamic Mechanical Analyzer (DMA)

CHAPTER 4

COMPUTATIONAL MICROMECHANICS MODEL AND MESH GENERATION

This chapter describes the development of micromechanics model of 8-harness satin weave layer and the mesh generation approach.

4.1 Geometry of 8-harness Satin Unit Cell

Micromechanics model of 8-HS woven composite is an assemblage of neat resin and fiber bundles/tows. The development of 8-harness unit cell involves three steps. First, the dimensions and fiber volume fraction of the fiber bundles were measured from the photomicrographs of woven composite as shown in the Figure 31. Then, the overall fiber volume fraction of 8-harness was evaluated using acid digestion method from the samples of cured laminate. The design parameters required to model the weave architecture of the unit cell were evaluated for a desired overall fiber volume fraction of woven fabrics. Fiber volume fraction and cross section geometry of the tows are assumed to be constant for entire unit cell model.

The samples of 5320-8HS were cut from the cured laminate to desired dimensions using a water jet cutter and potted with an epoxy resin and cured at room temperature. Then, the potted specimens were polished to fine surface finish and examined under an optical microscope with a magnification of 50X to obtain the yarn dimensions. A typical potted samples and sectional view of 5320-8HS were displayed in Figure 30 and Figure 31. Unit cell and measurement of geometric parameters were illustrated in Figure 32 and Figure 33. In order to evaluate the fiber volume fraction in the tows, photomicrographs were converted to binary image as shown in Figure 33 and Figure 34. Based on the evaluation of black and white scales, fiber volume fraction of tows was averaged to be 0.77. From the results of acid digestion tests of 5320-8HS, overall fiber volume fraction of 5320-8HS was calculated to be 0.56.

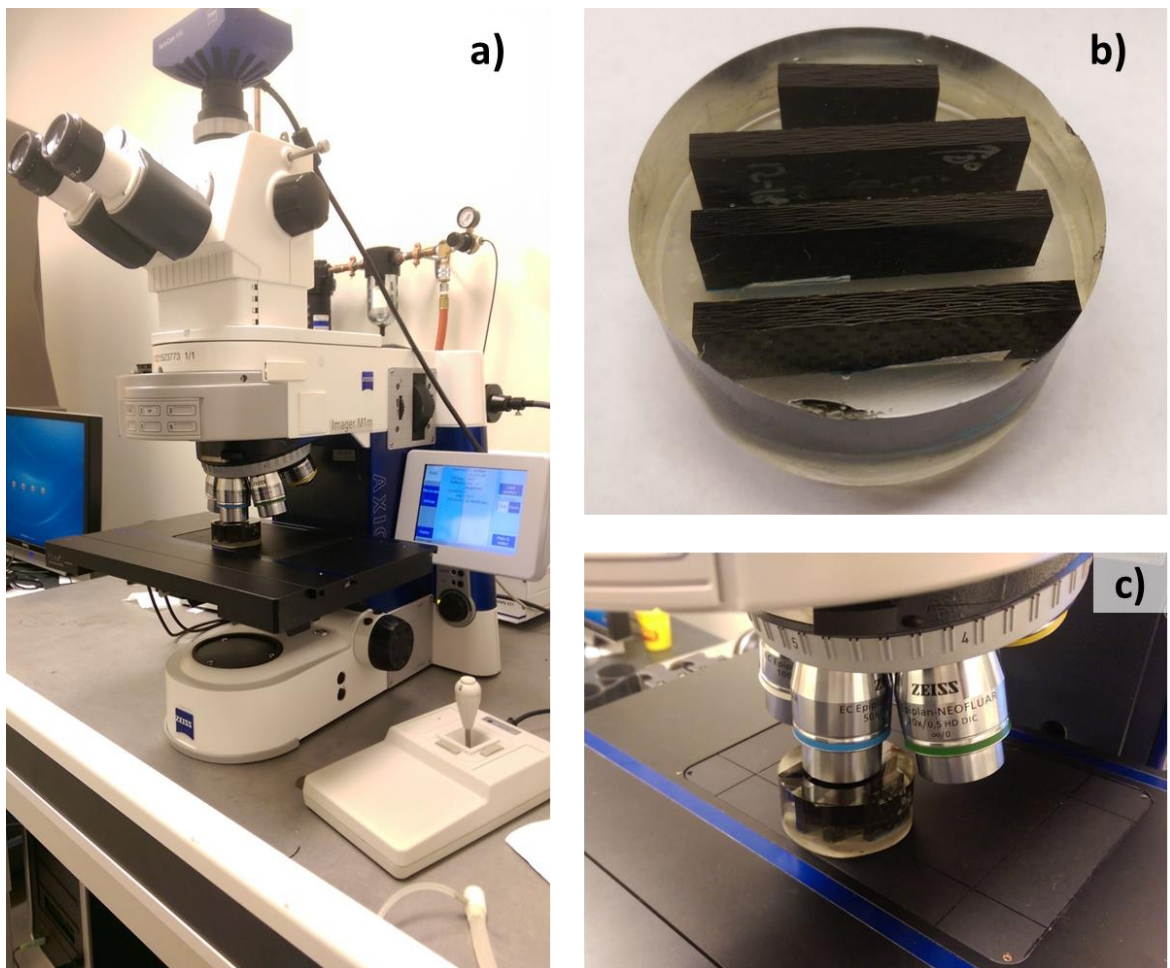


*Figure 30. Schematics of a) Axio Vision Microscope b) Potted 5320-8HS Specimens
c) Specimen under 50X magnification*

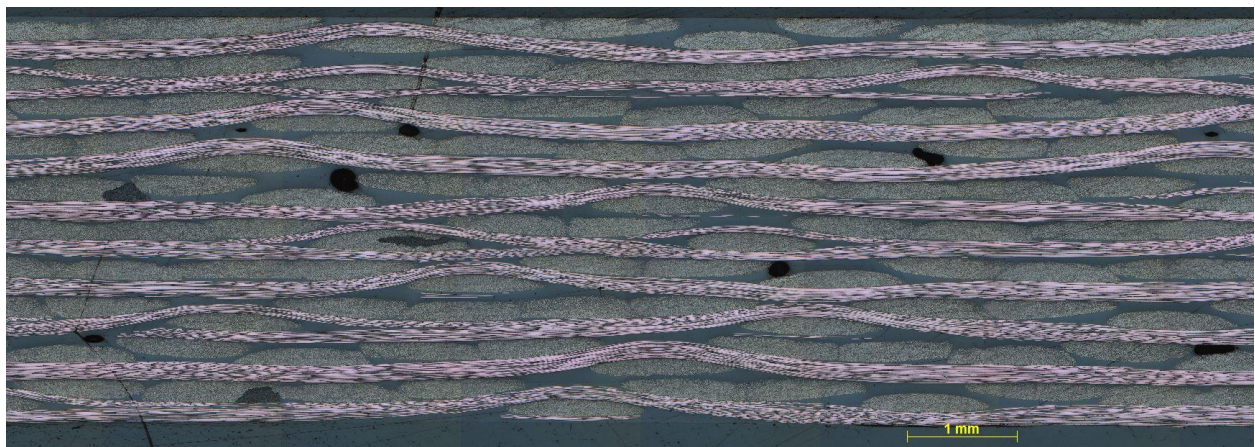


Figure 31. Photomicrograph of 5320-8HS Laminate

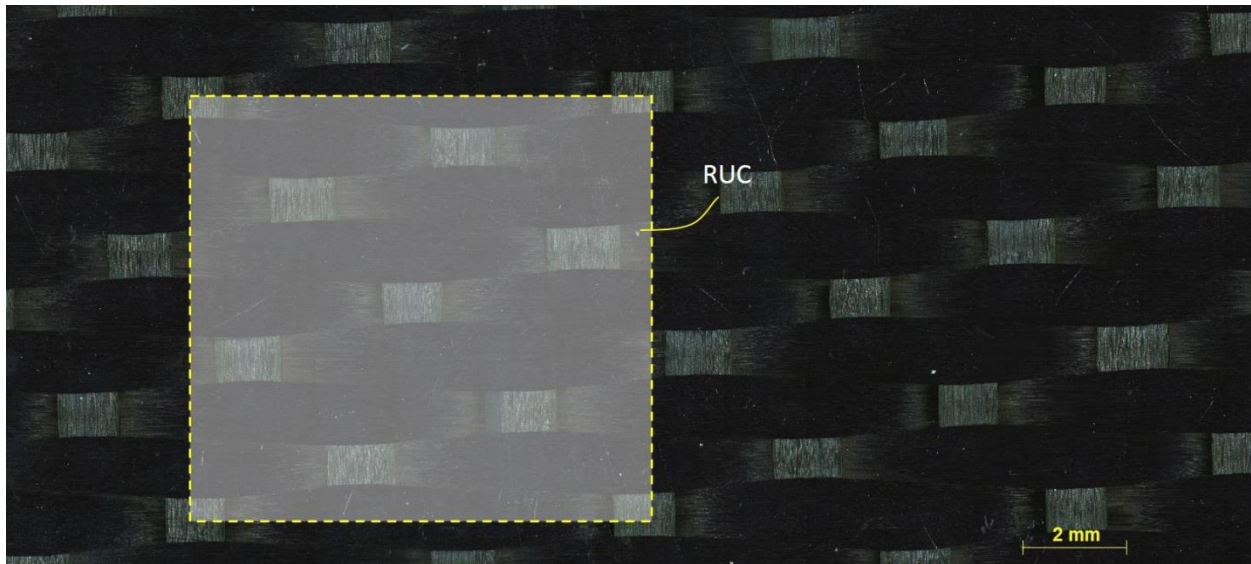


Figure 32. Repetitive Unit Cell (RUC) Of 5320-8HS Woven Composite (Top View of 5320-8HS Prepreg material)

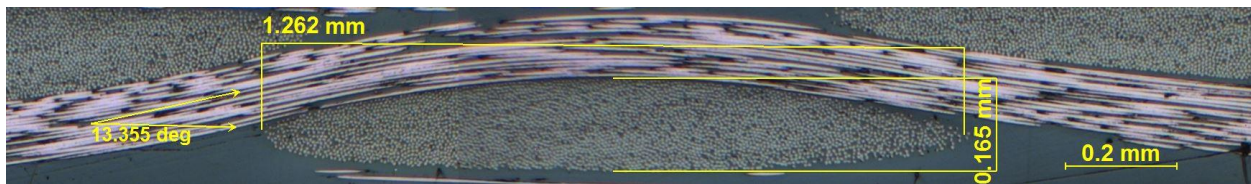


Figure 33. Dimensions of 5320-8HS Unit cell

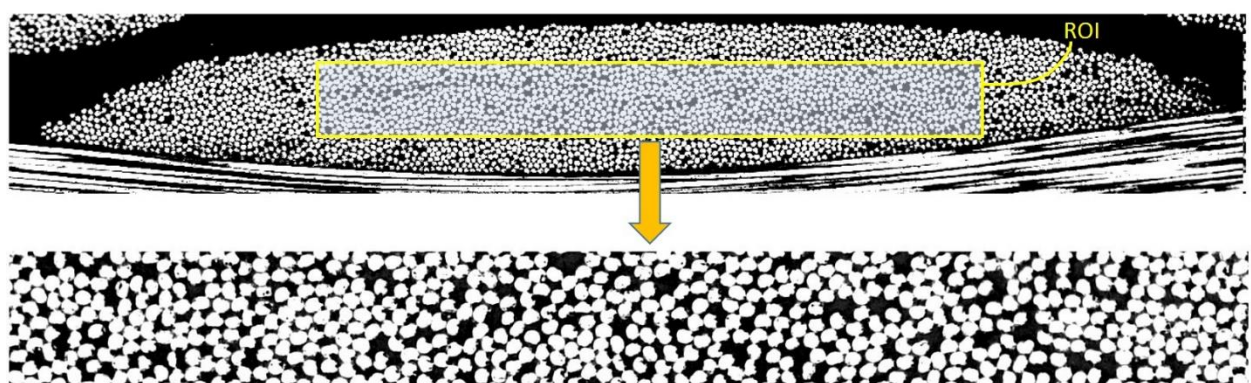


Figure 34. Greyscale image of tow cross section (ROI-Region of Interest)

Table 1. Measured dimensions of an 8-harness satin unit cell

Dimensions	
Length (mm)	10.56±0.072
Width (mm)	10.56±0.072
Thickness (mm)	1.33±0.003
Yarn width (mm)	2.28±0.072
Yarn thickness (mm)	0.176±0.005
Crimp angle (degree)	12±0.015
Fiber volume fraction of tows	0.76±0.02

In order to model the complex geometry of 8-harness satin weave, it is necessary to understand their intricate micro-structural architecture. Accuracy of the geometry is important to get better results in the modeling. Generally, the structure of woven fabrics is a network of orthogonally interlaced fiber bundles called the fill and warp tows [50]. For satin weave fabric, the tows morphology is characterized by undulation as well as floating/ straight regions as shown in Figure 31.

The most challenging part in the modeling is the complex microstructure due to waviness of the fiber bundles. Since the tow fiber volume fraction is greater than $\frac{2}{\pi}$, the cross section of the tow was modelled to be a flattened lenticular shape [50]. This is because, flattened tow architecture leaves less space for the matrix pockets and thereby allowing more overall fiber volume fraction [50]. Figure 35 and Figure 36 illustrate the geometric parameters of 5320-8HS unit cell model.

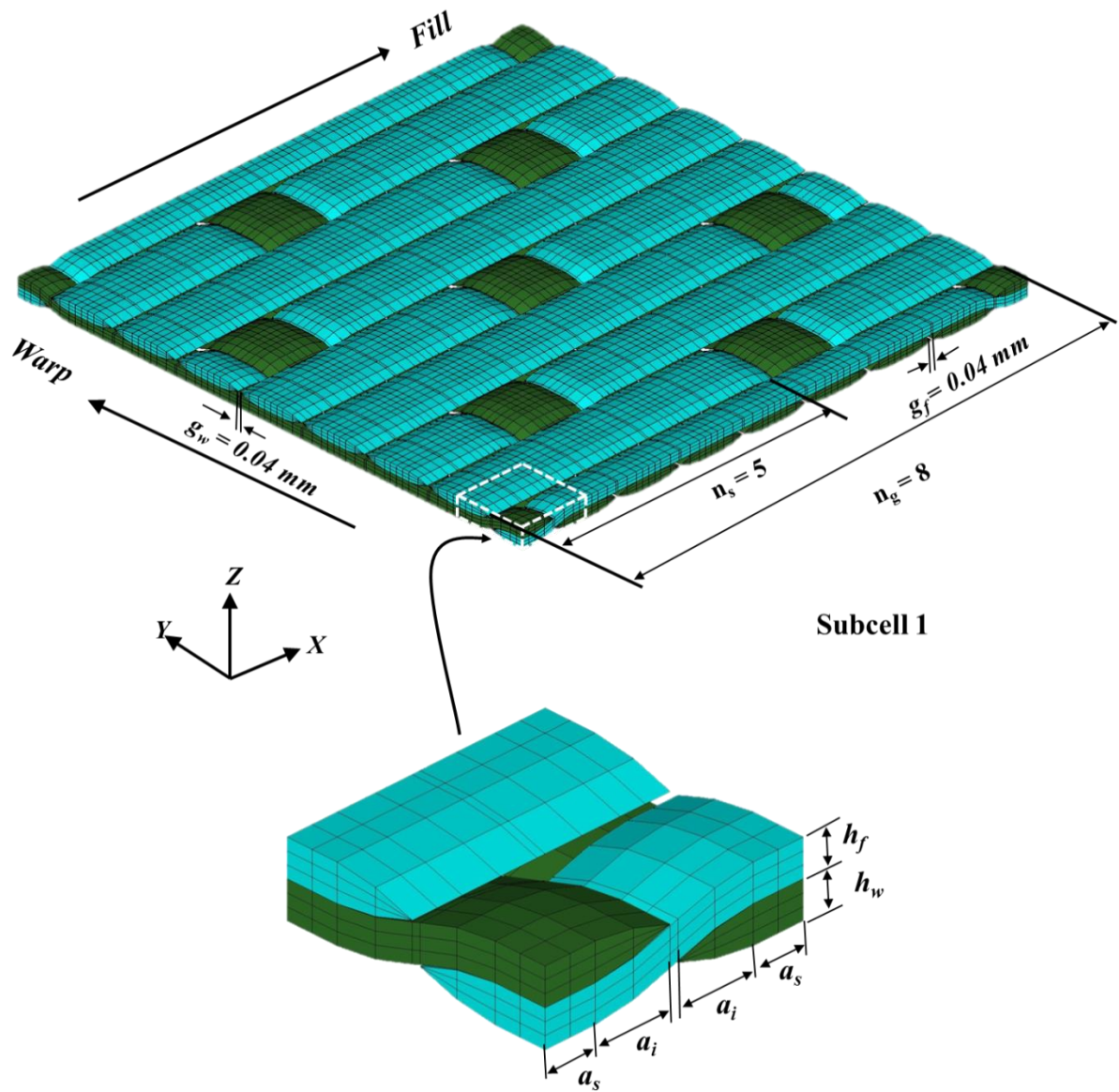


Figure 35. Geometry of 5320-8HS unit cell with no resin

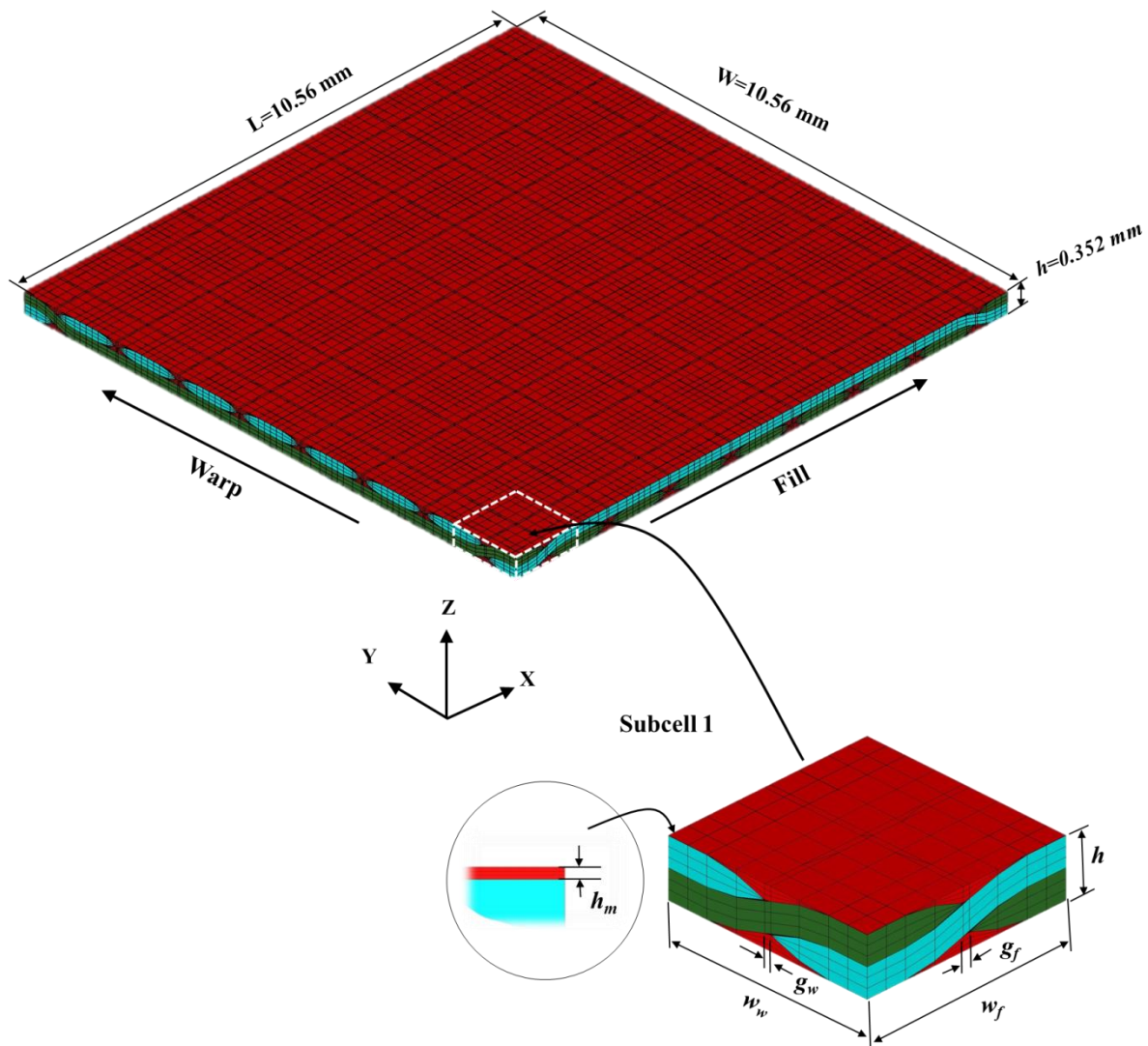


Figure 36. Geometry of 5320-8HS unit cell with resin

In order to model an idealized geometry of the flat lenticular tows, sine functions of Barbero [51] were modified to include flatness next to wavy region of tow cross section. Modified undulation function of fill tows for satin weave architecture was defined as follows.

If $(j-1)w_f + \frac{g_f}{2} \leq y \leq jw_f - \frac{g_f}{2}$

$z_f(x, y, j) =$

$$\left\{ \begin{array}{l} \text{for } k \in 1 \dots \text{trunc} \left[\frac{n_s(j-1)+1}{n_g} \right] + 1 \\ \quad \text{Undulation region with flatness embedment (1)} \\ \quad \frac{h_f}{2} \quad \text{if } \left[n_s(j-1) - \frac{1}{2} - kn_g \right] w - 17a_s \leq x \leq \left[n_s(j-1) - \frac{1}{2} - kn_g \right] w - 16a_s \\ \quad (-1)^{(kn_g+1)} \left(\frac{h_f}{2} \right) \sin \left(\frac{\pi(x+16a_s)}{w} + n_s(j-1)\pi \right) \\ \quad \quad \quad \text{if } \left[n_s(j-1) - \frac{1}{2} - kn_g \right] w - 16a_s \leq x \leq \left[n_s(j-1) - \frac{1}{2} - kn_g \right] w - 16a_s + w \\ \quad -\frac{h_f}{2} \quad \text{if } \left[n_s(j-1) - \frac{1}{2} - kn_g \right] w - 16a_s + w \leq x \leq \left[n_s(j-1) + \frac{3}{2} - kn_g \right] w - 14a_s - w \\ \quad (-1)^{(kn_g+1)} \left(\frac{h_f}{2} \right) \sin \left(\frac{\pi(x+14a_s)}{w} + n_s(j-1)\pi \right) \\ \quad \quad \quad \text{if } \left[n_s(j-1) + \frac{3}{2} - kn_g \right] w - 14a_s - w \leq x \leq \left[n_s(j-1) + \frac{3}{2} - kn_g \right] w - 14a_s \\ \quad \frac{h_f}{2} \quad \text{if } \left[n_s(j-1) + \frac{3}{2} - kn_g \right] w - 14a_s \leq x \leq \left[n_s(j-1) + \frac{3}{2} - kn_g \right] w - 13a_s \\ \quad \text{Floating Region (1)} \\ \quad \frac{h_f}{2} \quad \text{if } (k-1) \geq 1 \text{ and } \left[n_s(j-1) + \frac{3}{2} - kn_g \right] w - 13a_s < x < \left[n_s(j-1) - \frac{1}{2} - (k-1)n_g \right] w - a_s \end{array} \right.$$

Undulation region with flatness embedment (2)

$$\left\{ \begin{array}{l} \frac{h_f}{2} \quad \text{if } \left[n_s(j-1) - \frac{1}{2} \right] w - a_s \leq x \leq \left[n_s(j-1) - \frac{1}{2} \right] w \\ \quad \left(-\frac{h_f}{2} \right) \sin \left(\frac{\pi x}{w} + n_s(j-1)\pi \right) \\ \quad \quad \quad \text{if } \left[n_s(j-1) - \frac{1}{2} \right] w \leq x \leq \left[n_s(j-1) - \frac{1}{2} \right] w + w \\ \quad -\frac{h_f}{2} \quad \text{if } \left[n_s(j-1) - \frac{1}{2} \right] w + w \leq x \leq \left[n_s(j-1) - \frac{1}{2} \right] w + w_w \\ \quad \vdots \end{array} \right.$$

$$\left\{
\begin{array}{l}
\vdots \\
\left(-\frac{h_f}{2} \right) \sin \left(\frac{\pi(x-2a_s)}{w} + n_s(j-1)\pi \right) \\
\quad \text{if } \left[n_s(j-1) - \frac{1}{2} \right] w + w_w \leq x \leq \left[n_s(j-1) + \frac{3}{2} \right] w + 2a_s \\
\frac{h_f}{2} \quad \text{if } \left[n_s(j-1) + \frac{3}{2} \right] w + 2a_s \leq x \leq \left[n_s(j-1) + \frac{3}{2} \right] w + 3a_s
\end{array}
\right.$$

Undulation region with flatness embedment (3)

$$\left\{
\begin{array}{l}
\frac{h_f}{2} \quad \text{if } \left[n_s(j-1) - \frac{1}{2} + n_g \right] w + 15a_s \leq x \leq \left[n_s(j-1) - \frac{1}{2} + n_g \right] w + 16a_s \\
(-1)^{(n_g+1)} \left(\frac{h_f}{2} \right) \sin \left(\frac{\pi(x-16a_s)}{w} + n_s(j-1)\pi \right) \\
\quad \text{if } \left[n_s(j-1) - \frac{1}{2} + n_g \right] w + 16a_s \leq x \leq \left[n_s(j-1) - \frac{1}{2} + n_g \right] w + 16a_s + w \\
-\frac{h_f}{2} \quad \text{if } \left[n_s(j-1) - \frac{1}{2} + n_g \right] w + 16a_s + w \leq x \leq \left[n_s(j-1) - \frac{1}{2} + n_g \right] w + 18a_s + w \\
(-1)^{(n_g+1)} \left(\frac{h_f}{2} \right) \sin \left(\frac{\pi(x-18a_s)}{w} + n_s(j-1)\pi \right) \\
\quad \text{if } \left[n_s(j-1) - \frac{1}{2} + n_g \right] w + 18a_s + w \leq x \leq \left[n_s(j-1) + \frac{3}{2} + n_g \right] w + 18a_s \\
\frac{h_f}{2} \quad \text{if } \left[n_s(j-1) + \frac{3}{2} + n_g \right] w + 18a_s \leq x \leq \left[n_s(j-1) + \frac{3}{2} + n_g \right] w + 19a_s
\end{array}
\right.$$

Floating Region (2)

$$\left\{
\begin{array}{l}
\frac{h_f}{2} \quad \text{if } \left[n_s(j-1) + \frac{3}{2} - n_g \right] w - 13a_s < x < \left[n_s(j-1) - \frac{1}{2} \right] w - a_s \\
\quad \text{or } \left[n_s(j-1) + \frac{3}{2} \right] w + 3a_s < x < \left[n_s(j-1) - \frac{1}{2} + n_g \right] w + 15a_s
\end{array}
\right.$$

if $\left[(j-1)w_f \leq y < (j-1)w_f + \frac{g_f}{2} \text{ or } jw_f - \frac{g_f}{2} < y \leq jw_f \text{ and } g_f \neq 0 \right]$

$$z_f(x, y, j) = 0 \tag{4.1}$$

where $w = 2a_i + g_w$

note: (1),(2),(3) denotes different locations

For warp geometry, undulation functions were multiplied with minus one and $x, y, j, w_f, w_w, g_f, g_w, h_f$ were replaced with $y, x, i, w_w, w_f, g_w, g_f, h_w$

The other parameters like tow fiber volume fraction, overall fiber volume fraction, length, crimp angle, waviness and cross section area of the tow, etc., were calculated using the relations of Barbero [51] and are summarized in Appendix B. Similar to tow undulation, through thickness function for fill and warp tows was developed to model flattened lenticular tow cross section. Appendix C lists the FORTRAN program that generates the geometric parameters of both fill and warp tows. Modified through thickness function for fiber bundles was defined as follows

$$e_f(y, j) = \begin{cases} \left| \frac{h_f}{2} \sin \left(\frac{\pi \left(-(j-1)w_f + y - \frac{g_f}{2} \right)}{2a_i} \right) \right| & \text{if } (j-1)w_f + \frac{g_f}{2} \leq y \leq (j-1)w_f + \frac{g_f}{2} + a_i \\ \left| \frac{h_f}{2} \right| & \text{if } (j-1)w_f + \frac{g_f}{2} + a_i \leq y \leq (j-1)w_f + \frac{g_f}{2} + a_i + 2a_s \\ \left| \frac{h_f}{2} \sin \left(\frac{\pi \left(-(j-1)w_f + (y - 2a_s) - \frac{g_f}{2} \right)}{2a_i} \right) \right| & \text{if } (j-1)w_f + \frac{g_f}{2} + a_i + 2a_s \leq y \leq jw_f - \frac{g_f}{2} \\ 0 & \text{if } (j-1)w_f \leq y < (j-1)w_f + \frac{g_f}{2} \text{ or } jw_f - \frac{g_f}{2} < y \leq jw_f \end{cases} \quad (4.2)$$

Similar to undulation, through thickness functions of warp tows were multiplied with minus one and $x, y, j, w_f, w_w, g_f, g_w, h_f$ were replaced with $y, x, i, w_w, w_f, g_w, g_f, h_w$

4.2 Mesh Generation

To overcome the complexity of matrix pockets, binary subcell modeling approach of Hewitt [52] and Pantiuk et al [53] was adopted in the mesh generation process. Unit cell model of 8-harness satin weave is assumed to be an assemblage of a 64 binary subcells (square subcells). To model complete 8-harness satin weave unit cell, only 5 binary subcells were required to be distributed throughout the entire unit cell following the assembly matrix of Table 2. The following assembly matrix was designed based on the view point of 8-harness satin weave pattern.

Table 2. Assembly Matrix for Binary subcells of 8-harness weave architecture

Left bottom corner as origin		X-direction (Fill)							
Y-direction (warp)	Binary Subcell Row/Column No.	1	2	3	4	5	6	7	8
	1	1	2	2	2	3	4	2	5
	2	2	3	4	2	5	1	2	2
	3	2	5	1	2	2	2	3	4
	4	2	2	2	3	4	2	5	1
	5	3	4	2	5	1	2	2	2
	6	5	1	2	2	2	3	4	2
	7	2	2	3	4	2	5	1	2
	8	4	2	5	1	2	2	2	3

Note: Numbers inside the assembly matrix are binary subcell identifiers

4.2.1 Development of primary subcells

First, required number of tows along fill and warp direction (i.e. 2 fill tows and 3 warp tows) were modelled based on the calculated geometric parameters using CATIA v5 and then exported to Hypermesh v11 [36]. Figure 37 displays an imported geometry of fill and warp tows. Design parameters required to model 8-HS weave architecture are described in Appendix B. The imported solid geometry of fill and warp tows was meshed using hexahedral and pentahedral solid elements and then assigned to binary subcells (i.e. subcell1 and subcell 2). Matrix pockets surrounding the fill and warp tows were manually meshed using hexahedral, tetrahedral and pentahedral solid elements for required thickness.

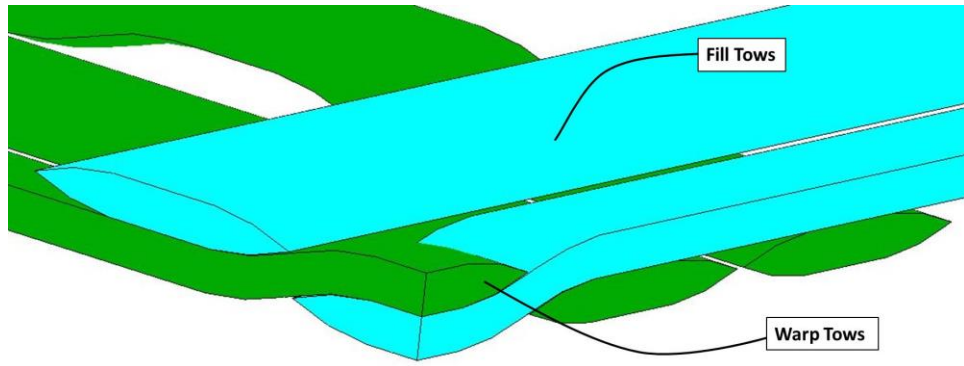


Figure 37. Solid geometry of fill and warp tows

Utilizing the symmetric plane of subcell 1, other 3 subcells were generated as illustrated in the following Figure 38. All five primary subcells required to model satin weave architecture were displayed in the Table 3.

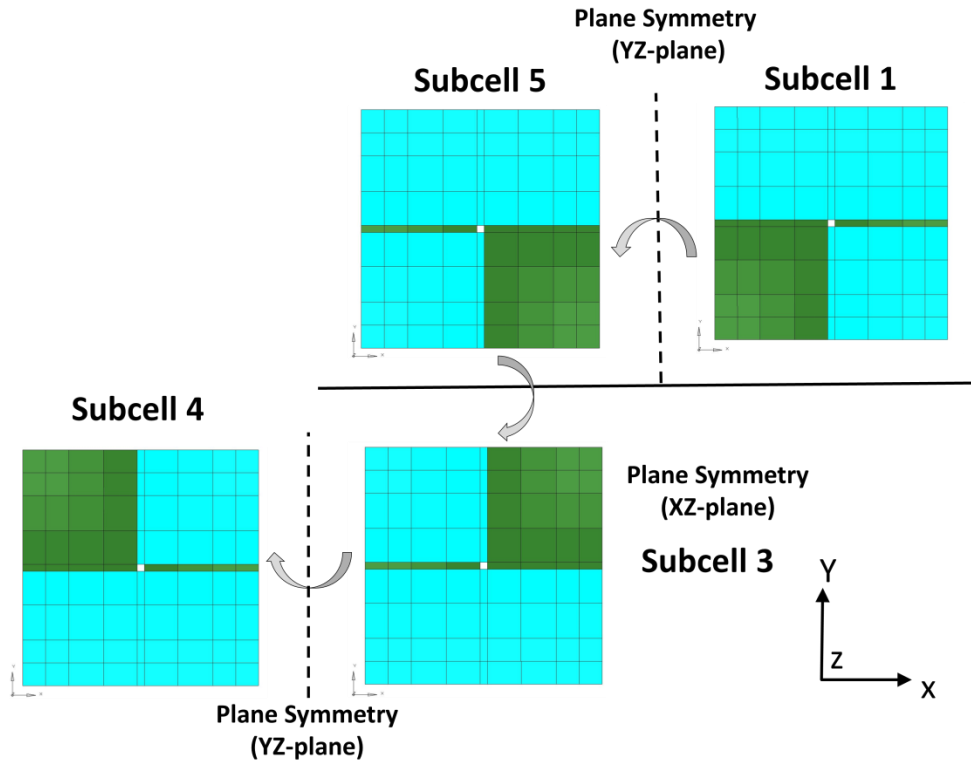
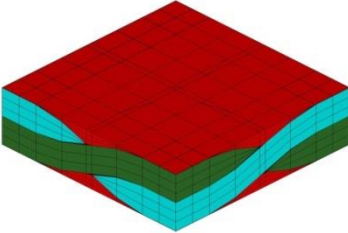
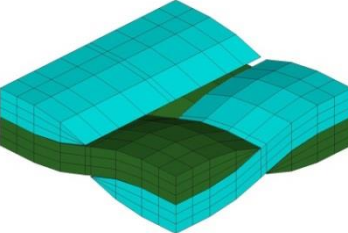
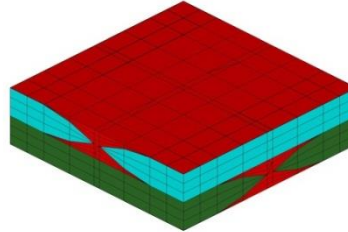
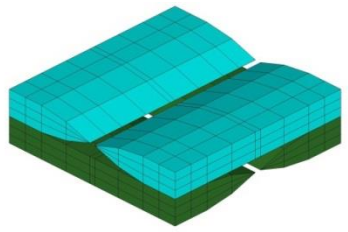
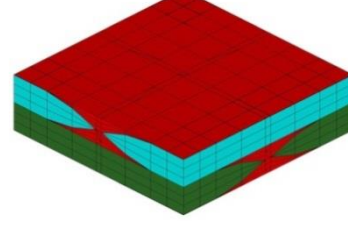
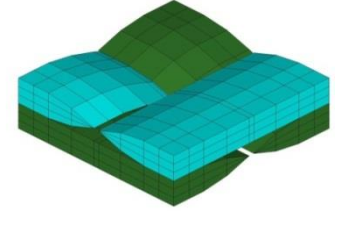
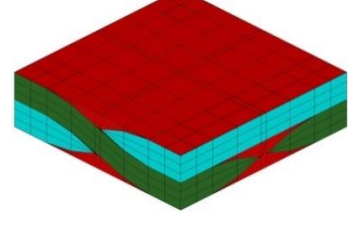
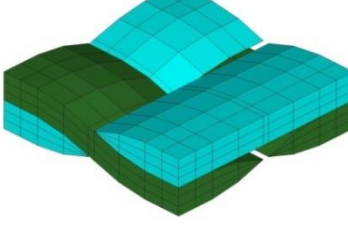
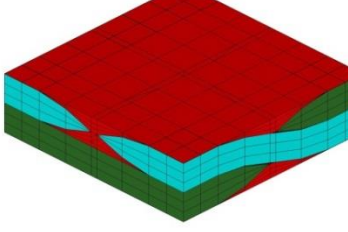
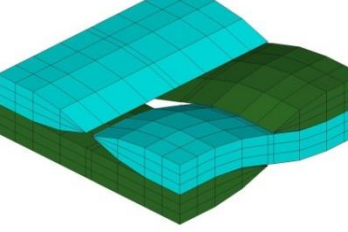


Figure 38. Reflectional symmetries of subcell 1

Table 3. Five primary subcells to model full 8-harness unit cell

Binary subcell ID	Subcells with neat resin	Subcells without resin
1		
2		
3		
4		
5		

4.2.2 Assembly of developed binary subcells

Based on the assembly matrix of 8-harness geometry, the binary subcells were assembled using bottom to top approach with (0, 0, 0) as an origin. Figure 39 illustrates the top view of assembled binary subcells.

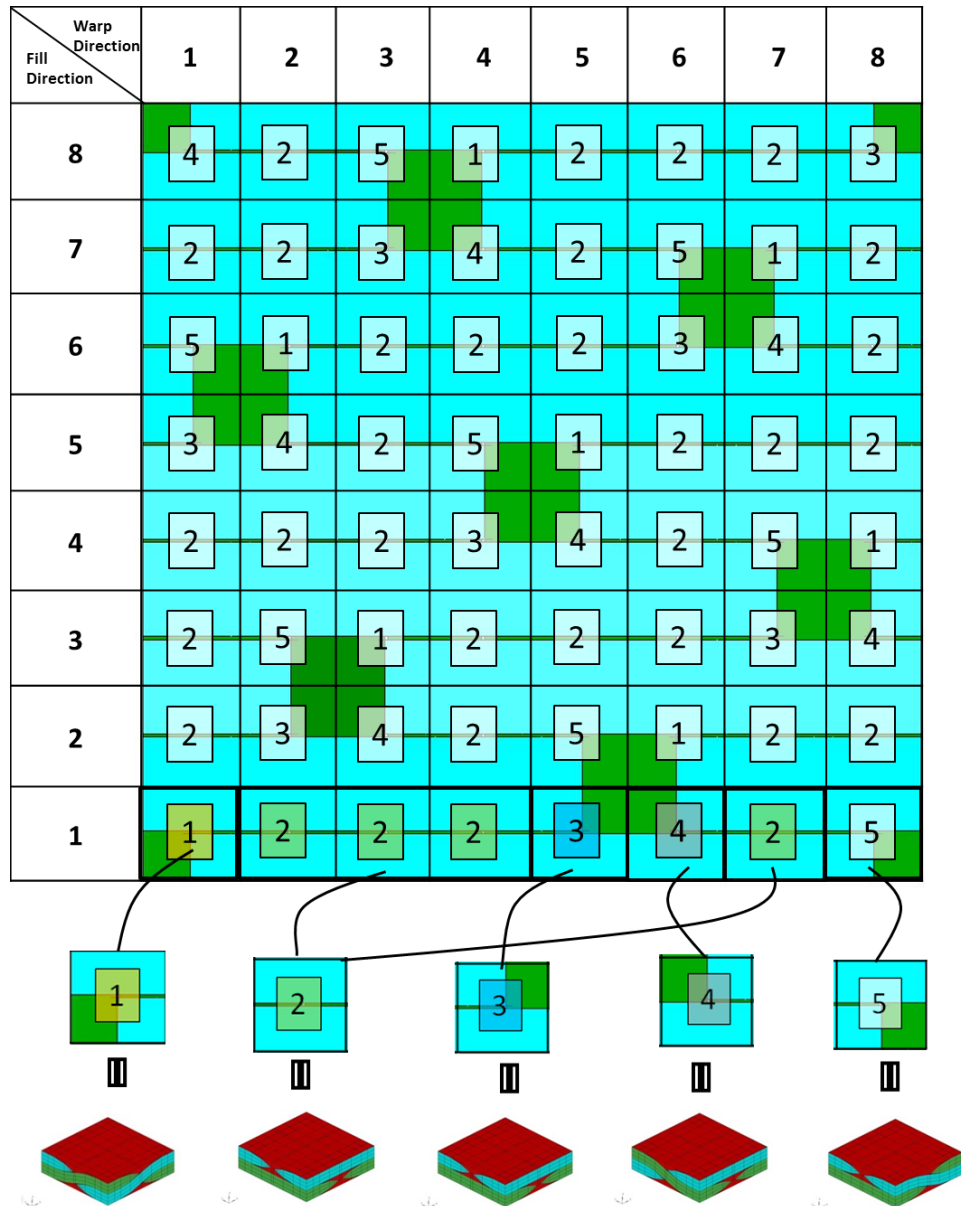


Figure 39. Assembly of binary subcells for 8-harness weave architecture

4.2.3 Development of complete unit cell of 8-harness weave architecture

After assembling the binary subcells, duplicate nodes were merged and elements were assigned to the corresponding tows and matrix. Figure 40, 41 and 42 illustrate the discretized model of 5320-8HS unit cell.

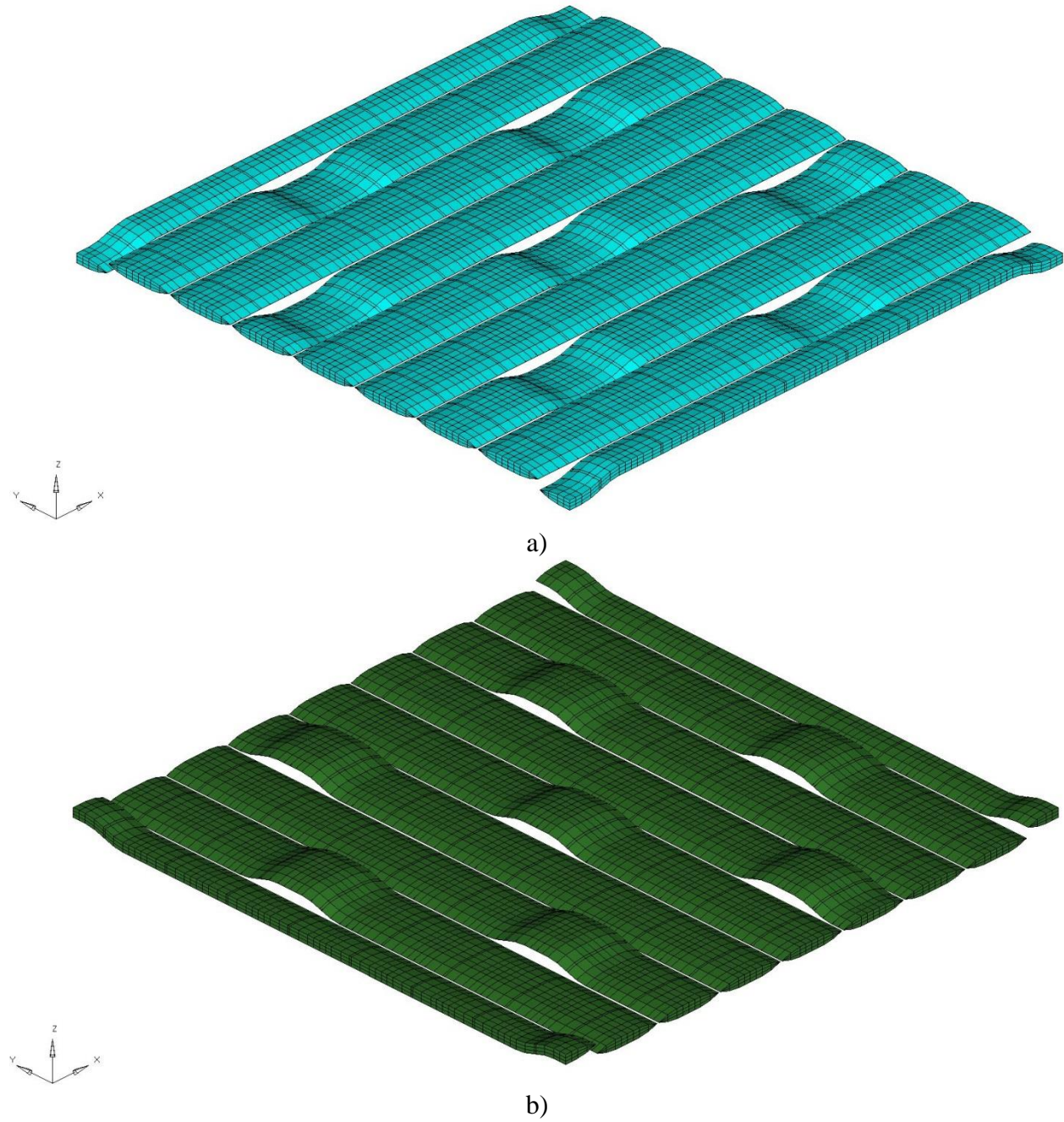


Figure 40. Generated mesh of a) Fill Tows and b) Warp Tows

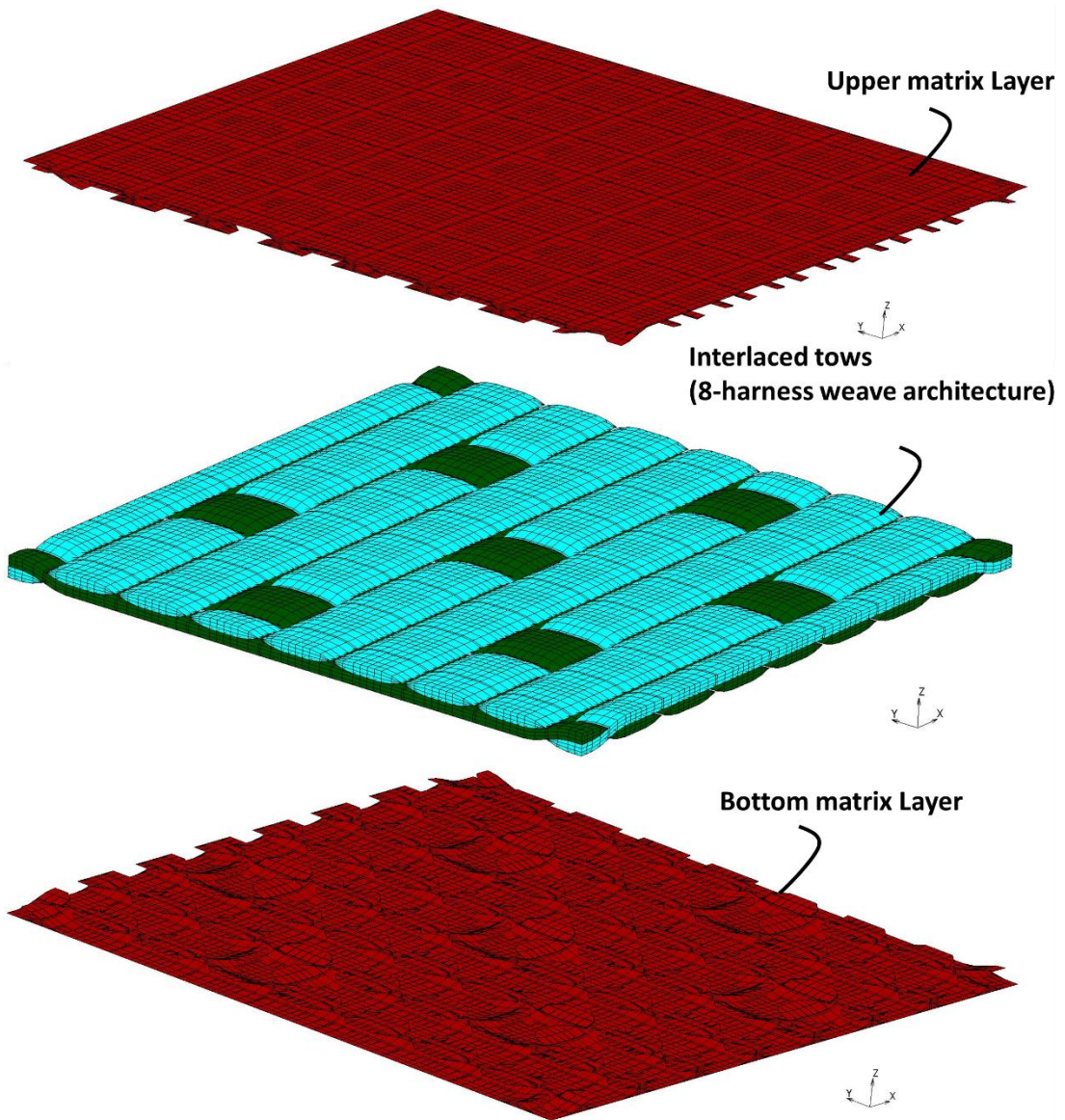


Figure 41. Generated mesh of Interlaced tows and neat resin

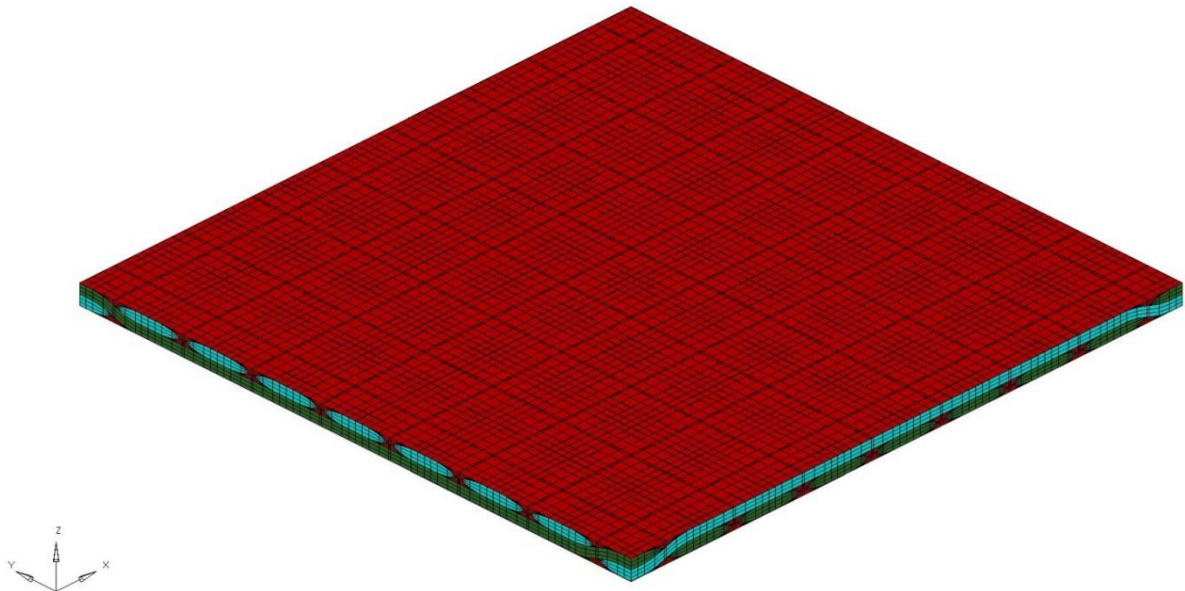


Figure 42. Fully assembled discretized unit cell model of 8-harness woven composite

CHAPTER 5

FINITE ELEMENT BASED MICROMECHANICS APPROACH

Finite element based computational micromechanics is a numerical approach of investigating the influence of complex microstructure on the macro-mechanical response of woven composite. This chapter describes the finite element approach of predicting the stress relaxation behavior of 5320-8HS woven composite. Also, it outlines the systematic procedure followed to validate the model predictions with experimental results.

5.1 Finite Element Approach

Usually, woven composites are modelled with cross-ply laminates of unidirectional layers [6]. The influence of detailed fiber weave architecture has not been widely investigated due to the complex microstructure. In this study, full unit cell enveloping weave architecture along with matrix pockets of 5320-8HS was investigated. The objective of this study is not only to predict the macro-mechanical response of woven composite, but also to understand the localized mechanisms that govern these macro-responses.

Computational micromechanics model developed from chapter 4 was imported to the commercial MSC MARC FEA software [13] and stress relaxation analysis was performed utilizing the mechanics of discretized microstructure of 5320-8HS [54]. Figure 43 illustrates the computational micromechanics methodology to predict viscoelastic behavior of 8-HS woven fabric composite.

Woven fabric model is an assemblage of neat matrix and tows/fiber bundles. The tows are assumed to be a hexagonally packed unidirectional composite with straight and wavy regions [54]. The first step in the micromechanics approach is the determination of the yarn/tows/fiber bundles properties.

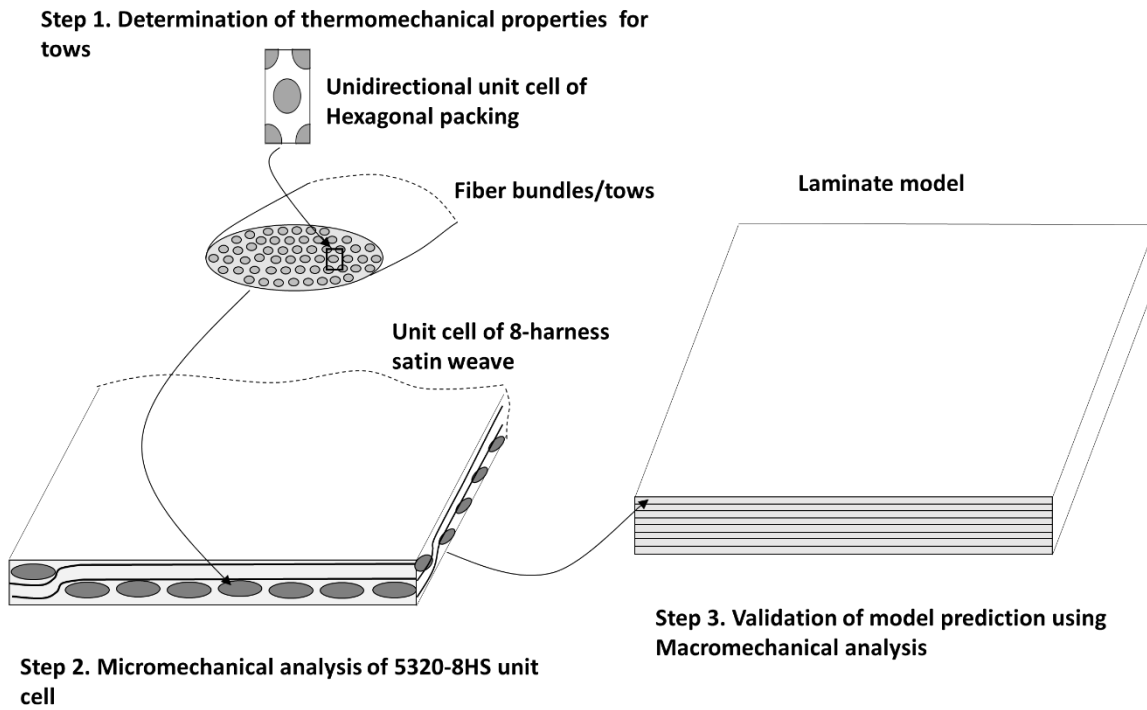


Figure 43. Micromechanics Approach for stress relaxation analysis of 5320-8HS woven composite

5.2 Thermomechanical properties of fiber bundles/tows

5.2.1 Unit Cell Model of Unidirectional Composite

A dimensionless unit cell model of unidirectional composite with hexagonal array packing was modelled to predict the thermomechanical properties of viscoelastic tows as shown in Figure 44. A cross section of the fibers was assumed to be circular in shape. The fiber radius r was decided based upon the fiber volume fraction V_f using the following relation [55]

$$V_f = \frac{v_f}{v_o} = \frac{2(\pi r^2 h)}{a \times b \times c} \quad (5.1)$$

Where c, a, b are the length, width and thickness of the unit cell. Also, v_f is the volume of fiber and v_o is the total volume of the unit cell.

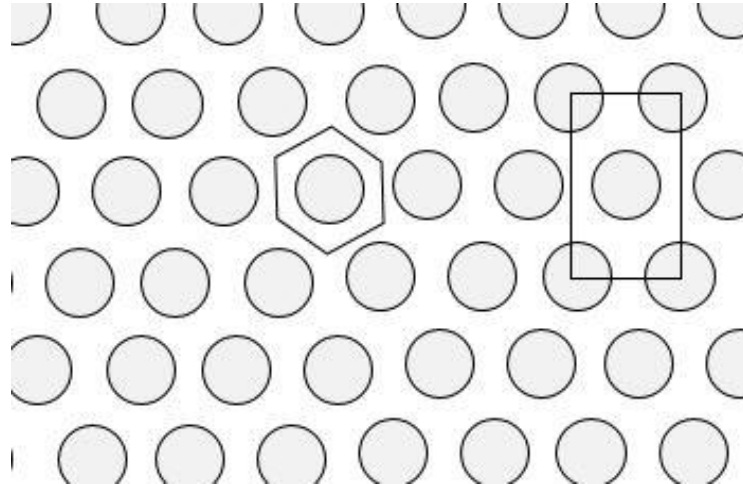


Figure 44. Unit cells of Unidirectional Composite

Dimensions of the unit cell are portrayed in the Figure 45. Carbon fiber and epoxy resin were represented by two material sections, where resin is defined as an isotropic solid and fiber is defined as a transversely isotropic solid. A local rectangular coordinate system (x, y, z) was created to associate the carbon fiber orthotropic properties. The mesh of hexagonal array consists of 1800 hexahedral elements in fiber and 700 hexahedral elements in resin and their type is Element 7. Element 7 is an 8-noded, isoparametric, arbitrary hexahedral element used for stress/displacements problems. It has 3 global degrees of freedom u, v and w per node [56].

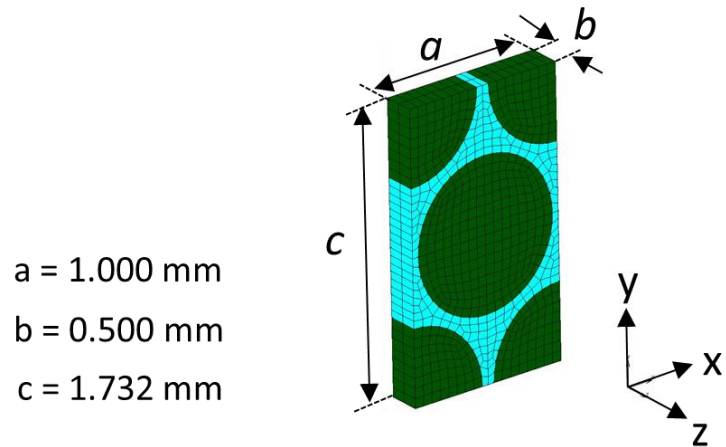


Figure 45. Hexagonal array Of unidirectional composite

The thermomechanical properties of the yarn were evaluated from the constituent properties of the T650/35-3K carbon fiber and the cured CYCOM 5320-1 Epoxy resin [37,38] as listed in Table 4 and Table 5. Carbon fibers were modelled as an elastic material, where neat resin is assumed to be a viscoelastic material. Constitutive model of neat resin assumed to follow the Prony series [13]. Instantaneous modulus of viscoelastic material at each temperature increment was defined through WLF shift function [47].

Table 4. Elastic and thermal properties of the fiber and neat resin

Material (carbon/epoxy)	Young's Modulus		Shear Modulus		Poisson's Ratio	Coefficient of Thermal Expansion (CTE)	
	E_{1f} (GPa)	E_{2f}, E_{3f} (GPa)	G_{12f}, G_{13f} (GPa)	G_{23f} (GPa)	ν_{12f}	α_{1f} ($\mu\text{m}/\text{m }^\circ\text{C}$)	α_{2f} ($\mu\text{m}/\text{m }^\circ\text{C}$)
Carbon Fiber T650/35 3K	241	40	25	14	0.26	-0.5	15
Epoxy Resin 5320-1 EO	3.809		1.4107		0.35	45.45	

Table 5. Relaxation times and coefficients of the Prony series for 5320-1 Epoxy Resin

i	E_i (MPa)	λ_i (s)
1	2.56×10^2	2.75×10^2
2	2.33×10^2	5.41×10^3
3	2.35×10^2	9.41×10^4
4	2.59×10^2	1.47×10^6
5	3.73×10^2	1.38×10^7
6	5.86×10^2	9.67×10^7
7	4.79×10^2	8.05×10^8
8	3.70×10^2	5.58×10^9
9	4.72×10^2	3.34×10^{10}

5.3 Thermomechanical Properties of 8-HS Unit cell

Experimentally and numerically determined thermomechanical properties of pure epoxy resin and hexagonal array were substituted as input variables for both neat matrix and fiber bundles of 8-harness unit cell. The tows are assumed to be an orthotropic solid material and its orientations were defined through ORIENT2 FORTRAN subroutine [57]. Neat matrix was modelled as an isotropic solid and viscoelastic material. Constitutive model of both neat resin and tows were assumed to follow the Prony series. For orthotropic material, constitutive model is defined through HOOKVI FORTRAN subroutines [57] for each element at every increment of analysis. Appendix E lists the user defined FORTRAN subroutines of MSC MARC FEA software. Also, relaxation times of both neat resin and tows were considered to be same

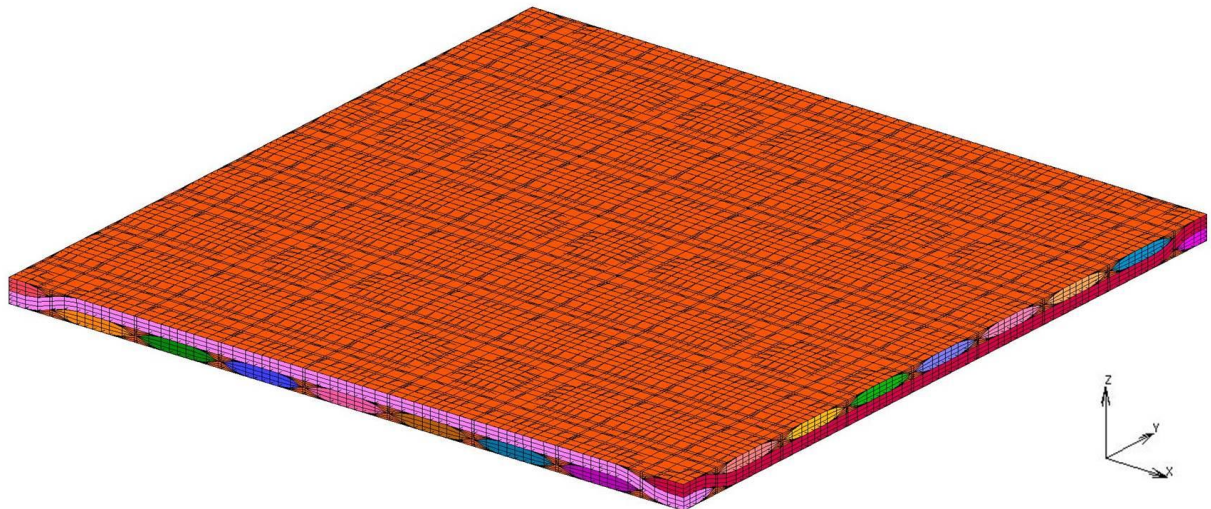
throughout the analysis. Instantaneous modulus of viscoelastic material for every temperature increment was defined through the table input, which collects the data of young's modulus as a function of temperature.

5.4 Geometry and contact body definition

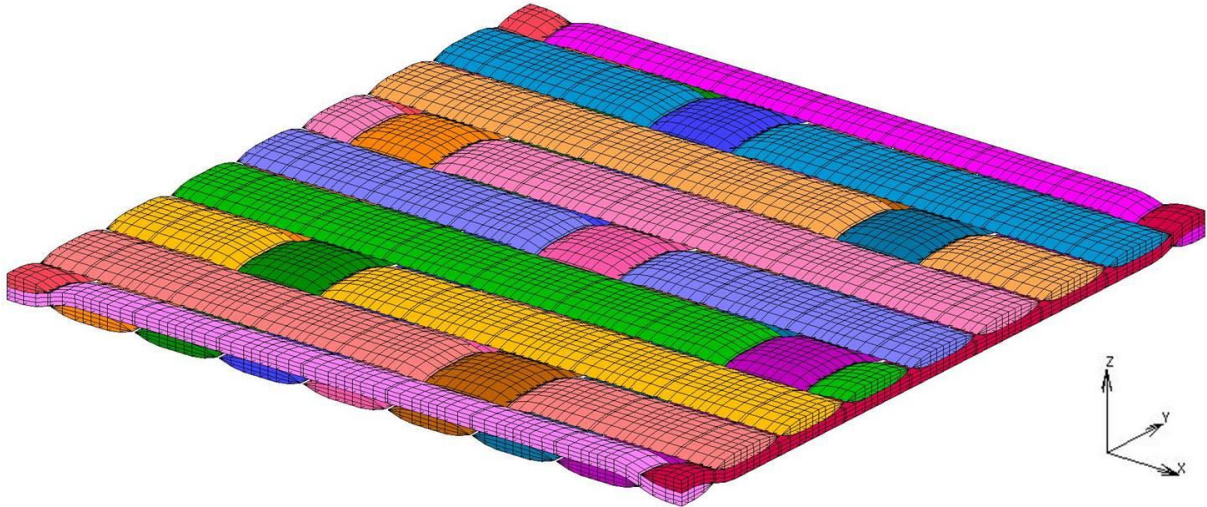
Micromechanical model was assumed to an assemblage of 19 contact bodies for 8HS unit cell and 6 contact bodies for hexagonal array. Fiber, neat resin and tows were defined as an individual deformable contact bodies. Here, contact between two different bodies was assumed to be glued, which mean a normal and tangential displacement of bodies were considered to be zero [13]. Contact table illustrating the contact between various deformable bodies was illustrated in the following Figure 46.

The screenshot shows the 'Contact Table Properties' dialog box. The 'Name' field is set to 'ctable1'. The 'View Mode' dropdown is set to 'Entry Matrix'. The matrix itself is a 15x15 grid of cells. The first row is labeled 'First' and the first column is labeled 'Second'. The second row is labeled '1-15' and the third row is labeled '16-30'. The columns are numbered 1 through 15. Most cells in the matrix contain the letter 'G', indicating a glued contact. The matrix is mostly symmetric, reflecting the physical symmetry of the unit cell. There are some empty cells, particularly in the top-left and bottom-right quadrants, which likely represent non-contacting pairs of bodies.

Figure 46. Contact table [13] for 5320-8HS Unit cell model



a)



b)

Figure 47. Contact Bodies of 5320-8HS Unit cell model a)With Resin b)Without Resin

Geometry of all contact bodies were defined as a solid element which includes hexahedral, pentahedral and tetrahedral elements. To overcome shear locking effect of higher order elements and to have better bending and shear behavior of solid elements, constant dilatation and constant strain were activated in the MSC MARC FEA software for the geometric property of the model [13] as shown in Figure 48.

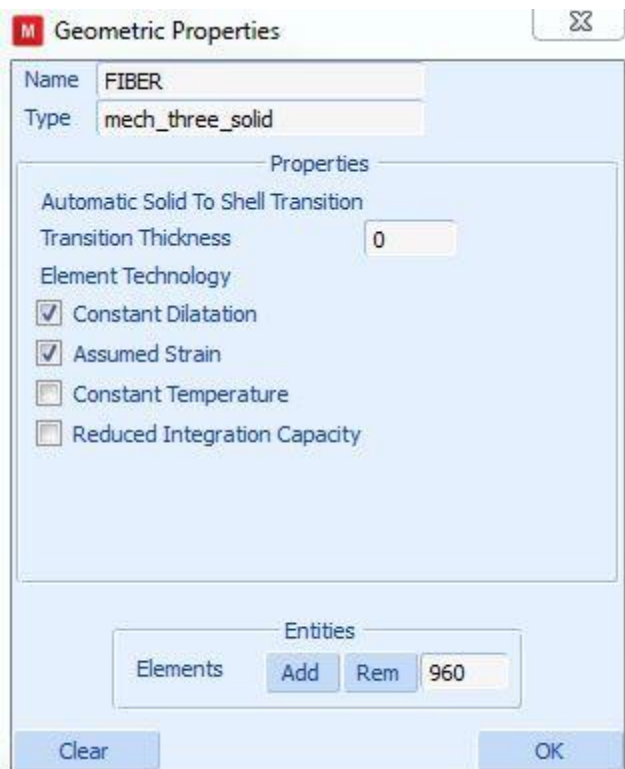


Figure 48. Defining constant dilatation and assumed strain in the MSC MARC FEA software [12]

5.5 Load cases and Boundary Conditions

5.5.1 Periodic Constraints and Boundary Conditions

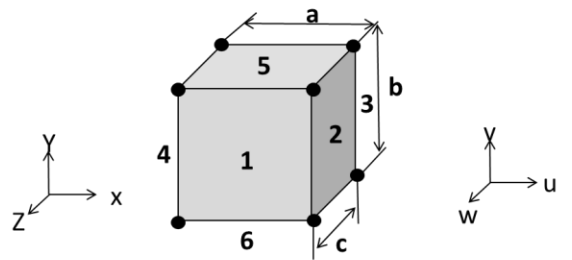
Unit cell model is a periodic representation of entire fiber reinforcement structure which represents the macro mechanical response of overall composite. Therefore, opposite faces of a unit cell model should deform identically and parallel to one another for any loading conditions. This in turn, creates kinematic conditions of periodic motion throughout an analysis. In order to maintain periodicity, nodes on the opposite faces were tied to a common node to create identical deformation.

For normal load cases, periodic boundary conditions (PBC) were applied on the free surfaces of the unit cell to reconstruct the kinematic behavior of the unidirectional composite as

illustrated in Figure 49. In addition to PBC, symmetric boundary conditions (SBCs) were applied in the 8-harness unit cell on one of the traction free surfaces along thickness to prevent the out of plane warpage due to weave architecture. For shear load cases, loading and boundary conditions are followed as shown in Figure 50. Moreover, a master node was tied to the nodes on the loading face to ensure uniform displacement and capture effective response of complete unit cell. Here, an effective stress relaxation behavior of 8-HS is captured by using the force component of the master node and area of the loading face.

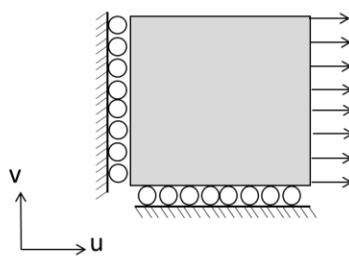
5.5.2 Load cases

Unit cell models of both unidirectional and 8-HS woven composite were subjected to a constant deformation for a limited duration followed by a free thermal expansion. In order to overcome the problems due to large deformation gradients between the contact bodies, stress relaxation in the unit cell model was achieved by coupling thermal load and thermomechanical load in 2 steps. In step 1, model is thermally loaded for specific temperature (i.e., 80 °C, 100 °C, 120 °C and 160 °C) to capture the stress and strain due to thermal soaking. Then, in the step 2, with final results of step 1 as an initial condition, 0.1% strain was applied in the unit cell model under isothermal condition for 60 seconds and then the strain was kept constant for 2000 seconds. Similarly, the unit cell model is examined under four different load cases (i.e. two normal and shear loads). Appendix D illustrates the test procedure of stress relaxation analysis.

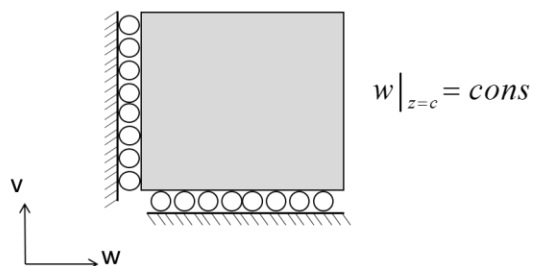


a)

$$v|_{y=b} = \text{cons}$$

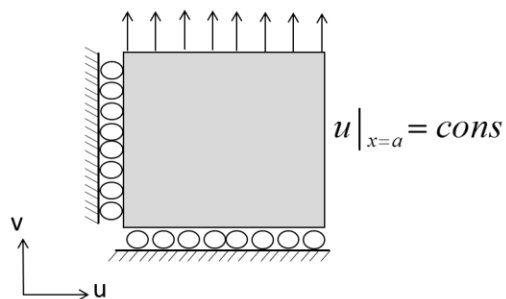


$$v|_{y=b} = \text{cons}$$



b)

$$v|_{y=b} = v_o$$

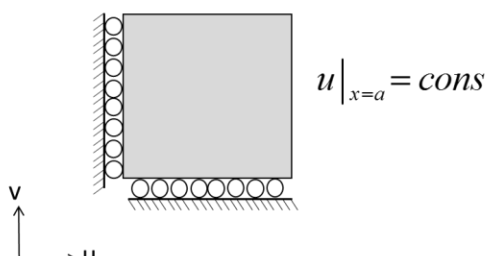


$$v|_{y=b} = \text{cons}$$

$$w|_{z=c} = \text{cons}$$

c)

$$v|_{y=b} = \text{cons}$$



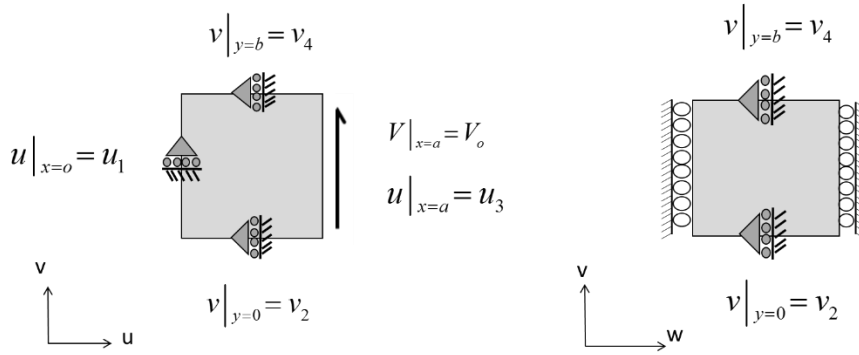
$$v|_{y=b} = \text{cons}$$

$$w|_{z=c} = w_o$$

d)

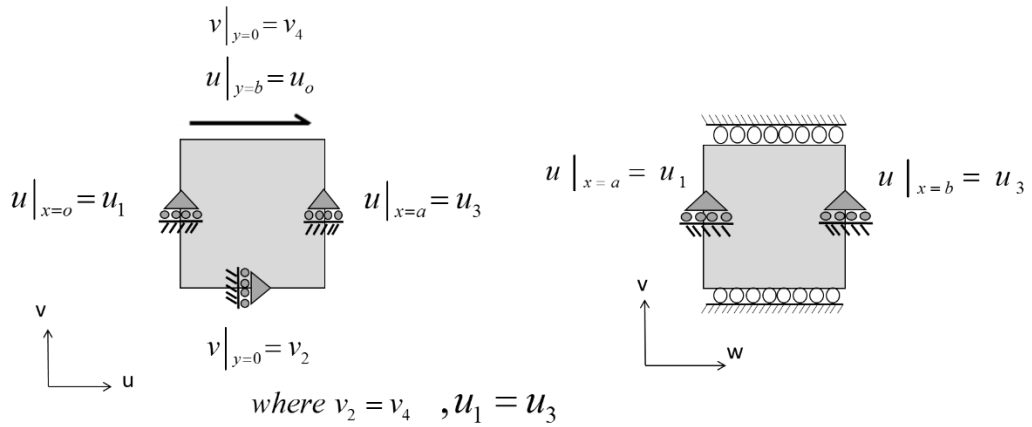
Figure 49. Schematics of a) unit cell, and their periodic boundary conditions for axial load cases along b) x-axis c) y-axis d) z-axis [58]

Note: 1,2,3,4,5 and 6 denote faces of the unit cell



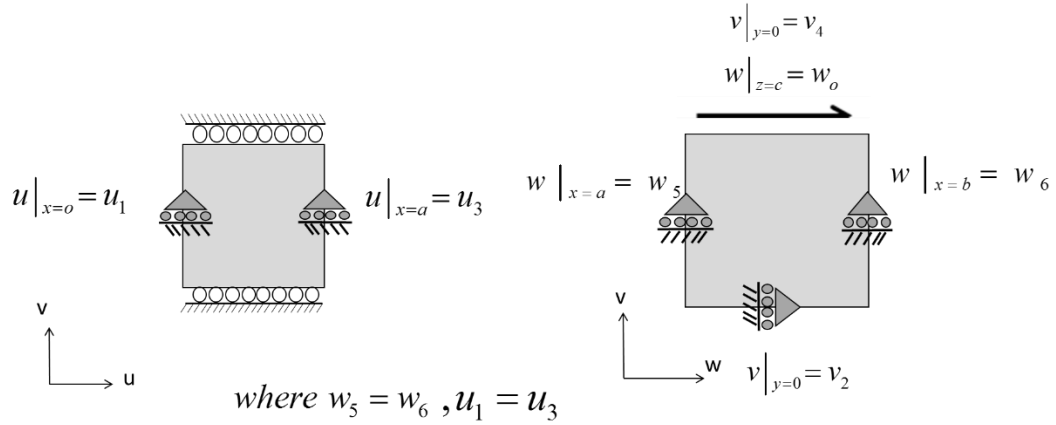
where $V_2 = V_4$, $u_1 = u_3$

a)



where $v_2 = v_4$, $u_1 = u_3$

b)



where $w_5 = w_6$, $u_1 = u_3$

c)

Figure 50. Schematics of periodic boundary conditions of unit cell for shear load cases along a) y-axis b) x-axis c) z-axis [58]

Note: subscripts 1,2,3,4,5,6 denote faces

5.6 Determination of Thermomechanical properties

5.6.1 Elastic Properties

For each loading cases, with known axial or tangential displacements and dimensions of unit cell, applied strains were calculated as follows [59]

$$\varepsilon_{ij} = \frac{u_{i,j}}{l_i} \quad i, j = 1, 2, 3 \quad (5.2)$$

Stresses were then calculated by dividing the reactional forces obtained from the master node and area of the loading face [59].

$$\sigma_{ij} = \frac{F_{Rj}}{A_{f,i}} \quad i, j = 1, 2, 3 \quad (5.3)$$

Using the Hooke's law, independent constants C_{ij} of stiffness matrix were calculated from above stress and strain variables [59]

$$\{\sigma_{ij}\} = [C_{ij}] \{\varepsilon_{ij}\} \quad i, j = 1, 2, 3 \quad (5.4)$$

With calculated independent constants, stiffness matrix $[C_{ij}]$ was inverted to compliance matrix $[S_{ij}]$. From the compliance matrix, elastic moduli, shear moduli and Poisson's ratio of the viscoelastic tows and 8HS model were extracted [59].

$$[S_{ij}] = [C_{ij}]^{-1} = \begin{pmatrix} \frac{1}{E_1} & -\frac{\nu_{12}}{E_1} & -\frac{\nu_{13}}{E_1} & 0 & 0 & 0 \\ -\frac{\nu_{21}}{E_2} & \frac{1}{E_2} & -\frac{\nu_{23}}{E_2} & 0 & 0 & 0 \\ -\frac{\nu_{31}}{E_3} & -\frac{\nu_{32}}{E_3} & \frac{1}{E_3} & 0 & 0 & 0 \\ 0 & 0 & 0 & \frac{1}{E_3} & 0 & 0 \\ 0 & 0 & 0 & 0 & \frac{1}{E_3} & 0 \\ 0 & 0 & 0 & 0 & 0 & \frac{1}{E_3} \end{pmatrix} \quad (5.5)$$

5.6.2 Coefficient of Thermal Expansion (CTE) and Viscoelastic Properties

Coefficient of thermal expansion (CTE) is defined as a ratio between the change in temperature and strain in the i^{th} direction, as written below [59]

$$CTE(\alpha_i) = \frac{\varepsilon_i}{\Delta T} \quad (5.6)$$

where strain ε_i was calculated using equation (5.2), ΔT is a change in temperature.

Viscoelastic properties were calculated using the hereditary integral approach where constitutive model follows the Prony series to capture the fading memory of the viscoelastic materials. The components of long term stiffness matrix were defined using HOOKVI subroutines in the MSC MARC FEA codes [57]. Similar to elastic properties, effective viscoelastic response of hexagonal array and 8HS unit cell were captured using equation (5.2) – equation (5.5) with the aid of master node and loading face.

5.7 Macro mechanical Model of 5320-8HS woven composite

Numerical results predicted under axial and tangential loading of 8HS unit cell were validated using homogenized solid model loaded under 3-point bending. This is because; experimental results of uniaxial loading were not reliable to compare with numerical prediction due to micro-level slippage and localized relaxation in the clamping region. In simply supported analysis, those effects were avoided. Half-symmetric homogenized solid model of 3 point bending was developed and analyzed for two different stacking sequence (i.e., $[\pm 45]_s$ and $[0/90]_s$) with similar load cases of unit cell model. Figure 51 shows the homogenized solid model supported by steel rollers along with its boundary conditions.

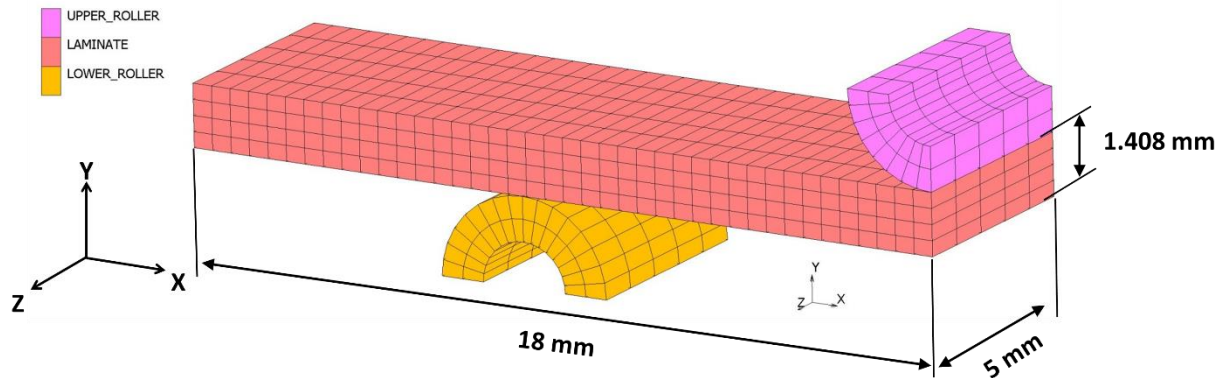


Figure 51. Homogenized solid model of 5320-8HS laminate

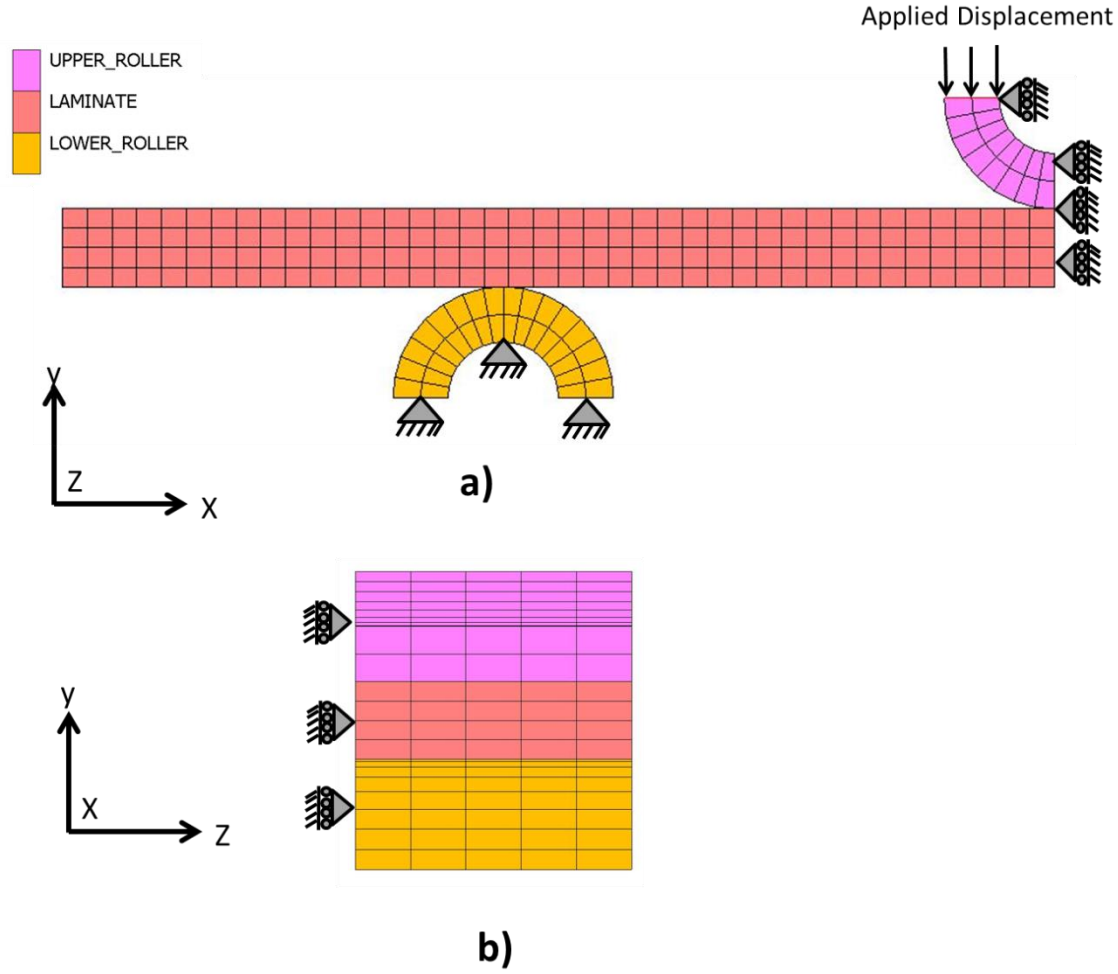


Figure 52. Boundary conditions of 3-Point Bending Model a) Front View b) Side view

CHAPTER 6

VALIDATION OF MICROMECHANICS MODEL

Before characterizing the stress relaxation behavior of woven fabric, elastic behavior of developed model was verified. Due to the complexities in the stress relaxation experiments, micromechanics model was validated using two test methods (i.e., Tension and 3-point bending). The results of axial loading were directly compared with model predictions under different load cases. Due to the computational cost, results of flexural loading were compared with macromechanics model (i.e., homogenized solid model) which utilizes the thermomechanical properties predicted from the micromechanics model. In this chapter, we will study the validation of both micromechanics and macromechanics model predictions with experimental results. In addition, comparative study was also performed between 5320-8HS and 5320-1 epoxy resin to characterize the influence of weave architecture on the relaxation behavior of polymers.

6.1 Validation of Elastic Properties

Developed micromechanics model of 5320-8HS was statically loaded to predict its elastic properties using MSC MARC FEA software. To compare, experimental data of 5320-8HS collected from the data sheet of Cytec [37] were used for this study. Elastic properties of 5320-8HS as listed in the Table 6 imply that the developed finite element based micromechanics model shows good agreement in elastic behavior when compare with experimental results.

Table 6. Elastic Properties of 5320-8HS woven composite

5320-8HS Carbon/Epoxy	Experiment [35]	FEA (Unit Cell Model)	% difference
E ₁₁ (GPa)	69.085	73.731	6.7
E ₂₂ (GPa)	68.258	73.784	8.1
E ₃₃ (GPa)	-	12.424	-
ν_{12}	0.048	0.045	6.7
ν_{23}	-	0.486	-
ν_{13}	-	0.485	-
G ₁₂ (GPa)	5.585	5.036	9.8
G ₂₃ (GPa)	-	3.946	-
G ₃₁ (GPa)	-	3.949	-

6.2 Uniaxial Tension

Due to the nature of higher stiffness and complexity of testing in DMA, 5320-8HS woven composites tested using 810 MTS machine were utilized to validate the stress relaxation behavior of micromechanics model under uniaxial tension. The 5320-8HS specimens tested under isothermal condition of four different temperatures (i.e., 80 °C, 100 °C, 120 °C and 160 °C) below T_g of the material were utilized for this study. Stress relaxation behavior of 5320-8HS was investigated under three cases (i.e., 0 degree, 90 degree and 45 degree orientations).

6.2.1 Case 1 and Case 2: 0 and 90 degree (Fill and Warp direction)

The effective stress relaxation response of micromechanics model loaded along fill and warp direction were compared with an experimental results of 5320-8HS and 5320-1 resin in the following figures (i.e., from Figure 54 to Figure 61). At elevated temperatures, micromechanics model under predicted the relaxation response of 5320-8HS as compare with test results. This may due to the assumption of constant fiber volume fraction and lack of investigation in the thermal behavior of fiber bundles. From the comparative study of both 5320-8HS and 5320-1 epoxy resin under uniaxial tension, it infers that the relaxation behavior of polymer was

influenced by an interlaced fiber bundles till 1000s and approaches closer to the neat resin at 1500 s as illustrated in Figure 53. With progress in time, 5320-8HS woven composite was found to be relaxing more than that of neat resin. This may attributed to the problems associated with uniaxial experiments as explained in chapter 3.

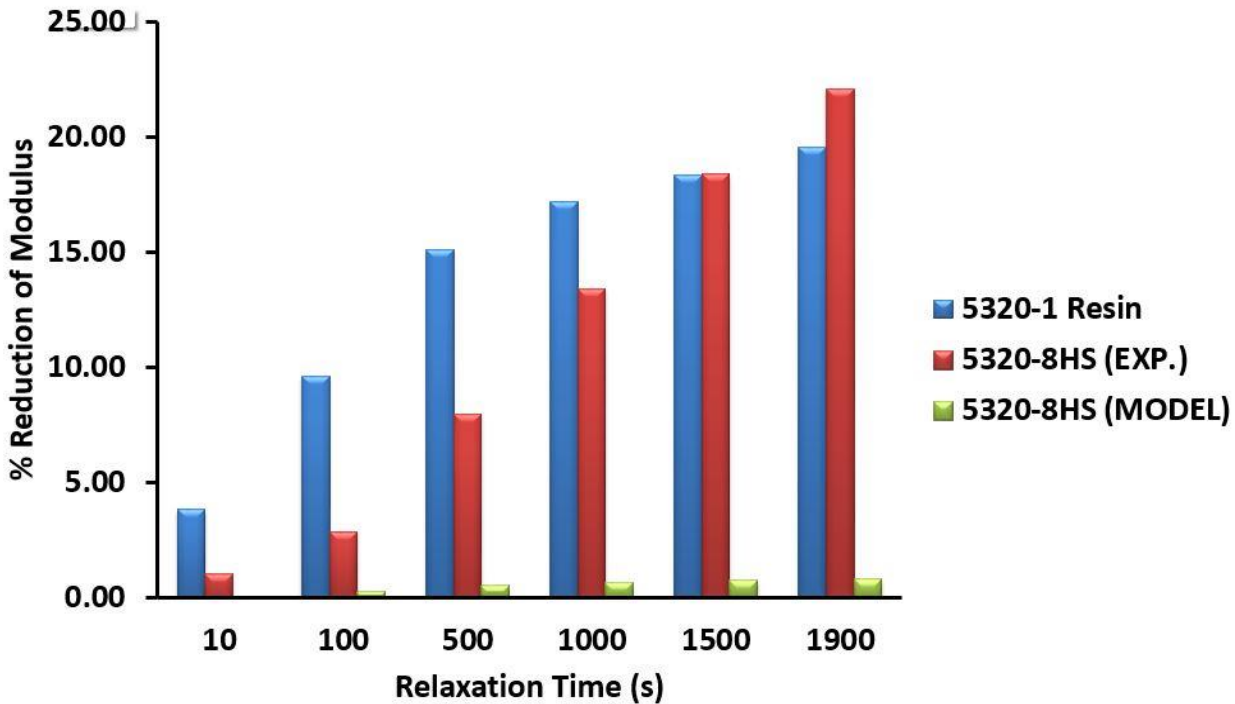


Figure 53. Comparison of reduction in modulus among numerical and experimental results of 5320-8HS [0/90]loaded along fill direction and 5320-1 Resin at 80 °C (Tension)

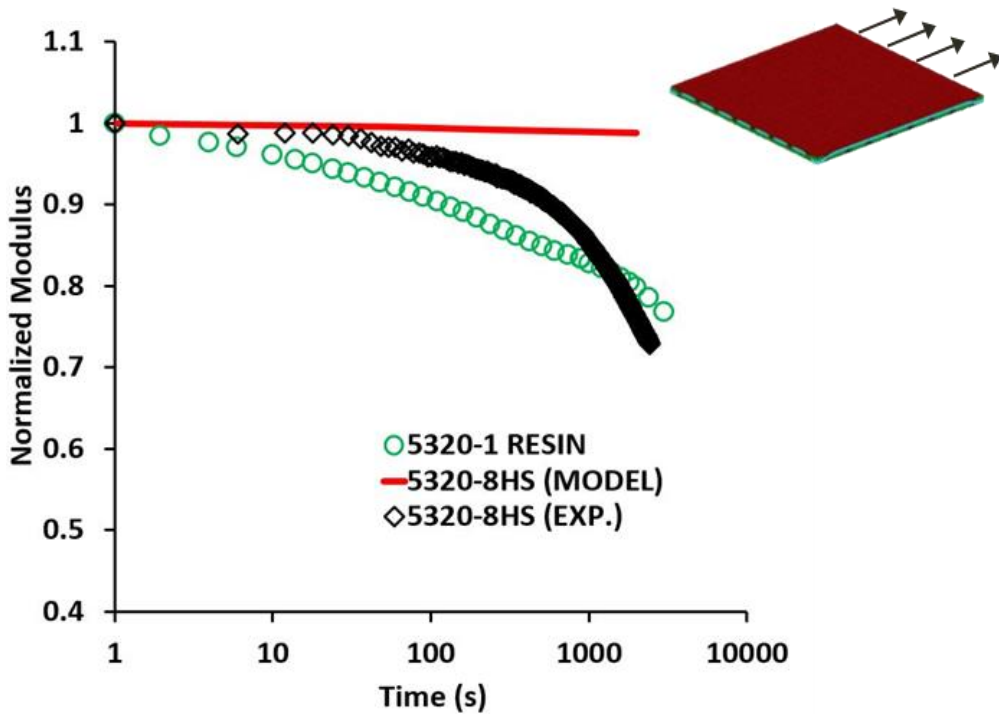


Figure 54. Normalized relaxation curves of 5320-8HS [0/90] loaded along fill direction and 5320-1 Epoxy resin under isothermal condition of 80 °C (Tension)

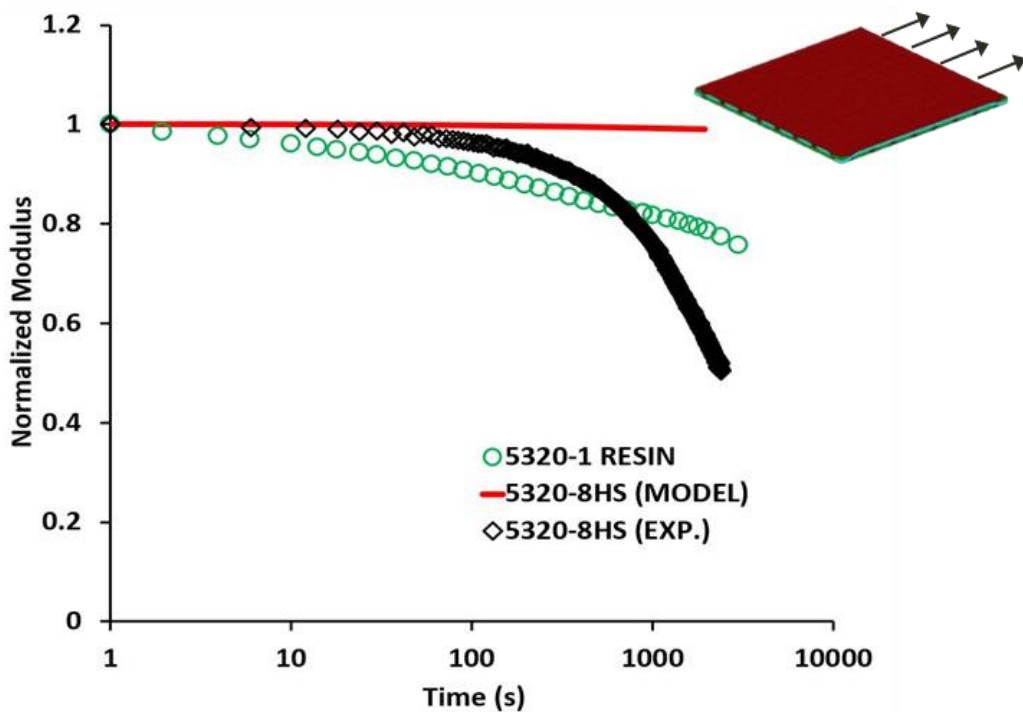


Figure 55. Normalized relaxation curves of 5320-8HS [0/90] loaded along fill direction and 5320-1 Epoxy resin under isothermal condition of 100 °C (Tension)

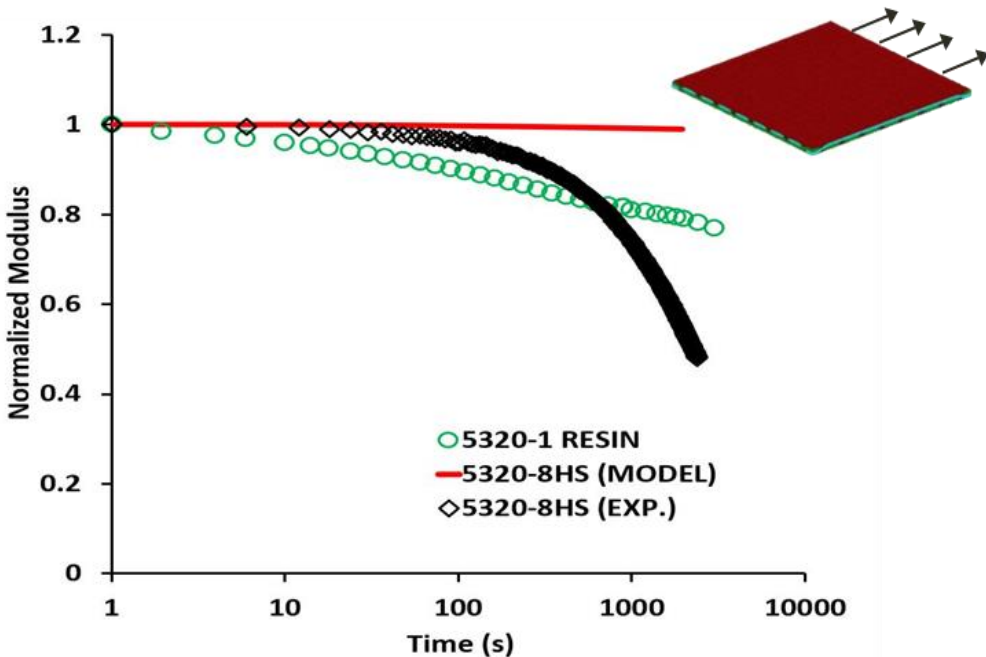


Figure 56. Normalized relaxation curves of 5320-8HS [0/90] loaded along fill direction and 5320-1 Epoxy resin under isothermal condition of 120 °C (Tension)

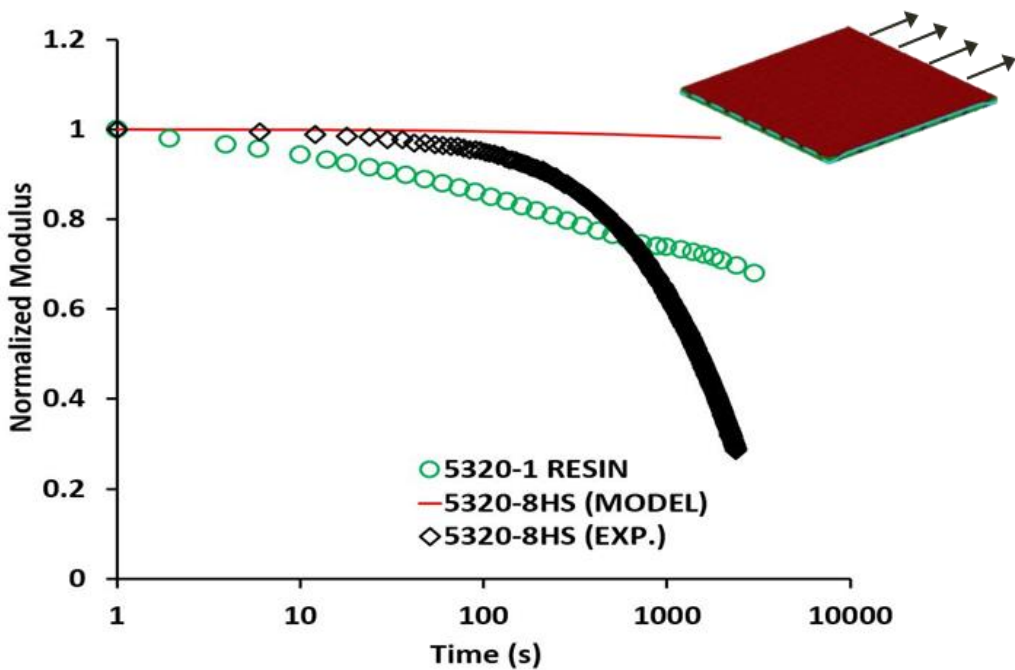


Figure 57. Normalized relaxation curves of 5320-8HS [0/90] loaded along fill direction and 5320-1 Epoxy resin under isothermal condition of 160 °C (Tension)

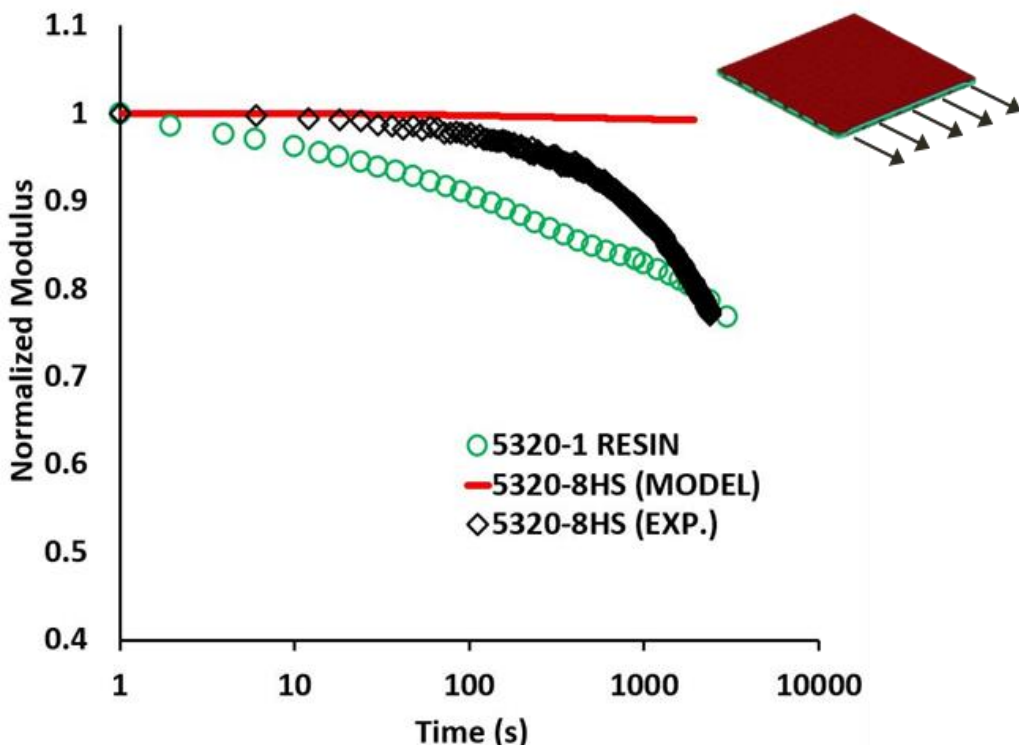


Figure 58. Normalized relaxation curves of 5320-8HS [0/90] loaded along warp direction and 5320-1 Epoxy resin under isothermal condition of 80 °C (Tension)

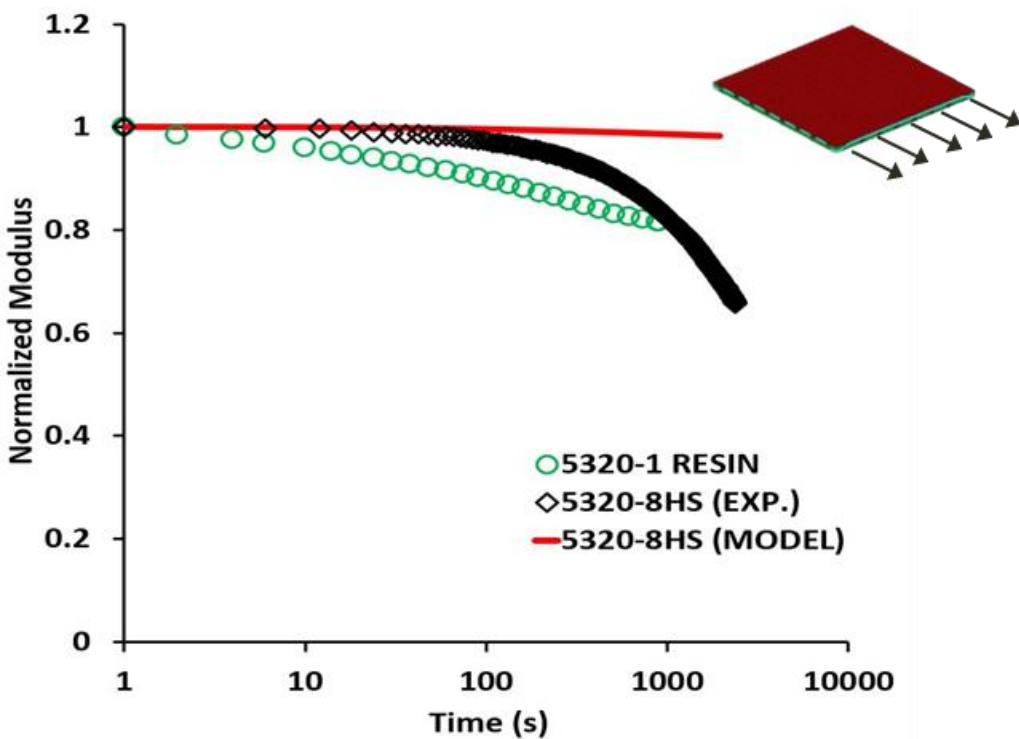


Figure 59. Normalized relaxation curves of 5320-8HS [0/90] loaded along warp direction and 5320-1 Epoxy resin under isothermal condition of 100 °C (Tension)

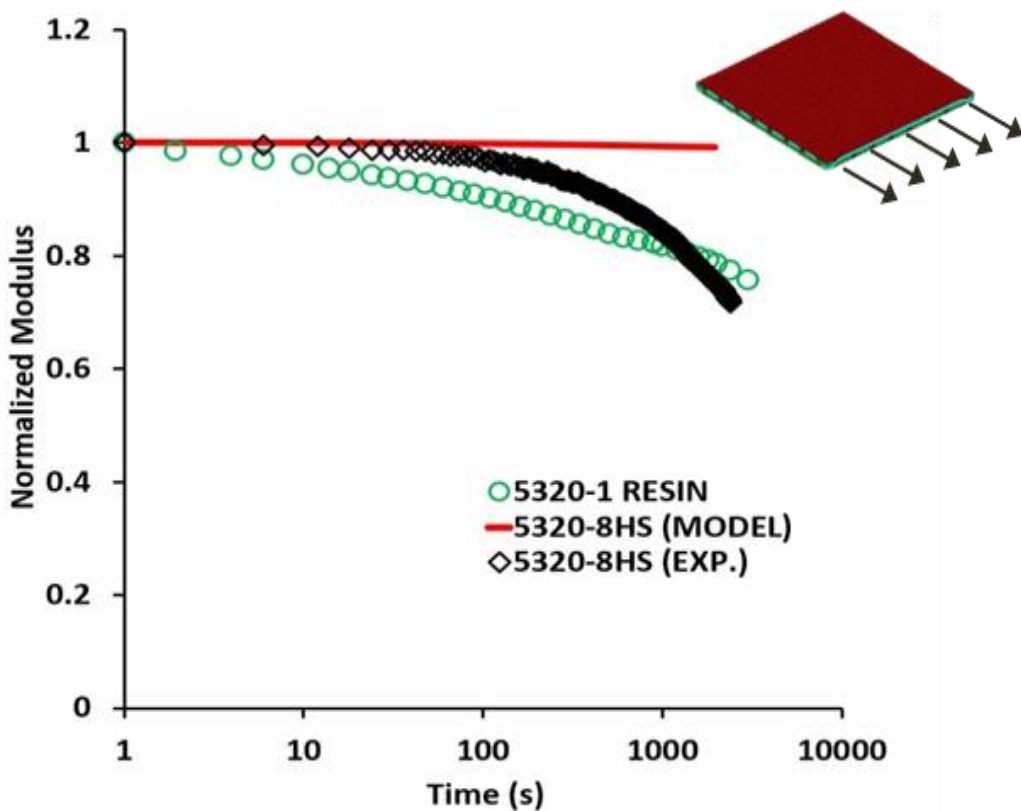


Figure 60. Normalized relaxation curves of 5320-8HS [0/90] loaded along warp direction and 5320-1 Epoxy resin under isothermal condition of 120°C (Tension)

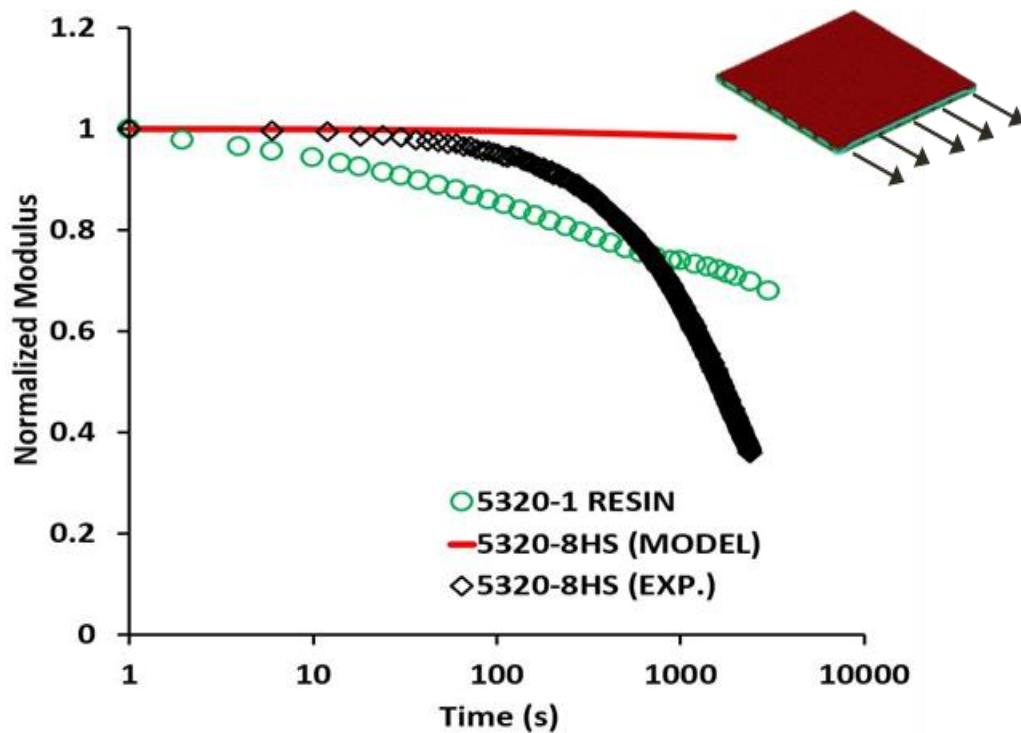


Figure 61. Normalized relaxation curves of 5320-8HS [0/90] loaded along warp direction and 5320-1 Epoxy resin under isothermal condition of 160 °C (Tension)

6.2.2 Case 3: 45 degree (In-Plane Shear)

The effective stress relaxation response of micromechanics model loaded under in-plane shear was compared with the test results of 5320-8HS stacked at $[\pm 45]$ and 5320-1 resin in the following figures (i.e., from Figure 63 to Figure 66). At elevated temperatures, predictions of micromechanics model were observed to be closer when compare with experimental results. This is because; under in-plane shear loading relaxation was dominated by the neat resin. From the comparative study of both 5320-8HS and 5320-1 epoxy resin, it implies that the relaxation behavior of polymer was strongly influenced by an interlaced fiber bundles till 500s. With progress in time, after 500s 5320-8HS woven composite relaxes more than that of neat resin as illustrated in Figure 63. Similar behavior was observed in the test results of 5320-8HS at elevated temperatures. Besides, experimental results of $[\pm 45]$ stacking sequence loaded under uniaxial tension did not capture the pure in-plane shear.

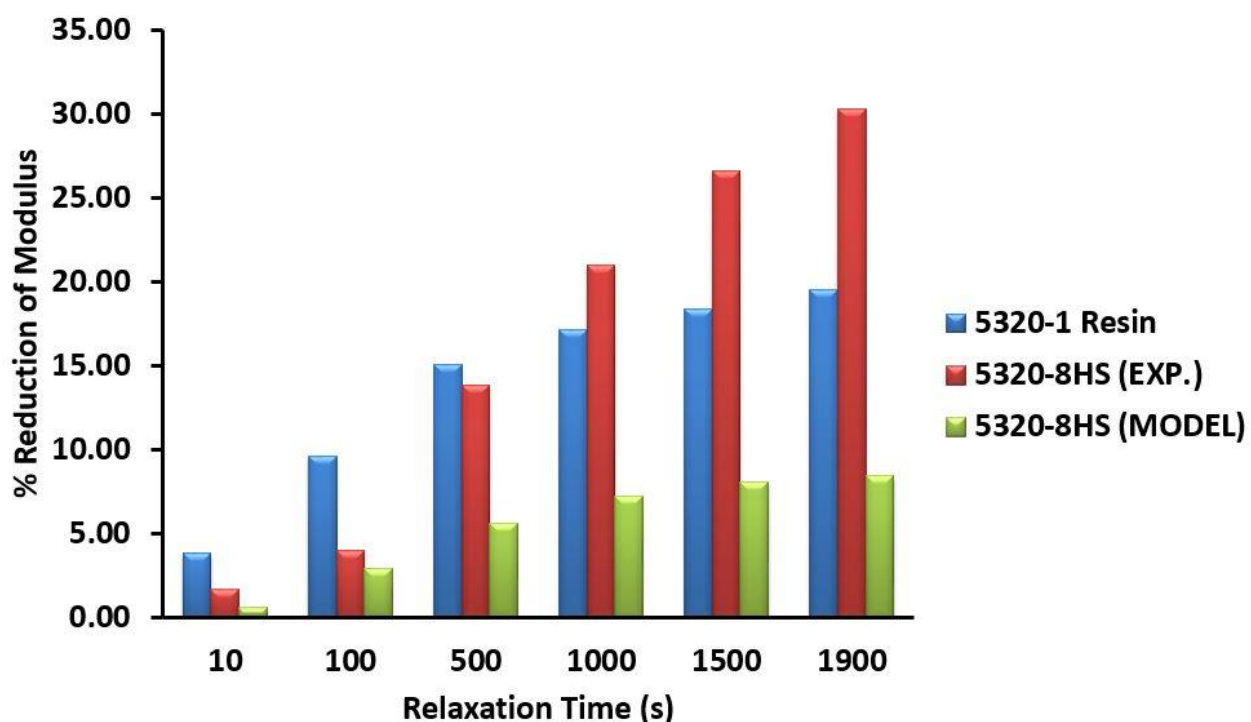


Figure 62. Comparison of reduction in modulus among 5320-8HS oriented at $[\pm 45]$ and 5320-1 Resin at 80 °C (Tension)

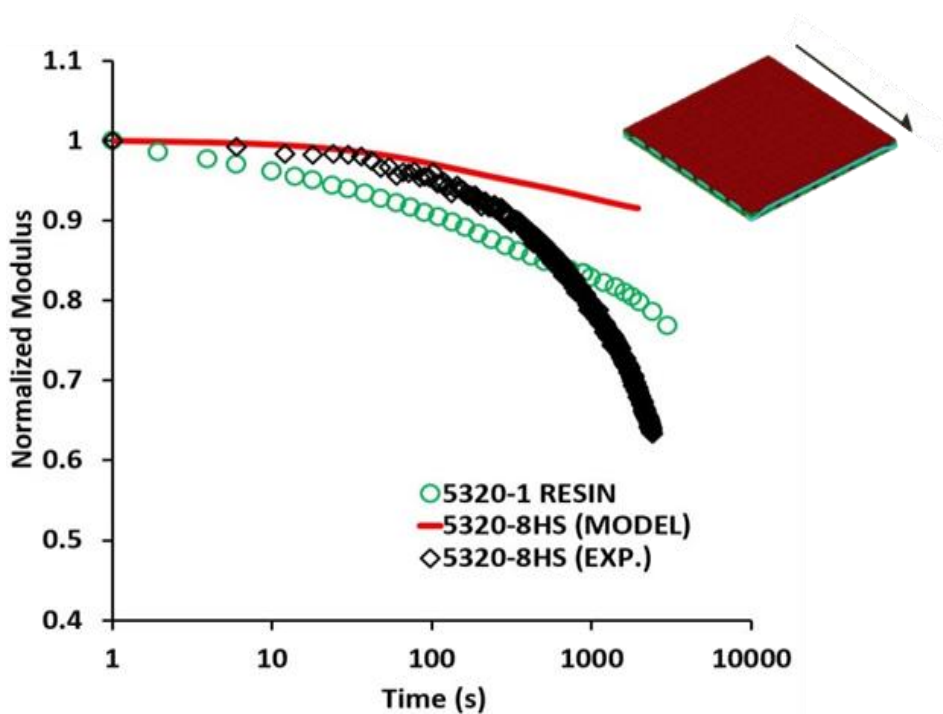


Figure 63. Normalized relaxation curves of 5320-8HS [± 45] and 5320-1 Epoxy resin under isothermal condition of 80 °C (Tension)

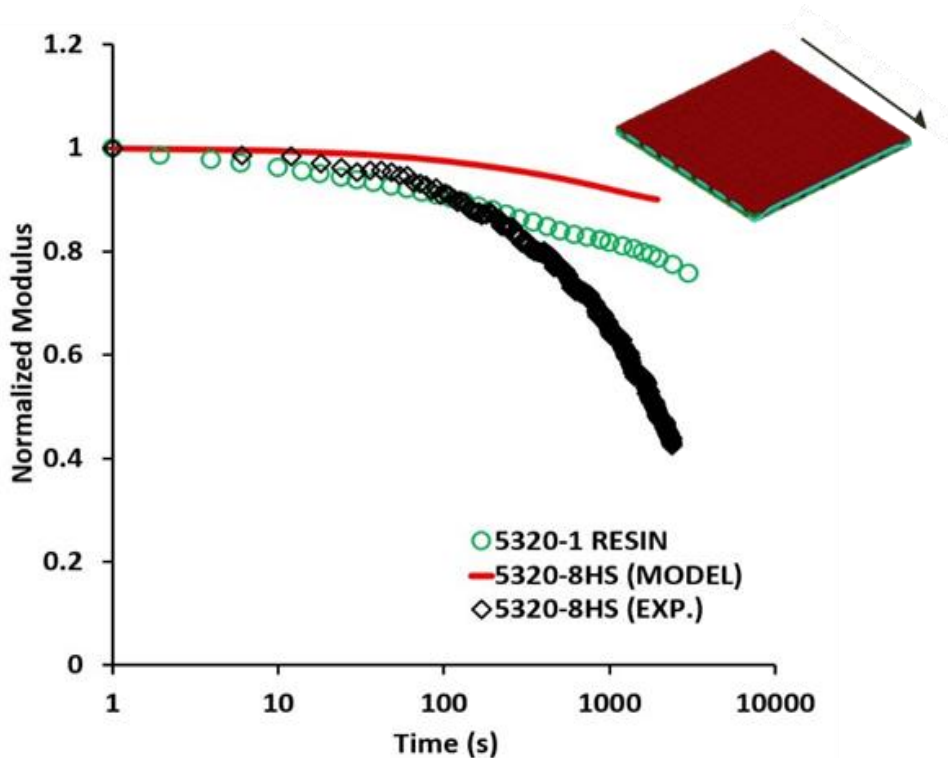


Figure 64. Normalized relaxation curves of 5320-8HS [± 45] and 5320-1 Epoxy resin under isothermal condition of 100 °C (Tension)

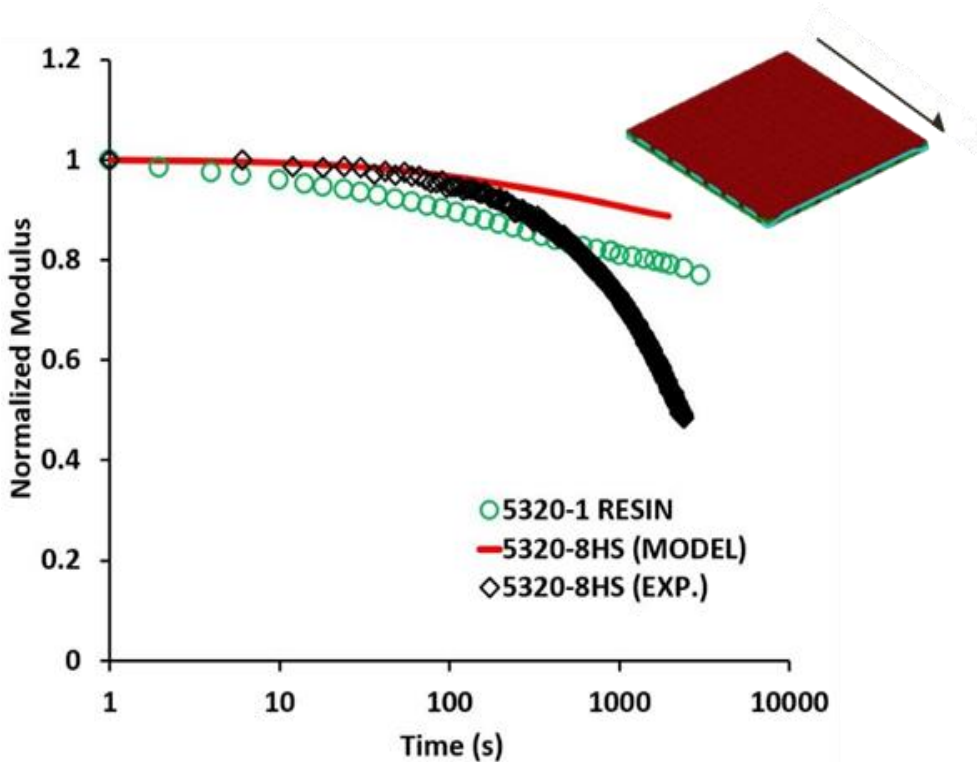


Figure 65. Normalized relaxation curves of 5320-8HS [± 45] and 5320-1 Epoxy resin under isothermal condition of 120 °C (Tension)

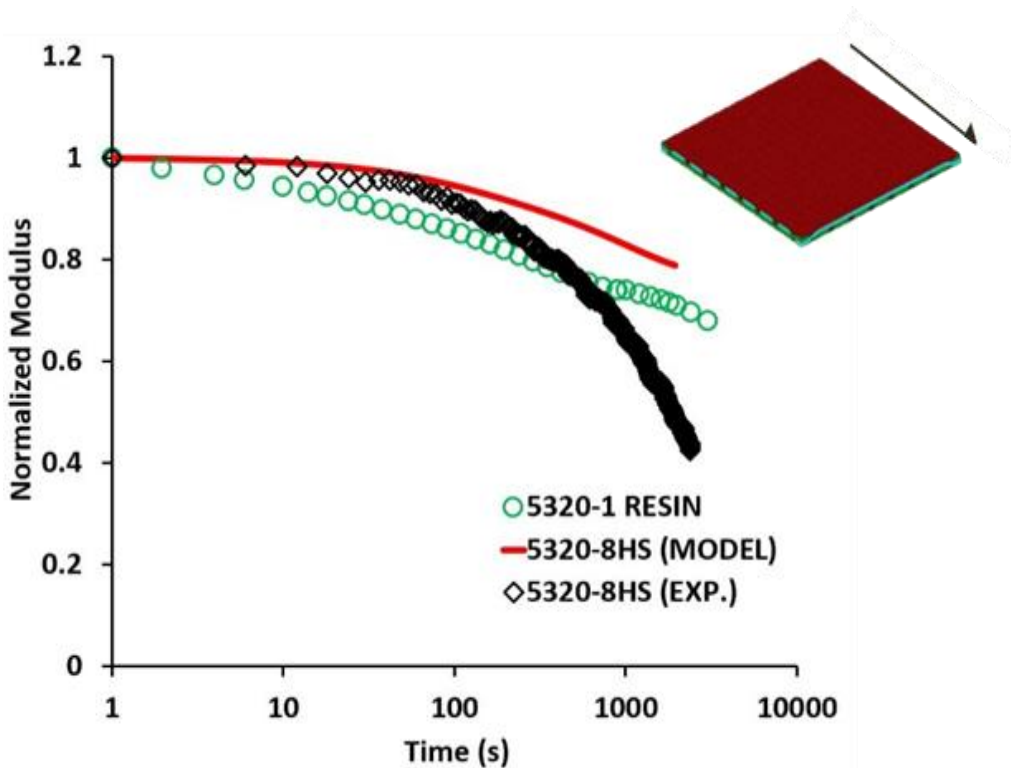


Figure 66. Normalized relaxation curves of 5320-8HS [± 45] and 5320-1 Epoxy resin under isothermal condition of 160 °C (Tension)

6.3 3-Point Bending

Due to the complexity and problems in the uniaxial tension test, experimental results of 5320-8HS obtained under axial loading was not considered as a reliable data to compare model predictions. Therefore, model predictions were validated with test results of 3-point bending at elevated temperatures. In order to overcome the computational time, viscoelastic properties predicted from the micromechanics model of 5320-8HS under stress relaxation were validated using the macromechanics model. The homogenized half symmetric model of 3-point bending was analyzed under two cases of stacking sequence reflecting real time experiments (i.e., $[0/90]_s$ and $[\pm 45]_s$).

6.3.1 Case 1: $[0/90]_s$

The effective stress relaxation behavior of homogenized solid model with a stacking sequence of $[0/90]_s$ was analyzed under flexural loading. Predictions of macromechanics model were then compared with the test results of 5320-8HS and 5320-1 resin loaded under 3-point bending in the following figures (i.e., from Figure 67 to Figure 70). With increase in temperature, accuracy of model predictions was also increases and captures the relaxation trend of woven composite at 160 °C. Even though model captures the experimental trend for first 100s at 80 °C and 100 °C, results were then under predicted with increase in time. This may attributed to the reflection of under predicted viscoelastic properties of 5320-8HS unit cell model along fill and warp direction. From the comparative study of both 5320-8HS and 5320-1 epoxy resin, relaxation behavior of neat resin was observed to be dominant at elevated temperatures. Until 120 °C, relaxation of 5320-8HS captures the general trend of 5320-1 resin. This may due to less influence of weave architecture on the polymeric resin. But at 160 °C, 5320-1 resin relaxes more than the woven composite. This is because; effect of fully stretched fiber bundles resists further

relaxation of composite. Since the model predictions along both fill and warp were stiffer, numerical predictions shows good correlation with the experimental results at 160 °C.

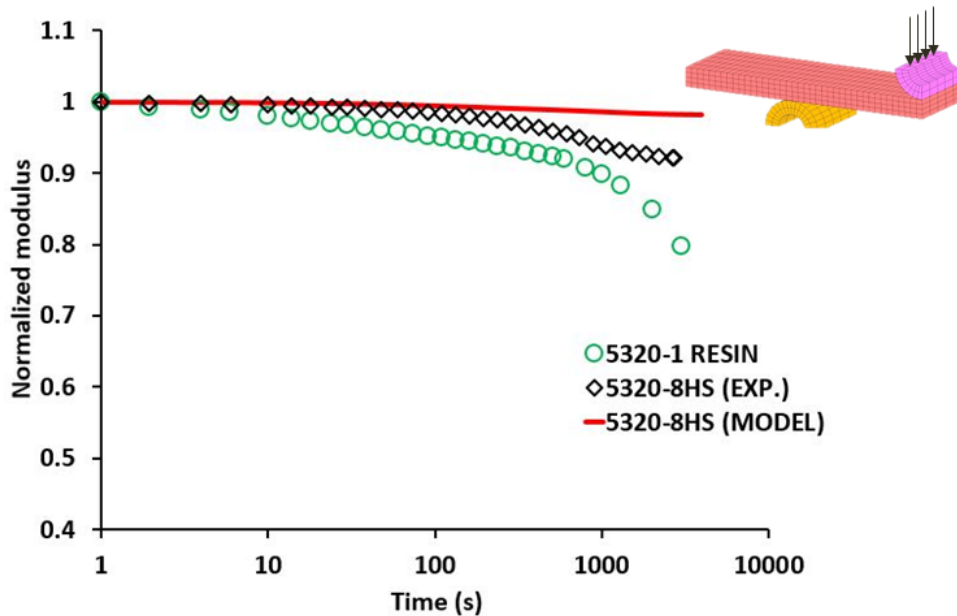


Figure 67. Normalized relaxation curves of 5320-8HS [0/90]s and 5320-1 Epoxy resin under isothermal condition of 80 °C (3-point bending)

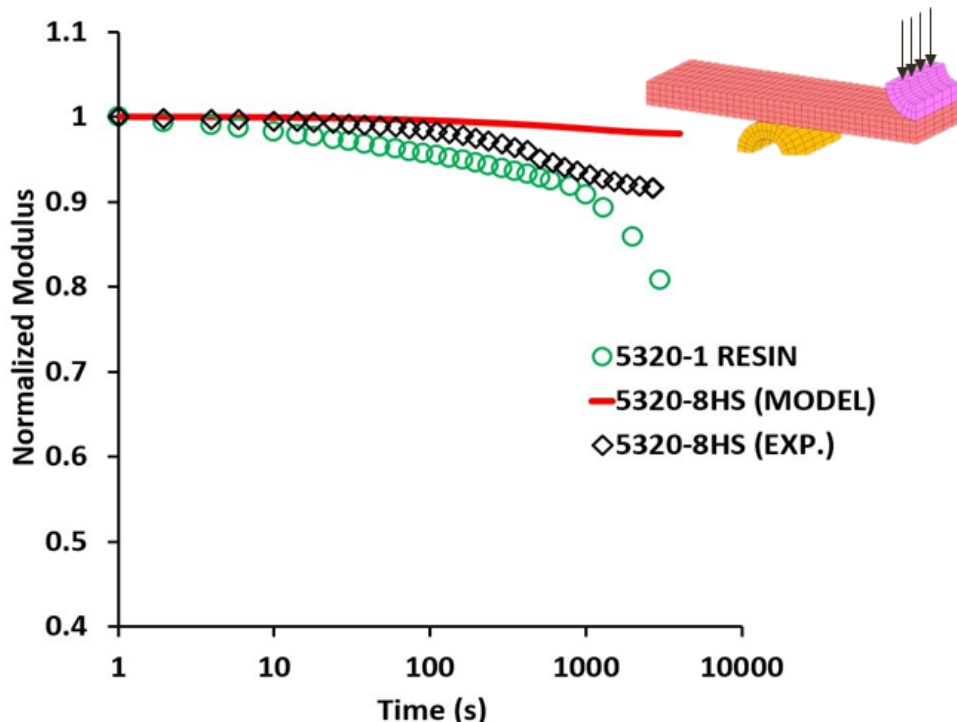


Figure 68. Normalized relaxation curves of 5320-8HS [0/90]s and 5320-1 Epoxy resin under isothermal condition of 100 °C (3-point bending)

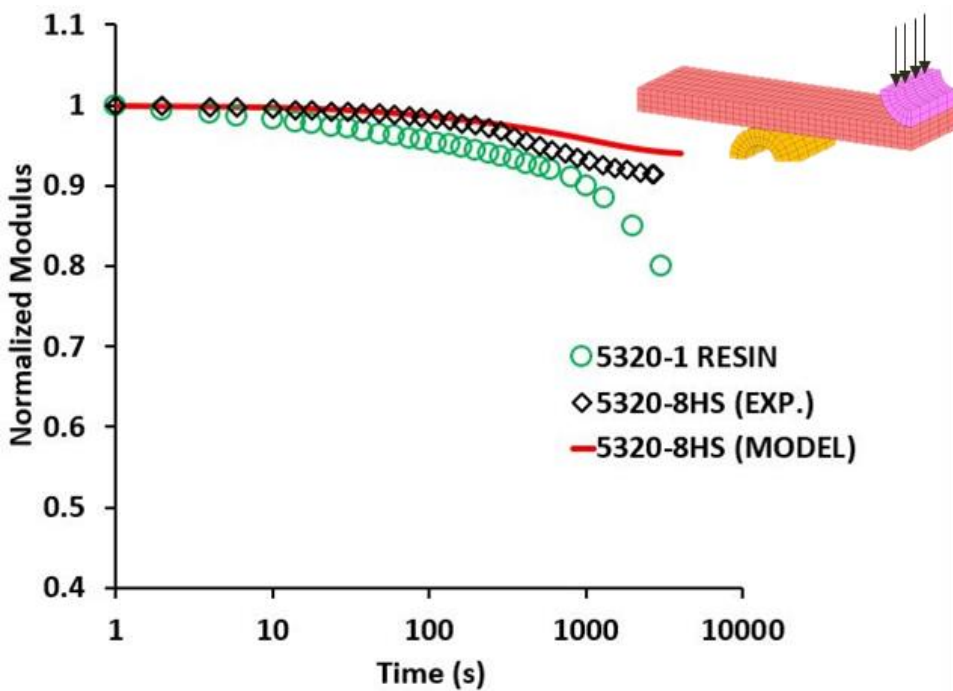


Figure 69. Normalized relaxation curves of 5320-8HS [0/90]s and 5320-1 Epoxy resin under isothermal condition of 120 °C (3-point bending)

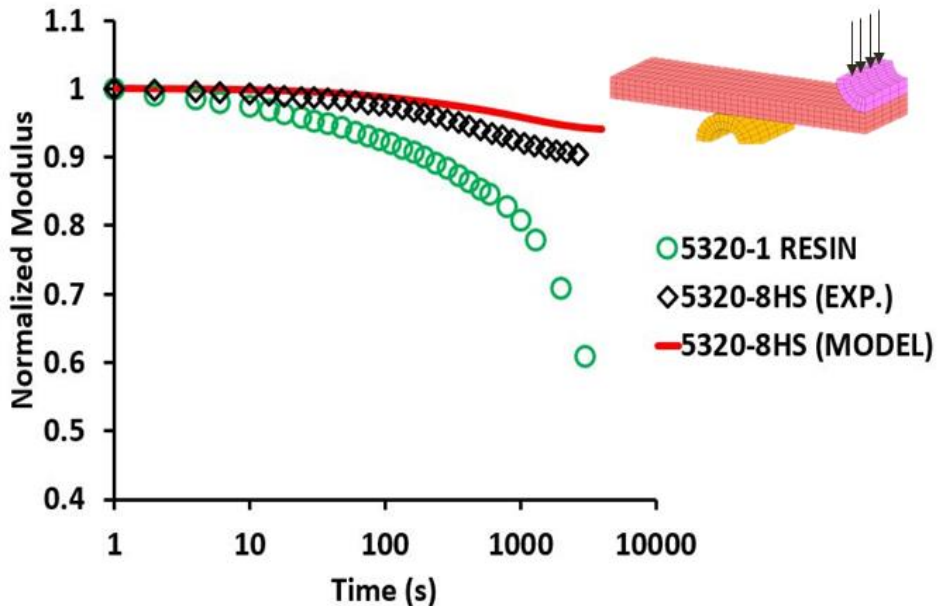


Figure 70. Normalized relaxation curves of 5320-8HS [0/90]s and 5320-1 Epoxy resin under isothermal condition of 160 °C (3-point bending)

6.3.2 Case 2: $[\pm 45]_s$

The effective stress relaxation behavior of homogenized solid model with a stacking sequence of $[\pm 45]_s$ was analyzed and compared with the experimental results of 5320-8HS and 5320-1 resin in the following figures (i.e., from Figure 73 to Figure 75). With increase in temperature, accuracy of model predictions increase and capture the general trend of experimental results. A very good correlation between test data and model prediction was also observed at 160 °C as shown in Figure 71. From the comparative of both 5320-8HS and 5320-1 epoxy resin, it implies that a woven composite relaxes more than that of the neat resin. This may attributed to the combined effect of fiber bundle and neat resin. At elevated temperatures, stretching of interlaced fiber bundle along with viscoelastic behavior of polymer increases the overall relaxation response of the woven composite. With increase in temperature, influence of weave architecture was found to be reducing and relaxation become identical to the neat resin.

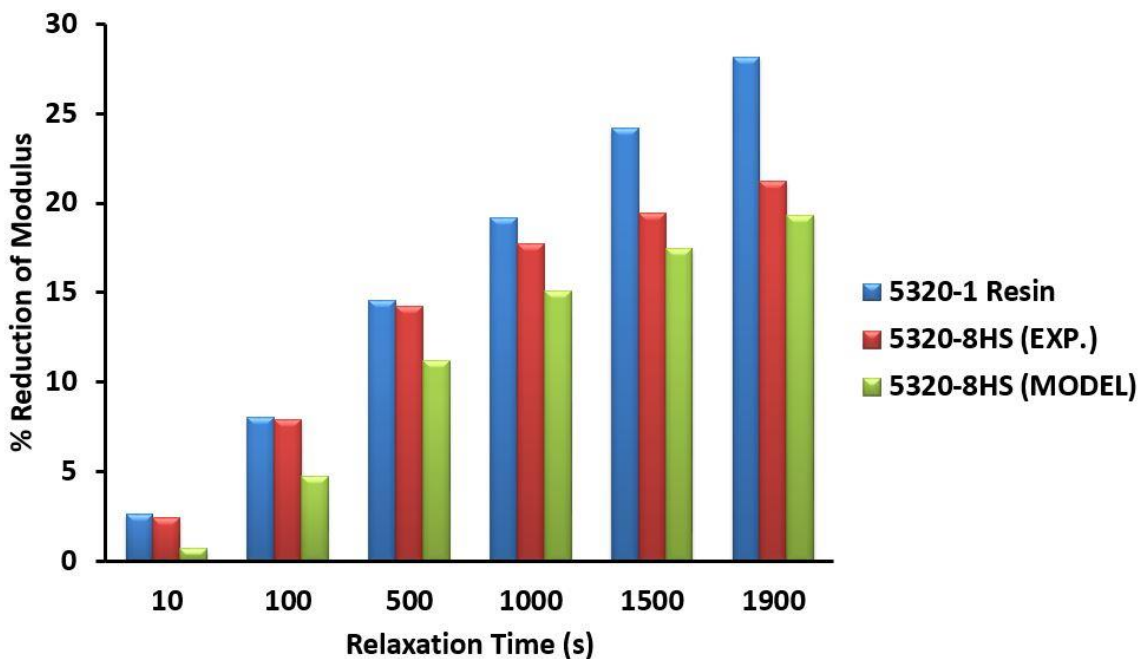


Figure 71. Comparison of reduction in modulus among 5320-8HS oriented at $[\pm 45]_s$ and 5320-1 Resin at 160 °C (3-point bending)

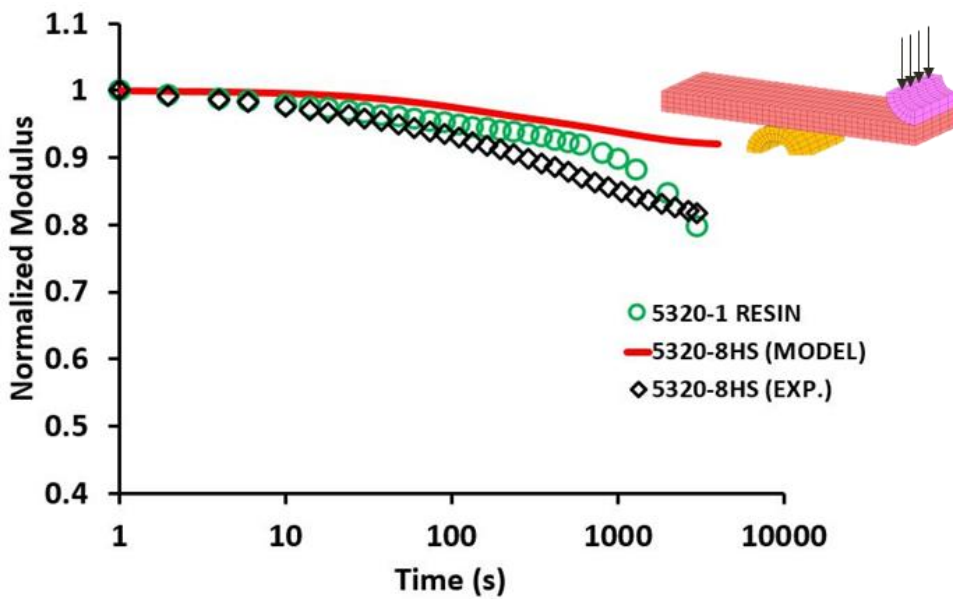


Figure 72. Normalized relaxation curves of 5320-8HS [± 45]s and 5320-1 Epoxy resin under isothermal condition of 80 °C (3-point bending)

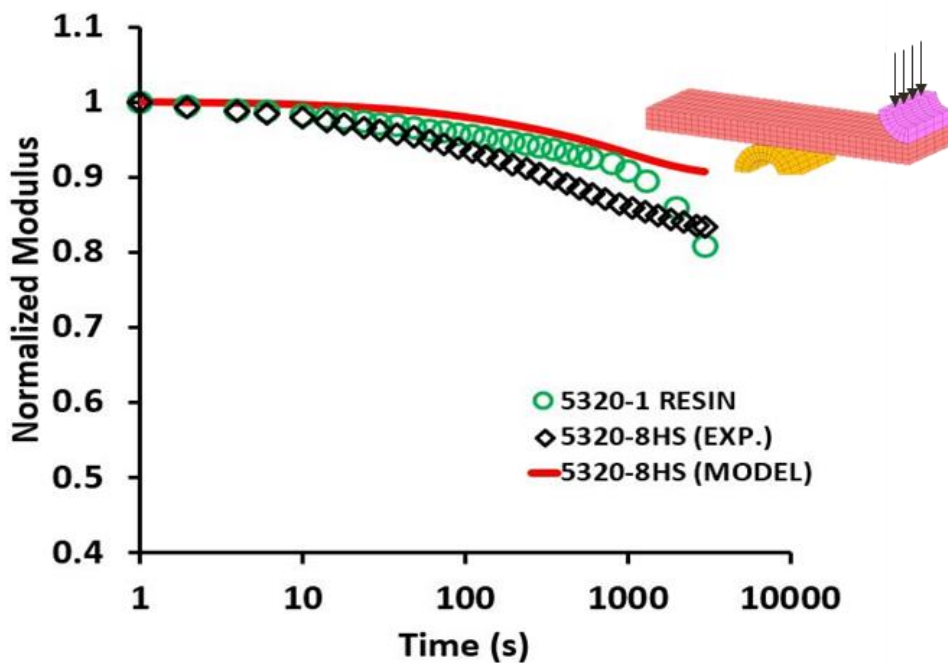


Figure 73. Normalized relaxation curves of 5320-8HS [± 45]s and 5320-1 Epoxy resin under isothermal condition of 100 °C (3-point bending)

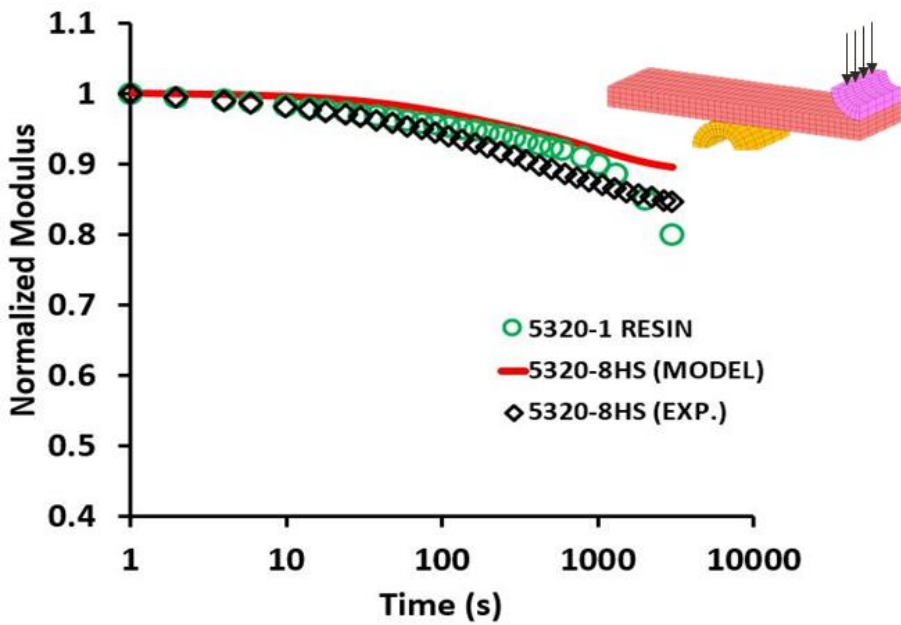


Figure 74. Normalized relaxation curves of 5320-8HS [±45]s and 5320-1 Epoxy resin under isothermal condition of 120 °C (3-point bending)

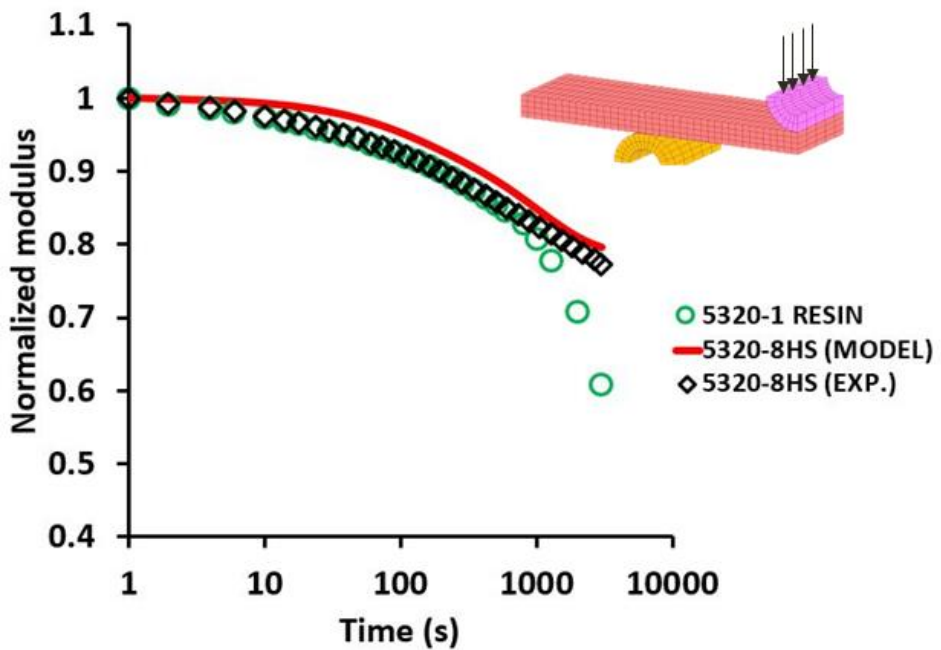


Figure 75. Normalized relaxation curves of 5320-8HS [±45]s and 5320-1 Epoxy resin under isothermal condition of 160 °C (3-point bending)

CHAPTER 7

RESULTS AND DISCUSSIONS

Even though effective response of axial loading are determined through experiments, the knowledge of heterogeneous state of stress that exists in the fiber bundles and a matrix pocket is imperative to understand the long term performance of woven fabric composites. Due to the complex weave architecture of woven fabric composite, predicting its stress state in the microstructure using classical laminate theory is difficult. Therefore, the assemblage of homogenized microstructure of unit cell model was analyzed using finite element method to reduce these complexities [50]. Here, each constituent is considered as a homogeneous continuum and analyzed with appropriate periodic constraints to represent the overall response of woven composite. In this chapter, stress distribution in the fiber bundles/tows and matrix pockets were studied as a function of time and deformation history. In addition, similar to micromechanics model, stress distribution in the laminate model was also studied.

7.1 Micromechanical Analysis of Satin Weave Architecture

7.1.1 Stress distribution

Since applied load cases produces all the six components of the stress both in matrix and tows, only axial extension along fill and tangential extension along warp direction of the fabric will be considered for this study. But stress contours will be shown in both the tows as well as in matrix with respect to time and deformation history.

In order to study the stress contours inside the tow and matrix, one has to slice the unit cell model to capture the interior. This in turn increases the number of stress contours even more.

Therefore the results were analyzed using the techniques like

- Stress components of selected region.
- Relaxation and loading curves of the contact region

Tow located at the center of the unit cell was chosen to study the stress distribution in both fill and warp direction. Path curves were plotted for the nodes located at the center of the contact region for both fill and warp tow. Global stresses based on corresponding loading were utilized in the study of path plots. In order to locate the peak stress, path curves of tows were normalized with stresses at $t=60s$. In addition, curves were shifted by 0.1 MPa to show the initially trend of stresses at $t=60s$. In case of resin, thin layer located between interlaced tows was chosen for this study. Relaxation of stress components for all the constituents was investigated in the location where stress concentration is more. Region of interest (ROI) for path curves in the tows and neat resin was illustrated in the Figure 76 and Figure 77. Stress contours of 5320-8HS unit model are illustrated in the Appendix F.

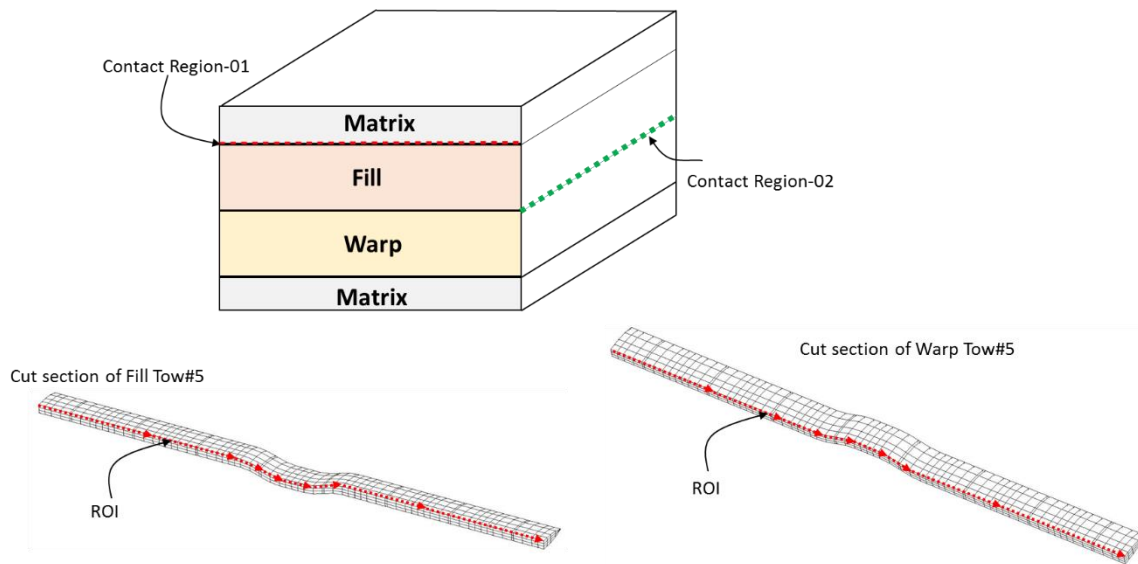


Figure 76. Region of Interest (ROI) in the tows of 5320-8HS unit cell model

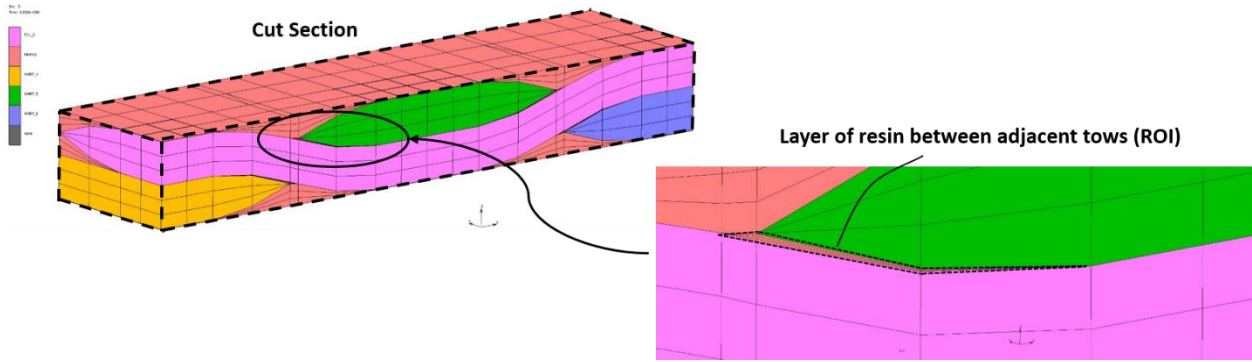


Figure 77. Region of Interest (ROI) in the neat resin of 5320-8HS unit cell model

7.1.2 Case 1: Axial loading along fill direction (along x-axis)

Even though effective relaxation response of 5320-8HS unit model was found to be less along axial direction, microstructure of 5320-8HS unit cell model was investigated further to understand the component of stress which relaxes more. Characterization of microstructure was explained through step by step procedure in the following paragraphs.

7.1.2.1 Thermomechanical Loading

Loading curves for the constituents of 5320-8HS unit cell model were illustrated in the figures (i.e., from Figure 78 to Figure 84). During thermal soaking, component 11 of stress for fill tows was observed to be concentrated more in the floating region next to undulation of fill under tension. In case of warp, undulation induces more stresses under compression. Wherein resin, the region just above the fill tows was more stressed under tension.

Since the unit cell model was loaded along fill direction, stress concentration was found to be more on the fill bundles as compare with other constituents. Furthermore, from the investigation of fill tow, these stress concentration was observed to be maximum in the vicinity of waviness. With increase in loading, peak stress due to thermal loading which existed in the floating region of bundles started shifting to the wavy region as shown in the Figure 78 and Figure 79 .

In case of warp tows, peak stress existed in the undulation due to thermal contraction started to decay with increase in load and shifted to the contact region of floats linearly as we move away from the undulation, which are illustrated in the following figures (i.e., from Figure 80 to Figure 82). For the selected region of resin, stress concentration was observed to be shifting towards the region located between the interlaced tows as shown in Figure 83 and Figure 84.

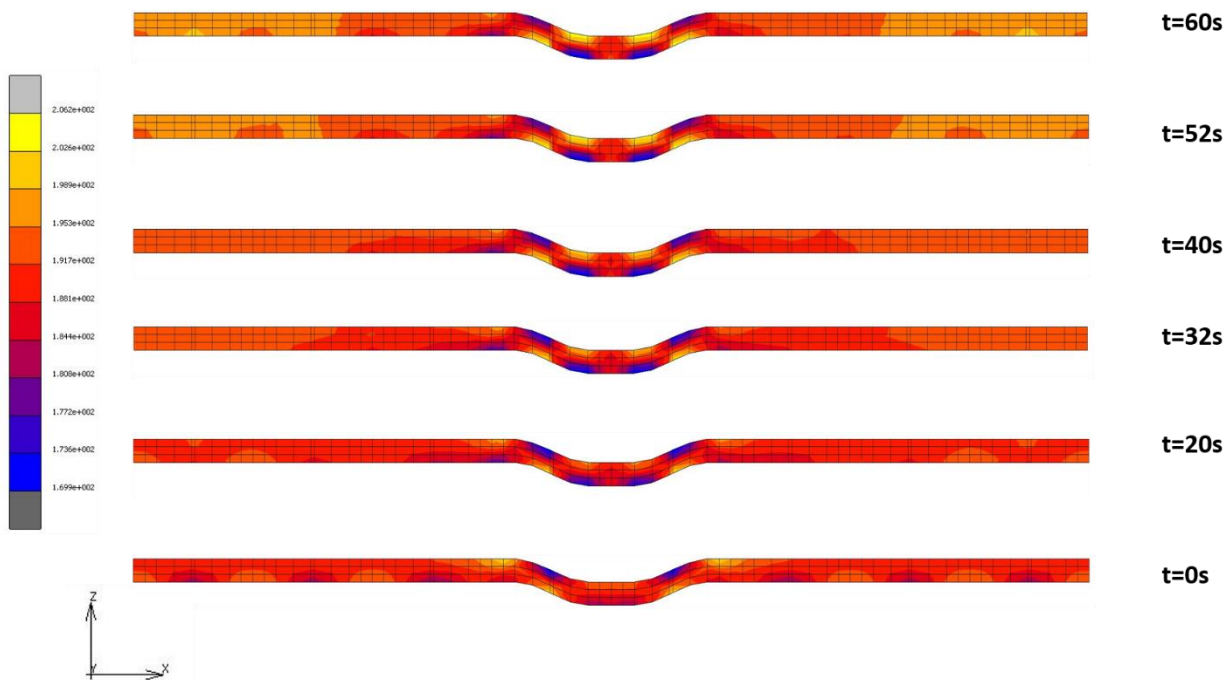


Figure 78. Stress contours for component 11 of stress (σ_{11}) of fill tow#5 at different loading times under isothermal condition of 80 °C

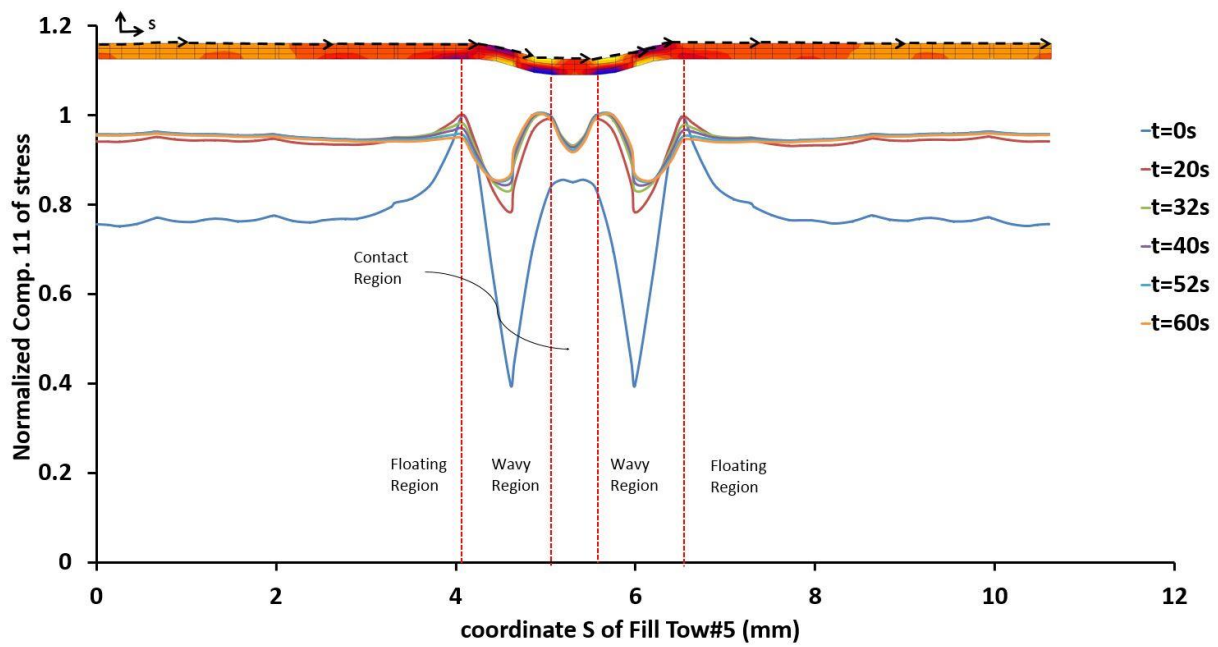


Figure 79. Distribution of normalized component 11 of stress (σ_{11}) for fill tow#5 at different loading times under isothermal condition of 80 °C

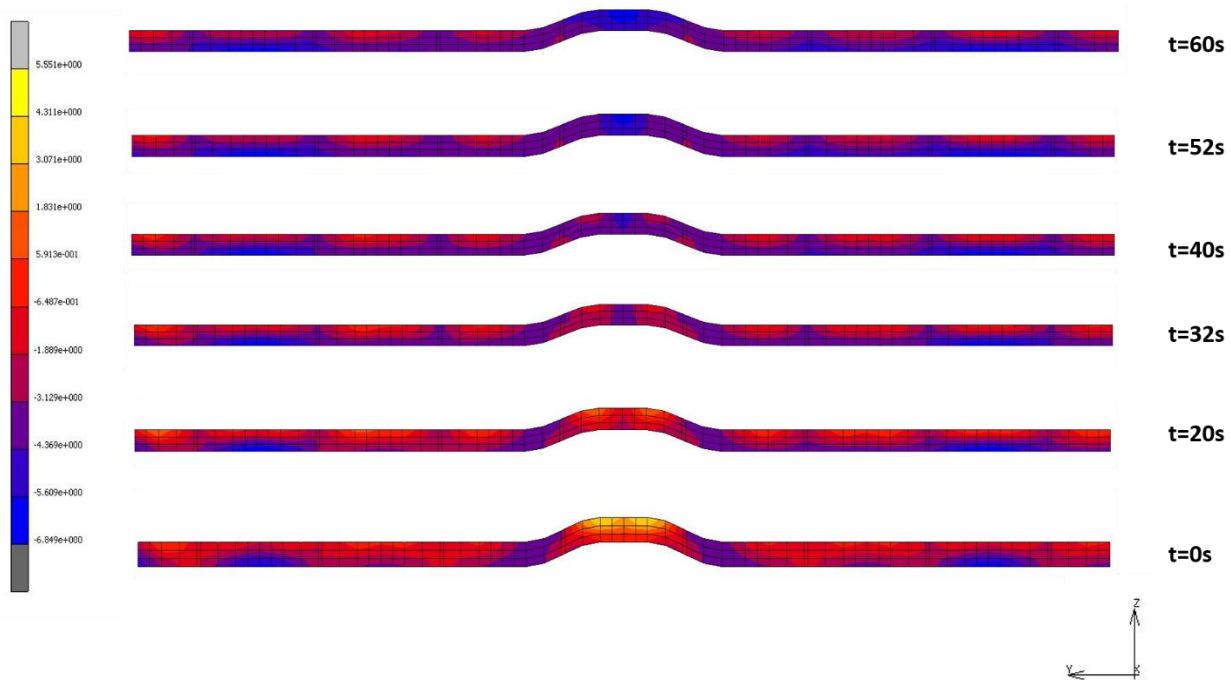


Figure 80. Stress contours for component 11 of stress (σ_{11}) of warp tow#5 at different loading times under isothermal condition of 80 °C

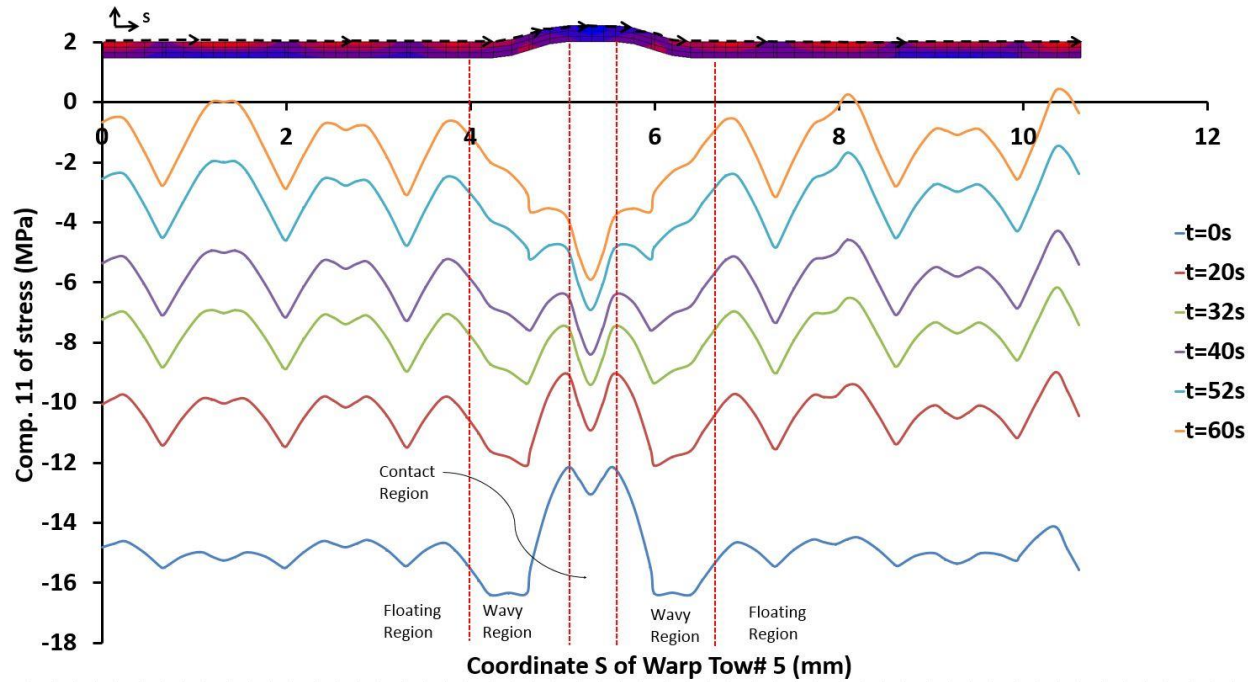


Figure 81. Distribution of component 11 of stress (σ_{11}) for warp tow#5 at different loading times under isothermal condition of 80 °C

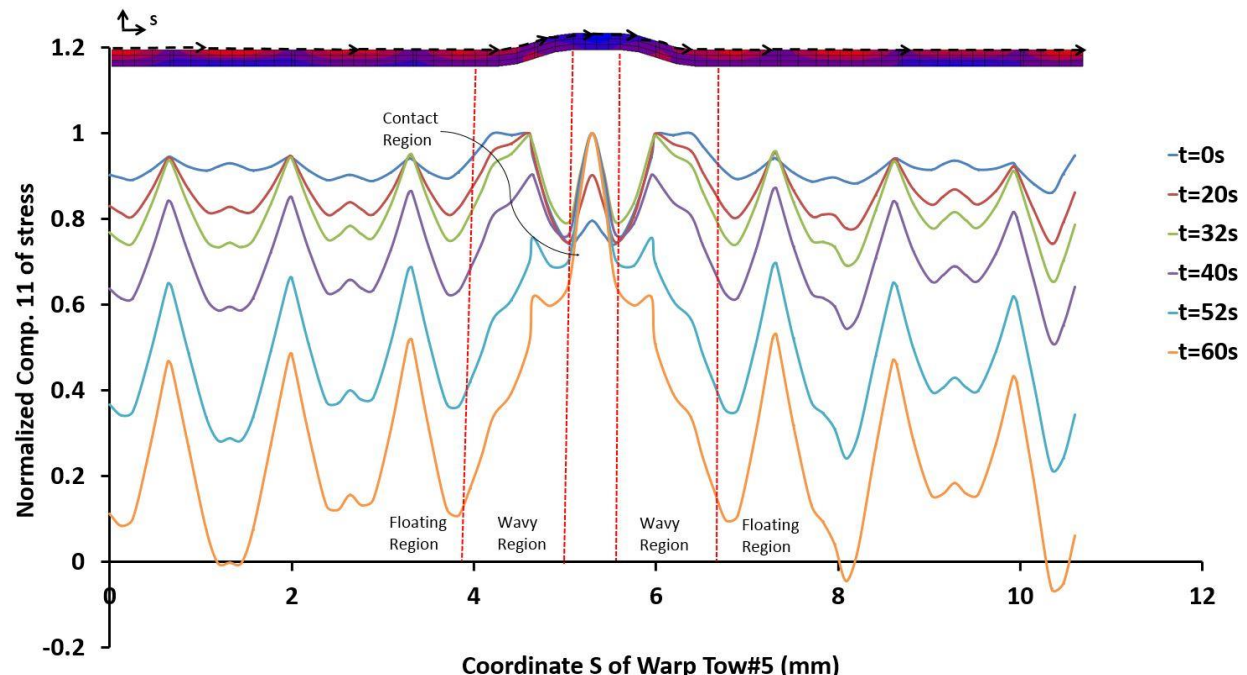


Figure 82. Distribution of normalized component 11 of stress (σ_{11}) for warp tow#5 at different loading times under isothermal condition of 80 °C

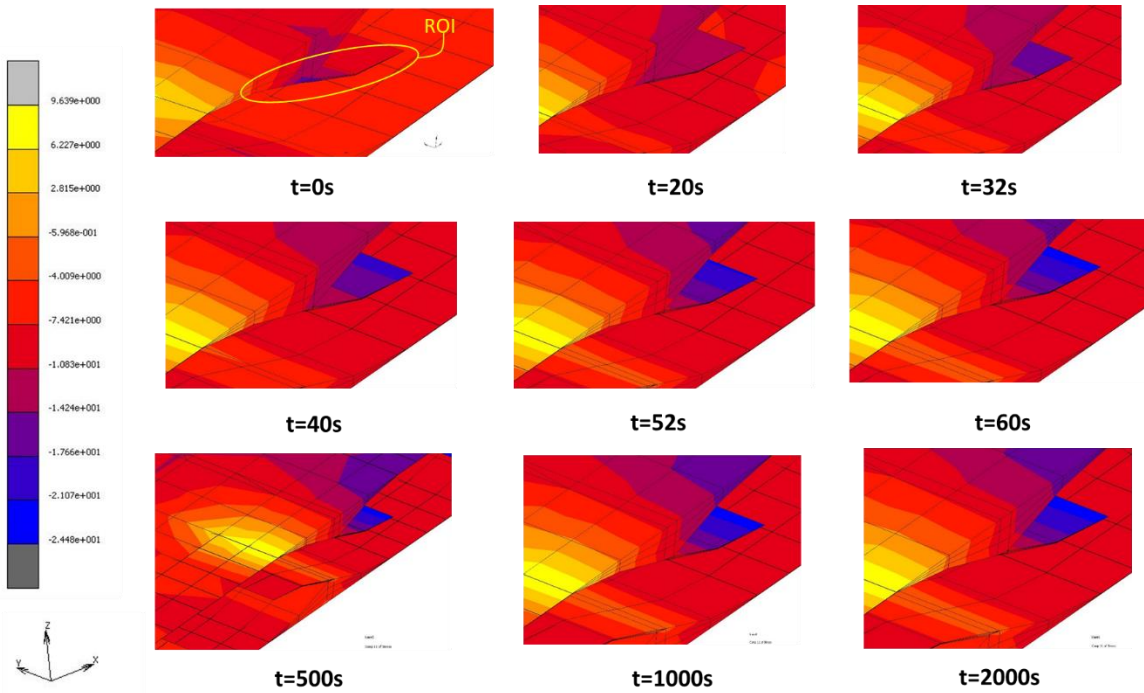


Figure 83. Stress contours for component 11 of stress (σ_{11}) of neat resin located between interlaced tows at different loading times under isothermal condition of 80 °C (ROI-Region of Interest)

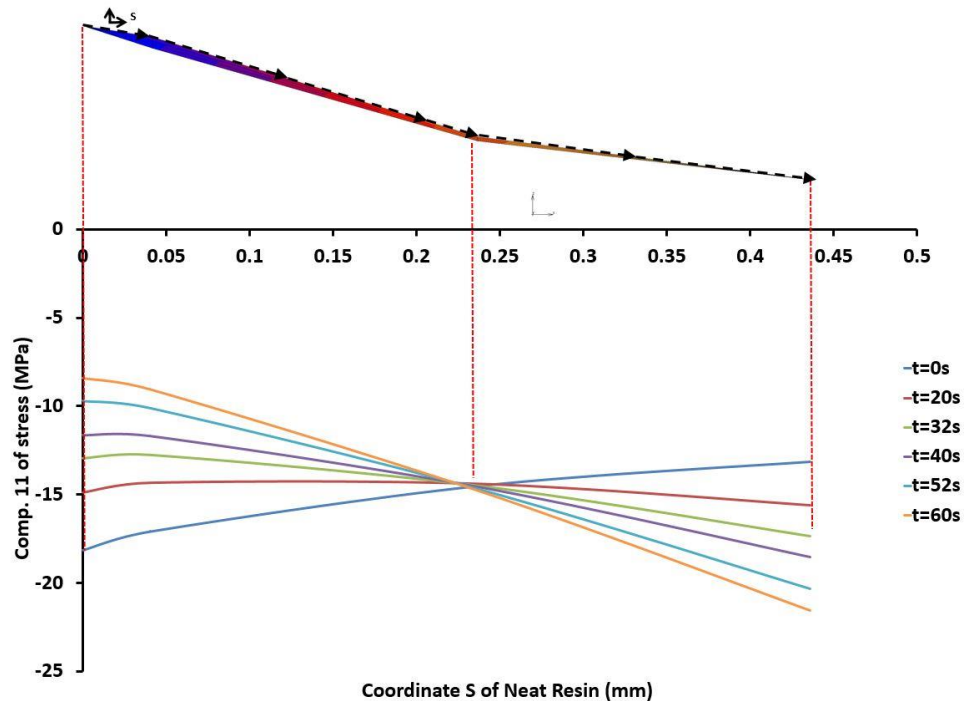


Figure 84. Distribution of component 11 of stress (σ_{11}) for neat resin located between interlaced tows at different loading times under isothermal condition of 80 °C

7.1.2.2 Stress relaxation

Even though component 11 of stress induced in the fill tow relaxes less, under constant strain this stress relaxation was observed to be increasing as we move away from the undulation as shown in Figure 85 and Figure 86. This is because; undulation region of fill tow was tightly locked by the warp tow. Increase in relaxation along the floating region of fill tow may attributed to the difference in compressive force created by the adjacent undulations of warp tows.

In contrast, relaxation of warp under compression observed to be maximum in the region of interlaced tows as shown in Figure 87. Stress peaks located in the floats of warp were attributed to the gap region where compressive force was dominated by neat resin. Minimum stress concentration was noticed in the contact region of floats as shown in Figure 88. In case of resin, resin layer located between interlaced tows relaxes more than the region of contact above the fill tow as a function of time as shown in Figure 89.

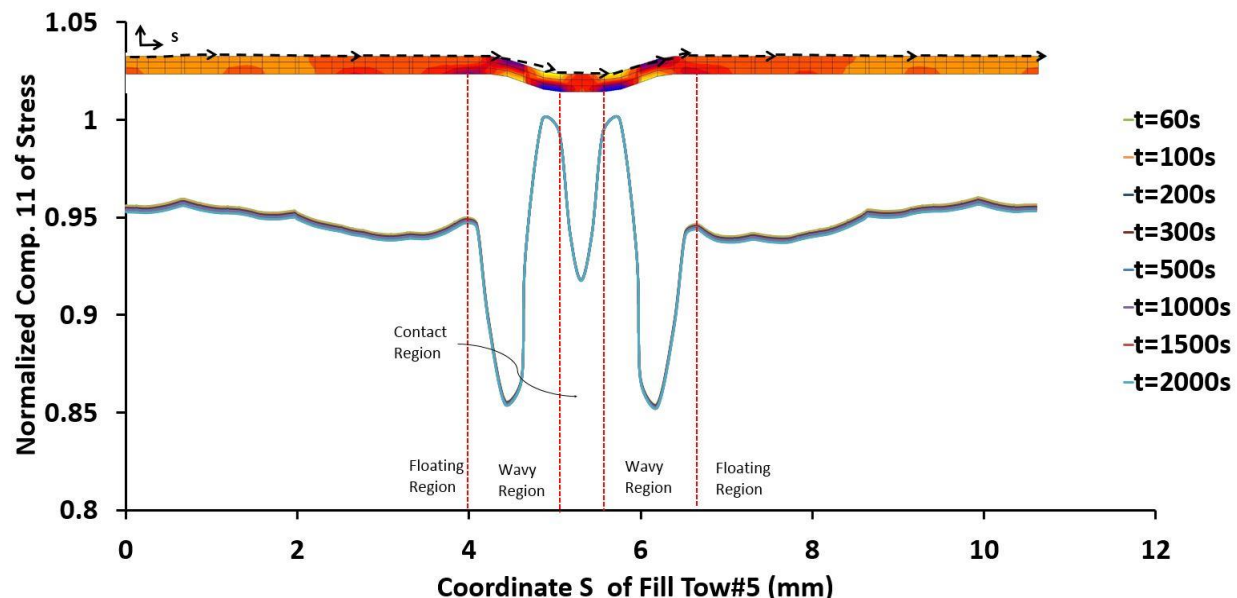


Figure 85. Distribution of normalized component 11 of stress (σ_{11}) for fill tow#5 at different relaxation times under isothermal condition of 80 °C (Base : Peak stress of every increment)

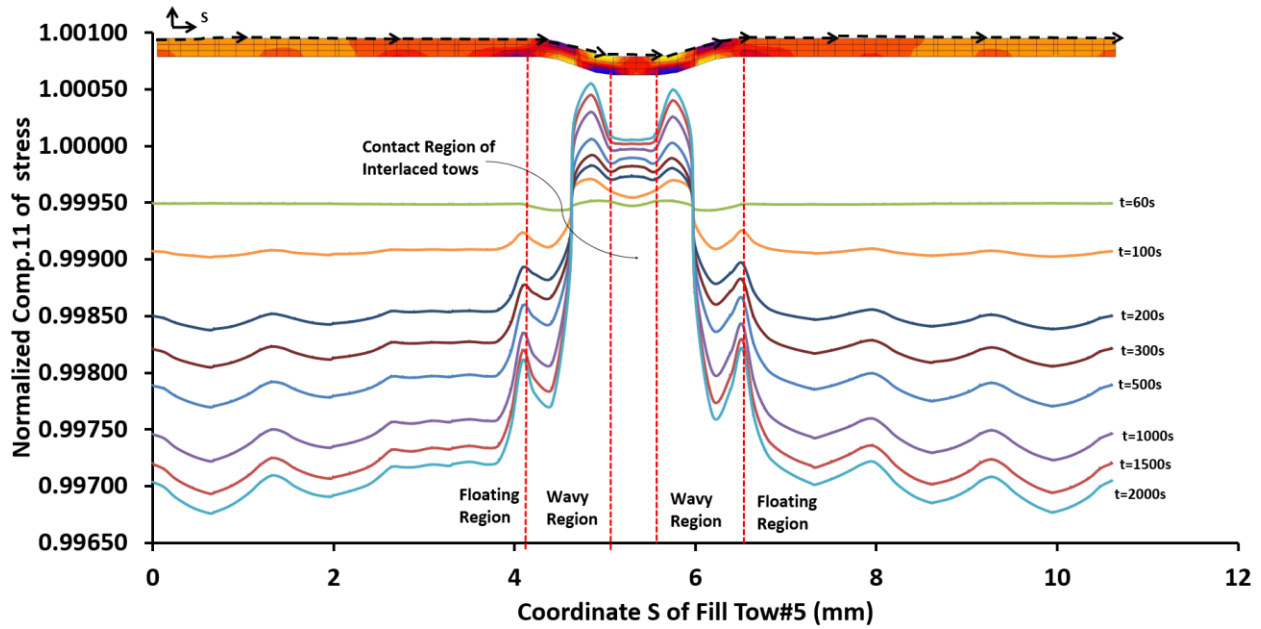


Figure 86. Distribution of normalized Component 11 of stress (σ_{11}) for fill tow#5 at different relaxation times under isothermal condition of 80 °C (Base : stress at $t=60s$)

Note: Base curve is shifted by 0.1 MPa to show the general trend of initial stress distribution

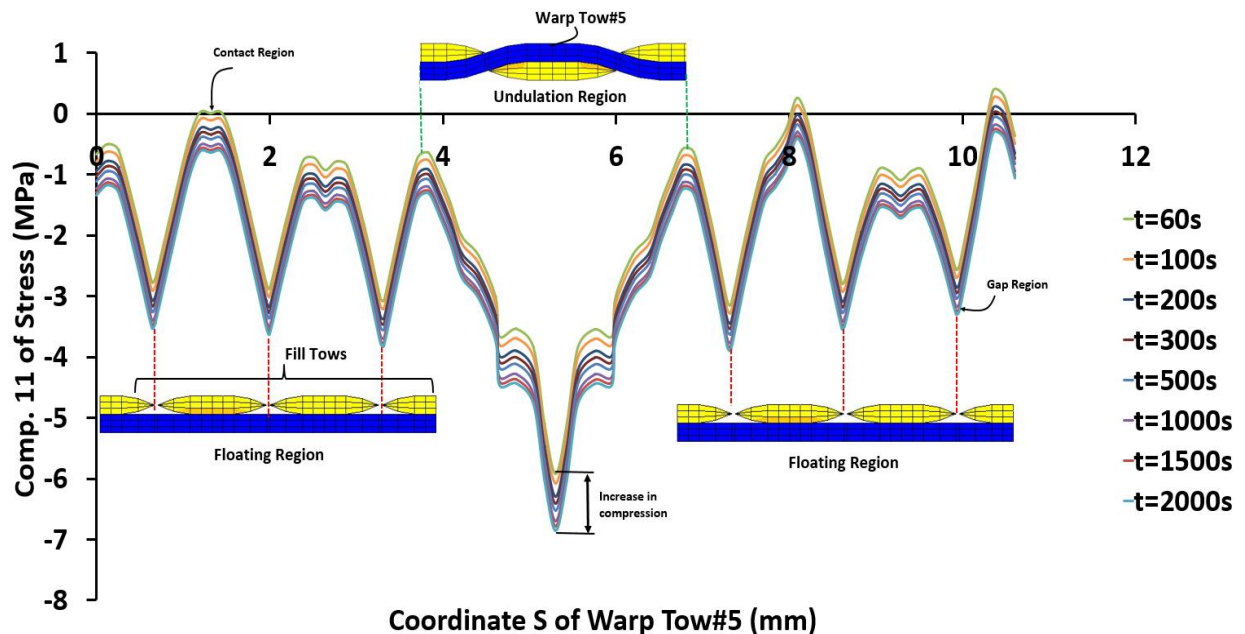


Figure 87. Distribution of component 11 of stress (σ_{11}) for warp tow#5 at different relaxation times under isothermal condition of 80 °C

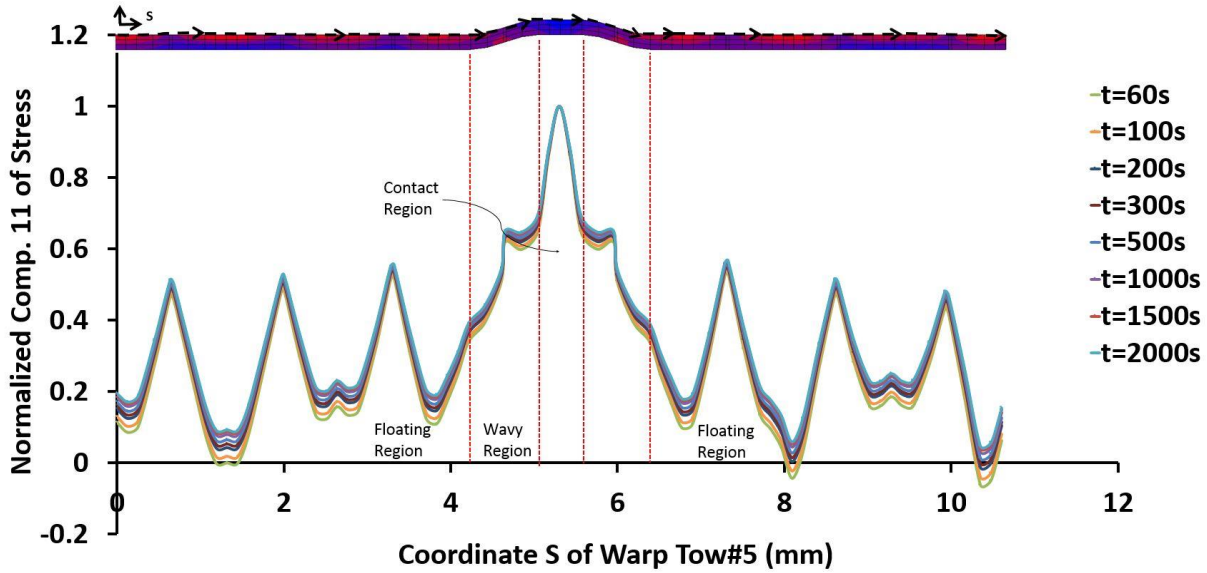


Figure 88. Distribution of normalized Component 11 for stress (σ_{11}) for warp tow#5 at different relaxation times under isothermal condition of 80 °C (Base : stress at $t=60s$)

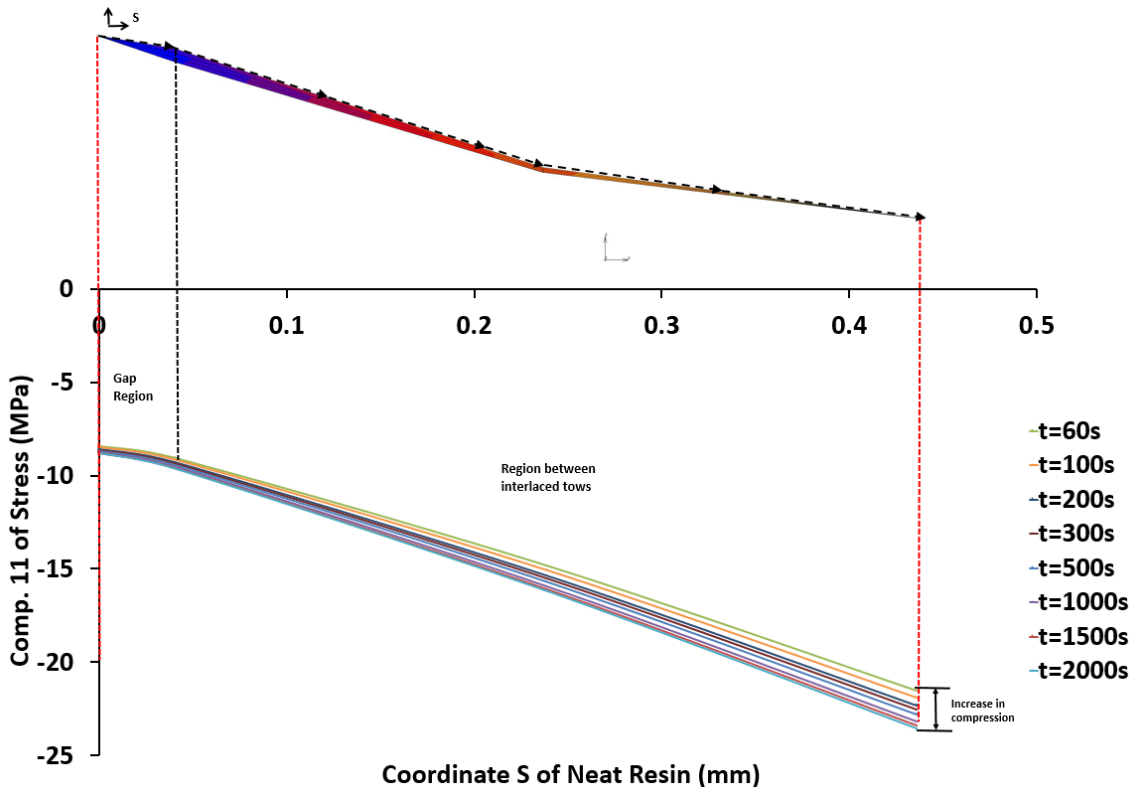


Figure 89. Distribution of Component 11 of stress (σ_{11}) for neat resin located between interlaced tows at different relaxation times under isothermal condition of 80 °C

7.1.2.3 Peak stress regions

In case of fill tow, locations as mentioned in the Figure 90 were selected to analyze the relaxation behavior of all the stress components. During stress relaxation at 80 °C, increase in stress components 12, 31 and 33 may attributed to the compressive force generated by the adjacent contact bodies. But in magnitude level, they are relatively small as compare with component 11 of stress. On other hand, relaxation of stress components 11, 22 and 23 were observed as a function of time which is shown in Figure 91. In the contact region of warp tow, all the stress components except component 33 of stress were observe to be increasing with respect to time as illustrated in the Figure 92. Interestingly, component 23 of stress in the contact region of resin relaxes more than the effective response of entire unit cell at 80 °C. From the overall comparison, relaxation in the fill tow was observed to be more in the contact region of warp. Therefore, for elevated temperatures, relaxation of stress components was discussed only in the contact region of warp. Relaxation of these stress components was observed to be varying with increase in temperature as illustrated in the following figures (i.e. from Figure 92 to Figure 95). At 100 °C component 23 of stress relaxes maximum of 8%, whereas at 120 °C relaxation was dominated by component 33 of stress. At 160 °C fill tow was observed to be relaxed by component 11 of stress, where relaxation was dominated by axial loading.

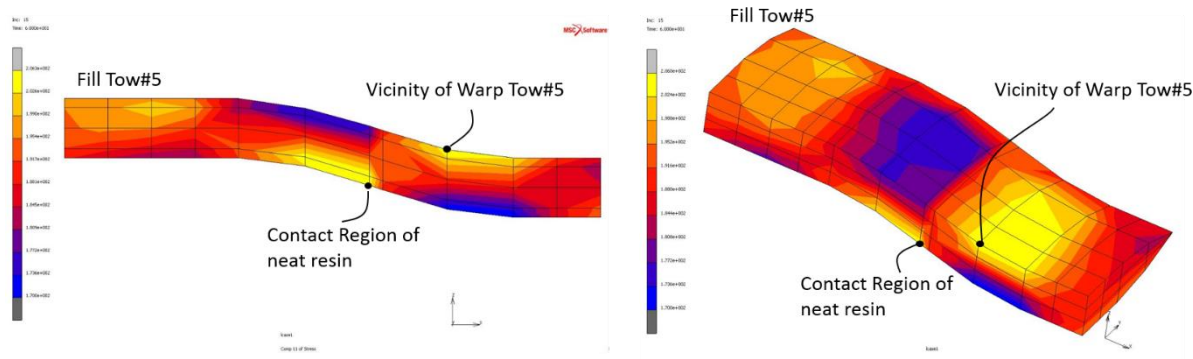


Figure 90. Region of Interest (ROI) from the cut section of fill tow#5

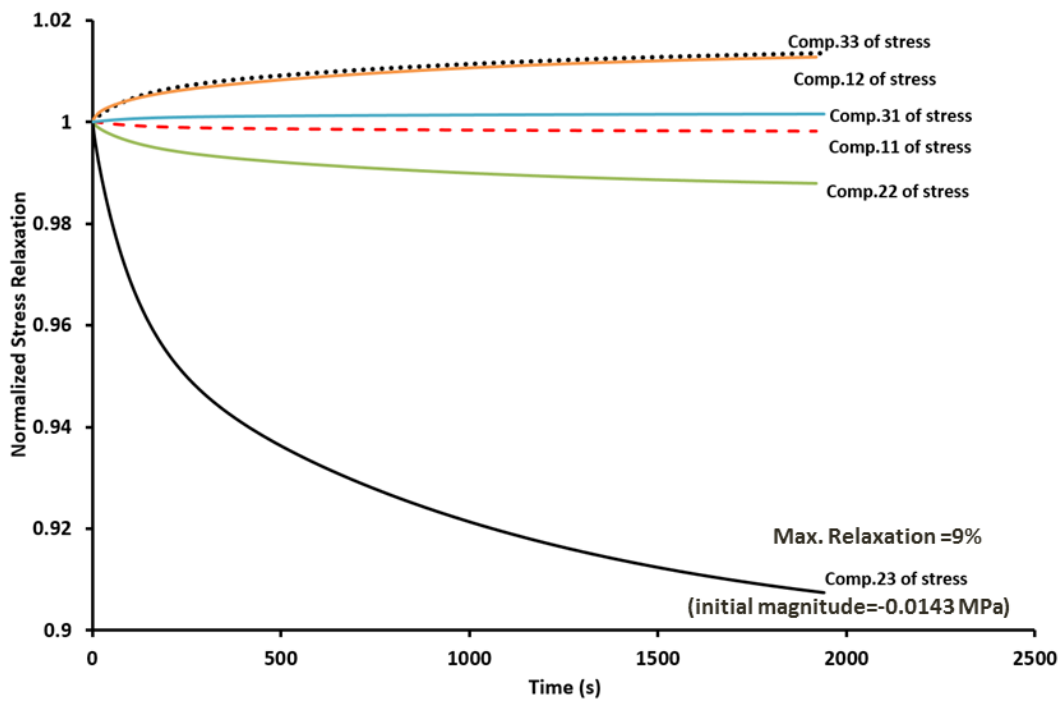


Figure 91. Comparison of all the stress components for fill tow#5 in the contact region of Resin during relaxation at 80 °C

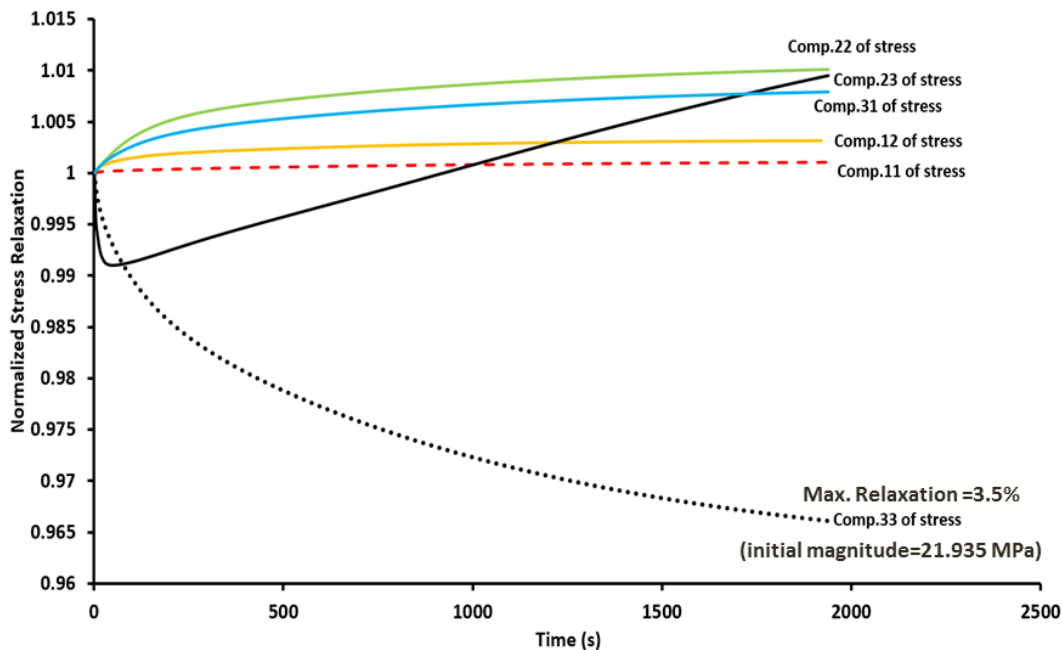


Figure 92. Comparison of all the stress components for fill tow#5 in the vicinity of Warp tow#5 during relaxation at 80 °C

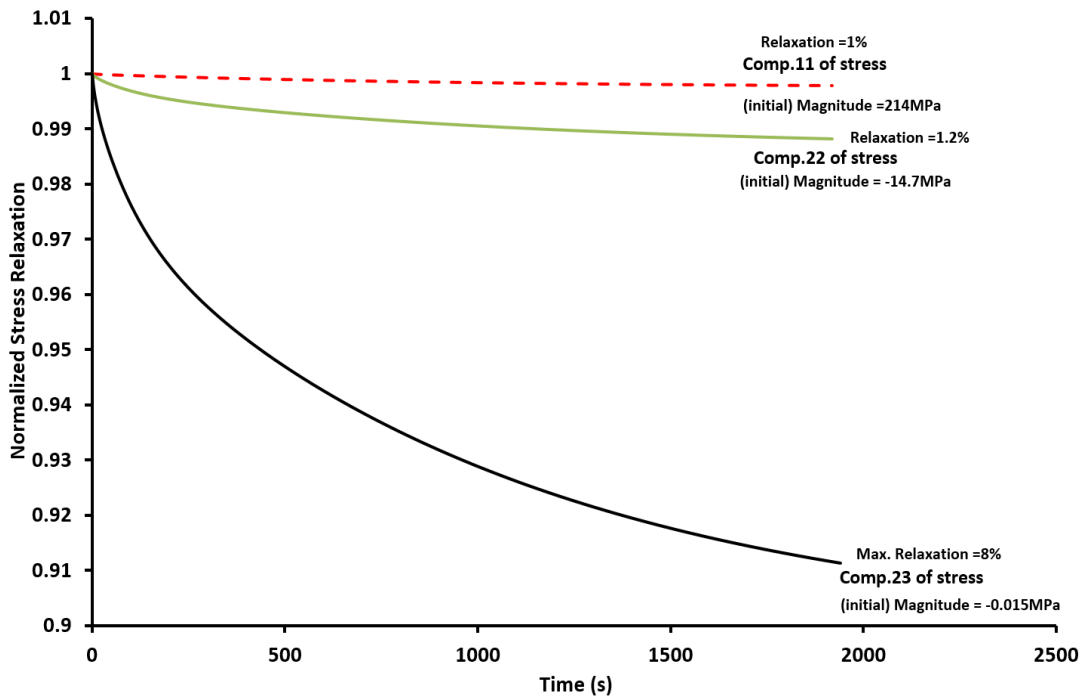


Figure 93. Relaxation curves of components 11, 22 and 23 of stress for fill tow#5 in the contact region of Resin at 100 °C

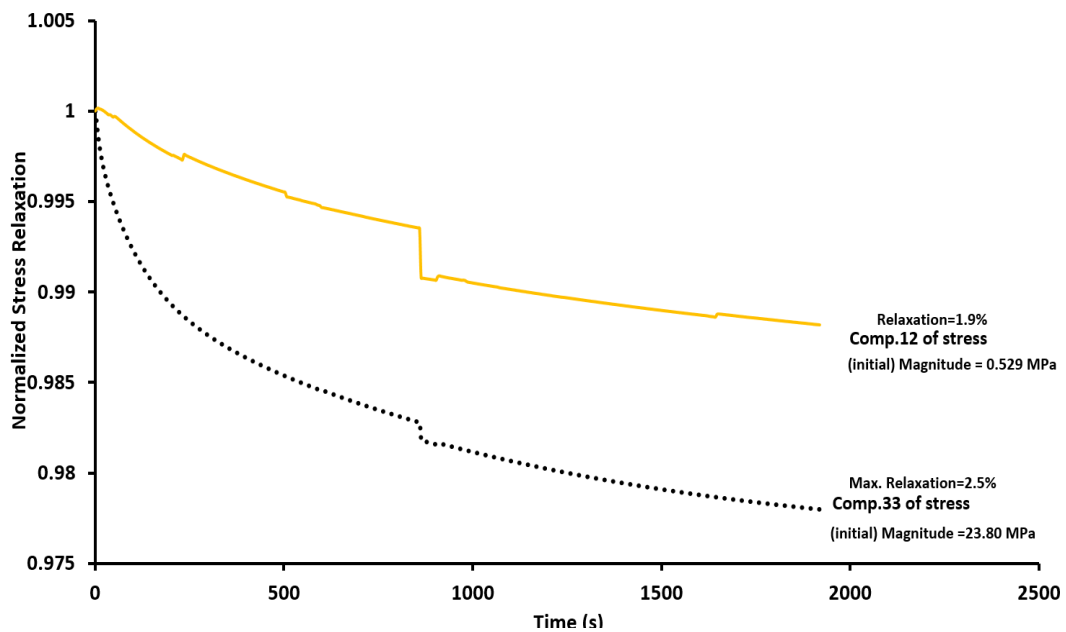


Figure 94. Relaxation curves of components 12 and 33 of stress for fill tow#5 in the contact region of Resin 120 °C

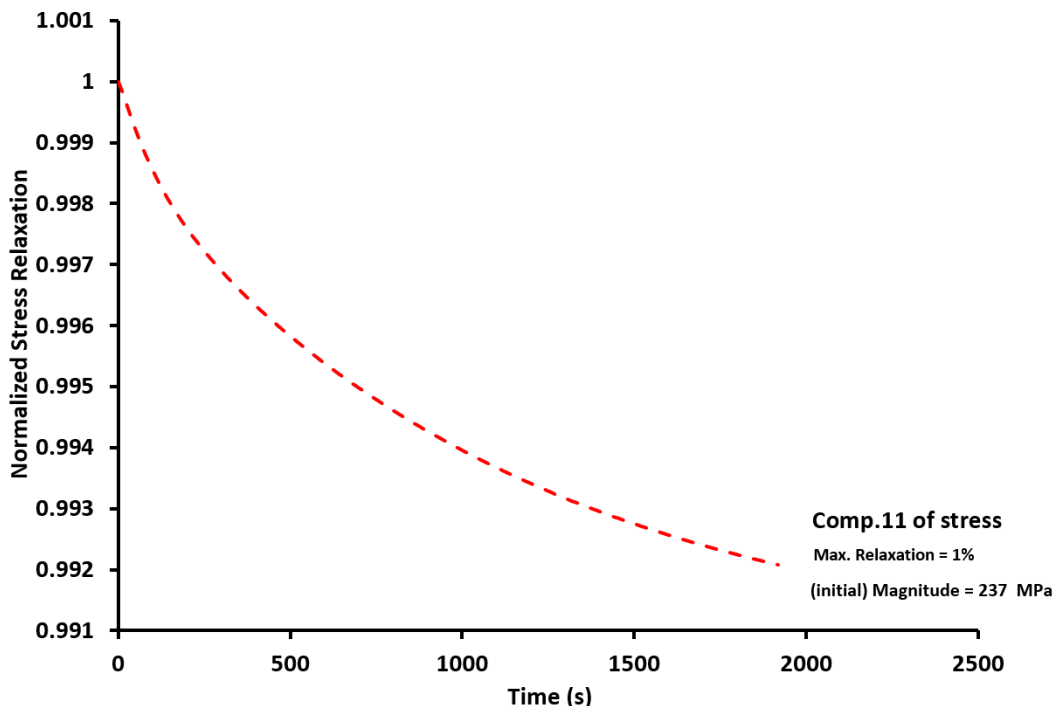


Figure 95. Relaxation curve of component 11 of stress for fill tow#5 in the contact region of Resin at 160 °C

For warp tow, region next to undulation of fill tow as shown in the Figure 96 was selected to analyze the stress components. During relaxation, component 11 and 12 of stresses were observed to be relaxed by 14%, whereas component 22, 33, 23 and 31 of stresses were increasing with respect to time. Similar to fill tows, relaxation of stress components for warp tow was observed to be varying at elevated temperatures as illustrated in the following figures (i.e. from Figure 97 to Figure 100).

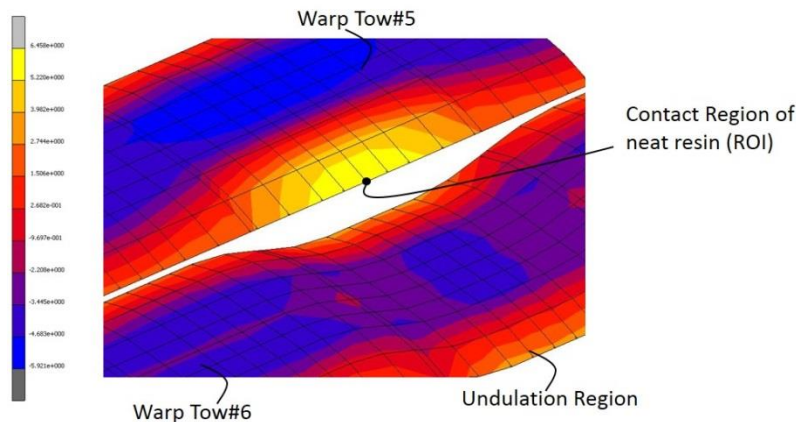


Figure 96. Region of Interest (ROI) from warp tow#5

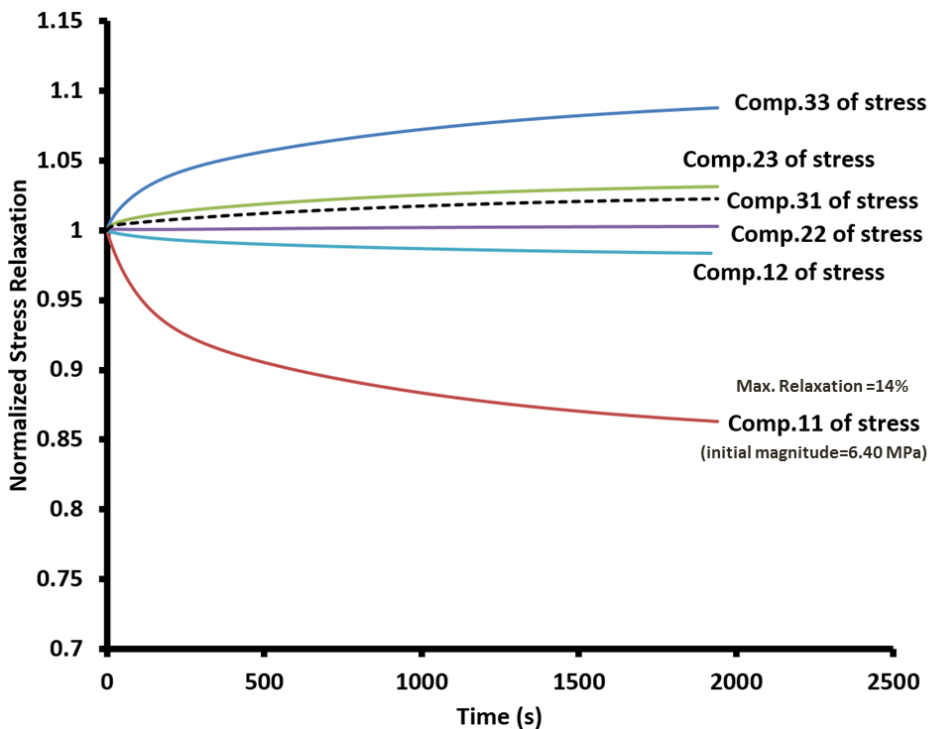


Figure 97. Comparison of all the stress components for warp tow#5 in the contact region of Resin during relaxation at 80 °C

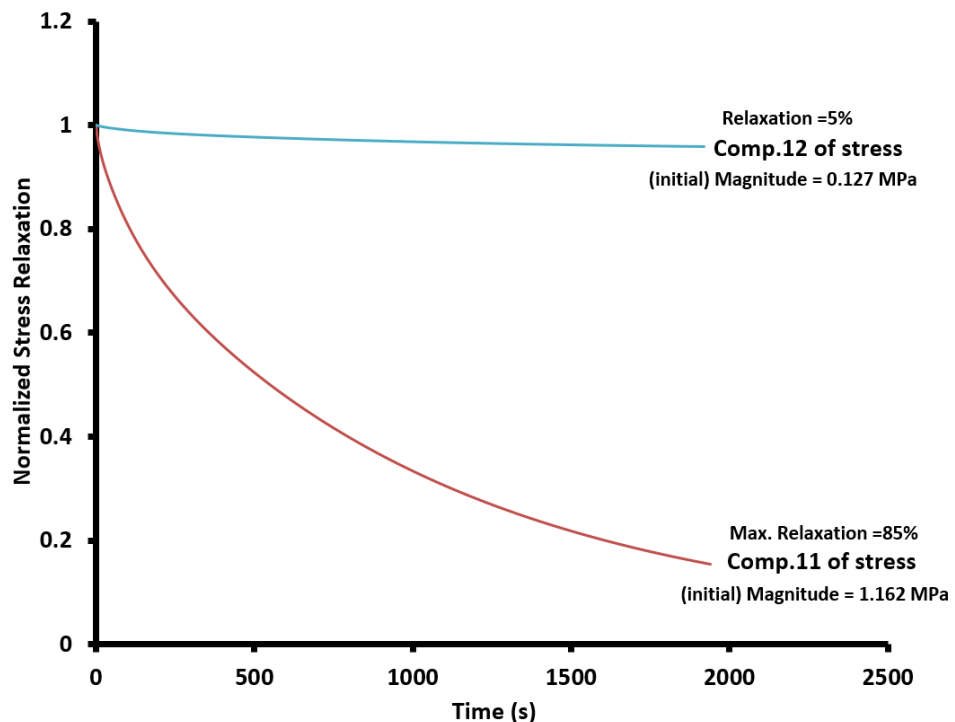


Figure 98. Relaxation curves of components 11 and 12 of stress for warp tow#5 in the contact region of Resin at 100 °C

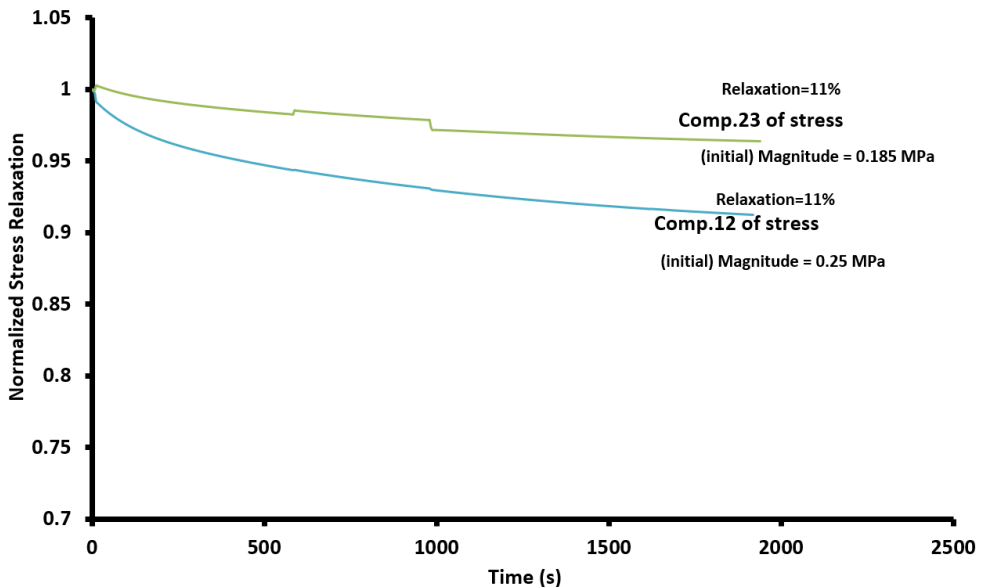


Figure 99. Relaxation curves of components 23 and 12 of stress for warp tow#5 in the contact region of Resin at 120 °C

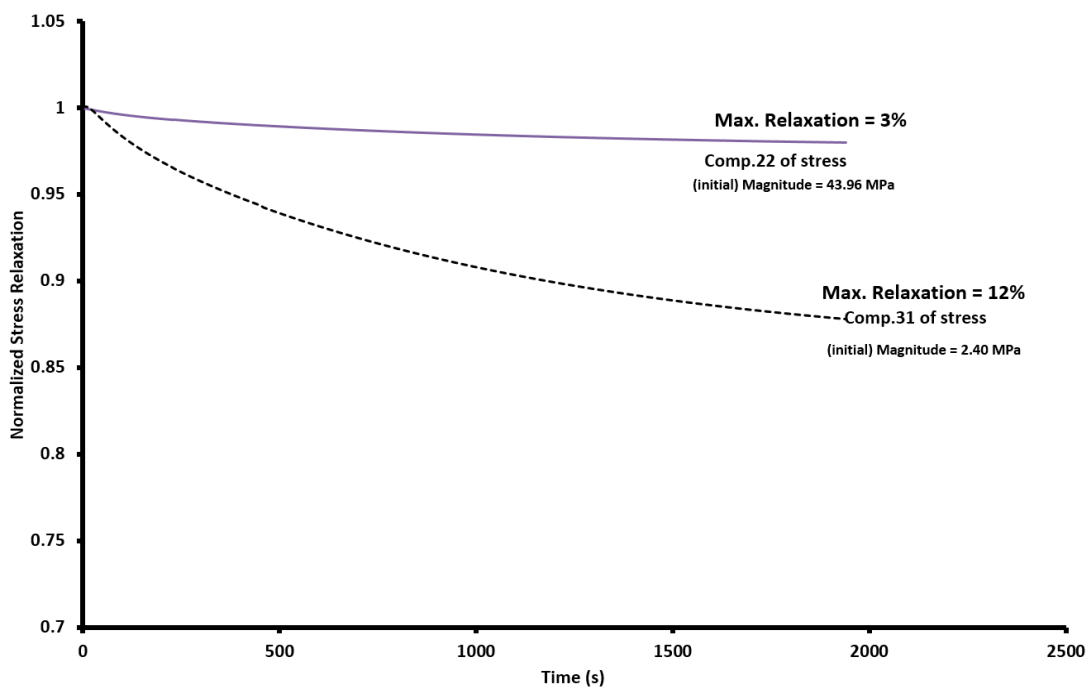


Figure 100. Relaxation curves of components 22 and 31 of stress for warp tow#5 in the contact region of Resin at 160 °C

In case of neat resin, relaxation behavior was analyzed in the regions as shown in the

Figure 101. Similar to fill and warp tows, increasing stress components corresponds to the

compressive behavior of undulation. Component 12 of stress relaxes by 5% in ROI-01, whereas in ROI-02 component 12 of stress relaxes by 8% and component 23 of stress relaxes by 26% as illustrated in the Figure 102 and Figure 103. From the comparison of selected regions at 80 °C, relaxation was observed to be dominant in the ROI-02. Therefore, for elevated temperatures, relaxation of stress components was discussed only for the ROI-02. Similar to both fill and warp tows, relaxation behavior of stress components was not consistent with increase in temperature as shown in the following figures (i.e., from Figure 102 to Figure 106). At 100 °C component 23 of stress changes its state from tension to compression as a function of time during relaxation. With increase in temperature, relaxation was observed only from the component 12 of stress by 11% at 120 °C and component 22 of stress by 78% at 160 °C.

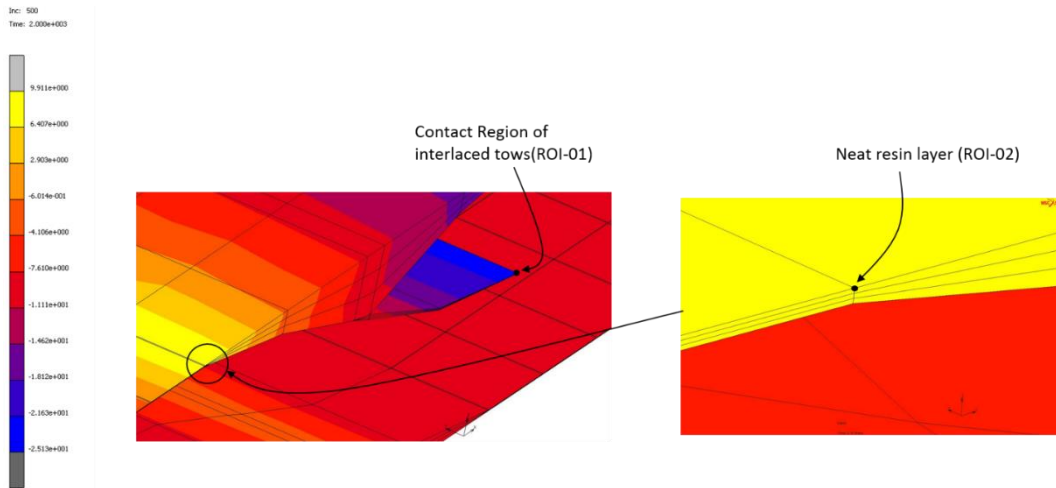


Figure 101. Region of Interest (ROI) from neat resin

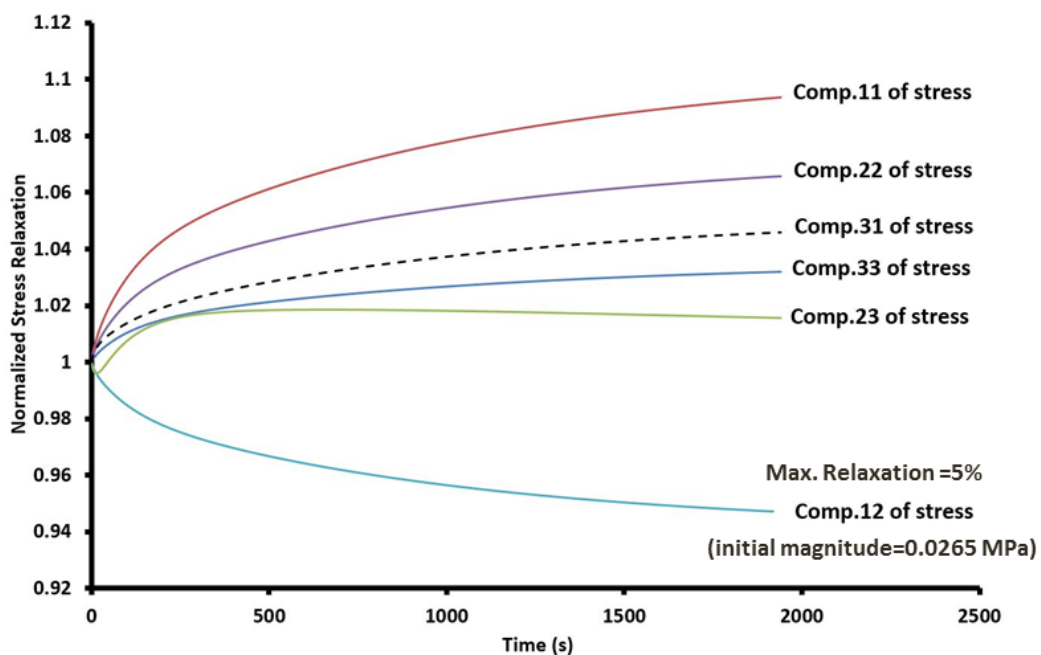


Figure 102. Comparison of all the stress components for neat resin in the vicinity of interlaced tows (ROI-01) during relaxation at 80 °C

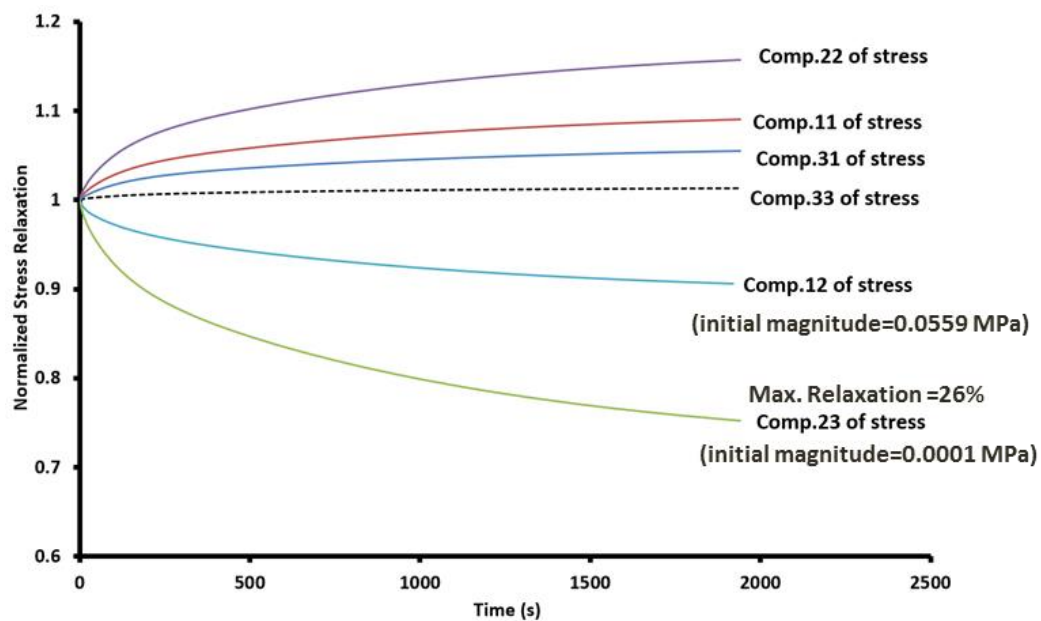


Figure 103. Comparison of all the stress components for neat resin in the vicinity of interlaced tows (ROI-02) during relaxation at 80 °C

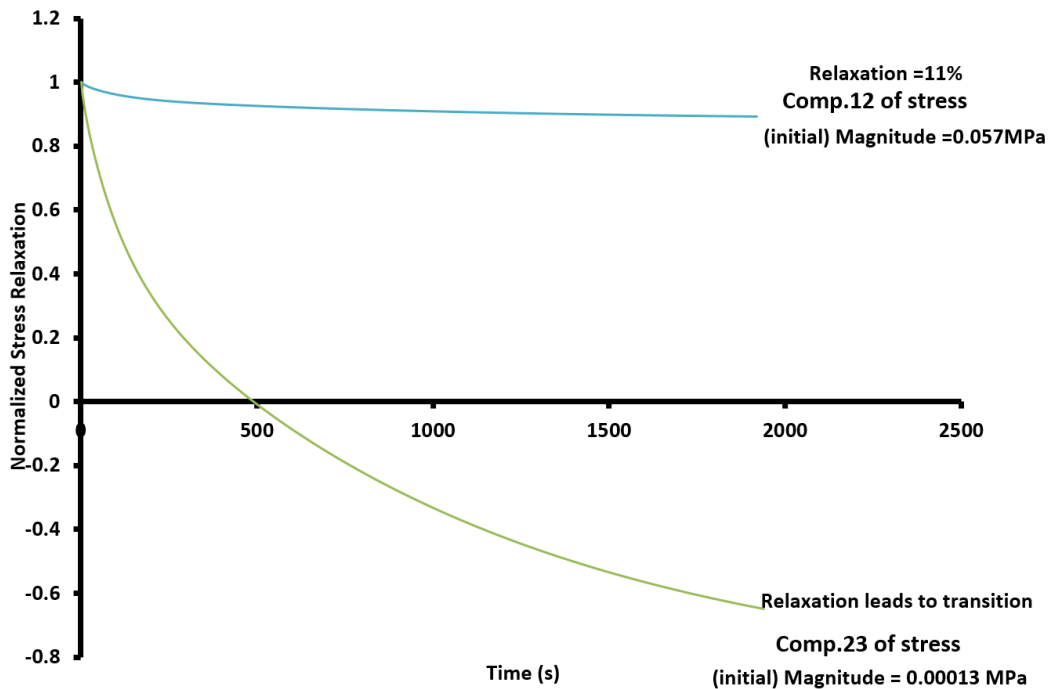


Figure 104. Relaxation curves of components 12 and 23 of stress for neat resin in the vicinity of interlaced tows (ROI-01) at 100 °C

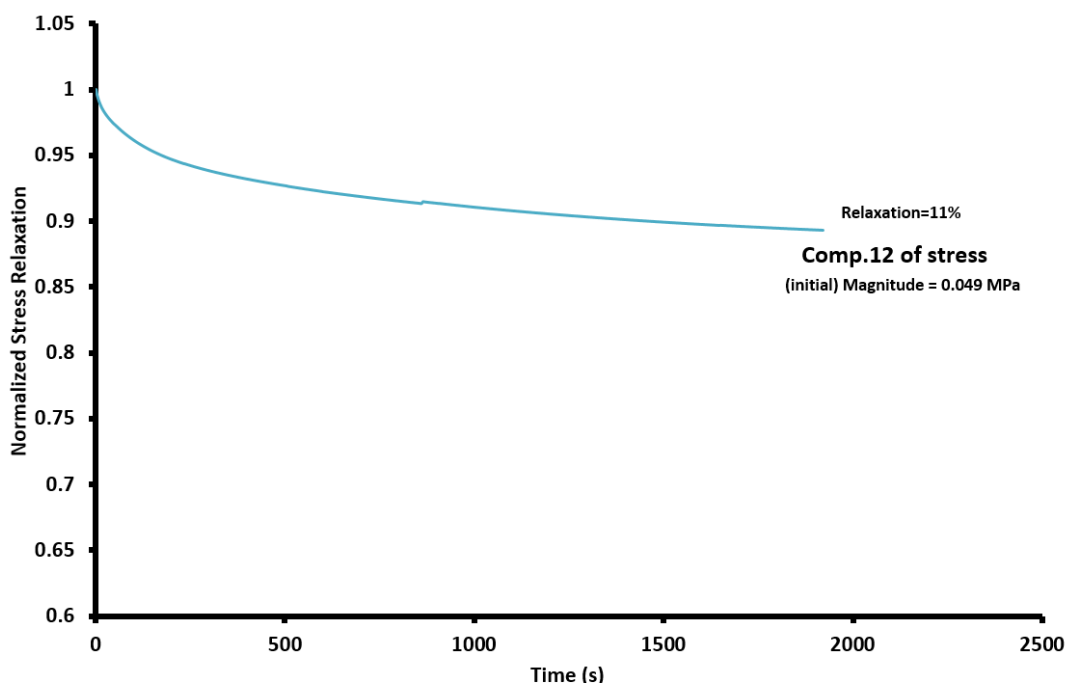


Figure 105. Relaxation curve of component 12 of stress for neat resin in the vicinity of interlaced tows (ROI-01) at 120 °C

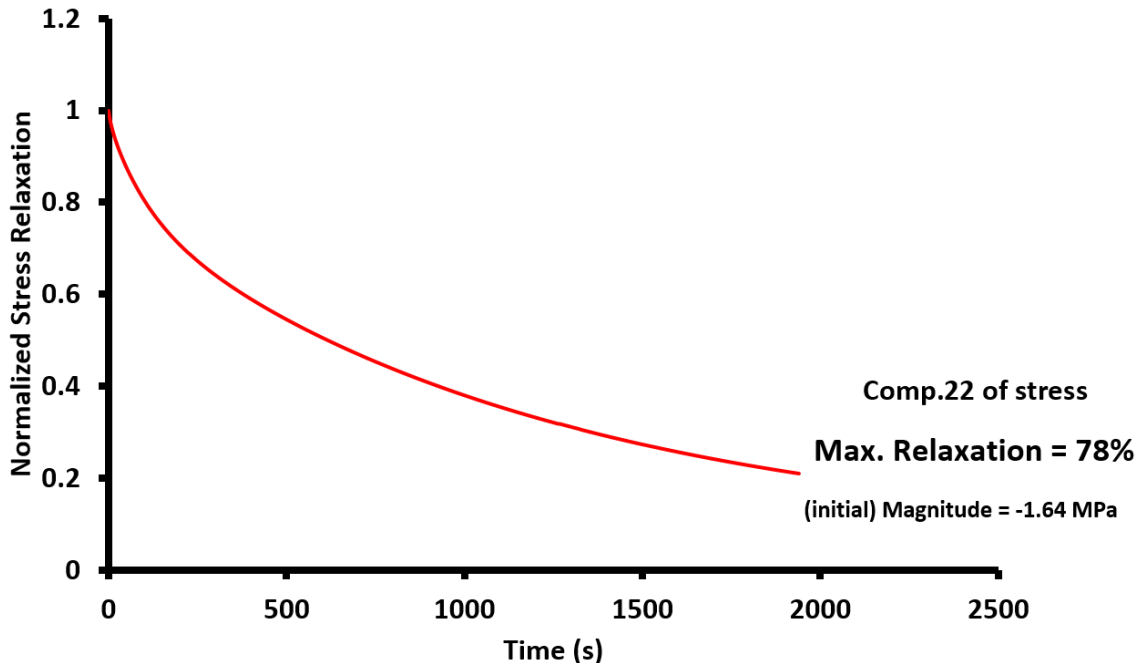


Figure 106. Relaxation curve of component 22 of stress for neat resin in the vicinity of interlaced tows (ROI-01) at 160 °C

Overall, relaxation of stress components in the microstructure of 5320-8HS woven composite was observed to be not consistent with change in temperatures.

7.1.3 Case 2: Tangential loading along warp direction (in-plane shear)

Based on the validation of results, effective relaxation behavior of unit cell model predicted under in-plane shear was even better than axial load. Therefore, detailed study of its stress distribution will give better understanding on shear relaxation of satin weave architecture. Shear stresses developed in the microstructure of 5320-8HS unit cell model was analyzed with help of the path curves following the same procedure of axial load case.

7.1.3.1 Thermomechanical loading

Loading curves for the constituents of 5320-8HS unit cell model under in-plane were illustrated in the following figures (i.e., from Figure 107 to Figure 109). During thermal soaking, component 12 of stress for fill and warp tows was found to be concentrated more in the gap region of their float located next to the undulation of perpendicular tow. Similar to axial load case, neat resin was also more stressed in the region just above the fill tows under thermal expansion.

Since the unit cell model was loaded tangentially along warp direction, component 12 of stress was observed to be concentrated more in the gap region of floats located between the adjacent tows. For both fill and warp tows, development of in-plane shear distribution was found to be identical during loading as illustrated in Figure 107 and Figure 108. From the selected region of resin layer, it clearly shows that component 12 of stress increases in the gap region as compare with region of interlaced tows as shown in the Figure 109.

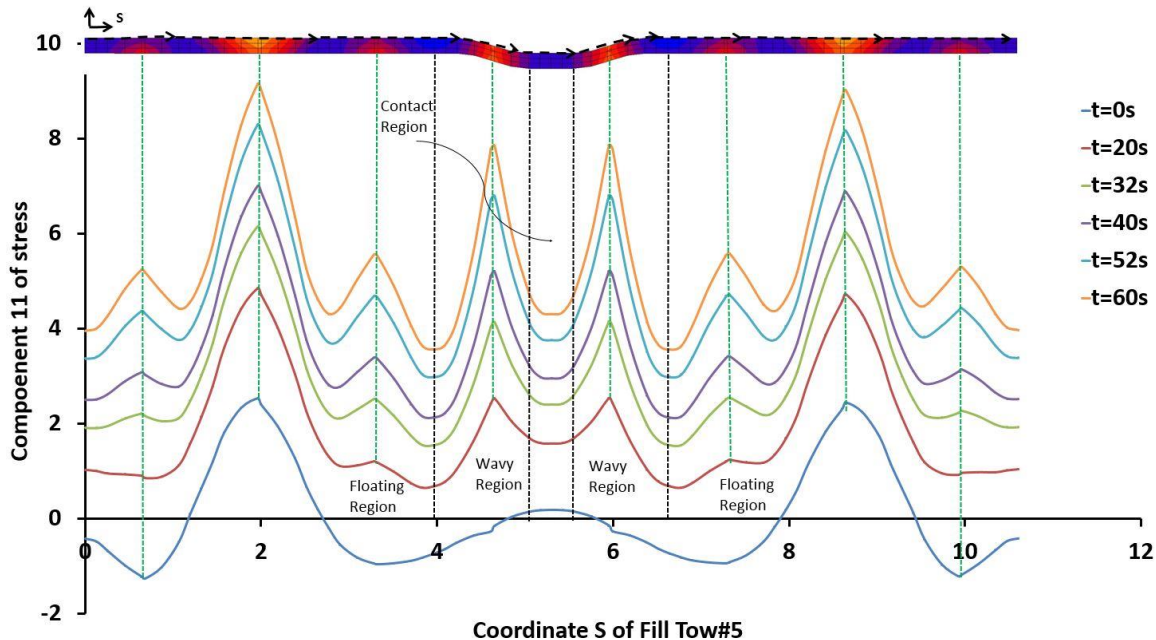


Figure 107. Distribution of component 12 of stress (σ_{12}) for fill tow#5 at different loading times under isothermal condition of 80 °C

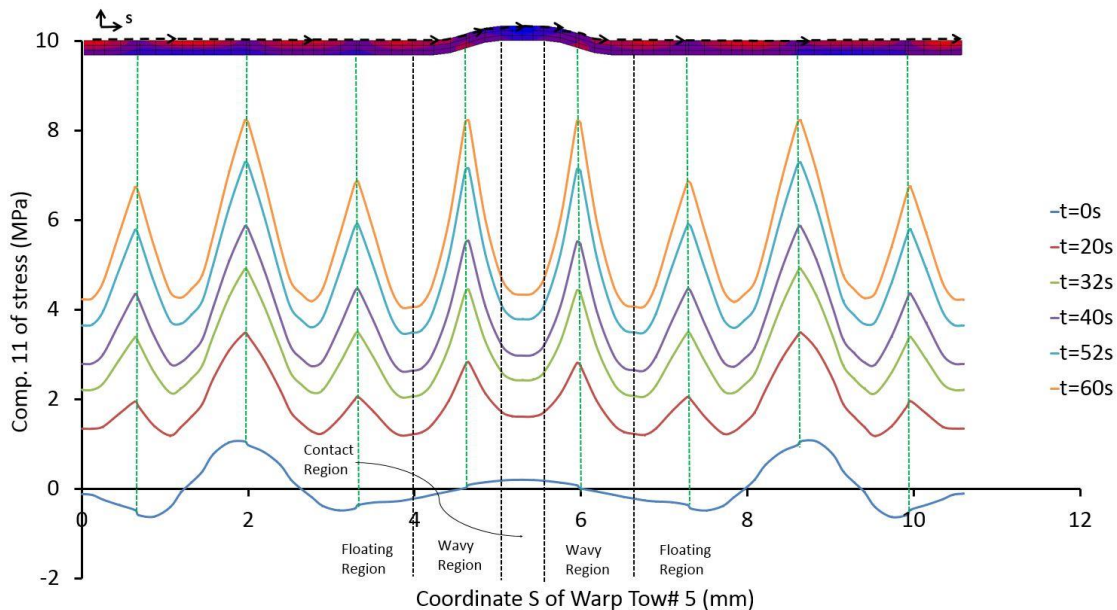


Figure 108. Distribution of component 12 of stress (σ_{12}) for warp tow#5 at different loading times under isothermal condition of 80°C

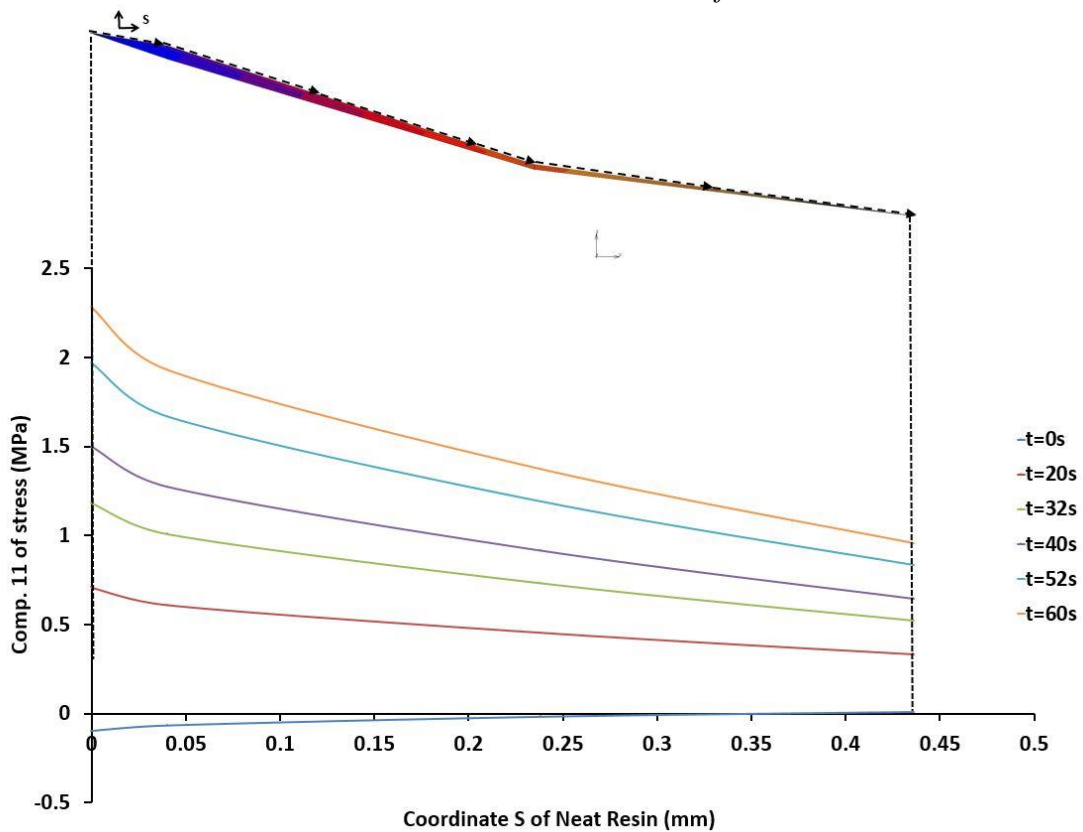


Figure 109. Distribution of component 12 of stress (σ_{12}) for neat resin located between interlaced tows at different loading times under isothermal condition of 80°C

7.1.3.2 Stress Relaxation

From the numerical results, component 12 of stress was observed to be relaxing more in the fill tow as compare with warp. Also, regions closer to the undulation relaxes more than the other regions in the fill tow as illustrated in Figure 110.

In case of warp tow, contact region of fill tow relaxes more than the other region as shown in Figure 111. Peak stress of component 12 was observed in the gap region of floats located next to the undulation of both fill and warp tow.

Once again, stress distribution of selected resin layer shows that gap region of resin relaxes more than the region of resin located in between interlaced tows as shown in Figure 112.

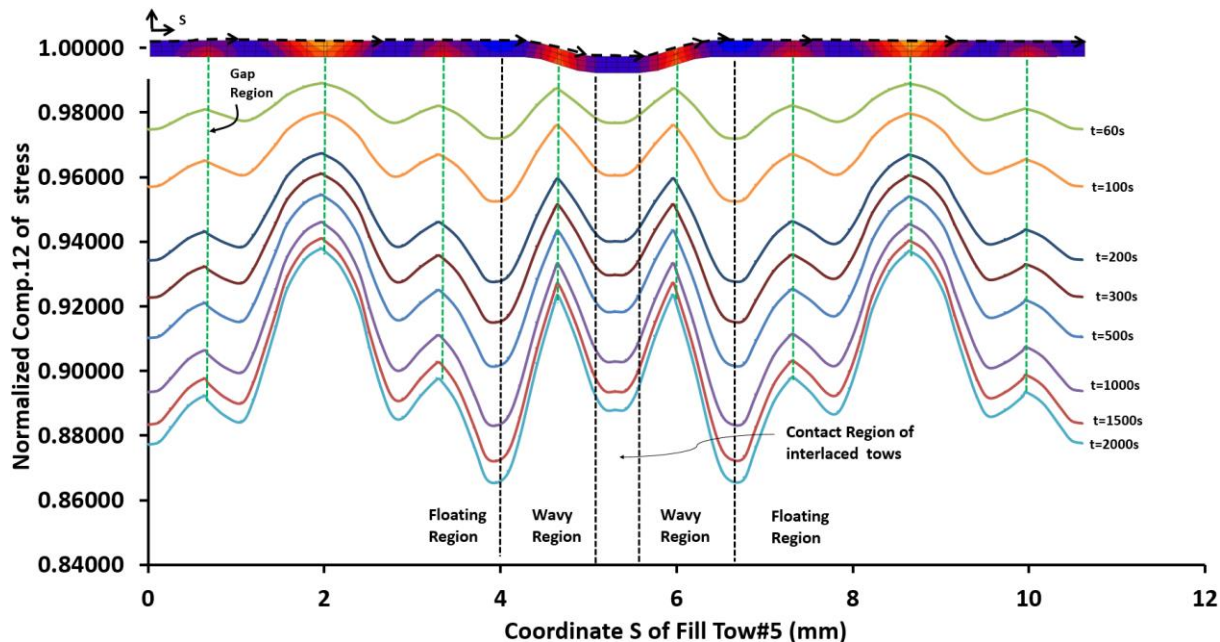


Figure 110. Distribution of normalized component 12 of stress (σ_{12}) for fill tow#5 at different relaxation times under isothermal condition of 80 °C (Base : Peak stress of every increment)

Note: Base curve is shifted by 0.1 MPa to show the general trend of initial stress distribution

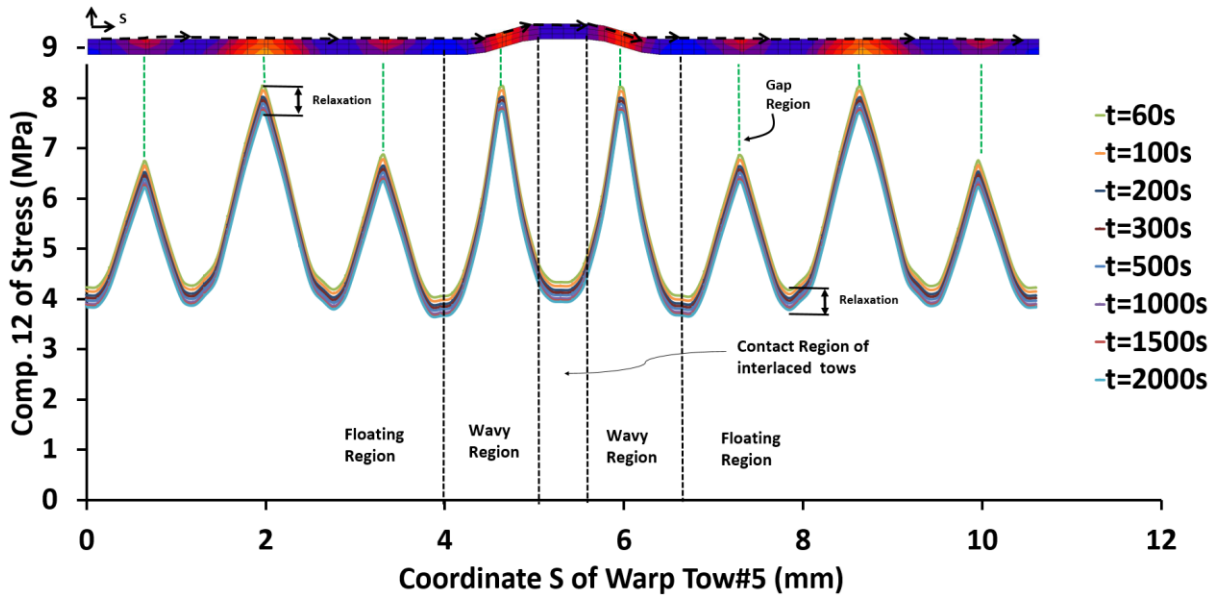


Figure 111. Distribution of component 12 of stress (σ_{12}) for fill tow#5 at different relaxation times under isothermal condition of 80°C (Base : Peak stress of every increment)

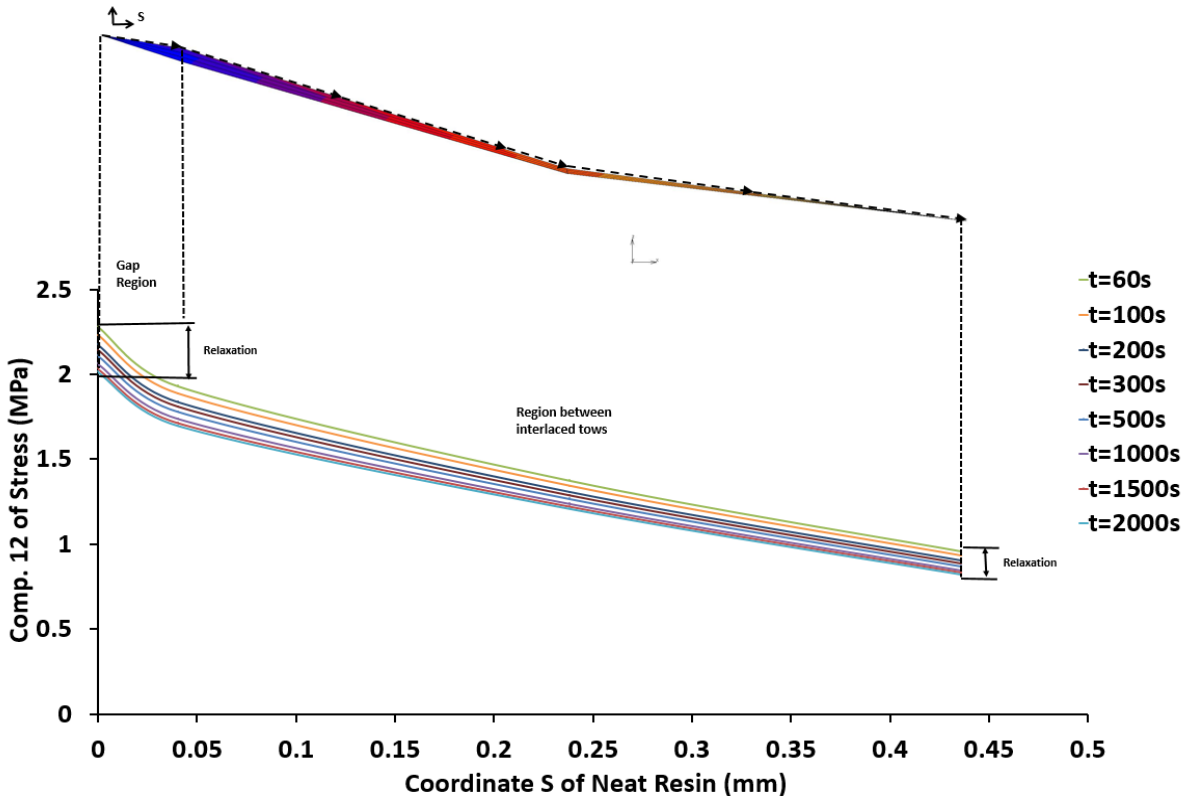


Figure 112. Distribution of component 12 of stress (σ_{12}) for neat resin located between interlaced tows at different relaxation times under isothermal condition of 80°C

7.1.3.3 Peak stress regions

In both fill and warp tows , peak stress of component 12 lies in the interlaced region, where both tows crosses perpendicular to each other. Therefore, one of the node was selected to investigate all the components of stress in both fill and warp tows as shown in Figure 113. At 80 °C, relaxation was observed from the components 22, 12 and 31 of stress in the fill tows as a function of time as shown in Figure 114. In contrast, components 11, 12 and 23 of stress in the warp tows display relaxation with respect to time as shown in Figure 116. With increase in temperature, relaxation in both fill and warp tows was observed to be dominated by component 12 of stress and it increases from 5% to 16% as illustrated in the Figure 115 and Figure 118. In case of warp tow, at 160 °C component 33 of stress shows relaxation by 3% as shown in Figure 117.

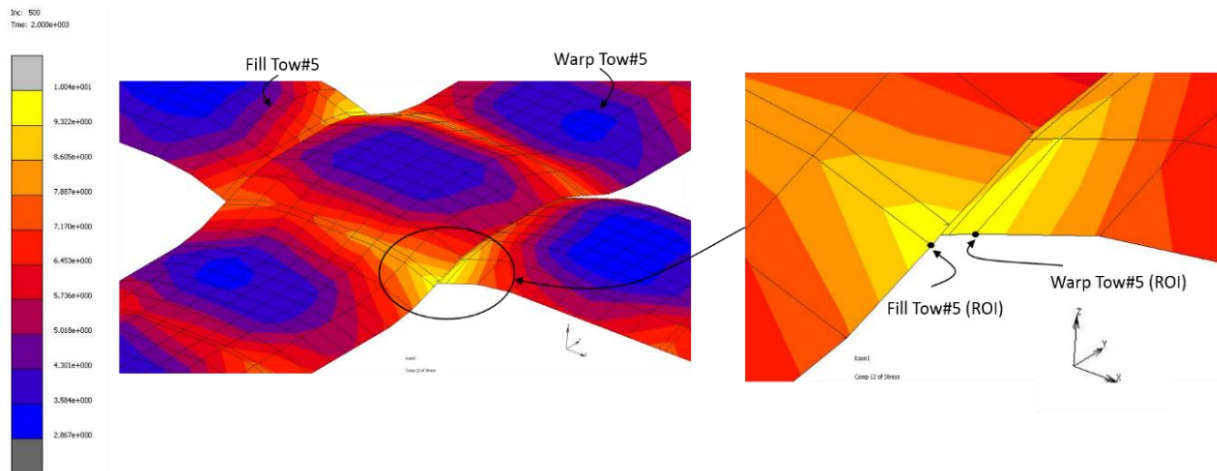


Figure 113. Region of Interest (ROI) from fill and warp tow#5

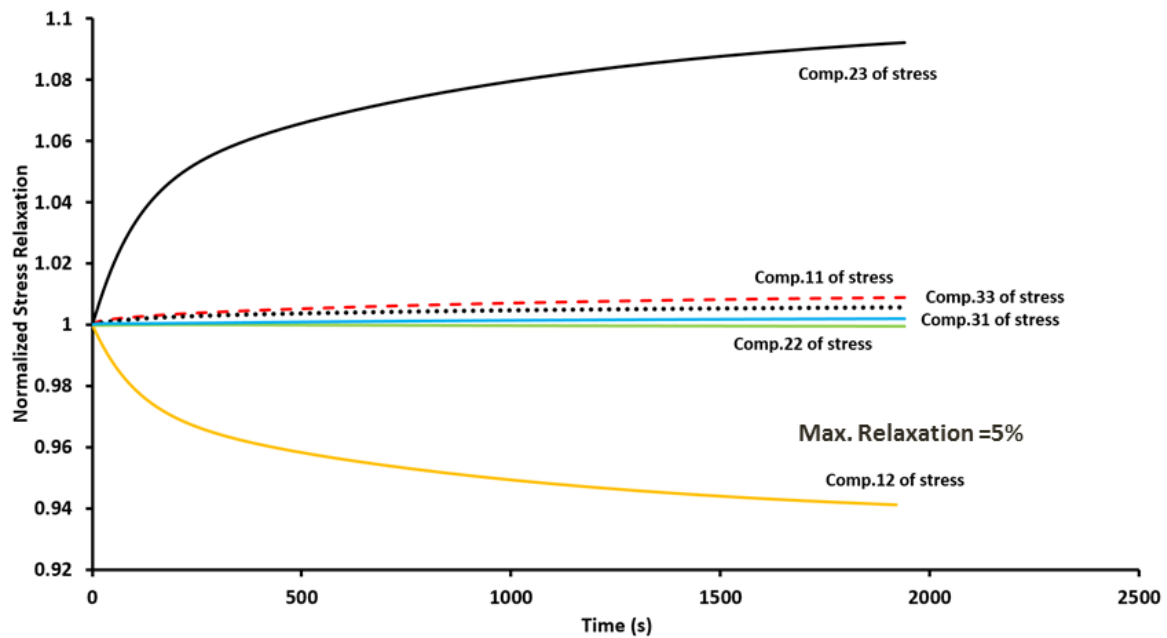


Figure 114. Comparison of all the stress components for Fill tow#5 in the region of interest (ROI) during relaxation at 80 °C

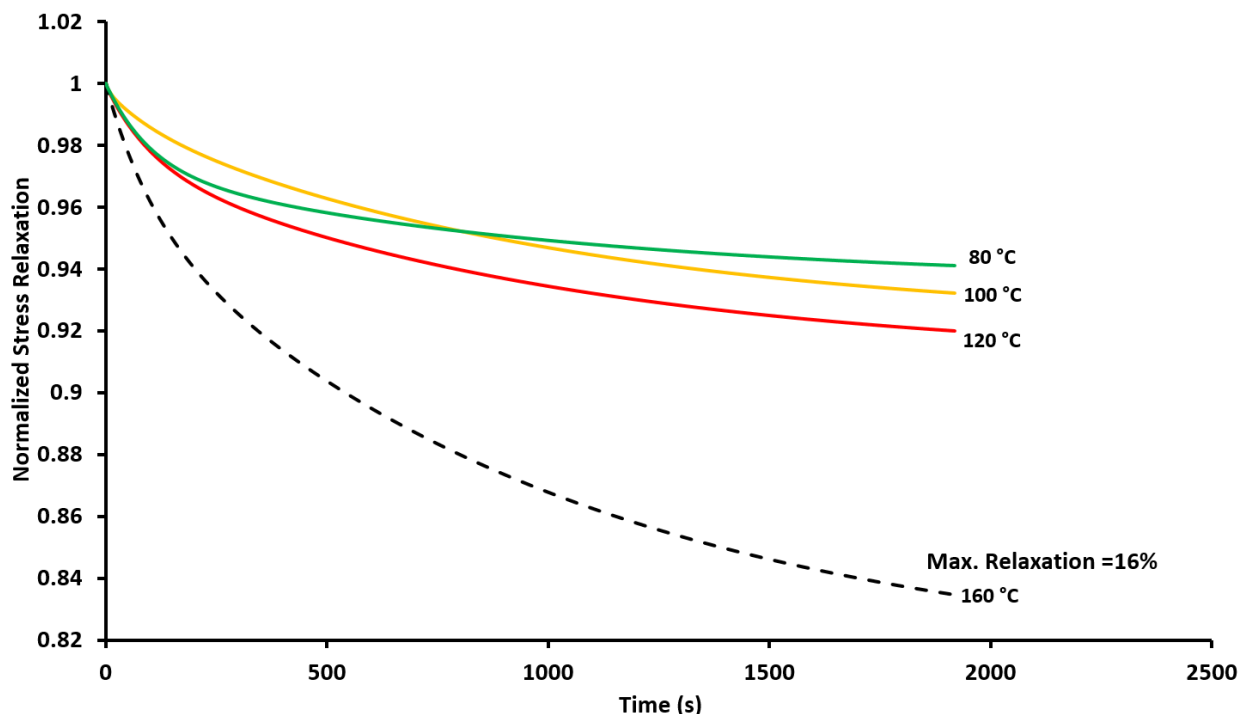


Figure 115. Relaxation curves of component 12 of stress for fill tow#5 at elevated temperatures

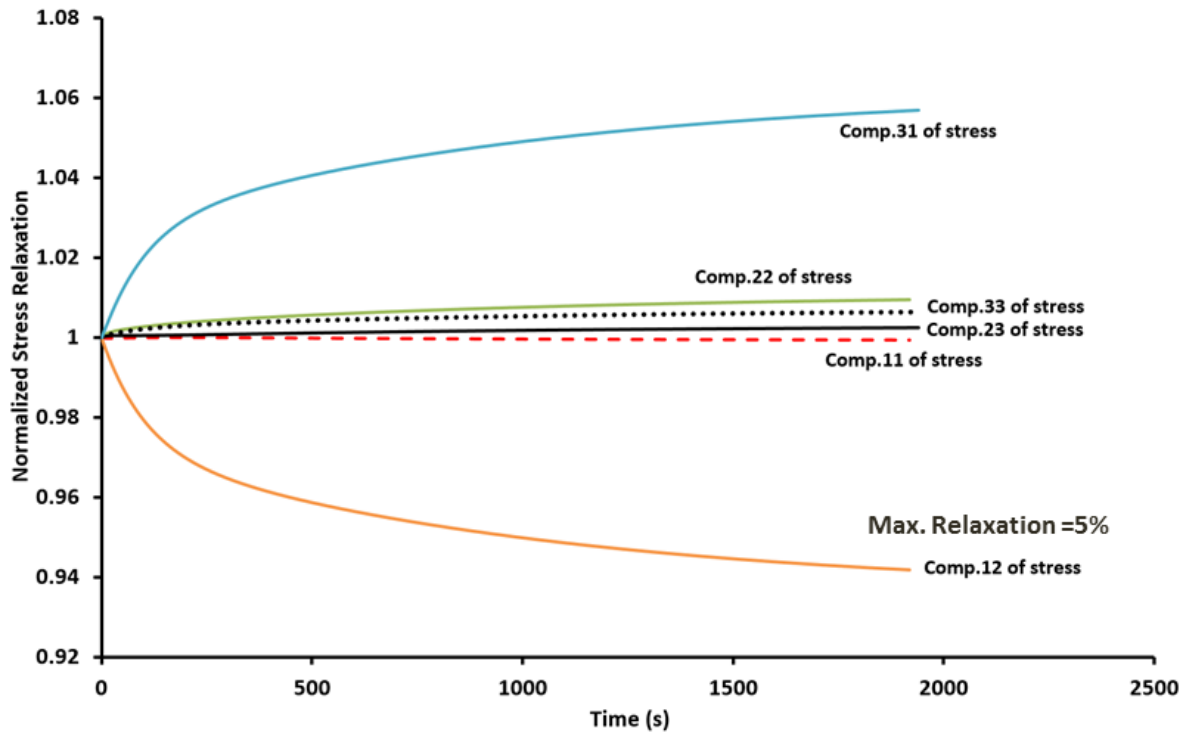


Figure 116. Comparison of all the stress components for warp tow#5 in the region of interest (ROI) during relaxation at 80 °C

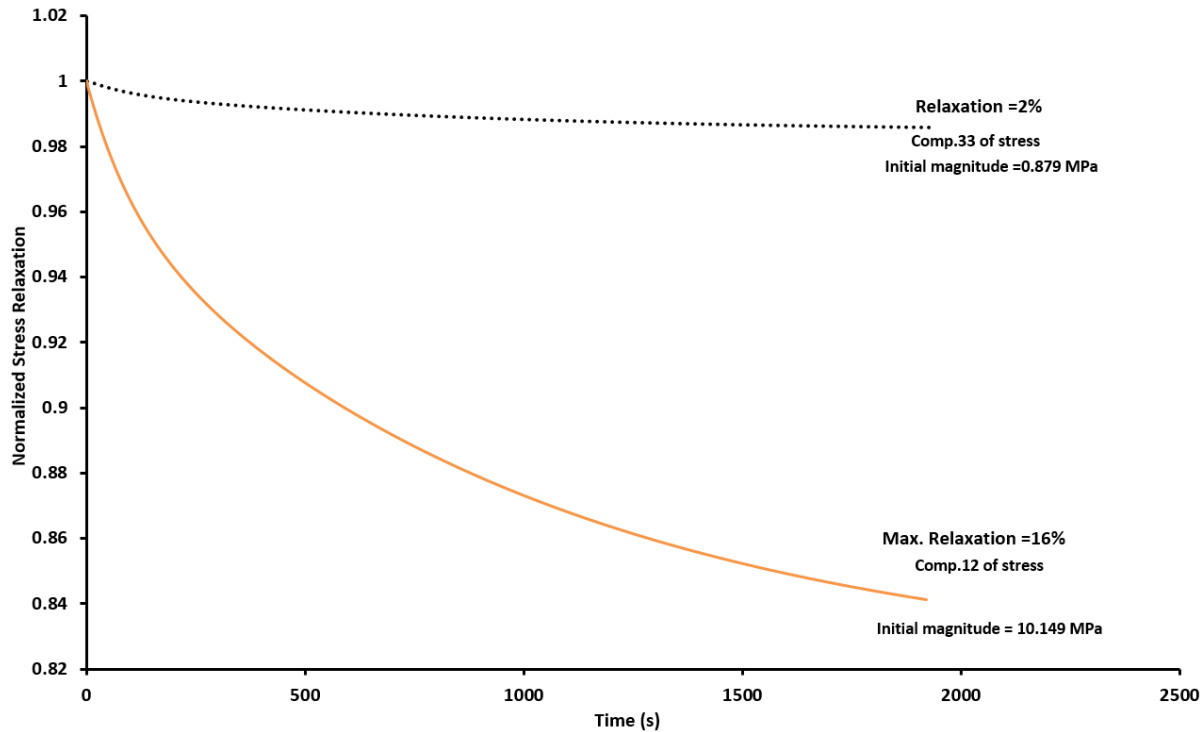


Figure 117. Relaxation curves of component 33 and 12 of stresses for warp tow#5 in the region of interest (ROI) at 160 °C

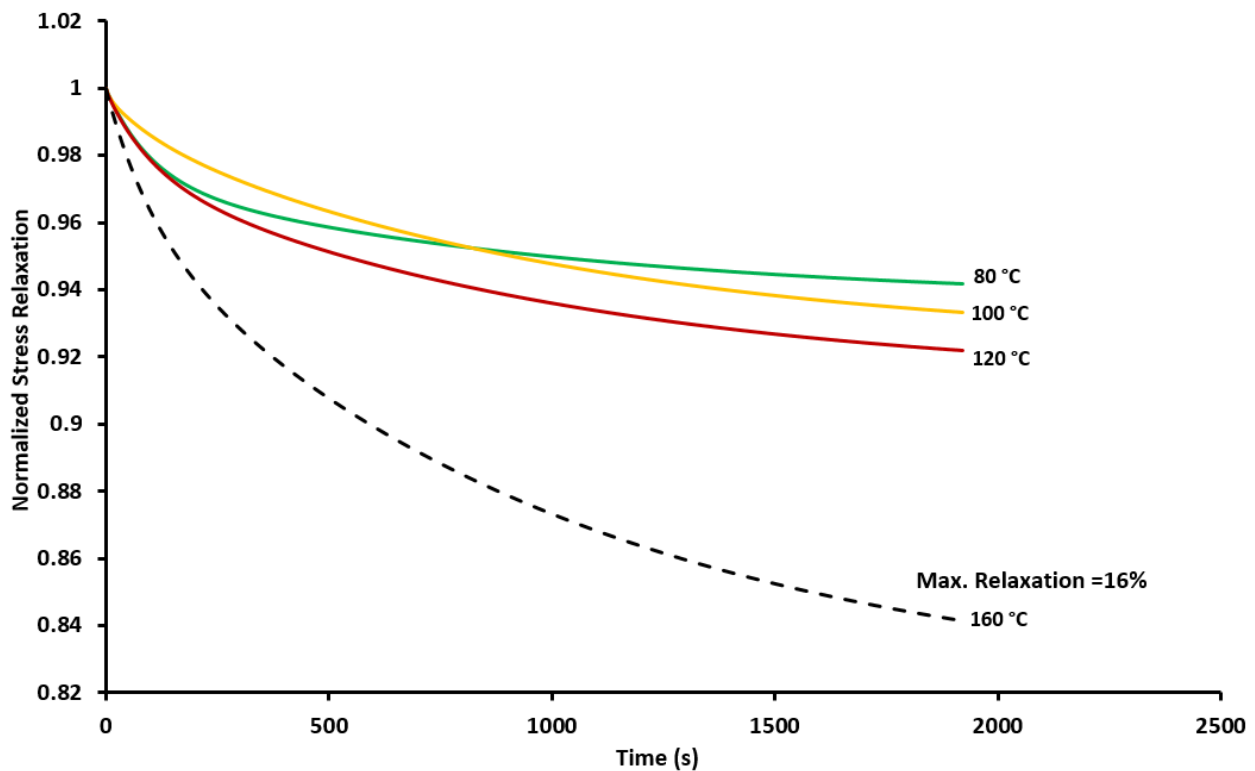


Figure 118. Relaxation curves of component 12 of stress for warp tow#5 at elevated temperatures

In case of neat resin, peak stress was observed to be located in the region of gap located between interlaced tows as illustrated in the Figure 119. During relaxation, component 11 and 23 of stresses increases with respect to time, where other components of stresses tend to relaxes more. At 80 °C, component 31 of stress relaxes by 28%, whereas component 12 of stress relaxes by 11% as shown in Figure 120. At elevated temperatures, relaxation was observed only from the components 12 and 33 of stress as illustrated in the Figure 121 and Figure 122. With increase in temperature, relaxation of component 12 of stress increases from 11% to 17%. In contrast, relaxation of component 33 of stress increases from 0.5% to 1.5%.

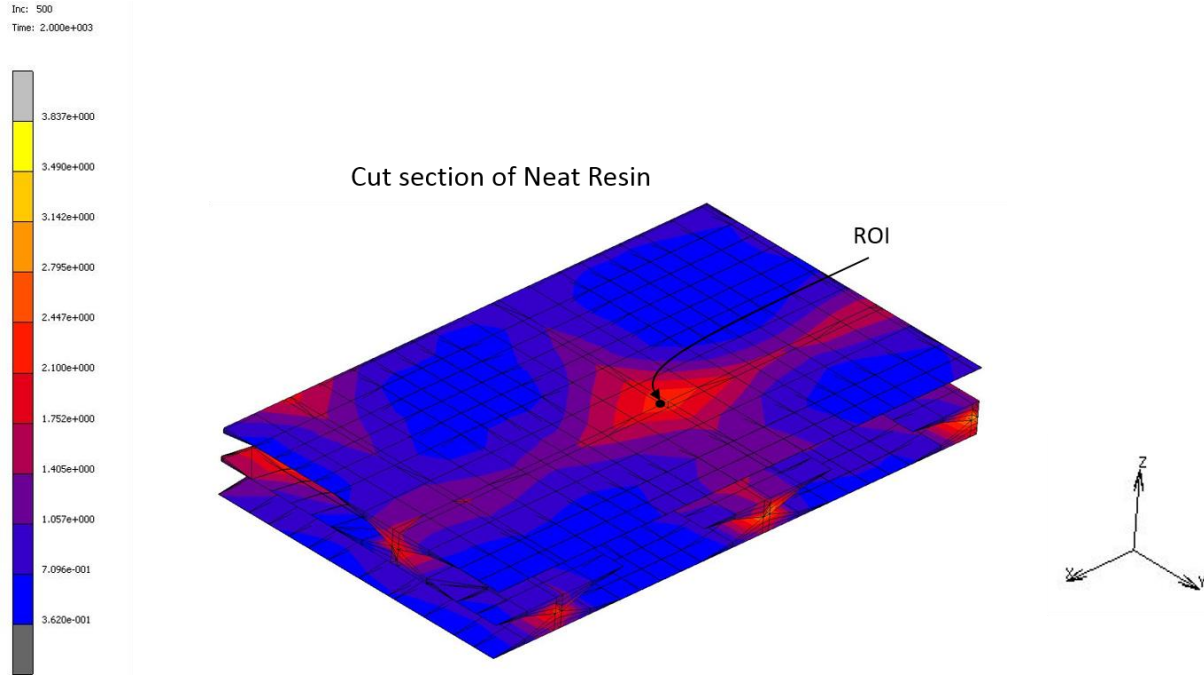


Figure 119. Region of Interest (ROI) from fill and warp tow#5

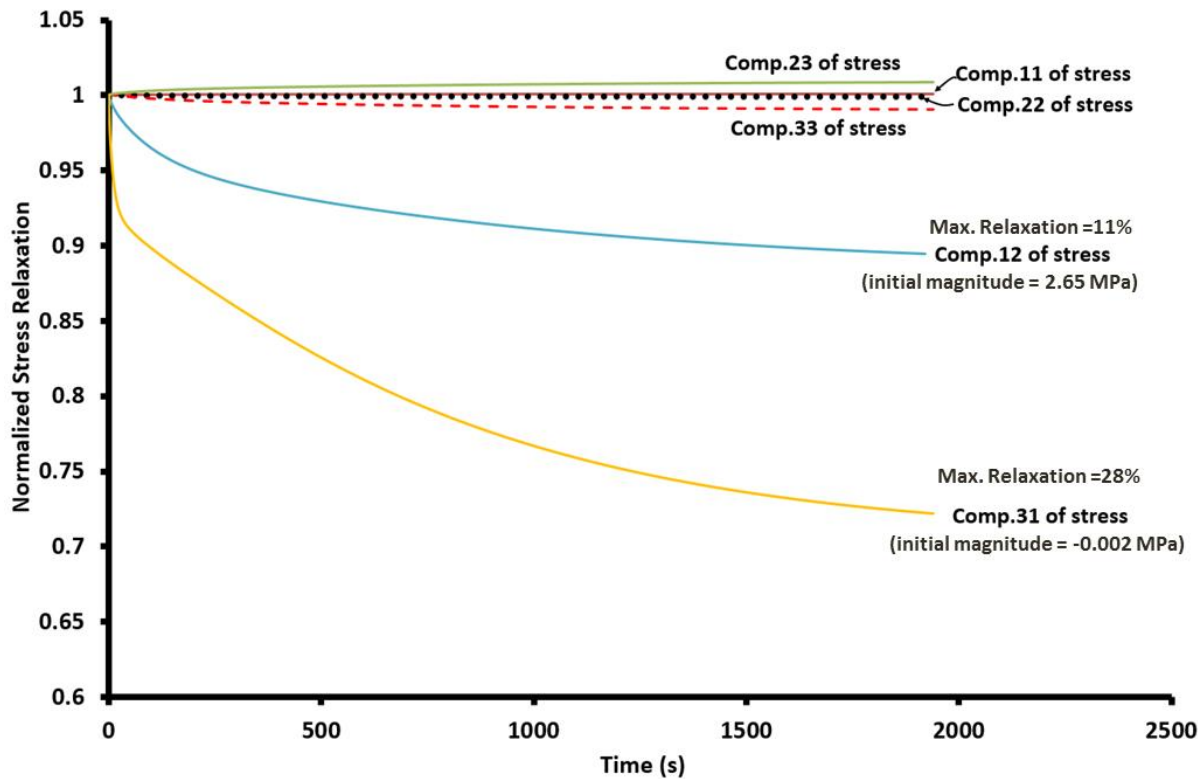


Figure 120. Comparison of all the stress components for neat region in the region of interest (ROI) during relaxation at 80 °C

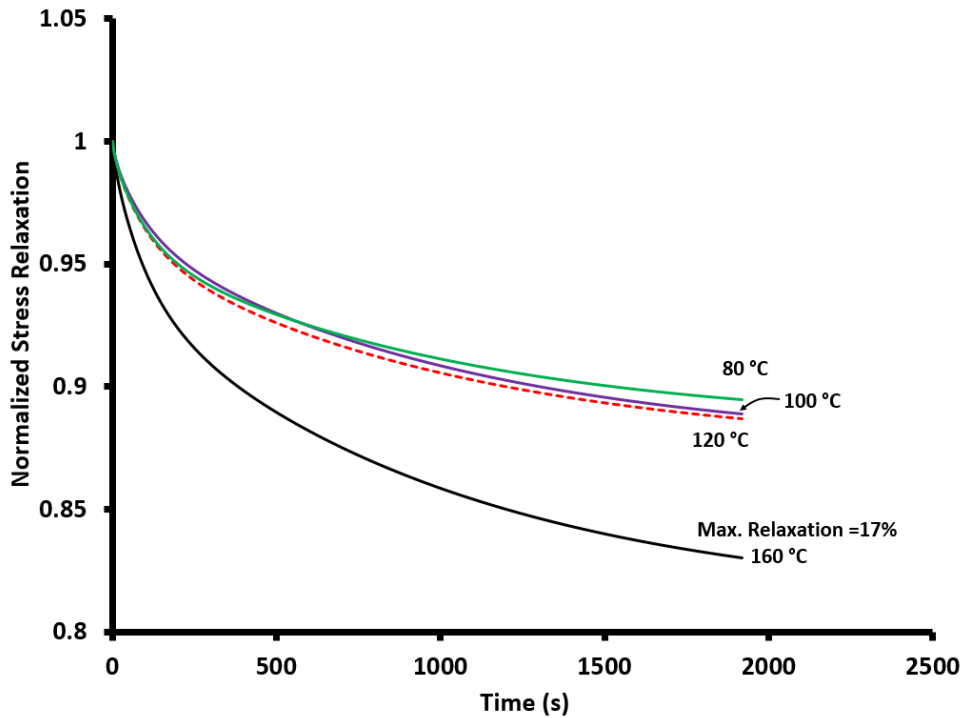


Figure 121. Relaxation curves of component 12 of stress for warp tow#5 at elevated temperatures

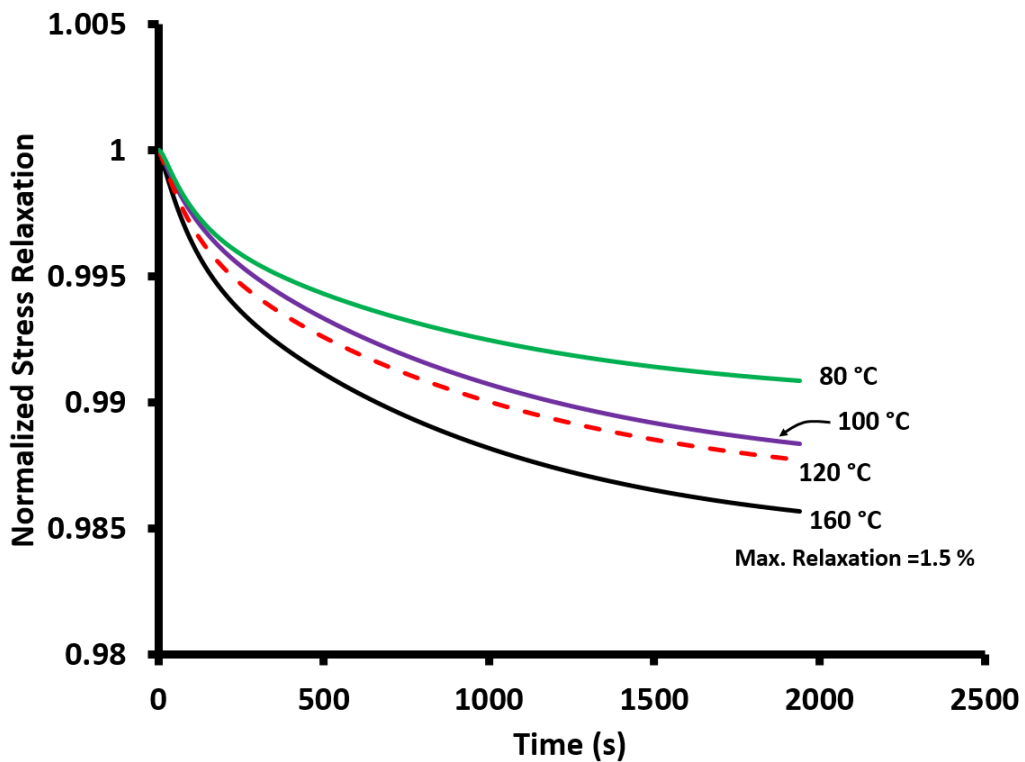


Figure 122. Relaxation curves of component 33 of stress for warp tow#5 at elevated temperatures

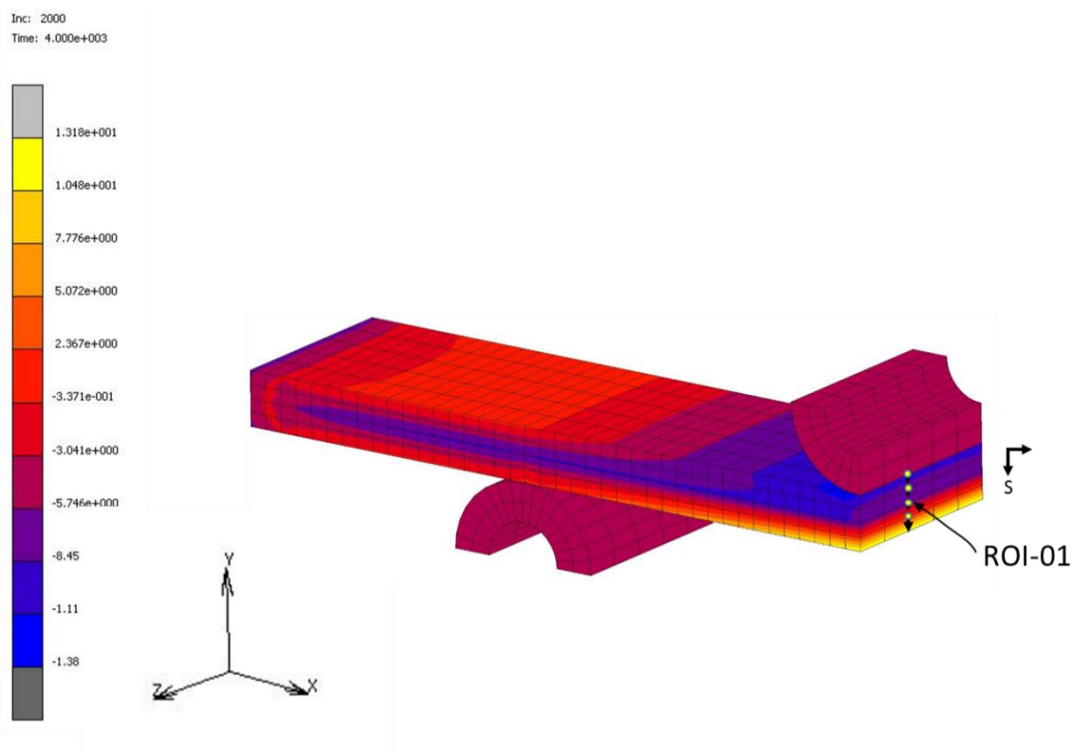
Overall under in-plane shear, stress relaxation behavior of 5320-8HS woven composite was observed to be dominated in the gap region of neat resin.

7.2 Macromechanical Analysis under flexural loading

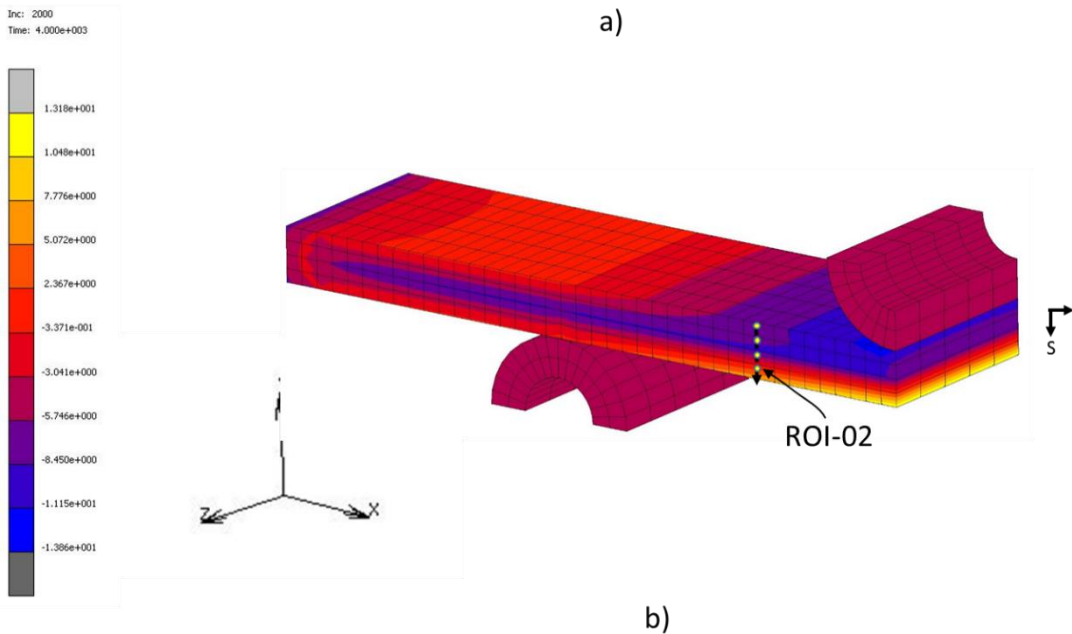
In addition to microstructural analysis, predicted relaxation response of the unit cell was implemented in the half symmetry laminate model of 3-point bending and analyzed with similar load case and stacking sequence of real time experiments. Stress distribution in the laminate was investigated by means of path plot in the selected regions (ROI-01 and ROI-02). Relaxation response of laminate model was analyzed for following two cases.

7.2.1 Case 1: [0/90]_s

Laminate model with stacking sequence of [0/90]_s was analyzed in the regions as shown in Figure 123. Relaxation curves for the component 11 and 12 of stress was studied in the following figures (i.e., from Figure 78 to Figure 84). In both of these selected locations, component 12 of stress relaxes more than the component 11 of stress. As we move from top to bottom of laminate model, component 12 of stress was observed to relaxing more in the bottom of the laminate in the region located below the loading nose. As we move away from the loading nose, this transverse shear was observed to be relaxing more in the middle of laminate as illustrated in the Figure 126 and Figure 127.



a)



b)

*Figure 123. Region of interest (ROI) in the laminate model [0/90]s a) Below loading nose b)
4.5mm away from loading nose*

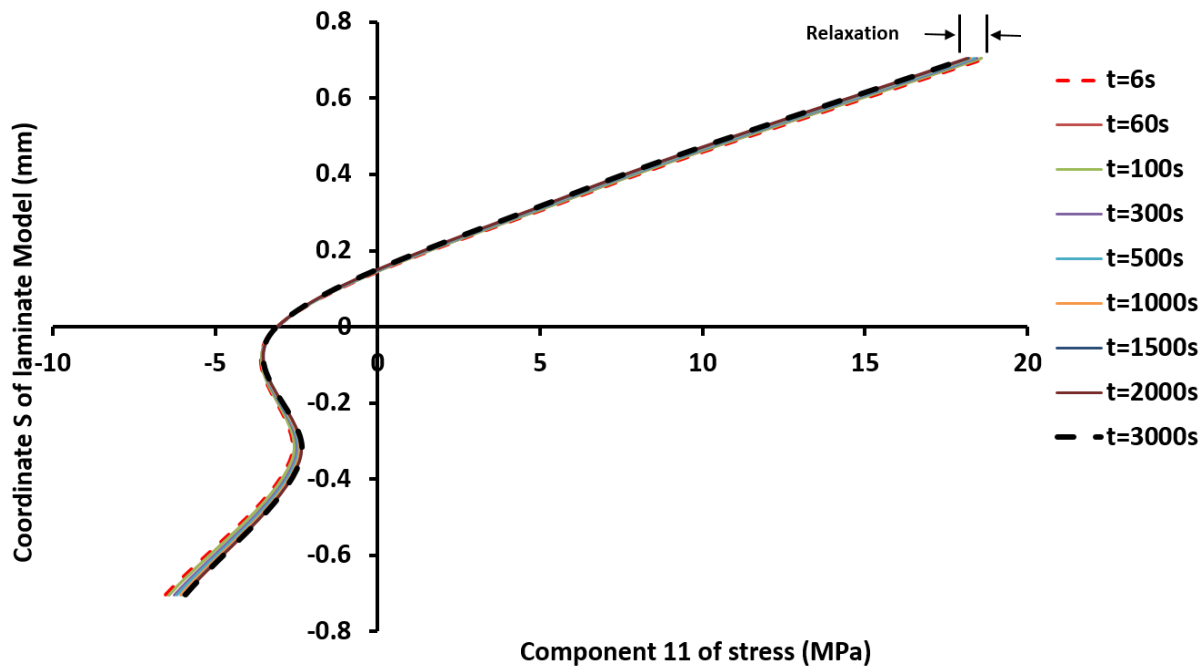


Figure 124. Relaxation curves of component 11 of stress for laminate model [0/90]s at different relaxation times under isothermal condition of 160 °C (ROI-01)

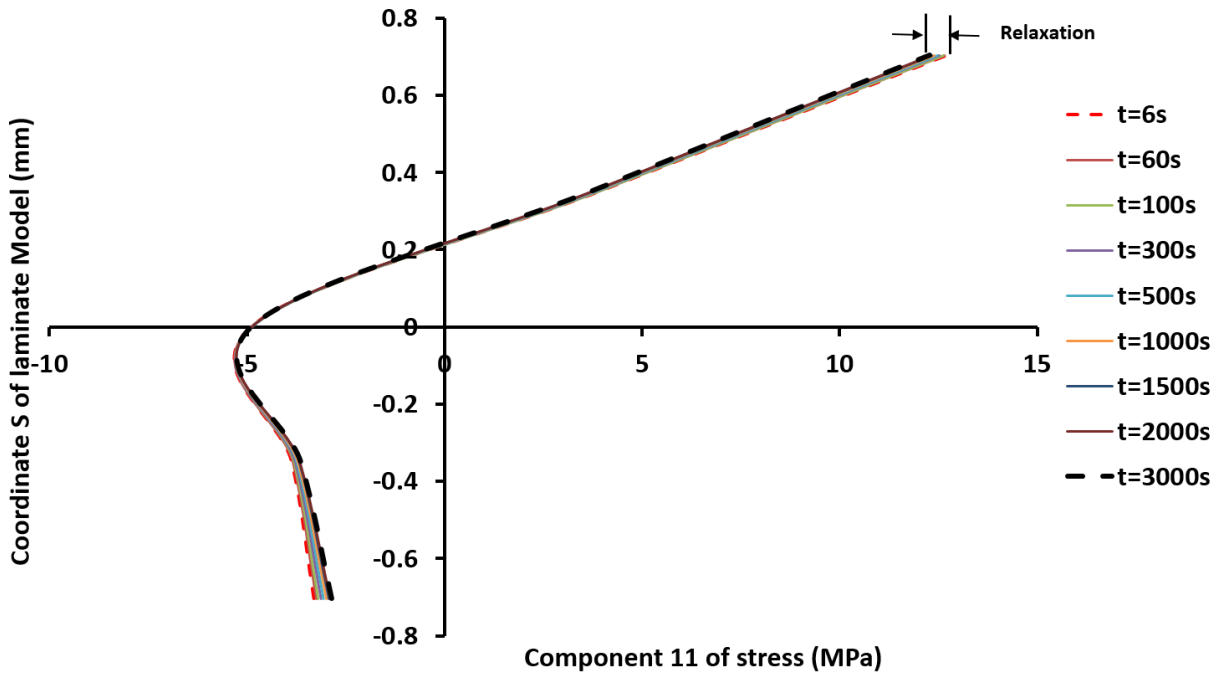


Figure 125. Relaxation curves of component 11 of stress for laminate model [0/90]s at different relaxation times under isothermal condition of 160 °C (ROI-02)

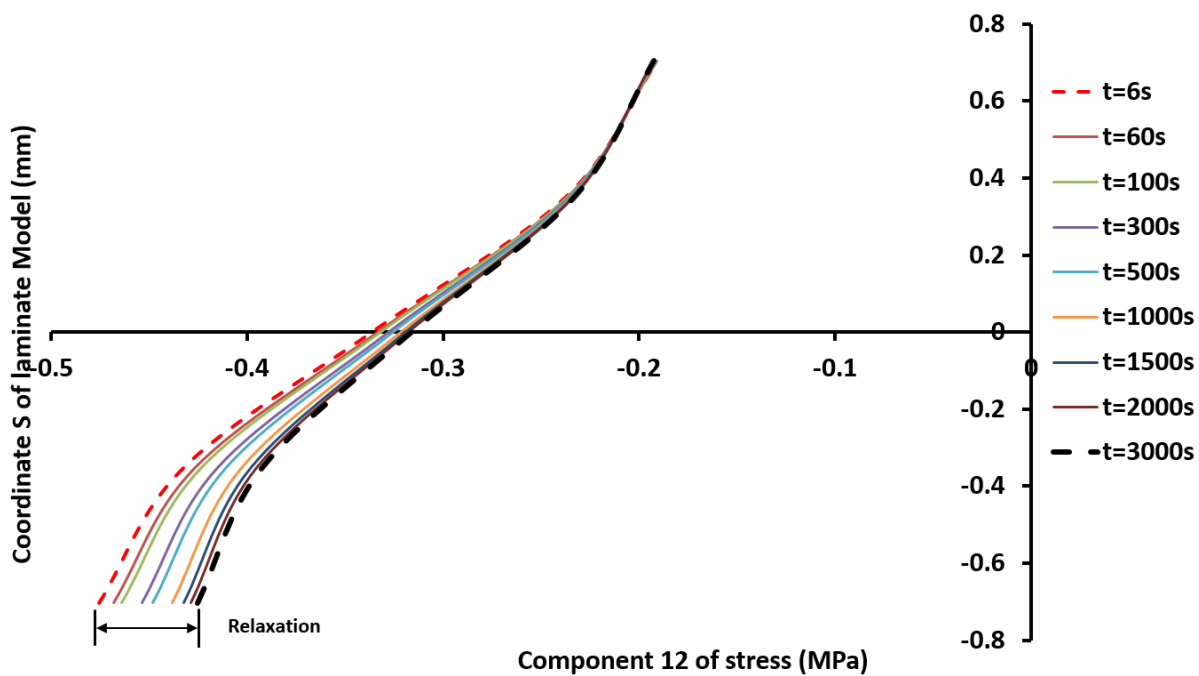


Figure 126. Relaxation curves of component 12 of stress for laminate model [0/90]s at different relaxation times under isothermal condition of 160 °C (ROI-01)

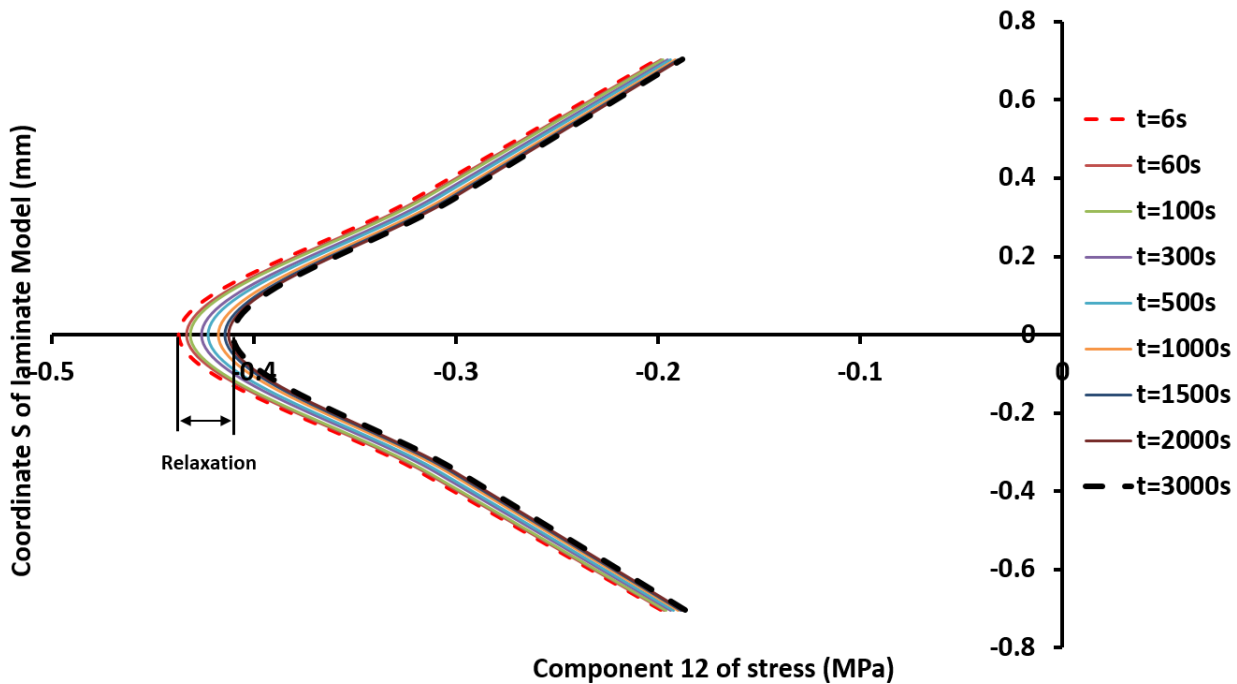


Figure 127. Relaxation curves of component 12 of stress for laminate model [0/90]s at different relaxation times under isothermal condition of 160 °C (ROI-02)

7.2.2 Case 2: $[\pm 45]_s$

Laminate model with stacking sequence of $[\pm 45]_s$ was analyzed in the regions as shown in Figure 129. Relaxation curves for the components of 11, 12 and 31 stresses were studied in the following figures (i.e., from Figure 130 to Figure 135). In both of these selected locations, component 12 of stress relaxes more as compare with other component of stresses. Similar to $[0/90]_s$ stacking sequence, below the region of loading nose, component 12 of stress was observed to relaxing more along the thickness of the laminate as shown in Figure 131. As we move away from the loading nose, component 11 of stress located at the top and bottom of laminate was observed to be relaxing more than the other components as illustrated in the Figure 133. Among all, component 31 of stresses located at both regions relaxes to a least amount as illustrated in the Figure 132 and Figure 135.

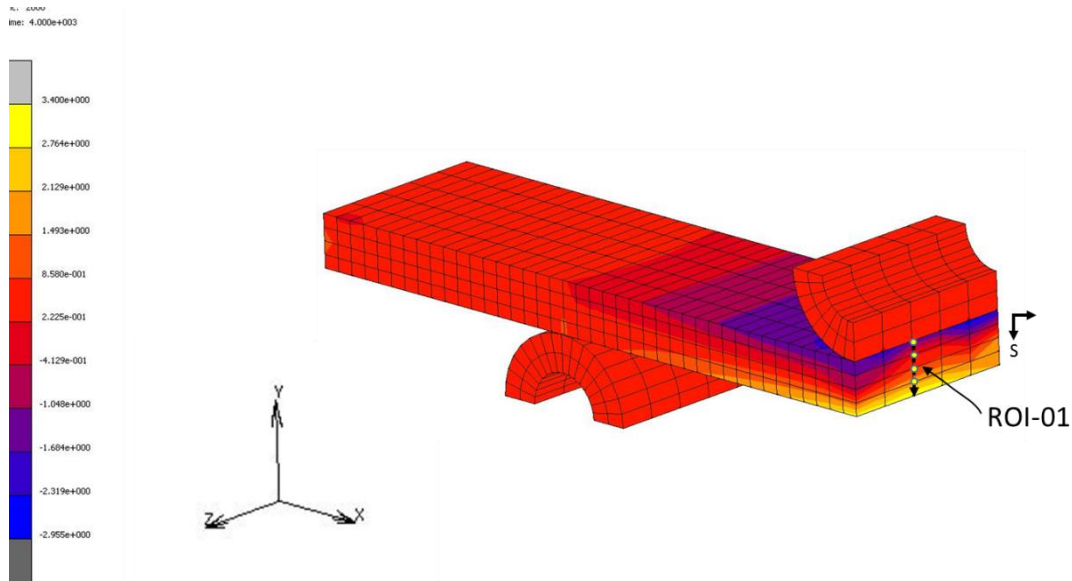


Figure 128. Region of interest (ROI) in the laminate model $[\pm 45]_s$ below loading nose

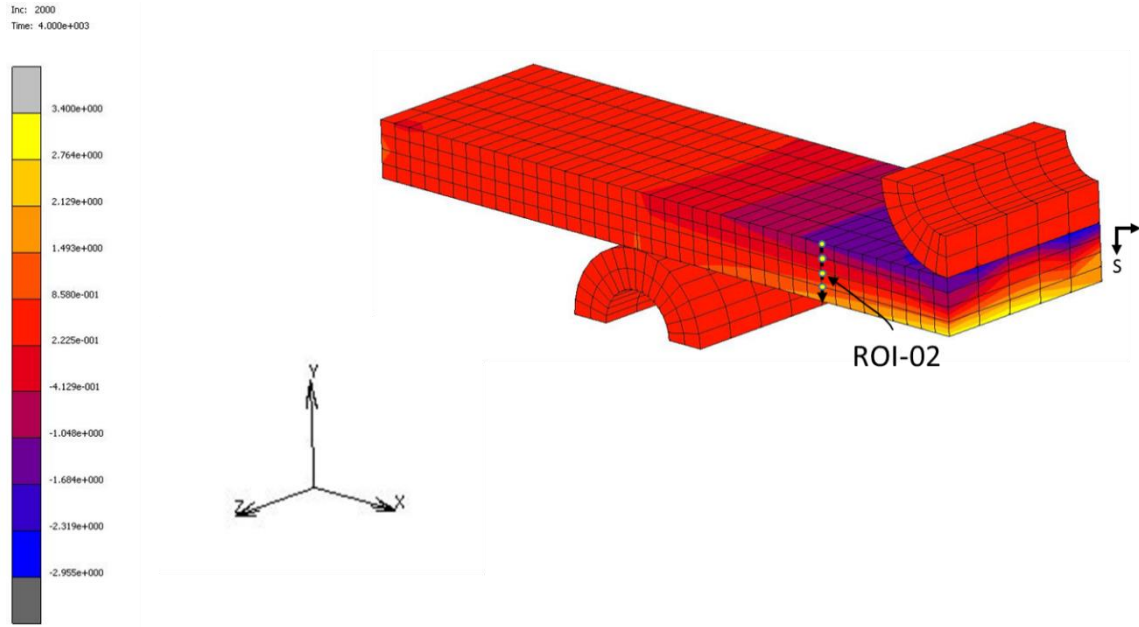


Figure 129. Region of interest (ROI) in the laminate model [$\pm 45^\circ$]s 4.5mm away from loading nose

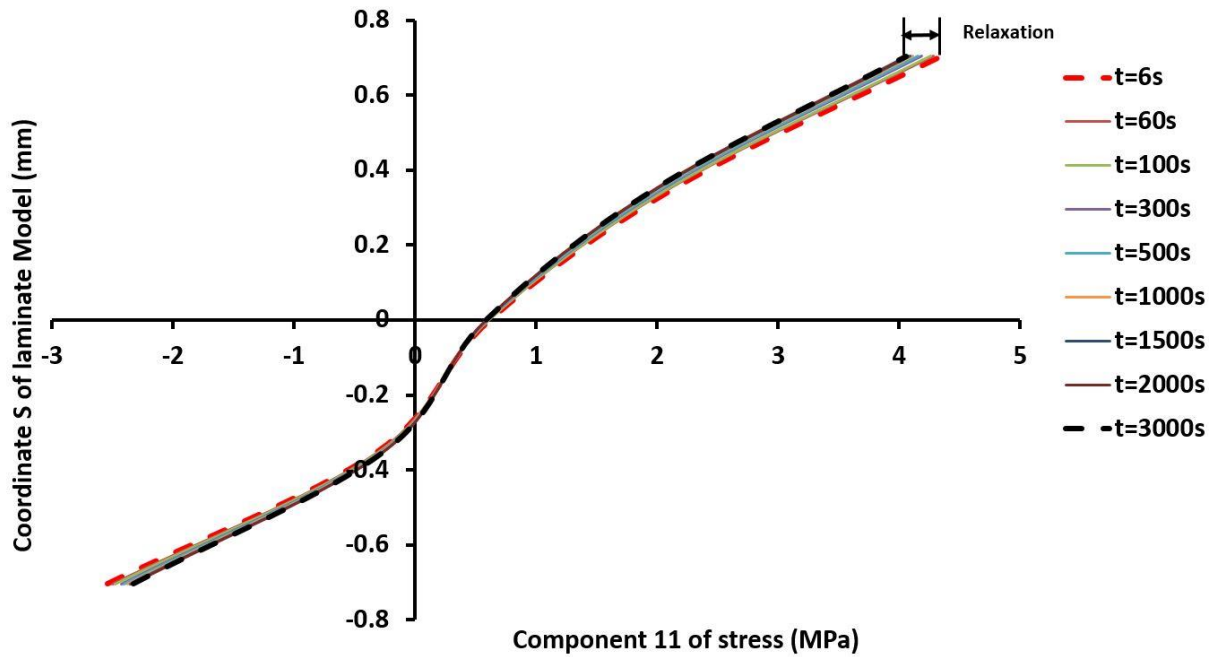


Figure 130. Relaxation curves of component 11 of stress for laminate model [$\pm 45^\circ$]s at different relaxation times under isothermal condition of 160 °C (ROI-01)

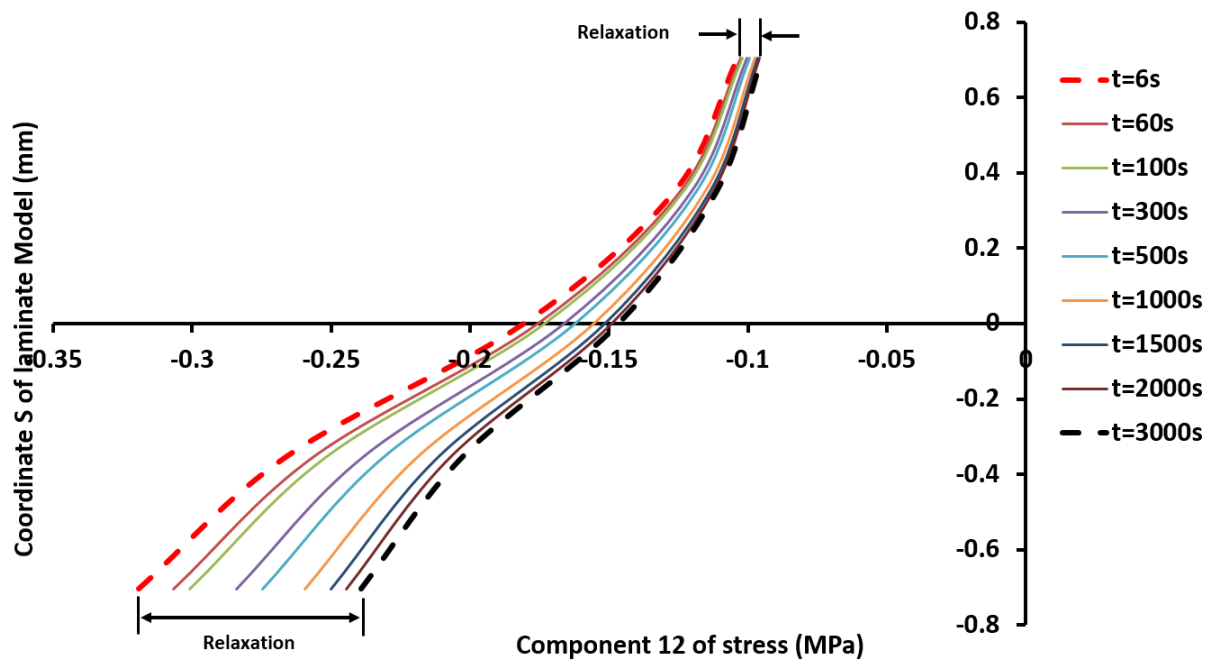


Figure 131. Relaxation curves of component 12 of stress for laminate model [±45]s at different relaxation times under isothermal condition of 160 °C (ROI-01)

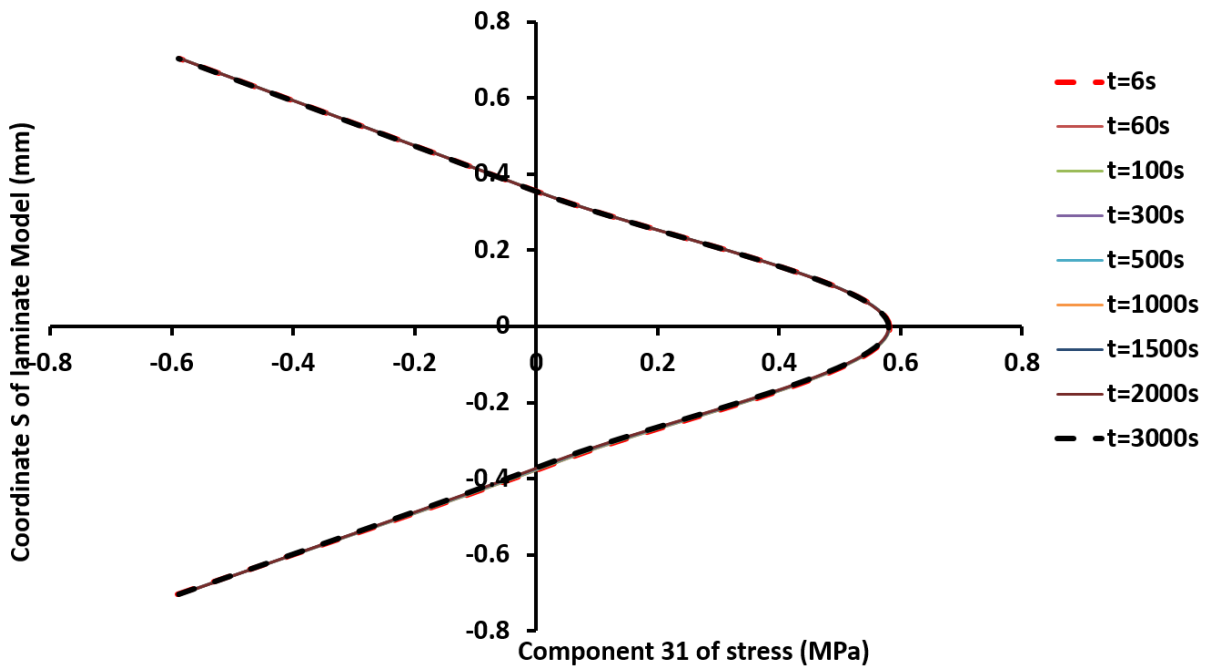


Figure 132. Relaxation curves of component 31 of stress for laminate model [±45]s at different relaxation times under isothermal condition of 160 °C (ROI-01)

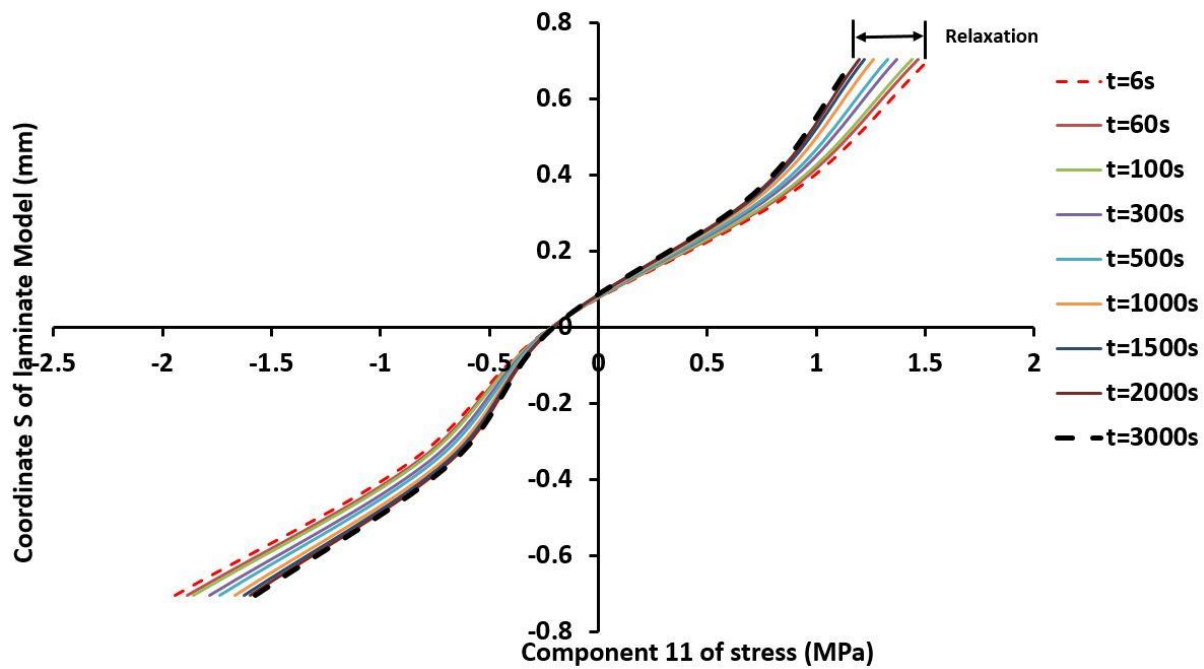


Figure 133. Relaxation curves of component 11 of stress for laminate model [±45]s at different relaxation times under isothermal condition of 160 °C (ROI-02)

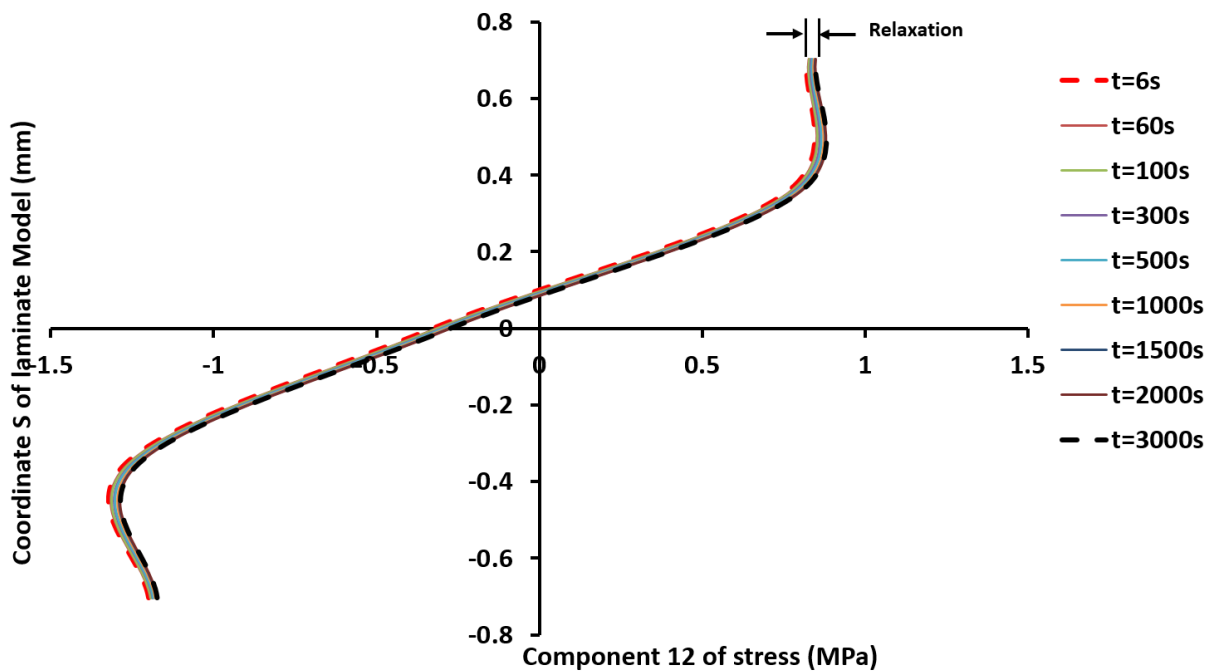


Figure 134. Relaxation curves of component 12 of stress for laminate model [±45]s at different relaxation times under isothermal condition of 160 °C (ROI-02)

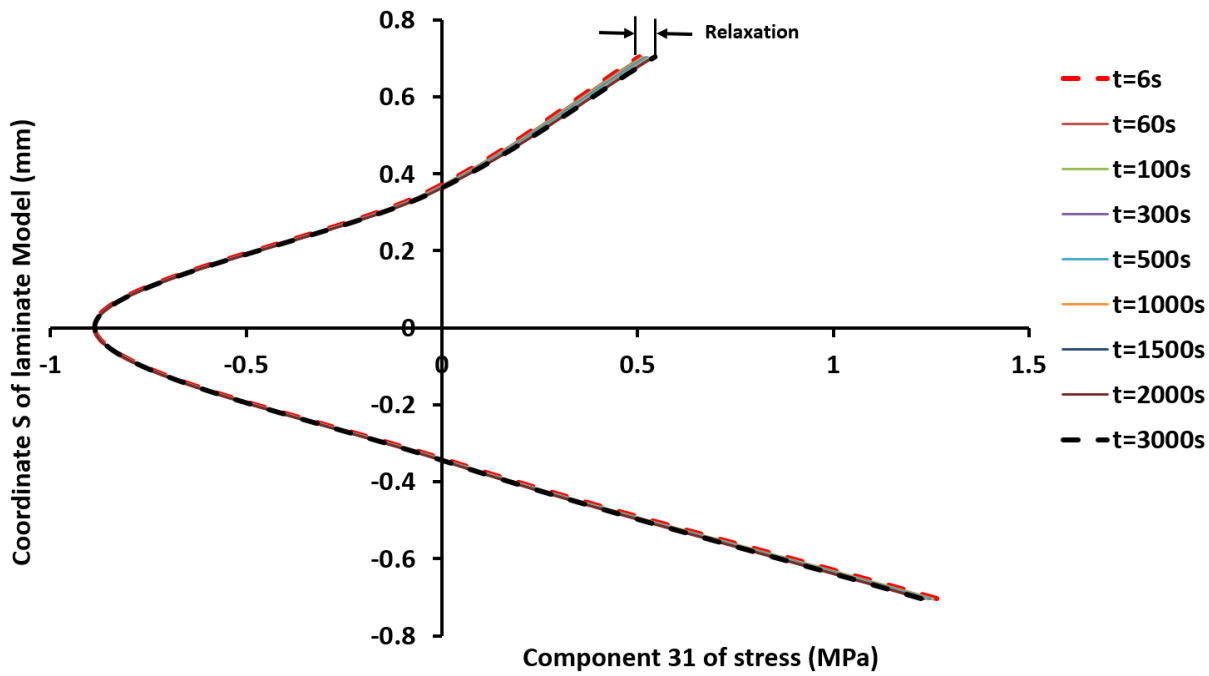


Figure 135. Relaxation curves of component 31 of stress for laminate model [±45]s at different relaxation times under isothermal condition of 160 °C (ROI-02)

CHAPTER 8

CONCLUSIONS AND FUTURE WORK

8.1 Conclusion

The main objective of this thesis is to predict the stress relaxation behavior of woven composite (i.e., 5320-8HS) and investigate the influence of weave architecture using finite element based micromechanics. Also, present study focuses to capture the combined effect of both floats and undulation of fabric composite. Material system used for this present study is 5320-8HS (carbon/epoxy woven composite) and 5320-1 EO epoxy resin. Stress relaxation analysis using micromechanics approach involves five following steps

- Stress relaxation of neat resin
- Development of micromechanics model
- Finite Element Analysis
- Validation of results
- Micromechanical analysis

First, 5320-1 pure epoxy resin specimens were fabricated with a developed methodology of specimen preparation. Stress relaxation testing was performed on the fabricated specimens at elevated temperatures under tension and 3-point bending using dynamic mechanical analyzer. In addition, Strain sweep and glass transition temperature testing also performed to ensure applied strain falls within linear viscoelasticity region (LVR) and instrument safety.

From the stress relaxation data, relaxation curves of every incremental temperature were manually shifted to calculate shift factor and generated master curve to capture overall relaxation

response of neat resin at elevated temperatures. Then, Prony series and William–Landel Ferry shift function were calculated from the experimental data for numerical analysis.

Second, from the microscopy of potted 5320-8HS specimens, design parameters to model geometry of microstructure were measured. Then, with help of calculated design parameters and developed mathematical functions, geometry of fabric was designed in CATIA V5 design software. Then, imported geometry of fabric composite was meshed using sub-cell modeling approach.

Furthermore, discretized model of 5320-8HS unit cell was imported to the commercial MSC MARC FEA software for analysis. Utilizing the thermomechanical properties of tows predicted from the hexagonal array model and neat resin, stress relaxation analysis was performed on the 8-harness unit cell model. The model was subjected to appropriate periodic boundary conditions to recreate the overall relaxation response of 5320-8HS woven composite. Besides, half symmetry laminate model of 3-bending was developed and their flexural relaxation response was analyzed to validate experimental results.

Moreover, stress relaxation experiments were performed on 5320-8HS woven composite under tension and 3-point bending to validate the model predictions. Specimens were tested for different stacking sequence and orientation. Problems associated with uniaxial tension were listed out. Then, both numerical and experimental results of tension and 3-point bending were compared.

Micromechanical analysis was performed on the microstructure of woven fabric composite to investigate the stress distribution and relaxation of stress components in the selected region of microstructure. This in turn, helps to study and identify the heterogeneous

state of stress and their relaxation behavior as a function of time. In addition, relaxation of component 12, 11 and 31 was also examined in the laminate model.

The present study shows good correlation between experimental and numerical results. Therefore, by knowing constituent properties it is possible to predict overall stress relaxation response of fabric composite that incorporates both undulations and floats. In case of axial load, relaxation response of stress components was observed to be varying with temperature. But in case of shear load, at all temperatures relaxation response was observed to be dominated by the component 12 of stress.

The current study also concludes that experimentally determined stress relaxation behavior of 5320-8HS is basically a combination of stress relaxation and creep strain development due to end effect of clamping wedges. To analyze axial behavior, it is always better to perform creep experiments with proper consideration of temperature tolerances of instruments.

8.2 Future Study

The present work raises a significant number of questions which need to be answered prior to making sweeping remarks on the stress relaxation of fabrics. For further accuracy and clear understanding in the mechanics of microstructure following recommendations are suggested:

- Thermomechanical properties of the fiber bundles need to be adjusted with help of unidirectional composite with same resin system.
- Appropriate clamping setup need to be designed to overcome localized stress relaxation and large CTE mismatch in the uniaxial testing of large specimens.
- Degree of cure for resin and woven needs to be considered and verified to capture the thermomechanical behavior of neat resin in the micromechanics model.

- Couple of experiments needs to be done with fresh specimens to capture the consistency of relaxation phenomena of woven composite.
- Unit cell models with varying gaps between tows and effect of varying fiber volume fraction need to be need studied.
- Unit cell need to be analyzed including the effect of process induced residual stresses.
- Influence of different loading rate needs to be studied to understand the relaxation of modulus in elastic region.
- Stress relaxation for other temperatures also needs to be investigated.
- In macromechanical analysis, component 12 of stress for $[\pm 45]_s$ stacking sequence need to be investigated further to understand its variation along the thickness.

REFERENCES

REFERENCES

- [1] Barbero, Ever J. Introduction to composite materials design. CRC press, 2010.
- [2] Anandvijay, K.R, Suresh, K.R., Kevontrez, K.J., Abhiruchika, S., "Predicting viscoelastic behavior of fabric composites using finite element based micromechanics model". --In Proceedings: 12th Annual Symposium on Graduate Research and Scholarly Projects. Wichita, KS: Wichita State University, p. 113 (2016).
- [3] Aliabadi, M.H., "Woven composites". Computational and Experimental methods in structures- vol.6. London, UK: Imperial College Press, 2015, ISBN-9781783266173.
- [4] Chawla, Krishan. Fibrous materials. Cambridge university press, 2016.
- [5] Das, Rony. "Stress relaxation behavior of carbon fiber-epoxy prepreg composites during and after cure." MS Thesis, Wichita State University, 2012.
- [6] Chen, Yu. "Finite Element Micromechanical Modeling of Glass Fiber/Epoxy Cross-ply Laminates" MS Thesis, University of Alberta, 2000.
- [7] Jones, Robert M., (1999). Jones/Mechanics of Composite Materials - Materials Science & Engineering Series (2nd Edition). Taylor & Francis.
- [8] Bergstrom, Jorgen S. Mechanics of solid polymers: theory and computational modeling. William Andrew, 2015.
- [9] Strong, A. Brent. (2008). Fundamentals of Composites Manufacturing - Materials, Methods, and Applications (2nd Edition). Society of Manufacturing Engineers (SME).
- [10] Findley, William N., and Francis A. Davis. Creep and relaxation of nonlinear viscoelastic materials. Courier Corporation, 2013.
- [11] Shaw, Montgomery T., and William J. MacKnight. Introduction to polymer viscoelasticity. John Wiley & Sons, 2005.
- [12] Osswald, Tim A. Menges, Georg. (2012). Material Science of Polymers for Engineers (3rd Edition) - 9. Mechanical Behavior of Polymers. Hanser Publishers.
- [13] MSC Marc 2014 r1 Reference Manual Vol. A: *Theory and User Information*, MSC. Software Corporation, Santa Ana, CA, 2014, pp 611.
- [14] Hashin, Zvi., "Viscoelastic behavior of heterogeneous media." Journal of Applied Mechanics 32.3 (1965): 630-636.

- [15] Hashin, Z. V. I. "Complex moduli of viscoelastic composites—I. General theory and application to particulate composites." *International Journal of Solids and Structures* 6.5 (1970): 539-552.
- [16] Aboudi J., "A Continuum Theory for Fiber-reinforced Elastic-Viscoplastic Composites," *Int. J. Engr. Sci.*, Vol. 20, 1982, pp. 605-621.
- [17] Yancey, R. N., and Marek-Jerzy Pindera. "Micromechanical analysis of the creep response of unidirectional composites." *Journal of Engineering Materials and Technology* 112.2(1990): 157-163.
- [18] Brinson LC, Knauss WG. Finite element analysis of multiphase viscoelastic solids. *Journal of Applied Mechanics* 1992; 59:730–7.
- [19] Barbero, E. J., and R. Luciano. "Micromechanical formulas for the relaxation tensor of linear viscoelastic composites with transversely isotropic fibers." *International Journal of Solids and Structures* 32.13 (1995): 1859-1872.
- [20] Aboudi, Jacob. "Micromechanical modeling of finite viscoelastic multiphase composites." *Zeitschrift für angewandte Mathematik und Physik ZAMP* 51.1 (2000): 114-134.
- [21] Simo, J. C., On a fully three-dimensional finite-strain viscoelastic damage model: reformulation and computational aspects. *Computer Meth. Appl. Mech. & Eng.* 60 (1987),153-173.
- [22] Fisher, F. T., & Brinson, L. C. (2001). Viscoelastic interphases in polymer-matrix composites: Theoretical models and finite element analysis. *Composites Science and Technology*, 61, 731–748.
- [23] Mori T, Tanaka K. Average stress in matrix and average elastic energy of materials with misfitting inclusions. *Acta Metallurgical* 1973; 21:571–4.
- [24] Benveniste Y. A new approach to the application of Mori–Tanaka’s theory in composite materials. *Mechanics of Materials* 1987;6:147–57.
- [25] Naik, Abhay, et al. "Micromechanical viscoelastic characterization of fibrous composites." *Journal of composite materials* 42.12 (2008): 1179-1204.
- [26] Abadi, Mohammad Tahaye. "Micromechanical analysis of stress relaxation response of fiber-reinforced polymers." *Composites Science and Technology* 69.7 (2009): 1286-1292.

- [27] Murman, Scott, and Srinivasan Suresh. "Modeling Effective Stiffness Properties of IAD Fabrics." 21st AIAA Aerodynamic Decelerator Systems Technology Conference and Seminar. 2011.
- [28] Govindarajan, S. B. A. R. U., N. A. Langrana, and G. J. Weng. "An experimental and theoretical study of creep of a graphite/epoxy woven composite." *Polymer composites* 17.3 (1996): 353-361.
- [29] Ishikawa, T., and T-W. Chou. "Stiffness and strength behaviour of woven fabric composites." *Journal of Materials Science* 17.11 (1982): 3211-3220.
- [30] Shrotriya, P., and N. R. Sottos. "Creep and relaxation behavior of woven glass/epoxy substrates for multilayer circuit board applications." *Polymer composites* 19.5 (1998): 567-578.
- [31] Sottos, N. R., J. M. Ockers, and M. Swindeman. "Thermoelastic properties of plain weave composites for multilayer circuit board applications." *Journal of electronic packaging* 121.1 (1999): 37-43.
- [32] Lee, Jong-Won, and Charles E. Harris. "A micromechanics model for the effective Young's modulus of a piecewise-isotropic laminate with wavy patterns." *Journal of composite materials* 22.8 (1988): 717-741.
- [33] Shrotriya, Pranav. "Dimensional stability of multilayer circuit boards". PhD thesis, University of Illinois at Urbana-Champaign 2001.
- [34] Zhu, Qi, et al. "Three-dimensional viscoelastic simulation of woven composite substrates for multilayer circuit boards." *Composites science and technology* 63.13 (2003): 1971-1983.
- [35] Shrotriya, P., and N. R. Sottos. "Viscoelastic response of woven composite substrates." *Composites science and technology* 65.3 (2005): 621-634.
- [36] Altair® Hyperworks® Version11.0. Accessed on [02/12/2015]; Available from <http://www.altairuniversity.com/wp-content/uploads/2014/02/3DMeshing.pdf>
- [37] Cytec. CYCOM 5320-1 Epoxy Resin System. Accessed on [12/18/2015]; Available from http://www.cemselectorguid.com/pdf/CYCOM_5320-1_031912.pdf.
- [38] Cytec. CYCOM T650-35K Carbon Fiber. Accessed on [12/21/2015]; Available from: http://cytec.com/sites/default/files/datasheets/THORNEL_T650-35_052112.pdf.
- [39] Shin-Etsu Chemical Co., Ltd. Accessed on [11/12/2015]; Available from: https://www.shinetsusilicone-global.com/catalog/pdf/mold_rtv_e.pdf

- [40] ASTM D1708, Standard Test Method for Tensile properties of Plastics by Use of Microtensile Specimens, American Society of Testing Materials, 2013.
- [41] Differential Scanning Calorimeter (DSC), TA instruments, 159 Lukens Drive, New Castle, DE USA.
- [42] ASTM E1356-08, for Assignment of the Glass Transition Temperatures by Differential Scanning Calorimetry, American Society of Testing Materials, 2014.
- [43] TA instruments. Accessed on [12/02/2015]; Available from:
http://www.tainstruments.com/pdf/literature/AAN016_V1_U_StructFluids.pdf
- [44] Dynamic Mechanical Analyzer (DSC), TA instruments, 159 Lukens Drive, New Castle, DE USA.
- [45] TA instruments. Accessed on [09/06/2016]; Available from: <http://www.tainstruments.com/pdf/literature/RS23.pdf>
- [46] Tobolsky, A. V., and R. D. Andrews. "Systems manifesting superposed elastic and Viscous behavior." *The Journal of Chemical Physics* 13.1 (1945): 3-27.
- [47] TA instruments. Accessed on [09/06/2016]; Available from:
http://www.tainstruments.com/pdf/literature/AAN005e_Generating_Mastercurves.pdf
- [48] MTS 810 materials systems, MTS systems, 14000 Technology Drive Eden Prairie, MN USA.
- [49] MTS systems. Accessed on [09/11/2016]; Available from
https://www.mts.com/cs/groups/public/documents/library/dev_002042.pdf
- [50] Goyal, D., “Analysis of 2×2 Braided Composites”, Texas A&M University, college station, Thesis (2003).
- [51] Barbero, E. J., “Fabric-Reinforced Composites”. Introduction to Composite Materials Design, Textbook, Chapter 9. CRC Press Taylor & Francis Group, 2011 ISBN-978142007915.
- [52] Hewitt, J. A., D. Brown, and R. B. Clarke. "Computer modelling of woven composite materials." *Composites* 26.2 (1995): 134-140.
- [53] Pantiuk, M., Rao, M. P., “Modeling the Geometry of satin weave fabric Composites”. *Journal of Composite Material*, Vol. 43, No. 01/2009, SAGE Publications.

- [54] Anandvijay, K.R, Suresh, K.R., Kevontrez, K.J., Abhiruchika, S., “Predicting Stress Relaxation Behavior of Fabric Composites using Finite Element Based Micromechanics Model,” Proceedings of SAMPE Technical Conference and Exhibition 2016, Long Beach, CA.
- [55] Daniel, Isaac M., et al. Engineering mechanics of composite materials. Vol. 3. New York: Oxford university press, 1994.
- [56] MSC Marc 2014 r1 Reference Manual Vol. B: *Element Library*, MSC. Software Corporation, Santa Ana, CA, 2014, pp 611.
- [57] MSC Marc 2014 r1 Reference Manual Vol. D: *User Subroutines*, MSC. Software Corporation, Santa Ana, CA, 2014, pp 611.
- [58] Younes, Rafic, et al. Comparative review study on elastic properties modeling for unidirectional composite materials. INTECH Open Access Publisher, 2012.
- [59] Khoun, L.,” Process induced residual Stresses and Deformations in woven composites Manufactured by Resin Transfer Molding”,McGill University, Montreal,Dissertation (2009).

APPENDICES

Appendix A

Experimental Analysis

A1. Cure profile

Table A1. Manufacture Recommended Cure cycle of 5320-1 and 5320-8HS materials

Material	First Ramp Up (°C/min)	First Part Temperature (°C)	First Dwell Time (minutes)	Second Ramp Up (°C/min)	Second Part Temperature (°C)	Second Dwell Time (minutes)
5320-1 Epoxy Resin 5320-8HS	1.68±0.03	121	60	1.68±0.03	177	120

A2. 5320-1 Epoxy Resin

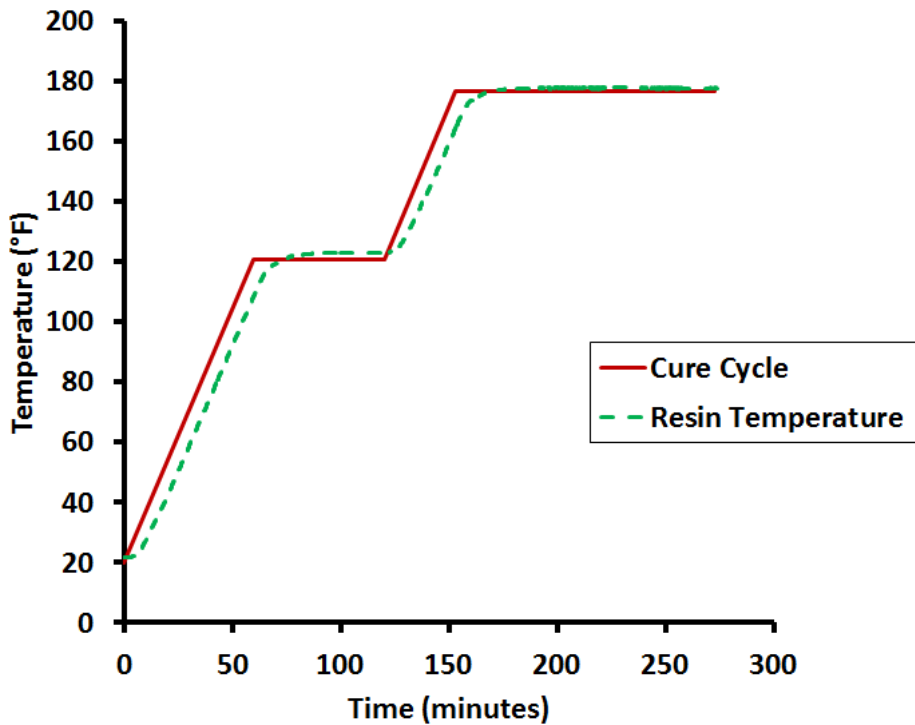


Figure A1. Temperature log of 5320-1 Epoxy Resin

A3. 5320-8HS Woven composite

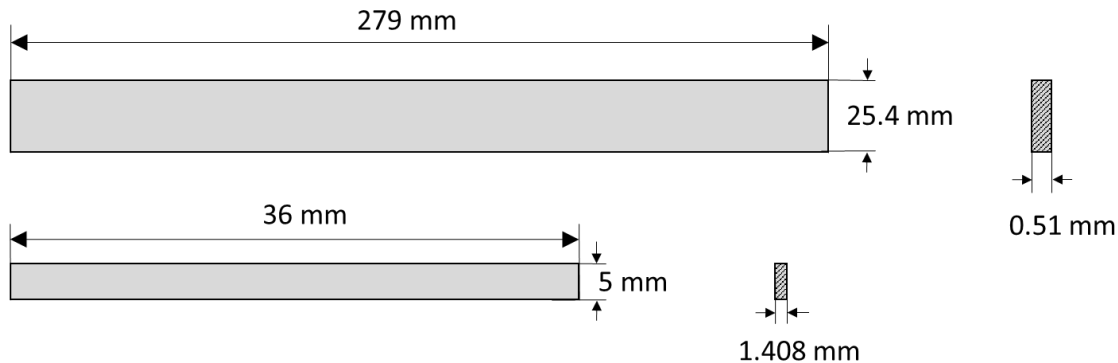


Figure A2. Schematics of 5320-8HS specimens

Table A2. Test Matrix of 5320-8HS

Test Method	Stacking Sequence	Laminate (mm)	Specimen Orientation	Isothermal Condition ($^{\circ}\text{C}$)	Applied strain (%)
Tension	0/90	304 × 304	0 $^{\circ}$	80,100,120,160	0.28
			90 $^{\circ}$		
			45 $^{\circ}$		
3-Point Bending	[0/90]s	152 × 152	0 $^{\circ}$	80,100,120,160	0.1
			90 $^{\circ}$		
			45 $^{\circ}$		

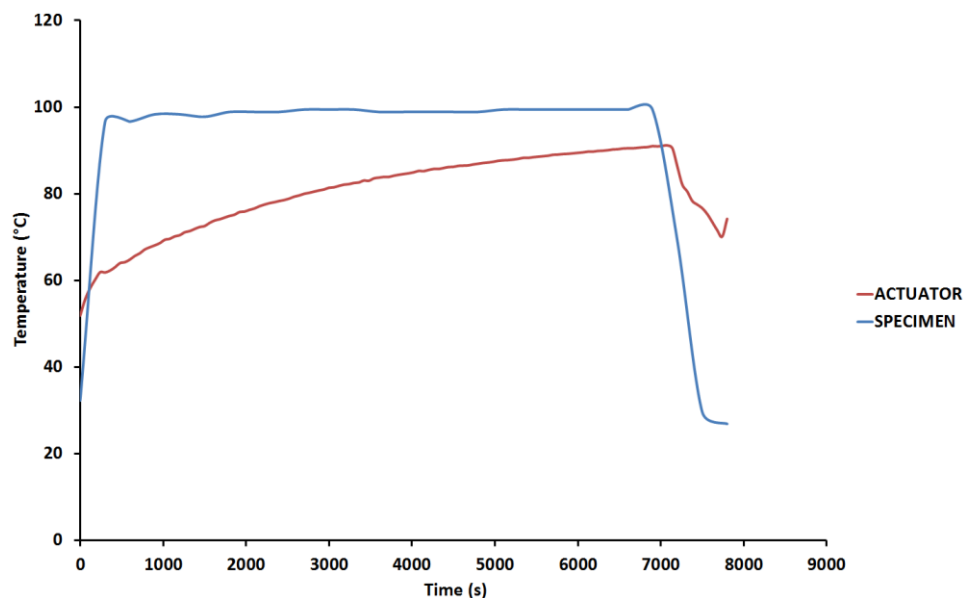


Figure A2. Temperature log of 5320-8HS specimen under isothermal condition of 100 $^{\circ}\text{C}$

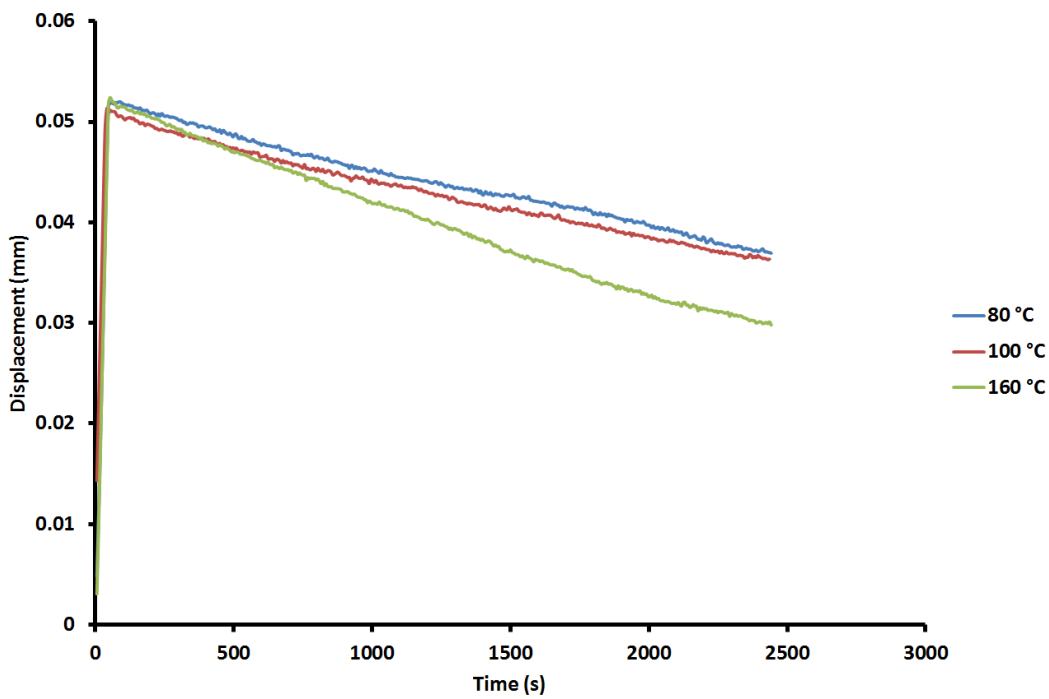


Figure A3. Extension of gauge length for 5320-8HS [±45]specimen using Extensometer

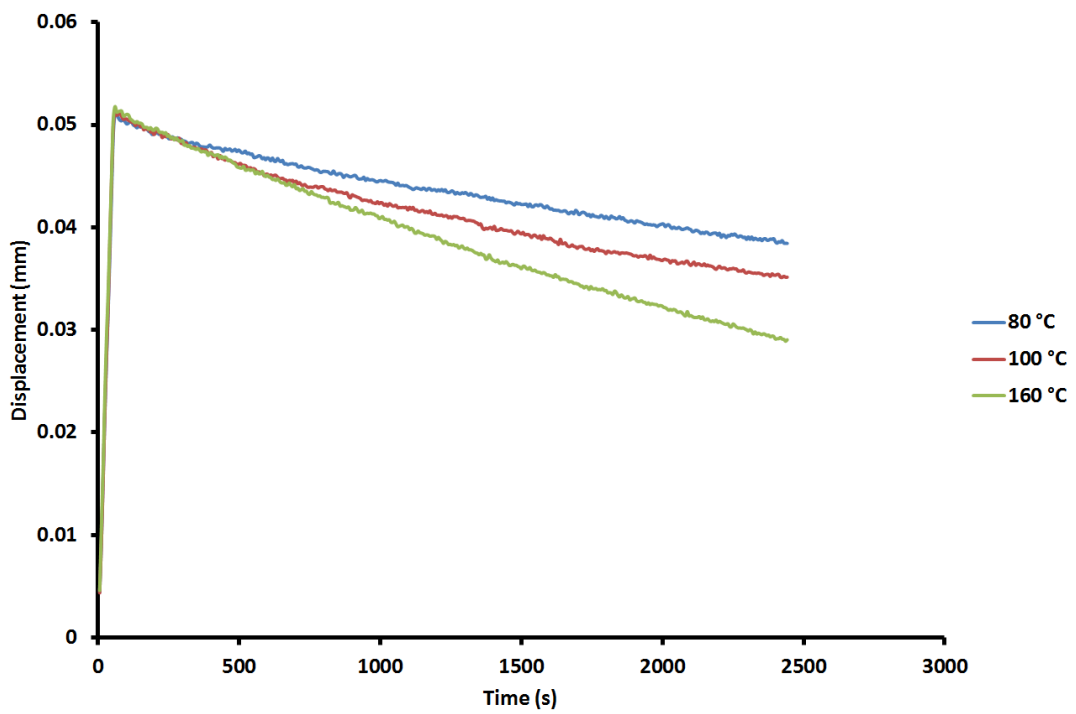


Figure A3. Extension of gauge length for 5320-8HS [0/90]specimen using Extensometer

Appendix B

Modeling of 8-harness unit cell

B1. Geometric parameters of 5320-8HS unit cell

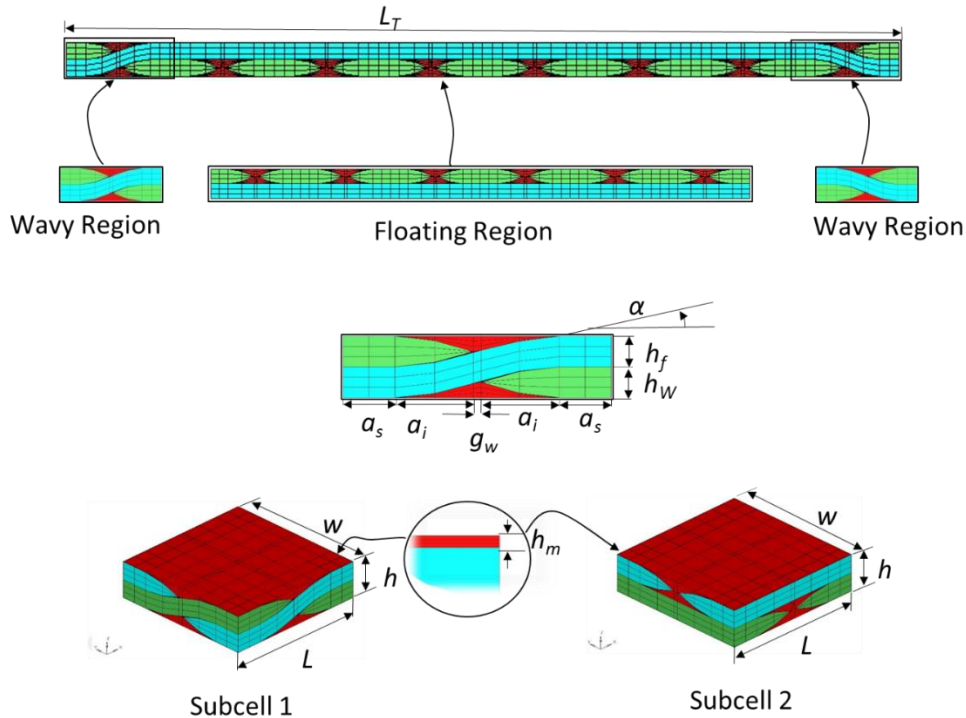


Figure B1. Dimensions of 8-harness Weave Architecture

Table B1. Design parameters of 8-harness micromechanics model

Tow Thickness, h_f/h_w (mm)	0.175
Gap b/w tows, g (mm)	0.040
Waviness length of Tows, λ (mm)	2.640
Flatness of Tow cross section, $2a_s$ (mm)	0.512
Lenticular shape of Tow cross section, $2a_i$ (mm)	0.768
Unit Cell Length, L_T (mm)	10.560
Resin Thickness, h_m (mm)	0.002
Unit Cell Thickness, h (mm)	0.352
Crimp angle (deg) α	14.000

B2. Relations to calculate design parameters of 8-harness unit cell [1]

All relations from equation (B.1)-equation (B.16) were referred from the text book of Barbero [1].

Width of tow (a_f) and subcell (w_f) [1],

$$a_f = 2(a_s + a_i) \quad (\text{B.1})$$

$$w_f = g_f + a_f \quad (\text{B.2})$$

Volume fraction of the fill and warp tows in the RVE [1],

$$\begin{aligned} v_f &= n_g A_f L_f \\ v_w &= n_g A_w L_w \end{aligned} \quad (\text{B.3})$$

Total Volume fraction of the tows in the RVE [1],

$$V_{meso} = \frac{v_w + v_f}{v_{RVE}} = \frac{v_w + v_f}{n_g^2 w_f w_w h} \quad (\text{B.4})$$

Other design parameters of 8-harness unit cell were calculated using the following relations:

Wavelength of the waviness region,

$$\lambda = 2w_f \quad (\text{B.5})$$

Length of the floating region,

$$S_F = l - \lambda \quad (\text{B.6})$$

$$S_F = 6w_f \quad (\text{B.7})$$

Length of the unit cell,

$$l = \lambda + S_F \text{ (Or)} \quad l = 8w_f \quad (\text{B.8})$$

Tow undulation angle or crimp angle can be calculated as [1],

$$\theta_f(x) = \left| \arctan \frac{\partial}{\partial x} z_f(x) \right| \quad (\text{B.9})$$

$$\theta_w(y) = \left| \arctan \frac{\partial}{\partial y} z_w(y) \right| \quad (\text{B.10})$$

The length of the tows in the RVE can be calculated using the undulation function as follows [1],

$$L_f = \int_0^{(a_w+g_w)/2} \sqrt{1 + \left(\frac{d}{dx} z_f(x) \right)^2} dx \quad (\text{B.11})$$

$$L_w = \int_0^{(a_f+g_f)/2} \sqrt{1 + \left(\frac{d}{dy} z_w(y) \right)^2} dy \quad (\text{B.12})$$

The cross-sectional area of the tows in the RVE, as follows [1],

$$A_f = \int_0^{(a_f+g_f)/2} e_f(y) dy = \frac{ha_f}{2\pi} \quad (\text{B.13})$$

$$A_w = \int_0^{(a_w+g_w)/2} e_w(x) dx = \frac{ha_w}{2\pi} \quad (\text{B.14})$$

Waviness Ratio (WR) is defined as the thickness (h) of a woven mat divided by the wavelength of the undulation of a tow [1],

$$WR = \frac{h}{\lambda} \quad (\text{B.15})$$

Aspect ratio of the Tow [1],

$$AR = \frac{a_f}{h_f} \quad \text{Or} \quad \frac{a_w}{h_w} \quad (\text{B.16})$$

Appendix C

FORTRAN Program of 8-harness weave architecture

C1. Program that generates geometric parameters of fill/warp tow and its through thickness cross section.

```
C      Main Program
PROGRAM DESIGN_8HS
IMPLICIT NONE
C      declaration of variables
REAL:: X,Y,Z,E,as,ai,gf,gw,af,aw,wf,ww
INTEGER ::J,NOC,I ! NOC = Number of coordinates

C      Defining geometric dimensions of the weave. Refer to figure B1 and table B1 for details
as=0.256
ai=0.384
gf=0.04
gw=0.04
af=2.0*(ai+as)
aw=af
wf=gf+af
wW=gW+aW

C      Reading an input text file
OPEN(10,file='C:\Users\Anandvijay\Desktop\fortran\modeling 8HS\fill\x-coordinate.TXT')
OPEN(11,file='C:\Users\Anandvijay\Desktop\fortran\modeling 8HS\fill\y-coordinate.TXT')
OPEN(12,file='C:\Users\Anandvijay\Desktop\fortran\modeling 8HS\fill\z-coordinate.TXT')

PRINT *, "Enter the tow no. :"
read(*,*) J
read(10,*) NOC

C      Calling subroutines to calculate the waviness and cross section of fill/warp tows
Y=(gf/2.0)+wf*(J-1)
WRITE(12,*) 'WAVINESS COORDINATES ARE..'
do i=1,NOC
    read(10,*) x
    call waviness(x,y,j,z)
    write(12,*) z
END DO
CALL CROSS_SECTION(y,j,E)

close(unit=10)
close(unit=11)
end program DESIGN_8HS
C      End of main program
```

C SUBROUTINES

C Subroutine that calculates the geometry of fill/warp tow undulation
 subroutine waviness(x,y,j,z)
 implicit none

C declaration of variables
 REAL::WF,GF,CN1,CN2,X,Y,SCN1,WW,GW,AW,AF,PI,SCN2,SCN2A,Z,HF,SCN3,SCN4,SCN5,SCN6,SCN7,SCN8,
 SCN9,SCN10,CN3,CN4,CN5,CN6,TRUNC,EPS,as,ai
 REAL::SCNF1, SCNF2,SCNF3, SCNF4,SCNF5, SCNF6,SCNF7, SCNF8,SCNF9, SCNF10,SCNF11, SCNF12, w
 INTEGER::J,K,NS,NG,N

C Defining geometric dimensions of the weave. Refer to figure B1 and table B1 for details
 pi=4.0*atan(1.0)
 ns=5
 ng=8
 as=0.256
 ai=0.384
 gf=0.04
 gw=0.04
 af=2.0*(ai+as)
 aw=af
 wf=gf+af
 wW=gW+aW
 w=2.0*ai+gw
 EPS=1.0E-5
 hf=0.175

C Condition (1) for y-coordinate
 CN1=((J-1)*WF)+(GF/2.0)
 CN2=(J*WF)-(GF/2.0)

IF ((CN1.LE.Y) .AND. (Y.LE.CN2)) THEN

C X-CONDITIONS
 **** CASE(1) ****
 TRUNC= INT((NS*(J-1)+1)/NG)!..NINT=ROUND TO INTEGER
 N=TRUNC+1
 DO K=1,N
 SCNF1=(NS*(J-1)-(1.0/2.0)-(K*NG))*W-17.0*as
 SCNF1=(NS*(J-1)-(1.0/2.0)-(K*NG))*W-16.0*as
 SCNF2=(NS*(J-1)-(1.0/2.0)-(K*NG))*W-16.0*as+w
 SCNF3=(NS*(J-1)+(3.0/2.0)-(K*NG))*W-14.0*as-w
 SCNF2=(NS*(J-1)+(3.0/2.0)-(K*NG))*W-14.0*as
 SCNF4=(NS*(J-1)+(3.0/2.0)-(K*NG))*W-13.0*as
 SCN2A=(NS*(J-1)-(1.0/2.0)-((K-1.0)*NG))*W-as

C undulation region with flatness embedment (1)
 IF ((SCNF1.LE.X) .AND. (X.LE.SCN1)) THEN
 Z= (HF/2.0)
 ELSE IF ((SCN1.LE.X) .AND. (X.LE.SCNF2)) THEN
 Z=(-1)**((K*NG)+1) *(HF/2.0)*(SIN(((PI*(X+16.0*as))/W)+ (NS*(J-1)*PI)))
 ELSE IF ((SCNF2.LE.X) .AND. (X.LE.SCNF3)) THEN

```

        Z=-(HF/2.0)
    ELSE IF ( (SCNF3.LE.X) .AND. (X.LE.SCN2) ) THEN
        Z=(-1)**((K*NG)+1)*(HF/2.0)*( SIN( ((PI*(X+14.0*as))/W)+(NS*(J-1)*PI) ) )
    ELSE IF ( (SCN2.LE.X) .AND. (X.LE.SCNF4) ) THEN
        Z= (HF/2.0)
C     Floating Region (1)
    ELSE IF ( ((K-1).GE.1) .AND. ( ( SCNF4.LT.X).AND.(X.LT.SCN2A) ) ) THEN
        Z= (HF/2.0)
    END IF
END DO

C **** CASE(2) ****
SCNF5=( NS*(J-1)-(1.0/2.0) )*W-as
SCN3=( NS*(J-1)-(1.0/2.0) )*W
SCNF6=( NS*(J-1)-(1.0/2.0) )*W+w
SCNF7=( NS*(J-1)-(1.0/2.0) )*W+Ww
SCN4=( NS*(J-1)+(3.0/2.0) )*W+2.0*as
SCNF8=( NS*(J-1)+(3.0/2.0) )*W+3.0*as

C undulation region with flatness embedment (2)
IF ( (SCNF5.LE.X) .AND. (X.LE.SCN3) ) THEN
    Z= (HF/2.0)
ELSE IF ( (SCN3.LE.X) .AND. (X.LE.SCNF6) ) THEN
    Z=-HF/2.0)*(SIN( ((PI*X)/W)+(NS*(J-1)*PI) ) )
ELSE IF ( (SCNF6.LE.X) .AND. (X.LE.SCNF7) ) THEN
    Z=-(HF/2.0)
ELSE IF ( (SCNF7.LE.X) .AND. (X.LE.SCN4) ) THEN
    Z=-HF/2.0)*(SIN( ((PI*(X-2*as))/W)+(NS*(J-1)*PI) ) )
ELSE IF ( (SCN4.LE.X) .AND. (X.LE.SCNF8) ) THEN
    Z= (HF/2.0)
END IF

C **** CASE(3) ****
SCNF9=( NS*(J-1)-(1.0/2.0)+NG )*W+15.0*as
SCN5=( NS*(J-1)-(1.0/2.0)+NG )*W+16.0*as
SCNF10=( NS*(J-1)-(1.0/2.0)+NG )*W+16.0*as+w
SCNF11=( NS*(J-1)-(1.0/2.0)+NG )*W+18.0*as+w
SCN6=( NS*(J-1)+(3.0/2.0)+NG )*W+18.0*as
SCNF12=( NS*(J-1)+(3.0/2.0)+NG )*W+19.0*as

C undulation region with flatness embedment (3)
IF ( (SCNF9.LE.X) .AND. (X.LE.SCN5) ) THEN
    Z= (HF/2.0)
ELSE IF ( (SCN5.LE.X) .AND. (X.LE.SCNF10) ) THEN
    Z=(-1)**(NG+1)*(HF/2)*(SIN( ((PI*(X-16.0*as))/W)+(NS*(J-1)*PI) ) )
ELSE IF ( (SCNF10.LE.X) .AND. (X.LE.SCNF11) ) THEN
    Z=-(HF/2.0)
ELSE IF ( (SCNF11.LE.X) .AND. (X.LE.SCN6) ) THEN
    Z=(-1)**(NG+1)*(HF/2)*(SIN( ((PI*(X-18.0*as))/W)+(NS*(J-1)*PI) ) )
ELSE IF ( (SCN6.LE.X) .AND. (X.LE.SCNF12) ) THEN
    Z= (HF/2.0)
END IF

```

```

C      Floating Region (2)
SCN7=( NS*(J-1)+(3.0/2.0)-NG )*W-13.0*as
SCN8=( NS*(J-1)-(1.0/2.0) )*W-as
SCN9=( NS*(J-1)+(3.0/2.0) )*W+3.0*as
SCN10=( NS*(J-1)-(1.0/2.0)+NG )*W+15.0*as

IF ( ( (SCN7.LT.X) .AND. (X.LT.SCN8) ).OR.( (SCN9.LT.X) .AND. (X.LT.SCN10) ) ) THEN
    Z= (HF/2.0)
END IF
END IF

C      Condition (2) for y-coordinate
CN3=((J-1)*WF)
CN4=((J-1)*WF)+(GF/2)
CN5=(J*WF)-(GF/2)
CN6=(J*WF)
IF ( ( ((CN3.LE.Y).AND.(Y.LT.CN4)) .OR. ((CN5.LE.Y) .AND. (Y.LE.CN6)) ).AND.(GF.NE.EPS) ) THEN
    Z=0.0
END IF
end subroutine waviness

C      Subroutine that calculates the geometry of fill/warp tow cross section
subroutine CROSS_SECTION(y,j,E)
implicit none
C      declaration of variables
integer::J,I,N,np1
real::WF,GF,CN1,CN2,CN3,CN4,Y,E,PI,AF,HF,ai,as,CNF1,CNF2

C      Defining geometric dimensions of the weave. Refer to figure B1 and table B1 for details
pi=3.14159
as=0.256
ai=0.384
gf=0.04
af=2.0*(ai+as)
wf=gf+af
hf=0.175
WRITE(12,*)
WRITE(12,*) 'CROSS SECTION COORDINATES ARE..'
N=21 !...NO.OF COORDINATES
NP1=N+1
DO I=1,NP1
    CN1=((J-1)*WF)+(GF/2)
    CNF1=((J-1)*WF)+(GF/2)+ai
    CNF2=((J-1)*WF)+(GF/2)+ai+2.0*as
    CN2=(J*WF)-(GF/2)

C      Condition (1) for y-coordinate
    IF ( (CN1.LE.Y).AND.(Y.LE.CNF1) ) THEN
        E=ABS((HF/2)*SIN( PI*(-J-1)*WF+Y-(GF/2))/(2.0*ai) )
    ELSE IF ( (CNF1.LE.Y).AND.(Y.LE.CNF2) ) THEN
        E=ABS((HF/2))
    ELSE IF ( (CNF2.LE.Y).AND.(Y.LE.CN2) ) THEN
        E=ABS((HF/2)*SIN( PI*(-J-1)*WF+(Y-2.0*as)-(GF/2))/(2.0*ai) )
    END IF
END DO

```

```

END IF

C      Condition (2) for y-coordinate
CN1=((J-1)*WF)+(GF/2)
CN3=((J-1)*WF)
CN2=(J*WF)-(GF/2)
CN4=(J*WF)
IF ( ( (CN3.LE.Y) .AND.(Y.LT.CN1) ).OR.( (CN2.LT.Y).AND.(Y.LE.CN4) ) ) THEN
    E=0.0
END IF

      WRITE (12,1) E
      Y=Y+(af/N)
END DO

      WRITE(*,*) 
      1 format (1f8.4)
END SUBROUTINE CROSS_SECTION

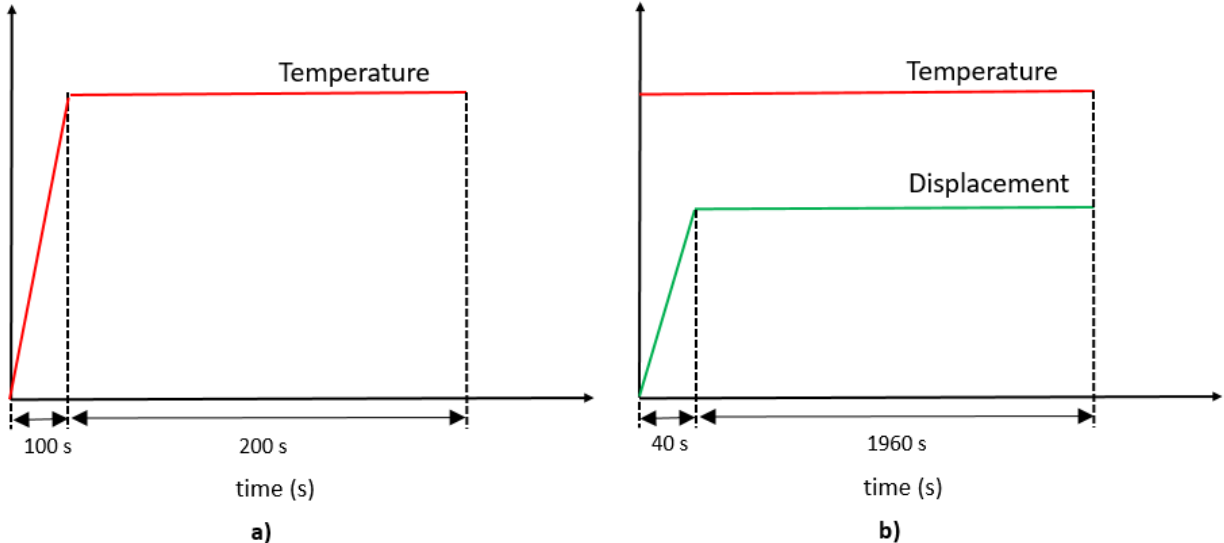
```

Note: To model warp tows, in both waviness and cross section subroutines, functions were multiplied with minus one and x, y, j, wf, ww, gf, gw, hf (fill tow) were replaced with y, x, I, ww, wf, gw, gf , hw (Warp tow).

Appendix D

Finite Element Analysis

D1. Test Method of finite element analysis



Test Procedure followed in the stress relaxation analysis

D2. Hexagonal Array of unidirectional composite

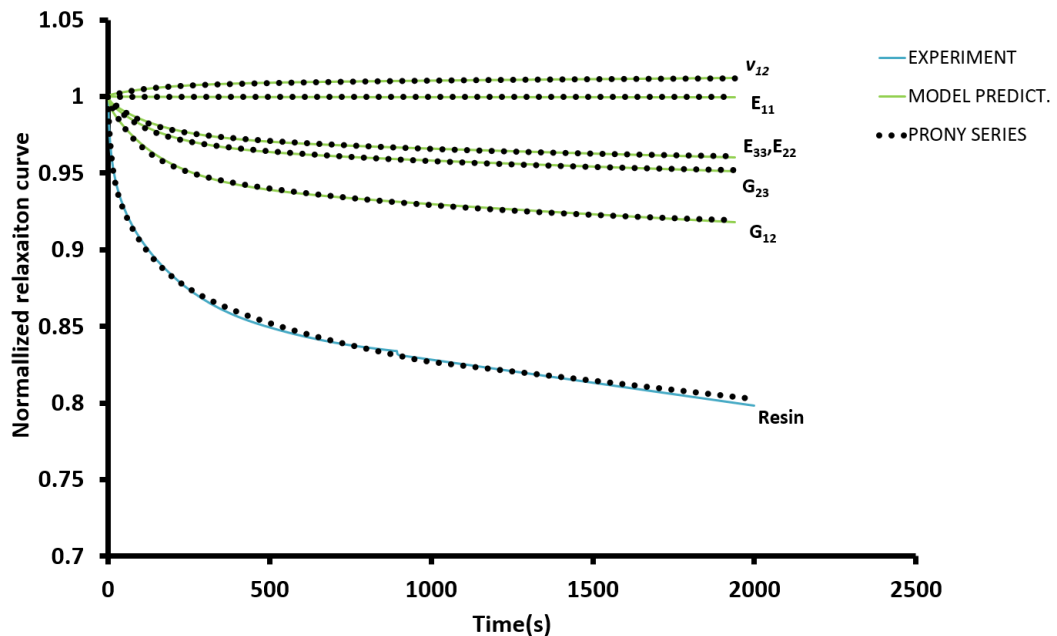


Figure D1. Relaxation curves of unidirectional unit cell model (Hexagonal array) under different load cases at 80 °C

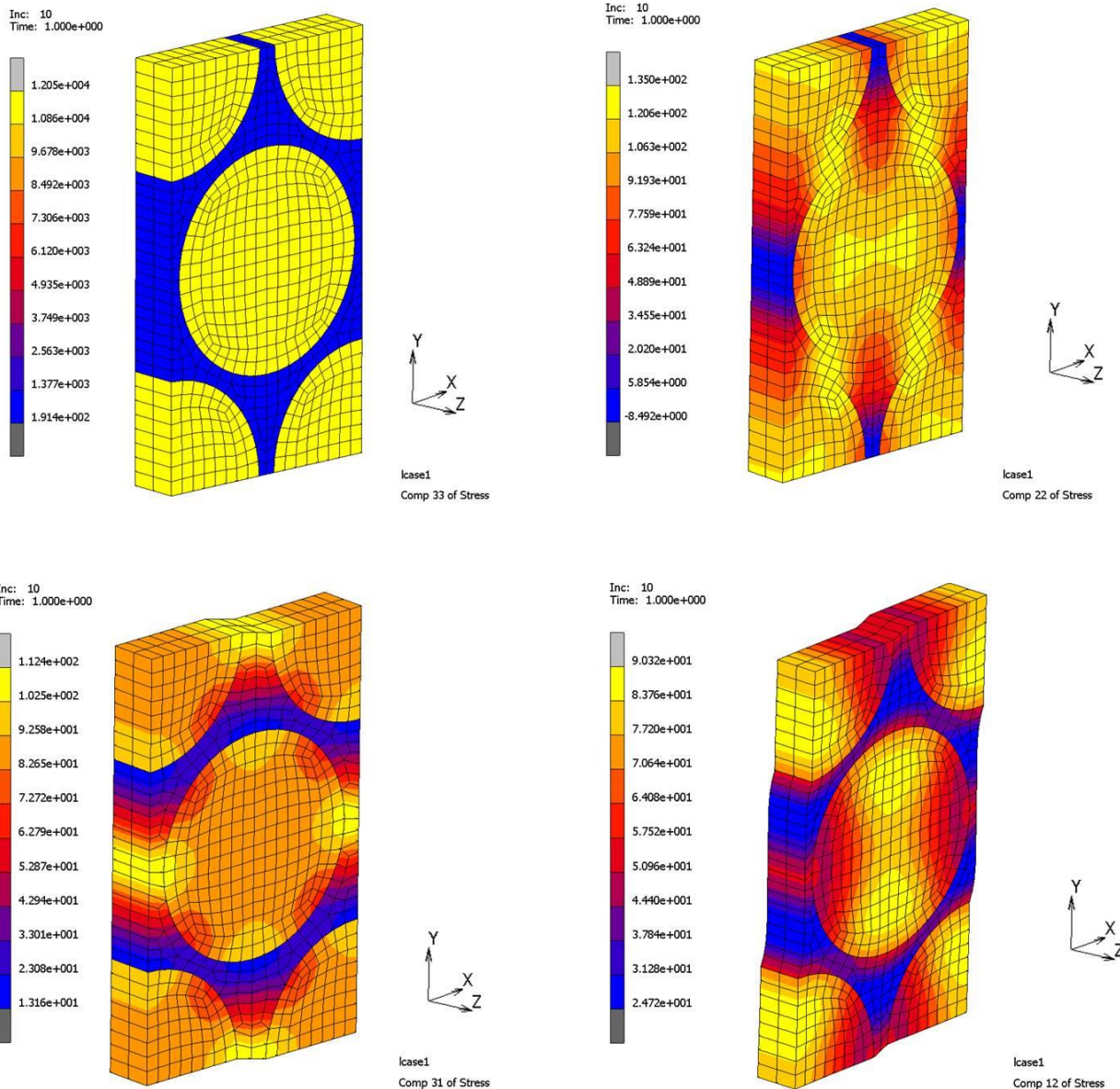


Figure D2. Axial and Shear Stress distribution of unidirectional unit cell with $V_f = 0.77$ (deformed configuration)

Note: Axis-z and -y denote longitudinal direction and transverse direction of unidirectional composites

Appendix E

FORTRAN Subroutines used in the finite element analysis

E1. Subroutine to define material orientation of fiber bundles (fill and warp tows)

Numerical algorithm was developed for the hexahedral (8-noded) and (6-noded) pentahedral solid elements to define material orientation for orthotropic and anisotropic materials. Material direction is controlled based on the criteria defined for edges of solid elements as shown in figure E1. Connected edges located at the corner of the solid are assumed to be a local coordinate system.

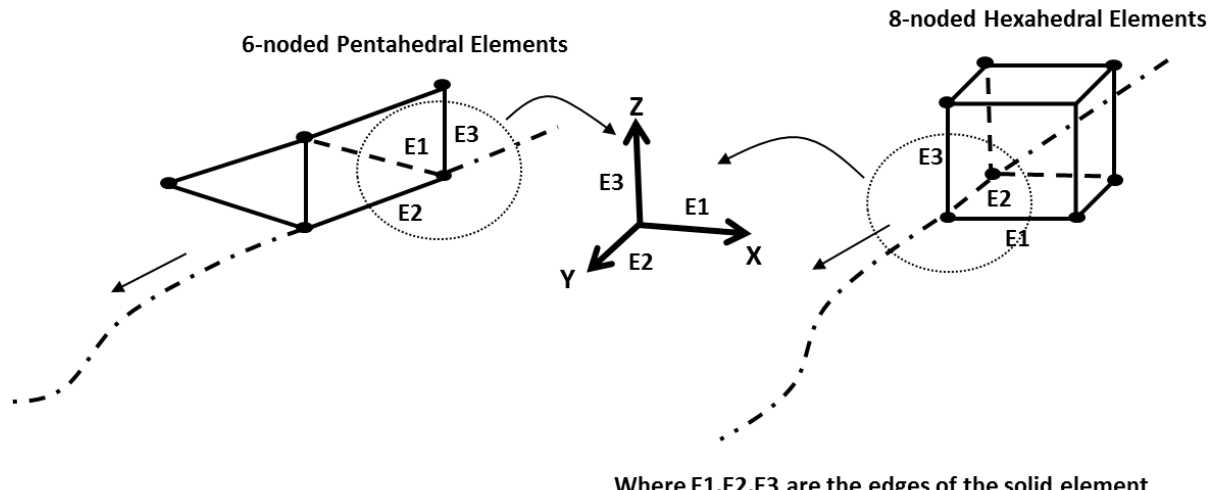


Figure E1. Schematics of solid elements

```

ORIENT2.f
subroutine orient2(n,nn,kcus,material,matname,icomp,nodes,nnodes,
    $   coord,coordint,ncoord,dircos,icall,iply,ilocal,ifast,
    $   vec1,vec2,integer_data,real_data)
c* * * * *
#ifndef _IMPLICITNONE
    implicit none
#else
    implicit logical (a-z)
#endif
integer kkus,n,nn,material,nodes,nnodes,ncoord,icall,iply,ilocal
integer icomp,ifast,integer_data
real*8 coord,dircos,vec1,vec2,coordint,real_data
character*24 matname
dimension n(2),kkus(2),material(2),nodes(*)
dimension coord(ncoord,*),dircos(3,3),vec1(3),vec2(3)
dimension coordint(*),integer_data(*),real_data(*)
real*8 u,v,l1,l2,l4,l5,TOL1,TOL,XMAX,XMIN,SAVE1
real*8 U1,V1,J1,J2,J4,J5,YMAX,YMIN,SAVE2
integer i,imin,imax,Y1,Y2,Y3
integer J,Jmin,Jmax,X1,X2,X3
dimension u(3),V(3)

```

```

dimension U1(3),V1(3)
!open(unit=10,file="F:\nodes.txt",status="old")

c INITIALIZING THE VARIABLES
ncoord=3
icomp=0
iply=0
TOL1=1.0e-02
TOL=0.0D0
If (material(2).eq.1) then
    go to 500
else

c X-DIRECTION (FILL)

c LOCATING THE APPROPRIATE ELEMENT NODES FOR THE X_DIRECTION.....
IMIN=1
c CASE (I)..EDGE_1 OF AN ELEMENT
Y1=coord(2,2)-coord(2,IMIN)
I1=coord(1,IMIN)
I2=coord(1,2)-I1
If ((Y1.EQ.TOL).AND.(ABS(I2).GT.TOL1) )THEN
    IMAX=2
END IF
c CASE (II)..EDGE_2 OF AN ELEMENT
I4=coord(1,4)-I1
Y2=coord(2,4)-coord(2,IMIN)
If ( (Y2.EQ.TOL).AND.(ABS(I4).GT.TOL1))THEN
    IMAX=4
END IF

c CASE (III)..EDGE_3 OF AN ELEMENT
I5=coord(1,5)-I1
Y3=coord(2,5)-coord(2,IMIN)
If ((Y3.EQ.TOL).AND.(ABS(I5).GT.TOL1))THEN
    IMAX=5
END IF

c FINDING XMAX AND XMIN TO CREATE PREFERRED DIRECTION
XMAX=coord(1,IMAX)
XMIN=coord(1,IMIN)
IF (XMAX.GT.XMIN) THEN
    !    REMAINS THE SAME
ELSE
    SAVE1=IMAX
    IMAX=IMIN
    IMIN=SAVE1
END IF

c FORMING THE LOCAL VECTOR IN THE ELEMENT COORDINATE SYSTEM
do 10 i=1,3
    u(i)=coord(i,IMAX)-coord(i,IMIN)
10    continue

```

```

c THE VECTOR(2)..BY ORTHOGONAL CONDITION
V(1)=0.0d0
V(2)=1.0d0
V(3)=0.0d0

c Y-DIRECTION (WARP)
c LOCATING THE APPROPRIATE ELEMENT NODES FOR THE X_DIRECTION
JMIN=1

c CASE (I)..EDGE_1 OF AN ELEMENT
X1=coord(1,2)-coord(1,JMIN)
J1=coord(2,JMIN)
J2=coord(2,2)-J1
If ((X1.EQ.TOL).AND.(ABS(J2).GT.TOL1) )THEN
    JMAX=2
END IF

c CASE (II)..EDGE_2 OF AN ELEMENT
J4=coord(2,4)-J1
X2=coord(1,4)-coord(1,JMIN)
If ((X2.EQ.TOL).AND.(ABS(J4).GT.TOL1))THEN
    JMAX=4
END IF

c CASE (III)..EDGE_3 OF AN ELEMENT
J5=coord(2,5)-J1
X3=coord(1,5)-coord(1,JMIN)
If ( (X3.EQ.TOL).AND.(ABS(J5).GT.TOL1))THEN
    JMAX=5
END IF

c FINDING YMAX AND YMIN TO CREATE PREFERRED DIRECTION
YMAX=coord(2,JMAX)
YMIN=coord(2,JMIN)
IF (YMAX.GT.YMIN) THEN
    ! REMAINS THE SAME
ELSE
    SAVE2=JMAX
    JMAX=JMIN
    JMIN=SAVE2
END IF

c FORMING THE LOCAL VECTOR IN THE ELEMENT COORDINATE SYSTEM.
do 20 i=1,3
    U1(i)=coord(i,JMAX)-coord(i,JMIN)
20 continue

c THE VECTOR(2)..BY ORTHOGONAL CONDITION
V1(1)=1.0d0
V1(2)=0.0d0
V1(3)=0.0d0

c TRANFORMATION OF GLOBAL TO LOCAL COORDINATE SYSTEM

```

```

c   DIRECTION-X
  If (material(2).eq.2) then
    do 30 i=1,3
      vec1(i)=u(i)
      vec2(i)=v(i)
  30   continue
  end if
c   DIRECTION-Y
  If (material(2).eq.3) then
    do 40 i=1,3
      vec1(i)=U1(i)
      vec2(i)=V1(i)
  40   continue
  end if
end if
500 continue
return
end

```

E2. Subroutine to define long term stiffness matrix for viscoelastic model of orthotropic material

```

HOOKVI.f
subroutine hookvi(m,nn,kcus,iterm,b,dt,dtdl,e,pr,g)
#ifndef _IMPLICITNONE
  implicit none
#else
  implicit logical (a-z)
#endif
real*8 b, dt, dtdl, e, g
integer iterm, kkus, m, nn
real*8 pr
dimension b(6,6),dt(*),dtdl(*),e(3),pr(3),g(3),m(2),nn(3),
*      kkus(2)
real*8 v21,v32,v13,v12,v23,v31,del,E11,E22,E33,G12,G23,G31
real*8 E11X,E22Y
INTEGER I,J,NPT
dimension E11(9),E22(9),E33(9)

c  units are in MPa_100C
E11X=185784.0647
E22Y=17135.7152

c  prony series coefficients (Vf=0.77)
c  x_direction_unit (MPa)
NPT=ITERM
E11(1)=1.71E-05*E11X
E11(2)=0.000129699*E11X
E11(3)=0.000291466*E11X

```

```

c y_direction_unit (MPa)
E22(1)=0.002536682*E22Y
E22(2)=0.009536213*E22Y
E22(3)=0.027698294*E22Y

c z_direction_unit (MPa)
do 5 i=1,NPT
    E33(i)=E22(i)
5 continue

G12=g(1)
G23=g(2)
G31=g(3)
v12=pr(1)
V23=pr(2)
V31=pr(3)
v21=V31
v32=V23
v13=V12
del=1.0-v12*v21-v23*v32-v31*v13-V12*V23*V31-V21*V32*V13

c STIFFNESS MATRIX FOR ORTHOTROPIC MATERIAL
b(1,1)=((1.0-v23*v32)*E11(NPT))/del
b(2,2)=((1.0-v31*v13)*E22(NPT))/del
b(3,3)=((1.0-v12*v21)*E33(NPT))/del
b(4,4)=G12
b(5,5)=G23
b(6,6)=G31
b(1,2)=((v21+v31*v23)*E11(NPT))/del
b(1,3)=((v13+v12*v23)*E33(NPT))/del
b(2,3)=((v32+v12*v31)*E22(NPT))/del
b(1,4)=0.0
b(1,5)=0.0
b(1,6)=0.0
b(2,4)=0.0
b(2,5)=0.0
b(2,6)=0.0
b(3,4)=0.0
b(3,5)=0.0
b(3,6)=0.0
b(4,5)=0.0
b(4,6)=0.0
b(5,6)=0.0

c SYMMETRY CONDITION OF THE MATRIX
b(4,1)=0.0
b(5,1)=0.0
b(6,1)=0.0
b(4,2)=0.0
b(5,2)=0.0
b(6,2)=0.0
b(4,3)=0.0

```

```
b(5,3)=0.0  
b(6,3)=0.0  
b(5,4)=0.0  
b(4,6)=0.0  
b(6,5)=0.0  
b(2,1)= b(1,2)  
b(3,1)= b(1,3)  
b(3,2)= b(2,3)
```

```
return  
end
```

Appendix F

Stress Contours of 5320-8HS Unit cell Model

F1. Axial and Shear Stress distribution

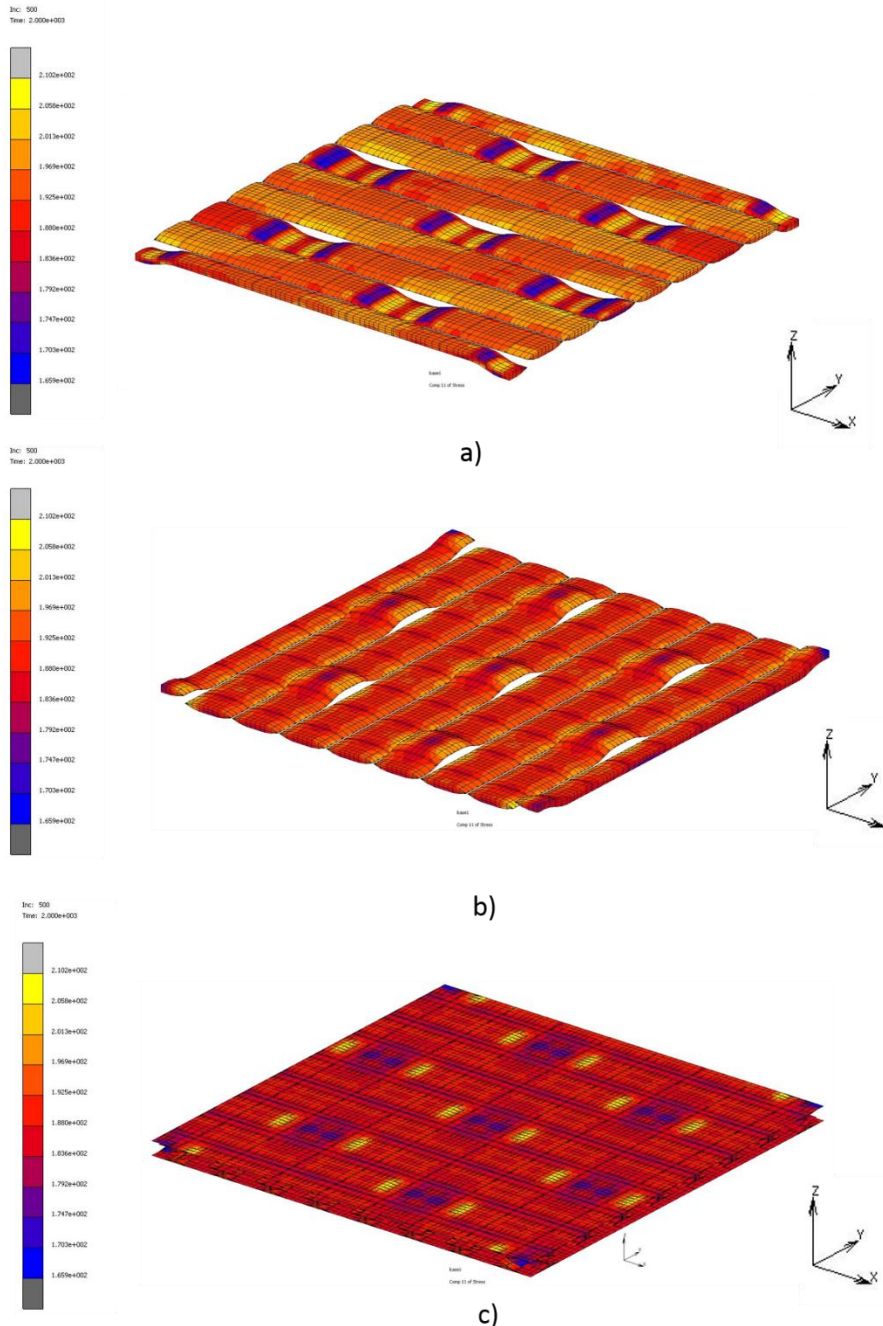


Figure F1. Axial stress distribution of 5320-8HS unit cell loaded along fill direction at t=2000s under isothermal condition of 80 °C a) Fill tows b) Warp tows c) Neat resin

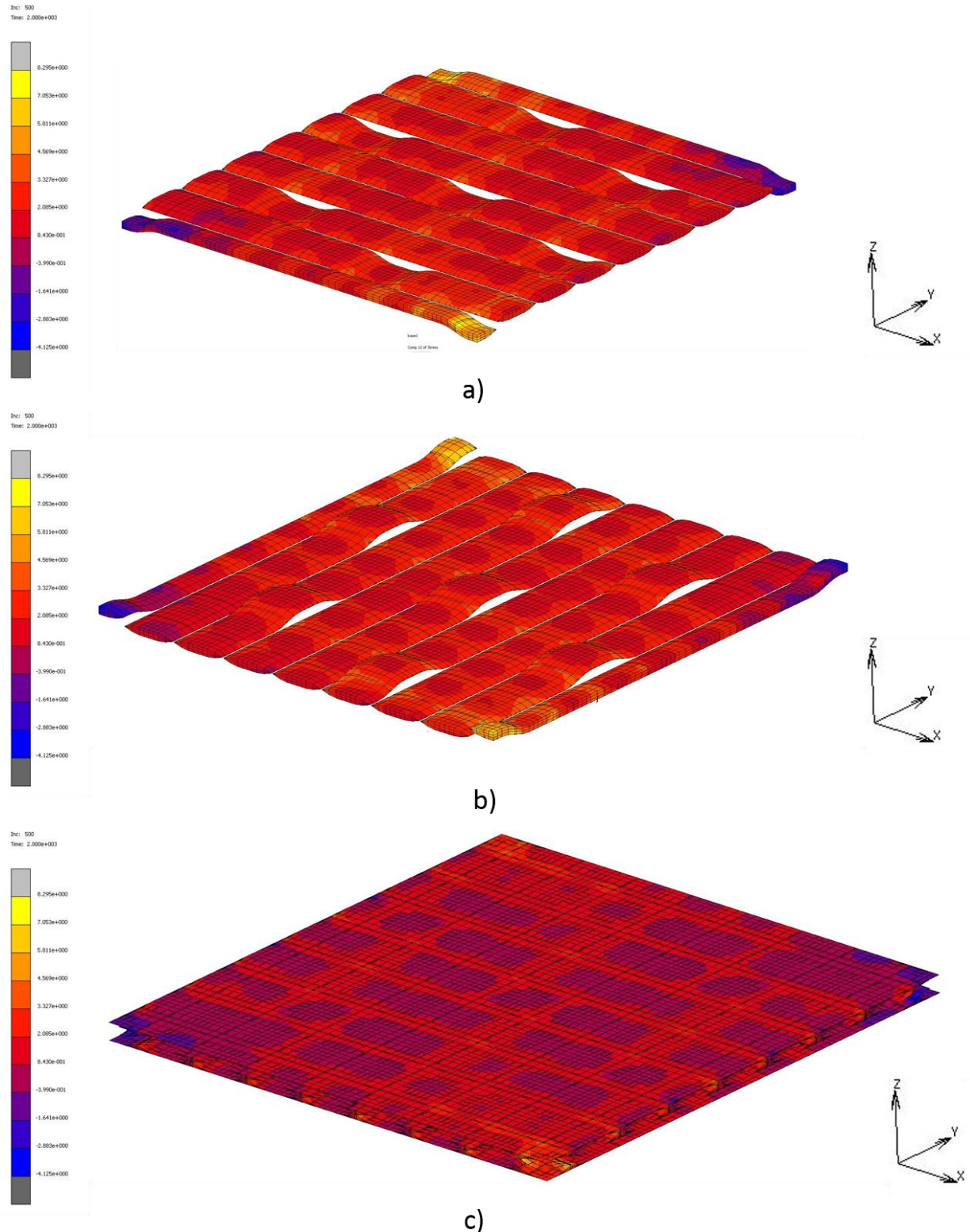


Figure F2. Shear stress distribution of 5320-8HS unit cell loaded along warp direction at $t=2000s$ under isothermal condition of $80^{\circ}C$

F2. Stress distribution at different relaxation times

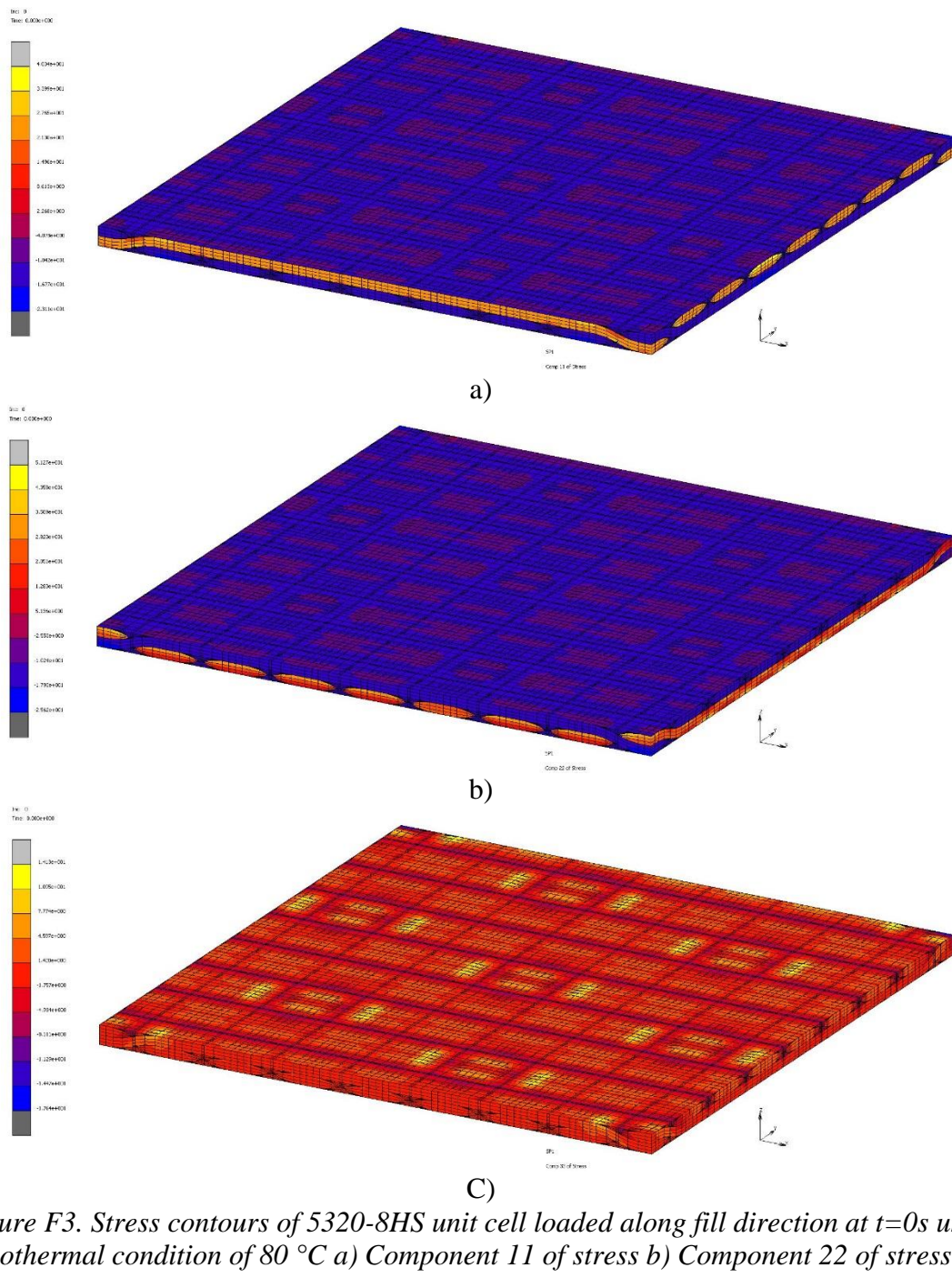
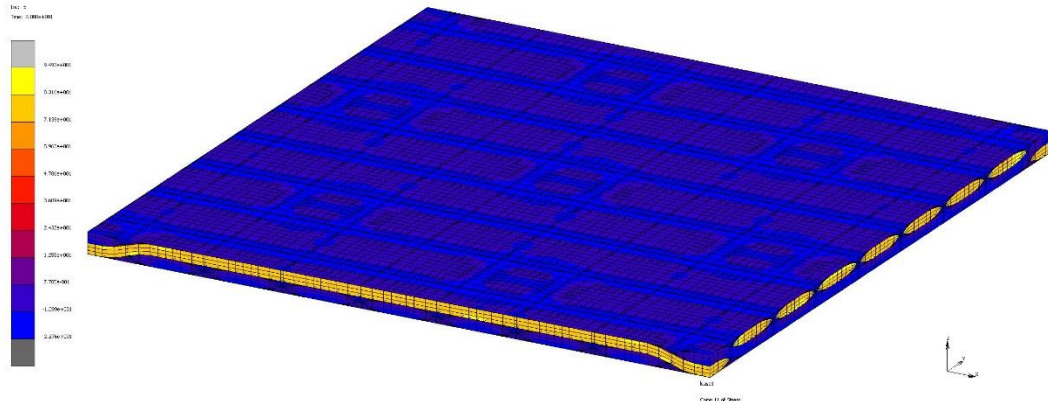
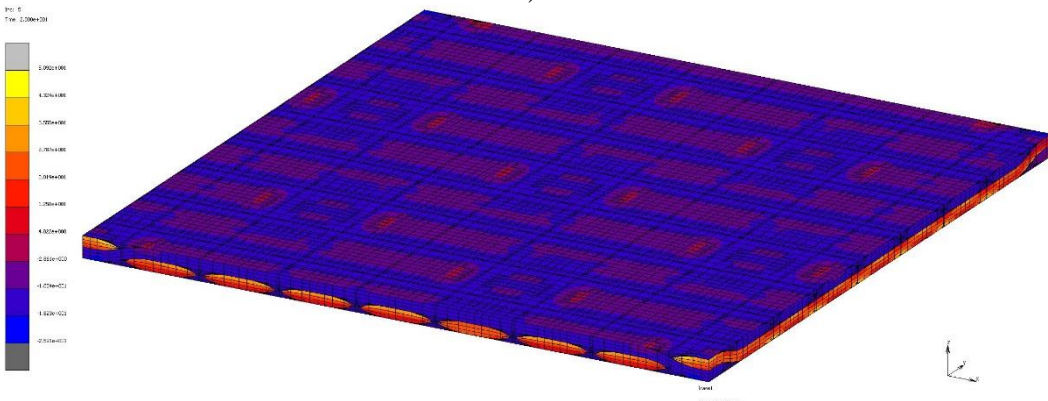


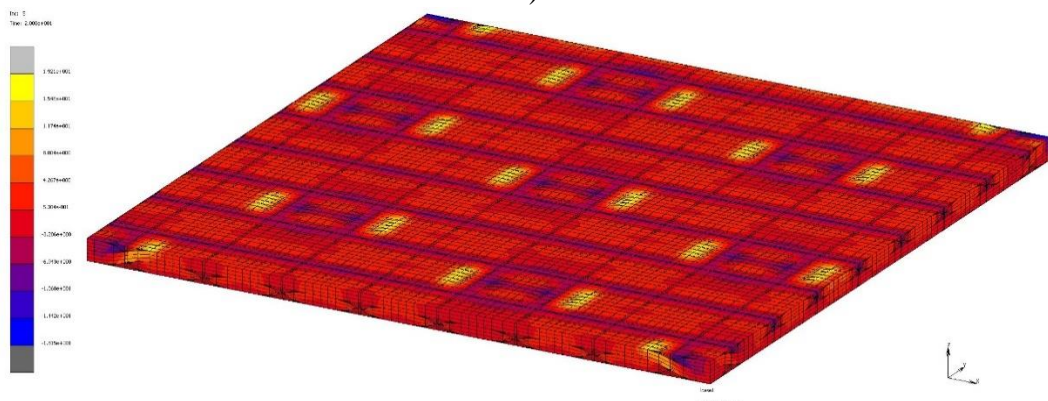
Figure F3. Stress contours of 5320-8HS unit cell loaded along fill direction at $t=0s$ under isothermal condition of 80°C a) Component 11 of stress b) Component 22 of stress c) Component 33 of stress



a)

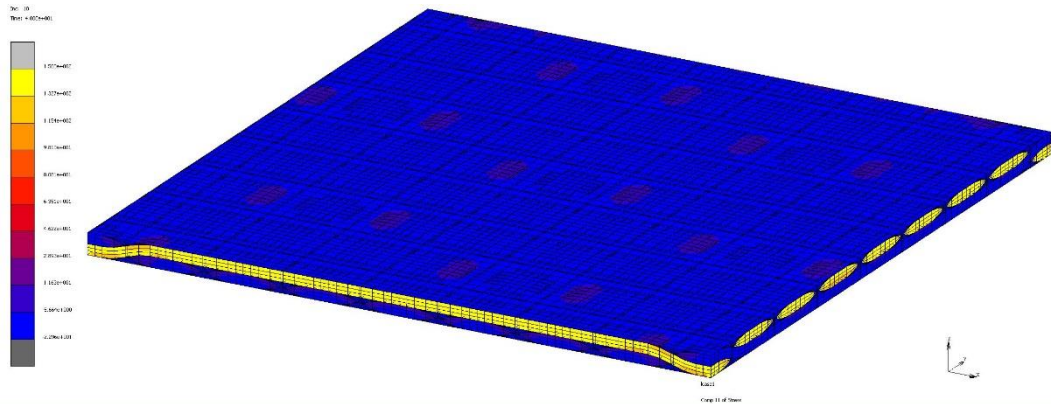


b)

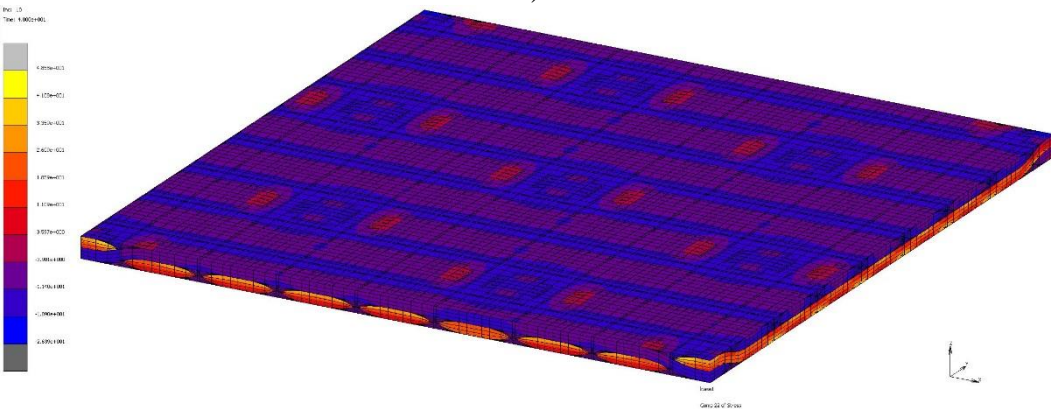


c)

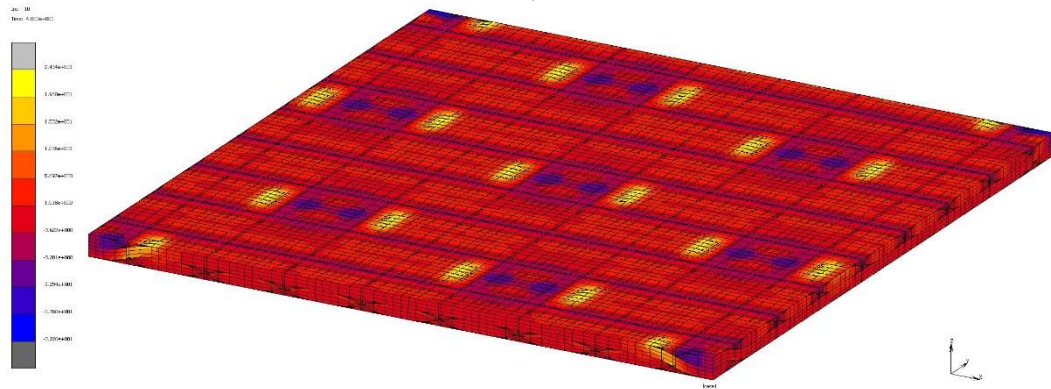
Figure F4. Stress contours of 5320-8HS unit cell loaded along fill direction at $t=20s$ under isothermal condition of 80°C a) Component 11 of stress b) Component 22 of stress c) Component 33 of stress



a)



b)



c)

Figure F5. Stress contours of 5320-8HS unit cell loaded along fill direction at $t=40s$ under isothermal condition of 80°C a) Component 11 of stress b) Component 22 of stress c) Component 33 of stress

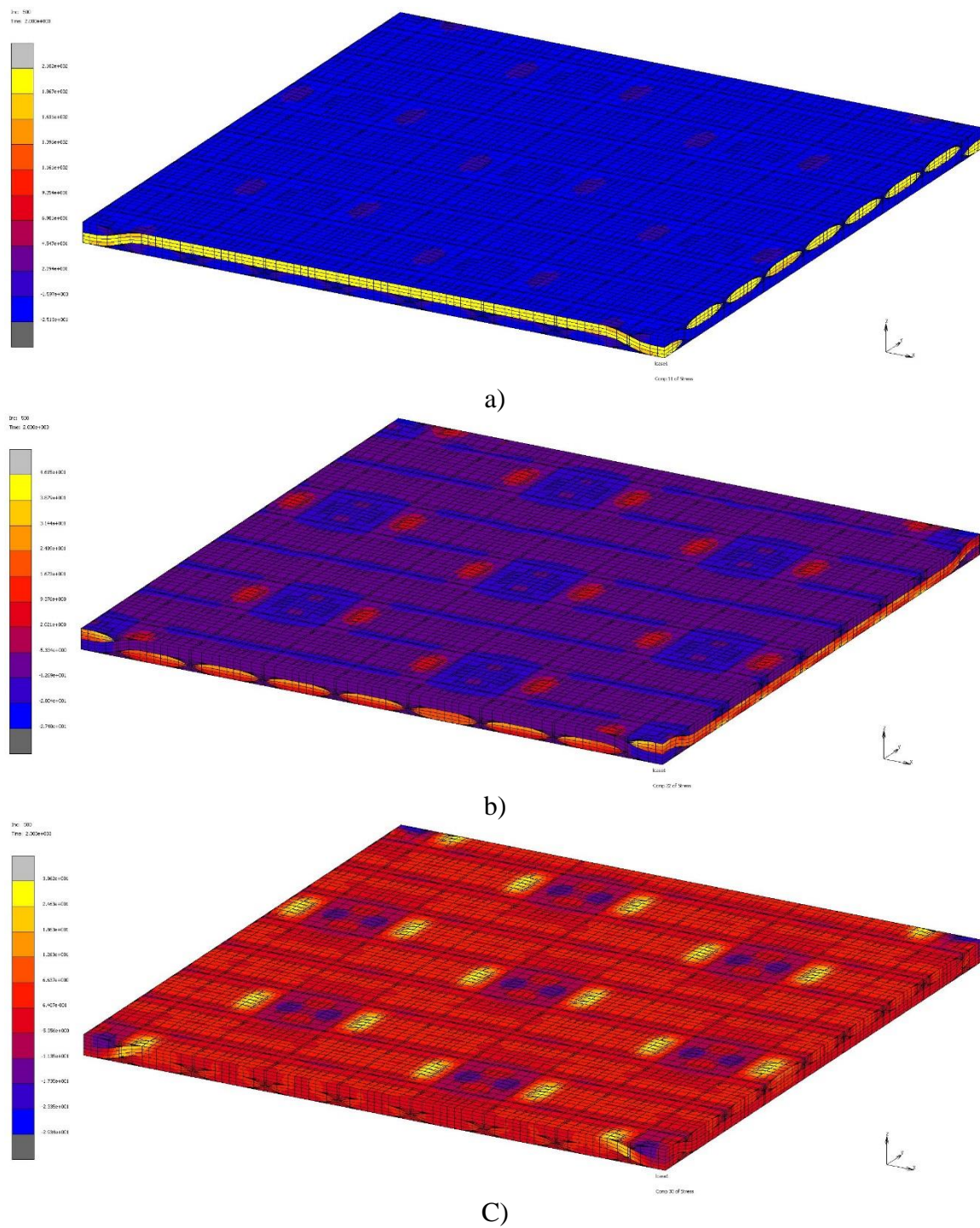


Figure F6. Stress contours of 5320-8HS unit cell loaded along fill direction at $t=2000$ s under isothermal condition of 80 °C a) Component 11 of stress b) Component 22 of stress c) Component 33 of stress

F3. Stress distribution of laminate model (Macromechanical analysis)

F3.1 [0/90]s Laminate model

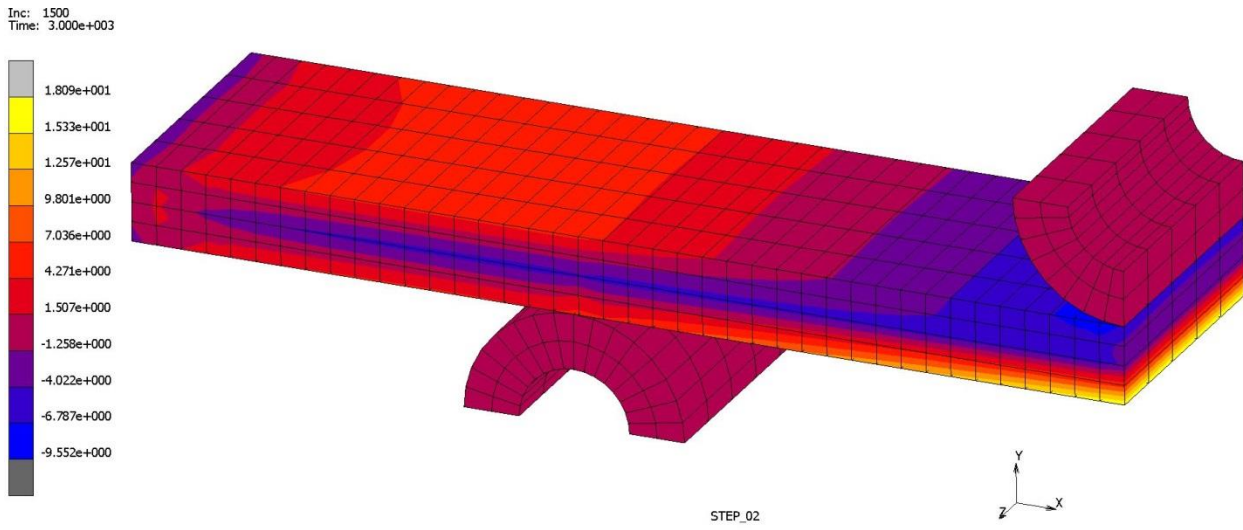


Figure F7. Stress contours for component 11 of stress

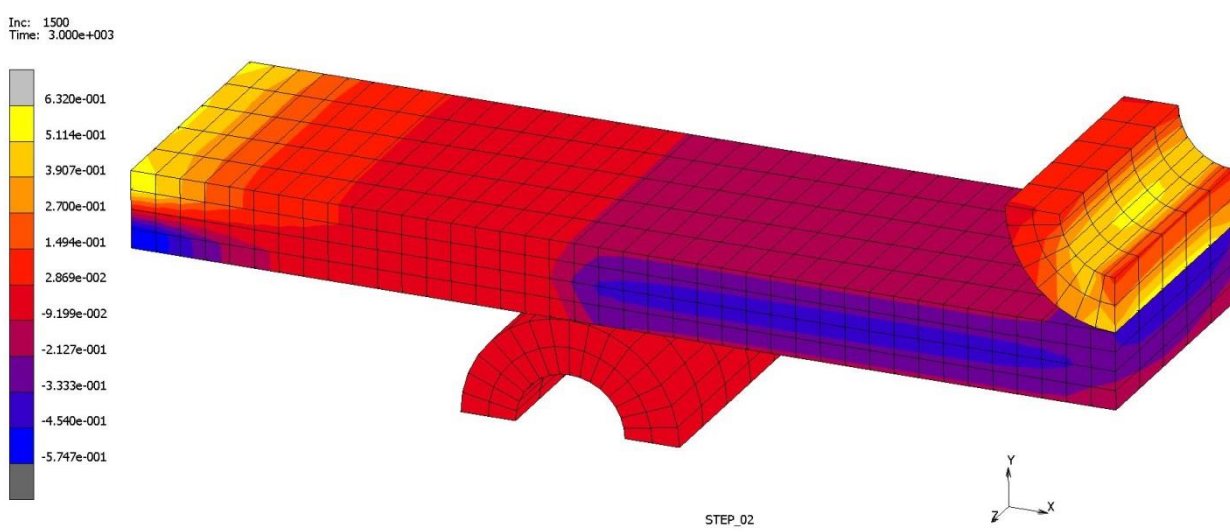


Figure F8. Stress contours for component 12 of stress

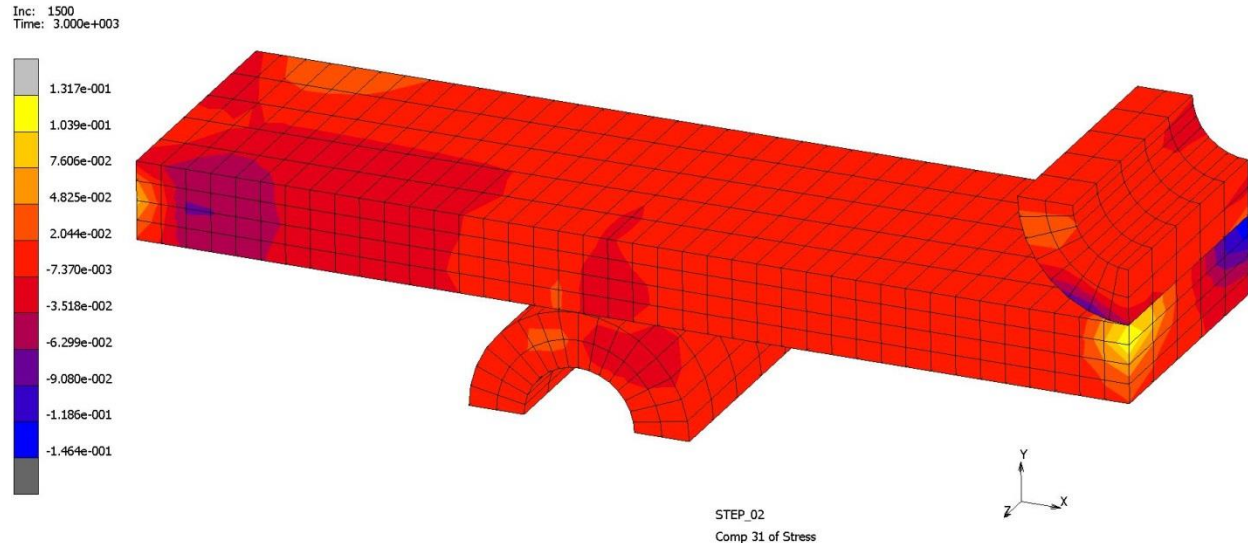


Figure F9. Stress contours for component 31 of stress

F3.2 [$\pm 45^\circ$]s Laminate model

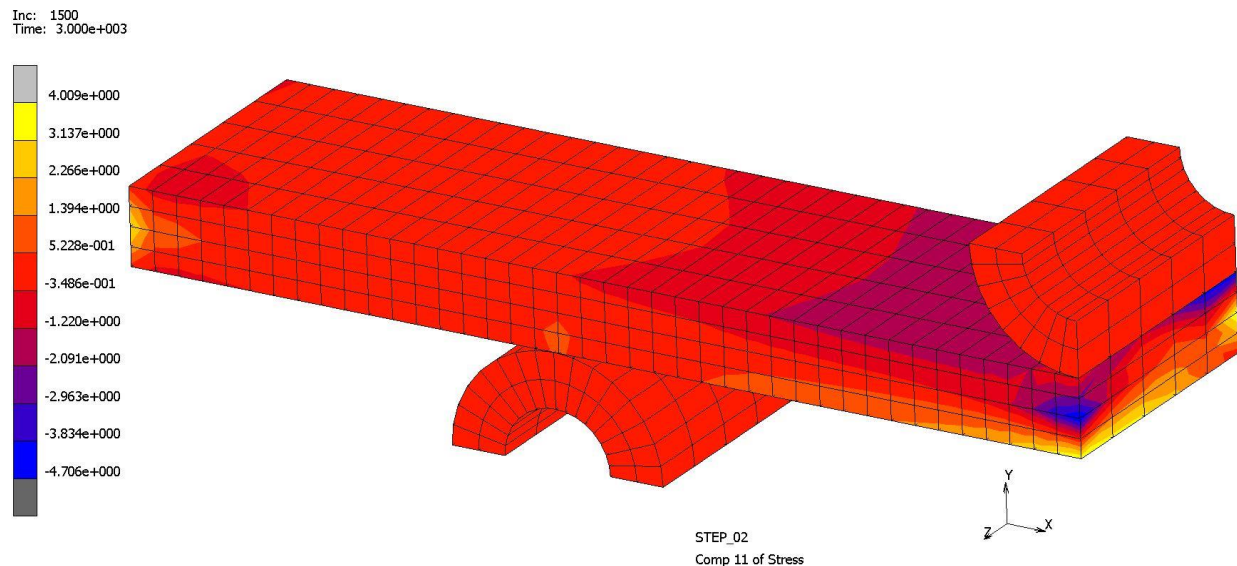


Figure F10. Stress contours for component 11 of stress

Inc: 1500
Time: 3.000e+003

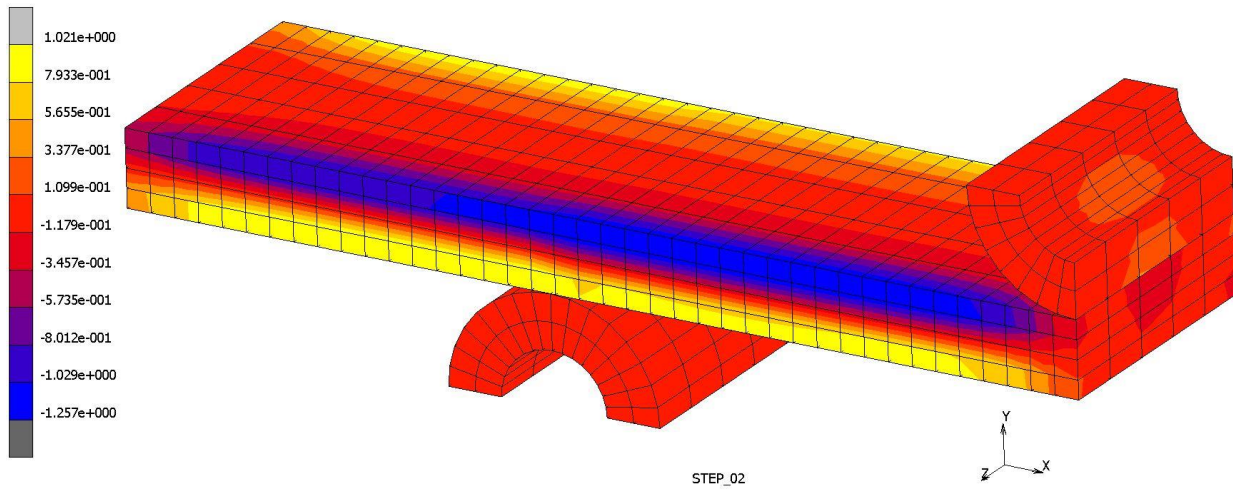


Figure F11. Stress contours for component 12 of stress

Inc: 1500
Time: 3.000e+003

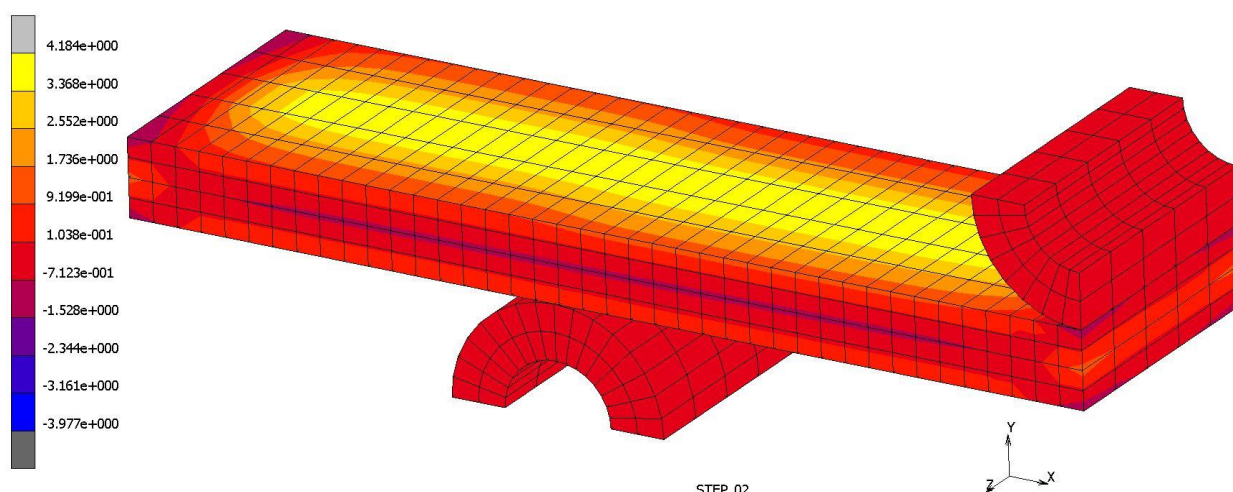


Figure F12. Stress contours for component 31 of stress